AD NUMBER

ADB028240

LIMITATION CHANGES

TO:

Approved for public release; distribution is unlimited.

FROM:

Distribution authorized to U.S. Gov't. agencies only; Test and Evaluation; JAN 1976. Other requests shall be referred to Arnold Engineering Development Center, Arnold AFB, TN.

AUTHORITY

AEDC ltr 28 Jul 1990

AEDC-TR-78-25
Cy. 1

WIND TUNNEL RESULTS FROM A NOZZLE AFTERBODY TEST OF A 0.1-SCALE FIGHTER AIRCRAFT IN THE MACH NUMBER REGIME OF 0.6 TO 1.6

Ernest J. Lucas
ARO, Inc., a Sverdrup Corporation Company

PROPULSION WIND TUNNEL FACILITY
ARNOLD ENGINEERING DEVELOPMENT CENTER
AIR FORCE SYSTEMS COMMAND
ARNOLD AIR FORCE STATION, TENNESSEE 37389

June 1978

Final Report for Period June 1975 — January 1976

Prepared for

ARNOLD ENGINEERING DEVELOPMENT CENTER/DOTA
ARNOLD AIR FORCE STATION, TENNESSEE 37389

NOTICES

When U. S. Government drawings, specifications, or other data are used for any purpose other than a definitely related Government procurement operation, the Government thereby incurs no responsibility nor any obligation whatsoever, and the fact that the Government may have formulated, furnished, or in any way supplied the said drawings, specifications, or other data, is not to be regarded by implication or otherwise, or in any manner licensing the holder or any other person or corporation, or conveying any rights or permission to manufacture, use, or sell any patented invention that may in any way be related thereto.

Qualified users may obtain copies of this report from the Defense Documentation Center.

References to named commerical products in this report are not to be considered in any sense as an indorsement of the product by the United States Air Force or the Government.

APPROVAL STATEMENT

This report has been reviewed and approved.

Russell B. Sorrells III

RUSSELL B. SORRELLS, III
Project Manager, Analysis and Evaluation Division
Directorate of Test Engineering

Approved for publication:

FOR THE COMMANDER

Marion L. Laster

MARION L. LASTER
Director of Test Engineering
Deputy for Operations

REPORT DOCUMENTATION PAGE		READ INSTRUCTIONS BEFORE COMPLETING FORM
1 REPORT NUMBER AEDC-TR-78-25	2 GOVT ACCESSION NO	3 RECIPIENT'S CATALOG NUMBER
4 TITLE (and Subtitle) WIND TUNNEL RESULTS FROM A NOZZLE AFTER-BODY TEST OF A 0.1-SCALE FIGHTER AIRCRAFT IN THE MACH NUMBER REGIME OF 0.6 TO 1.6		5 TYPE OF REPORT & PERIOD COVERED Final Report - June 1975 - January 1976 6 PERFORMING ORG REPORT NUMBER
7 AUTHOR(s) Ernest J. Lucas, ARO, Inc.		8 CONTRACT OR GRANT NUMBER(s)
9 PERFORMING ORGANIZATION NAME AND ADDRESS Arnold Engineering Development Center/DOT Air Force Systems Command Arnold Air Force Station, Tennessee 37389		10 PROGRAM ELEMENT PROJECT, TASK AREA & WORK UNIT NUMBERS Program Element 65807F and 62203F
11 CONTROLLING OFFICE NAME AND ADDRESS Arnold Engineering Development Center/DOS Arnold Air Force Station, Tennessee 37389		12. REPORT DATE June 1978 13 NUMBER OF PAGES 170
14 MONITORING AGENCY NAME & ADDRESS (if different from Controlling Office)		15 SECURITY CLASS (of this report) UNCLASSIFIED 15a DECLASSIFICATION DOWNGRADING SCHEDULE N/A

16 DISTRIBUTION STATEMENT (of this Report)
Distribution limited to U.S. Government agencies only; this report contains information on test and evaluation of military hardware; June 1978; other requests for this document must be referred to Arnold Engineering Development Center/DOS, Arnold Air Force Station, Tennessee 37389.

17 DISTRIBUTION STATEMENT (of the abstract entered in Block 20, if different from Report)

18 SUPPLEMENTARY NOTES

Available in DDC

19 KEY WORDS (Continue on reverse side if necessary and identify by block number)

fighter aircraft	aerodynamic loading	boundary layer transition
YF-17	pressure distribution	transonic flow
nozzles	tail assemblies	wind tunnel tests
performance (engineering)	deflection	

20 ABSTRACT (Continue on reverse side if necessary and identify by block number)

An investigation was conducted in the Propulsion Wind Tunnel (16T) to obtain throttle-dependent aft end drag on a one-tenth scale model of a twin-engine fighter aircraft (YF-17). These data will be used in assessing the validity of current wind tunnel data acquisition techniques. Pressure data were obtained for several configurations, using a wingtip support system, to define the effects of jet exhaust flow on afterbody pressure distributions.

DD FORM 1 JAN 73 1473 EDITION OF 1 NOV 65 IS OBSOLETE

20. ABSTRACT (Continued)

Data were also obtained with an dual sting support system and dummy wingtip booms to evaluate the interference introduced by the model wingtip support. This interference was on the order of twelve aircraft drag counts (ΔC_D = 0.0012) at Mach number 1.2 and tended to decrease as the test Mach number was either increased or decreased. Changes in nozzle exit area for afterburning simulation produced significant local flow-field disturbances on the model aft end, but the increased pressure levels produced on the afterbody were compensated for by the decreased pressure levels on the nozzle so that the effect on the drag was less evident. Model attitude changes and tail control surface deflections also produced significant effects in the local surface pressure distributions. However, these local differences also tended to produce compensating effects in the pressure drag integration over the aft end of the model.

PREFACE

The work reported herein was conducted by the Arnold Engineering Development Center (AEDC), Air Force Systems Command (AFSC), under sponsorship of the Air Force Aero-Propulsion Laboratory (AFAPL/TBA), Wright-Patterson Air Force Base, Ohio and AEDC/DOTA, under Programs Element 65807F and 62203F. The results were obtained by ARO, Inc., AEDC Division (a Sverdrup Corporation Company), operating contractor for the AEDC, AFSC, Arnold Air Force Station, Tennessee. Testing was conducted under ARO Projects No. P41S-30A and P41T-D3A during June 1975 and January 1976, respectively, in support of analysis Project P43T-71A. The Air Force project manager for this program was Mr. R. B. Sorrells, AEDC/DOTA. Data analysis was completed on October 12, 1977, and the manuscript was submitted for publication on March 16, 1978.

CONTENTS

ILLUSTRATIONS

Figure

Page

TABLES

1.0 INTRODUCTION

In general, the aerodynamic loads obtained with wind tunnel force models have to be extrapolated to predict the performance of the full-scale flight vehicle. Additionally, the data require corrections to the afterbody loads for local jet exhaust effects which cannot be adequately measured with a typical force model. These corrective increments are usually obtained from models which utilize high-pressure air to produce a jet flow stimulation. Thus, data in the form of afterbody shell balance loads or integrated surface pressure loads can be obtained to provide the change in the vehicle loading produced by afterbody configuration and jet exhaust plume interaction with the local flow field.

This investigation was part of an effort to verify the present wind tunnel data acquisition techniques and provide direction for improvements to provide the most accurate data base for flight vehicle performance calculations. Since it is not practical to obtain nozzle/afterbody force data from a flight vehicle, it was decided to obtain surface pressure data from a wind tunnel model for future direct comparison with data from a pressure instrumented flight vehicle. A 0.1-scale, YF-17 model previously tested at Arnold Engineering Development Center (AEDC) was modified to provide surface pressure data from the afterbody and nozzle outer surface. Throttle-dependent (jet exhaust) drag effects were defined by using a wingtip support system which allowed free, unaltered, nozzle exits for jet simulation. A second tunnel entry was conducted with the model installed on a sting support to define the effects of the wingtip support on the aft end pressure distributions.

Both wind tunnel entries were conducted in the Mach number range of 0.6 to 1.6. Reynolds number effects were investigated during the first entry (wingtip-supported model) along with the jet effects study for three nozzle closures. These nozzles which represented closures from dry power to maximum afterburning were operated from jet-off up to approximately twice the design pressure ratio. The sting support entry was conducted at a nominal Reynolds number of 2.8×10^6/ft and, since the model was then sting supported through the exhaust nozzles, only a solid cylindrical plume was simulated. An auxiliary exhaust, bay purge, was simulated on this support to define the extent and magnitude of this additional flow over the model aft end. Model angle of attack and horizontal tail deflection angles were varied in the ranges of 0 to 8 deg and 0 to -5 deg, respectively.

2.0 APPARATUS

2.1 TEST FACILITY

Tunnel 16T is a closed-circuit, continuous flow wind tunnel capable of being operated at Mach numbers from 0.20 to 1.60. The tunnel is capable of operating within a

stagnation pressure range from approximately 160 to 4,000 psfa, depending upon the Mach number, and over a stagnation temperature range from 80 to a maximum of 160°F. The specific humidity of the air is controlled by removing tunnel air and supplying conditioned makeup air from an atmospheric drier. A more extensive description of the tunnel and its operating characteristics is contained in Ref. 1.

2.2 TEST ARTICLE

2.2.1 Wingtip Support

Results discussed in this report were obtained from wind tunnel tests on a 0.1-scale model of the twin-engine YF-17 aircraft. The model was designed to be supported by the wingtips to obtain the aft end jet effects (see Fig. 1). Model location in the wind tunnel test section is indicated in Fig. 1c, and a dimensioned sketch of the model is shown in Fig. 2.

High-pressure air at approximately 100°F was used to simulate the jet exhaust flow during the initial test phase conducted with the wingtip support system. This air was supplied through the supports and wings to an internal model plenum from which the flow then accelerated through the model nozzles. Modifications were required to the wings outboard of 55 percent span for structural support and to provide room for the high-pressure air supply passages (see Fig. 2).

2.2.2 Sting Support

An additional model support system was used to define the effects of the wingtip supports on the model aft end surface pressures. For these investigations, the model was supported by dual stings through the twin nozzles (Fig. 3a) without altering the outer model contour. These support stings, 3.40-in.-diam, completely filled the cruise nozzle exit and were tapered as shown in Fig. 3b for structural consideration. Removable wingtip support simulators could be attached to the actual wing through the use of simulated wing gloves (Fig. 3c) which duplicated the modification required on the wingtip supported model.

The pitot probe used with the model during the wingtip support test was also installed during this phase of testing. Additionally, a simulation of the nose strake was utilized on the model for the sting support test. These items are shown in Fig. 4.

2.2.3 Empennage

Twin vertical tails and "all flying" horizontal tails were located as shown in Fig. 2. Root chord of the horizontal tail extended from fuselage station (FS) 61.2 to FS 68.9,

the nozzle connect station. Horizontal tail deflection was accomplished by using insert blocks which allowed tail rotation about FS 64.8. Deflection angles of 0, -2, and -5 deg (leading edge down) were available. The twin vertical tails were located on the outboard portion of each nacelle and extended from FS 52.3 to FS 63.8 at the model surface.

2.2.4 Exhaust Nozzles

The three nozzle configurations tested represent the closure range of the dual flap nozzles used on the flight vehicle. The flight vehicle nozzles have primary iris-type nozzle plates which rotate to alter the internal area ratio for proper jet expansion at a given throttle setting. The outer surface on these nozzles consists of sets of overlapping leaves which are driven by primary plate movement to maintain a continuous closed surface contour. Thus, as the closure changes, the effective axial projected area that is sensitive to the local surface pressures is altered.

The model representation of the three closure configurations used to span the aircraft operable range is shown in Fig. 5. Model nozzles consisted of an internal flow duct and a separate external shell which contained the surface pressure instrumentation. High-pressure air was uniformly distributed through the internal flow duct by the use of choke plates and screens. Total-pressure rakes located in the model plenum upstream of the nozzle throat were used to monitor the simulated jet flow.

2.2.5 Surface Pressures

Model afterbody and nozzle surface pressure distributions were obtained from approximately 200 orifices located on the left side of the model. Pressure orifice locations for the forebody, afterbody, and nozzle are shown in Figs. 6a, b, and c, respectively. These locations are defined in Tables 1 and 2 for the afterbody and nozzles.

2.2.6 Auxiliary Exhaust

An exhaust exit was simulated on the model, as shown in Fig. 7, to define the extent and magnitude of the disturbance created by the engine bay purge exhaust flow of the aircraft. Openings were located at the top and bottom centerline of the left afterbody. Flow to each exit was supplied through a common piping system that allowed for a top-to-bottom split depending on the local pressure at the exhausts. This system would also allow for crossflow between the top and bottom exhaust ports through the supply lines when the auxiliary airflow simulation was not required. Therefore, plugs were supplied to seal the exits when the auxiliary flow system was not being utilized.

2.3 INSTRUMENTATION

Model surface pressures were measured with five multiport Scanivalves® using 15-psid Druck® transducers. Transducer sensitivity and zero output level were checked on each data point. Reference pressure was applied to both sides of the transducer and this output recorded as the zero level at the beginning of each data scan. Calibrate pressure was also applied to each transducer during each data scan and the output recorded. At the same time, this calibrate pressure was measured on a 5-psid CEC® transducer such that a constant for the Scanivalve transducer in psi per count was obtained. Thus the system could maintain a current calibration and zero reference for each data scan. The Scanivalve was operated by a facility computer in a step-pause mode which monitored each pressure for stabilization before advancing to the next port. Pressures that did not meet the stabilization criteria were identified for engineering scrutiny.

Internal duct flow and the metering section pressures were measured on CEC transducers of the appropriate range. Temperature measurements were made with copper-constantan thermocouples and recorded on the standard tunnel integrating analog-to-digital converters. Calculated temperatures are considered accurate to within ±2°F.

Model attitude was determined utilizing a model-mounted, angular position indicator. This device operates on a strain-gage output activated by a pendulum deflection as the model is moved from the pre-established zero reference position. Model roll and yaw angles were set to zero during installation and were not varied for these tests.

3.0 PROCEDURE

3.1 DATA ACQUISITION AND TECHNIQUE

Model surface pressure data were obtained on several model configurations at transonic Mach numbers as itemized in Table 3. The model left nozzle and afterbody contained the majority of the pressure taps. Each pressure was assigned to a given surface area so that aft end forces could be obtained from a pressure-area integration. These pressure loads were converted to coefficients based on the free-stream dynamic pressure and the planform model-wing reference area. Adjustments were made in the area distribution by reassigning the bad pressure areas to selected pressures for that configuration. Empennage loads were not included in the aft end loads since pressure instrumentation was not included on the tails. The tails, however, were on the model throughout these investigations thus influencing the aft end.

Model mass flows for the main jet and auxiliary exhaust were measured with the facility venturi system. Main jet flow rate was calculated with a turbulent flow discharge coefficient based on the venturi throat Reynolds number. Additional corrections were applied for compressibility and real gas effects. Auxiliary flow utilized a smaller venturi at lower supply pressures so that a laminar discharge coefficient was used with the aforementioned corrections.

Data were obtained at established test conditions by either setting a constant nozzle pressure ratio (NPR) and varying the model angle of attack (α) or varying the NPR at a constant angle of attack.

3.2 UNCERTAINTY OF MEASUREMENTS

Data were obtained with the facility-maintained instrumentation for which valid calibrations are known. Based on a two-sigma statistical estimate of uncertainty (UCP = bias plus twice the precision) the following uncertainties are presented:

M_∞	$Re \times 10^6, ft^{-1}$	P_∞, psfa	$(P_j)_{avg}$, psfa	Q_∞, psfa	UCP_j
0.6	2.8	1,440	1,403	362	0.0157
0.9	2.8	868	831	490	0.0098
1.2	2.8	566	372	572	0.0096

Model angle of attack is considered accurate to within ±0.1 deg.

Observable trends and repeatability of the data indicate that a $\Delta C_p = 0.005$ is representative of the repeatability of the pressure coefficients from this investigation. Applying this delta over the axial projected area of both the nozzle and afterbody would produce an axial-force coefficient, $[(\Delta C_p) \times 2(\Sigma A_j/S)]$, of approximately three drag or axial-force coefficient counts (±0.0003).

4.0 RESULTS AND DISCUSSION

Results presented herein were obtained from wind tunnel investigations with a one-tenth scale model of a twin-engine fighter-type aircraft (YF-17) to define the throttle-dependent aerodynamic effects. This compilation of surface pressure data with support system interference definition will form the data base for a follow-on wind tunnel-to-flight correlation effort. Effects of model variables and attitude are thus documented in this report with data presentation oriented to the predicted flight attitudes.

4.1 SUPPORT SYSTEM INTERFERENCE

The definition of jet flow or throttle-dependent effects require testing with a model support system which will allow jet exhaust simulation with a valid aircraft aft end. This requirement leads the investigator to a strut or wingtip support system which will allow a full flowing jet, since a sting system normally would be restricted to solid plumes or annular jets. Previous force tests (Refs. 2, 3, and 4) have been conducted on this model for configuration optimization. These force tests were used to select the best available support system for definition of throttle-dependent effects. However, since the purpose of the present investigation is to obtain a data base for correlation with surface pressure data from a flight vehicle, the local effects of model variables on the flow field had to be defined. In addition, the support system interference effects also had to be defined for the model pressures. Thus a separate support using twin stings, which completely filled the nozzle exits, was used to assess the effects of the wingtip support. Differences between the sting-mounted model with and without the wingtip support simulation were defined as the support system interference effect.

Changes in the local surface pressures produced by the support system are presented in Fig. 8 for each aft end closure studied at the anticipated flight conditions. These differences between the individual pressure coefficient values from the simulated wingtip support minus the clean wing values are defined as the delta pressure coefficient (DCP). Effects of the wingtip support system are not significant (DCP ~ 0.005) at Mach number 0.6. Thus, at low subsonic Mach numbers, a support system correction would not be required. As the test region is increased to Mach numbers 0.9 and 1.2 (Figs. 8b and c), the maximum local support system interference effects increase (DCP = 0.09 and -0.07 at M_∞ = 0.9 and 1.2, respectively) such that corrections would be required before the data could be used for a free-flight comparison. Also of interest in these two data presentations is the compensating effect (positive and negative DCP's) which tend to cancel in the pressure area integration. Thus, it would be possible to indicate no significant effect of a parameter when analyzing the overall performance (C_A or C_D) while local differences could be important for design or strength consideration.

Since this study was oriented to throttle-dependent effects, the overall change in performance parameters was also of interest. Thus, as previously mentioned, the surface pressure data were used to define the aft end axial or drag pressure load by summing the pressure area terms. The axial area distribution associated with this calculation is shown in Fig. 9. Utilizing this method, the wingtip support system pressure drag interference is thus defined and presented in Fig. 10 for the three nozzle closures investigated. In general, the interference is relatively insensitive to model attitude. The interference increases with Mach number up to Mach number 1.2 (ΔC_D ~ 0.0012) then decreases at

the higher Mach number test conditions. This could indicate a support system-model blockage effect. Whatever the cause, it is evident that, if the data obtained on a particular support system are to be used for purposes other than configuration optimization, these effects must be properly defined and applied for performance predictions or wind tunnel-to-flight correlation attempts.

4.2 AUXILIARY EXHAUST FLOW EFFECTS

Engine bay purge exits were located on the aircraft so that their exhaust flow could affect flow over the afterbody and nozzle surfaces. Extent and magnitude of this flow was investigated with the maximum closure (cruise) and most open (maximum) nozzles. Engine bay purge flow, which vents the fuel vapors from the cavity between the vehicle outer skin and the engine shell, was simulated with externally supplied air. This air was exhausted through the interconnected top and bottom ducts on the model left nacelle.

Local effects of the bay purge flow are illustrated in the DCP plots of Fig. 11. As expected, the exhaust produced results similar to a jet exhausting normal to the flow. Pressures upstream of the jet exhaust are elevated and increase with bay purge weight flow. Maximum measured differences were on the order of DCP ~ 0.10 subsonically and 0.17 supersonically. These disturbances tend to feed outboard and downstream from the exhaust and, as with a lateral jet, decrease the downstream local pressures below the no-flow level on the aft end of the model. This compensation effect, though smaller on the aft end, has more projected area to act upon so that the overall effect on performance is lessened.

The pressurization of the aft facing areas decreased the vehicle drag from three to five counts (ΔC_D = 0.0003 to 0.0005) as shown in Fig. 12. These effects were fairly constant with model attitude and generally increased with flow rate. Flow rates were simulated which exceeded the estimated maximum scaled bay purge flows of the flight vehicle. The effects shown, therefore, should be larger in magnitude and extent than on the actual vehicle so that maximum differences and areas of influence attributable to the bay purge exhaust can be inferred.

4.3 NOZZLE CLOSURE EFFECTS

Data used in the previous sections were obtained with the sting support system to provide corrective increments for the wingtip-supported model data base. The remainder of the data discussed was obtained with the wingtip support system which allowed main-jet-flow exhaust simulation. Also, since the investigation is related to throttle-dependent effects, the overall effects on the wingtip-supported model will be presented in the thrust line axis (axial force).

Vehicles with variable exhaust nozzles, such as the YF-17, have the ability to alter the internal nozzle contour to obtain maximum utilization of the available jet thrust. Changing the internal surfaces, however, alters the external surface contour, affecting the axial projected area and the flow field which acts on it. The changes in the local surface pressure distributions as the nozzle contour is altered at a fixed nozzle pressure ratio, ratio of the nozzle total pressure to the free-stream static pressure (NPR), are shown in Fig. 13. This presentation indicates the errors one would have to account for should the flight vehicle nozzle closure be different than the test article. Opening the nozzle (decreasing closure) increases the surface pressures with a significant influence extending upstream to model station (MS) 62 or 64. The effect is more evident at the nozzle connect station (MS 69) where the external flow field expands over the afterbody and onto the nozzle. As the nozzle opens this expansion is lessened, thus increasing the local surface pressures at the expansion and surrounding areas. The nozzle surface pressures, though not so orderly as the afterbody region, indicate significant changes in the flow field with closure variation.

These surface pressure changes are more clearly shown in the DCP presentation of Fig. 14. As the nozzle is opened, in general, the nozzle surface pressures are lowered on the upstream portion of the nozzle then elevated on the downstream portion. Maximum surface pressure coefficient differences on the nozzle (FS > 69) are on the order of DCP = ±0.08. Afterbody differences (FS < 69) also shown in this presentation vary from DCP = 0 to 0.06 for the nozzle closures tested.

The increase in afterbody surface pressure with decreasing closure at a fixed nozzle pressure ratio tends to decrease the afterbody axial load (Fig. 15) since the projected area of the afterbody is invariant with closure. This decrease in loading at NPR = 5.0 was on the order of three counts ($\Delta C_A \sim 0.0003$) between the cruise and reheat nozzles and six counts ($\Delta C_A \sim 0.0006$) between the reheat and maximum nozzle configurations. In contrast to the afterbody, the nozzle loadings became less negative (increasing axial force) as the nozzle opened. This trend reflects the decrease in projected area with decreased closure (opening nozzle) as shown in Fig. 9. Thus, the change in axial projected area overpowers the random pressure trends on the nozzles such that the nozzle loads increase about four counts ($\Delta C_A \sim 0.0004$) between the cruise and reheat nozzle and an additional four counts between the reheat and maximum nozzle closure configurations.

Combining these effects produces the total aft end load effects which indicates a maximum difference of only two counts ($\Delta C_A = 0.0002$) at NPR = 5. Thus, the total aft end loads are relatively insensitive to nozzle closure while the components indicate measurable effect. Likewise, the surface pressure data indicate significant effects for

consideration in a correlation attempt. Also the configuration-dependent random variation of the nozzle area surface pressures would seem to preclude interpolation to the correct nozzle closure. Therefore, this configuration variable would require duplication between model and flight vehicle to obtain a valid correlation.

4.4 MODEL ATTITUDE

Data presented in Figs. 16, 17, and 18 indicate the effect of model attitude on the surface pressure distributions at Mach numbers 0.6, 0.9, and 1.2, respectively. Trends of the pressures with model pitch are as expected with the windward side pressures increasing and the lee side pressures generally lowered on the afterbody. These trends are distinct and consistent at Mach numbers 0.6 and 1.2, whereas the data at Mach number 0.9, Fig. 17, indicate less sensitivity to model attitude.

The effect of incremental changes in angle of attack on the local surface pressure distributions is presented in Fig. 19 for the above test conditions. Data at Mach number 0.6 indicate a quasi-linear variation of model surface pressures with model angle of attack (DCP $\sim$ $\pm$0.02 for 2-deg attitude change). Similar results are seen on the lee side of the reheat nozzle configuration at Mach number 1.2 (Fig. 19c) (DCP = $\pm$0.06). That is, changes in pressure are the same magnitude for each increment in angle of attack. Random variations are still evident at Mach number 0.9, ranging from DCP = -0.02 to 0.04, and the windward side of the model at Mach number 1.2, DCP = $\pm$0.08. Model attitude is thus shown to be a major influence in the surface pressure level and distribution but appears to be a parameter on which a linear interpolation could be used to define the pressure field at a specific attitude in a correlation attempt.

Overall performance effects of model attitude were on the order of only three to five counts (ΔC_A = 0.0003 to 0.0005) within the investigation region of up to 8 deg (see Fig. 20). Afterbody loads appear more sensitive to pitch attitude subsonically with the compensating pressure effects on the nozzle tending to hold the nozzle loads constant. The axial load levels are higher supersonically (Fig. 20b), and the nozzle region is more sensitive to model pitch attitude. This effect is about three counts (0.0003) which, though measurable and orderly, is on the order of the repeatability of the axial load from the pressure integration.

4.5 NOZZLE PRESSURE RATIO (JET EXHAUST) EFFECTS

The current wind tunnel test procedure utilizes high-pressure air at ambient temperature for plume simulation to obtain aft end jet effects on subscale models. The ratio of the nozzle total pressure upstream of the throat to the free-stream static pressure (NPR) is used to operate the nozzles at the required pressure for a specific test condition.

Nozzle design NPR is defined as a function of the nozzle throat-to-exit area such that the nozzle exit pressure is equal to the free-stream static pressure. Temperature effects are not covered in this investigation, but the results presented should be conservative since the general effect of higher temperature exhaust gas at design NPR has been found (Ref. 5) to reduce the aft end axial force.

Effects of varying the NPR in the vicinity of the design value at the three primary test Mach numbers are shown in Fig. 21. Local changes in the pressure field are generally confined to the nozzle and expansion region downstream of FS 69. The cruise nozzle configuration which operates mainly in the subsonic regime at low NPR's indicates small sensitivity to NPR changes ($DCP_{max} \sim 0.01$) at the model angle of attack presented (Fig. 21a). As the nozzle is opened to the afterburning settings, these effects are still confined to the nozzle and aft section of the afterbody (Figs. 21b and c). The magnitude of the effect, however, increases to $DCP_{max} = 0.04$ and 0.12 on the intermediate nozzle closure configuration at Mach numbers 0.9 and 1.2, respectively. Largest effects are observed on the maximum nozzle, least closure, at supersonic conditions (Fig. 21d). Pressure coefficient differences of up to DCP = 0.20 are evident on the nozzle's outboard row (ϕ = 225 deg). Even with these large local differences, the effects are still confined downstream of MS 66 to 68. These effects of NPR on the local surface pressures are orderly, and increase as NPR increases, so the data could probably be interpolated to off-test conditions for a correlation effort.

Aft end integrated surface pressure loadings presented in Fig. 22 further illustrate the isolation of NPR to the nozzle portion of the model. Pressurization of the aft-facing surface as the NPR is increased above the design value reduces the aft end loads. A unit change in NPR from the design ratio for each nozzle produces changes in the nozzle axial loads from one count on the cruise nozzle at subsonic conditions up to ±6 counts (ΔC_A = ±0.0006) on the maximum nozzle configuration at the supersonic conditions. Afterbody loading was not significantly affected by NPR variations around the design value.

4.6 HORIZONTAL TAIL DEFLECTION EFFECTS

The YF-17 all flying horizontal tail root chord extends from FS 61.2 to 68.9. As this surface is deflected for maneuvers or vehicle trim, changes in the local surface pressure distribution are evident on the afterbody and nozzle. Deflecting the horizontal tail leading edge down increases the local pressures above the tail plane and decreases those below the plane (see Fig. 23). These changes in the local pressure field are then readjusted through the expansion over the nozzle connect region (FS 69) to the aft end pressure level. A 2-deg deflection of the tail produces a change in the pressure coefficient

of DCP ~ ±0.04 subsonically and up to a maximum of DCP = 0.10 at M_∞ = 1.2. These changes with the tail deflection are orderly (Fig. 23c) such that adjustments could be made to the data for an off-condition match.

Effects on the axial loads with tail deflection are presented in Fig. 24 for the angles of attack investigated at M_∞ = 0.6. Afterbody integrated pressure load is increased approximately two counts (ΔC_A ~ 0.0002) for a 2-deg tail deflection. This effect is relatively insensitive to model angle of attack. Although surface pressure changes shown in Fig. 23 were of the same order on the nozzle as on the afterbody, the nozzle loading shown does not indicate any effect of tail deflections. The nozzle integrated loads thus conceal the local variations in the surface pressures. This again illustrates the need to obtain the surface pressure data for the correlation attempt to define local differences even though previous force data were available on the model.

4.7 REYNOLDS NUMBER EFFECTS

Changes in the local surface pressure coefficients as a result of varying the Reynolds number from the nominal test value of 2.8 x 10^6/ft are shown in Fig. 25a. Only the lowest Reynolds number produces any significant change in the afterbody distribution. This lowest test condition, Reynolds number of 1.7 x 10^6/ft, produced local changes of DCP = 0.01 over the total afterbody. Results at the higher Reynolds number conditions indicate less change in the afterbody surface pressures indicating a more fully developed flow; these data should be directly applicable to flight condition predictions. Nozzle area pressures again indicate local differences on the order of DCP = ±0.01 subsonically and increasing up to DCP = 0.06 at M_∞ = 1.2. These differences, in general, tend to be compensating.

Subsonically nozzle integrated pressure axial loads verify the compensating pressure effect since the effects of Reynolds number are too small to be measured (Fig. 25d and e). Afterbody loadings, however, show the low Reynolds number effect previously discussed. These pressure data obtained at the nominal Reynolds number should thus be applicable to the flight conditions since this appears to be the plateau level for the tunnel available range. Supersonically the cruise nozzle axial loading (Fig. 25f) indicate a larger Reynolds number effect, probably the result of local shock-boundary layer interaction. The cruise nozzle closure is not representative of the actual setting for Mach 1.2 flight and probably has an extensive separated region on the nozzle to accentuate the effects indicated. The reheat nozzle (Fig. 25f), which is more representative of the actual vehicle closure for M_∞ = 1.2, indicates trends similar to those discussed subsonically. Thus, if the proper nozzle closure is considered at the appropriate Mach number the supersonic results at the nominal test conditions should also be applicable to a correlation attempt.

Since there is a difference between the aircraft and test article boundary layers, an additional investigation to assess the effects of boundary-layer transition grit as normally used on force models was undertaken. Boundary-layer transition grit was applied to the nose and leading edge of the wings. Results of the boundary-layer trip was a general elevation of the afterbody and nozzle surface pressures. This difference was on the order of DCP = 0.01 as shown in Fig. 26a. Both the afterbody and nozzle axial pressure loadings were likewise decreased with the addition of the boundary-layer trip (Fig. 26b).

5.0 SUMMARY OF RESULTS

This investigation was performed to provide a data base for evaluating the currently accepted data acquisition methods used to define throttle-dependent aft end effects. The YF-17 vehicle was selected as the mechanism for the investigation since the 0.1-scale model of the twin-engine aircraft was available and matching flight data were to be obtained. Surface pressure data were obtained on the model using two support systems and were integrated to obtain the resultant aft end loads. These investigations were conducted at Mach numbers from 0.6 to 1.6 within the Reynolds number range of 1.7 to 5.6 million per foot. Results from this study are summarized as follows:

1. Support system interference was defined over the entire instrumented portion of the model aft end. Local surface pressure coefficient interference was minimal at Mach number 0.6, increasing to a maximum at Mach number 1.2. Overall support system loading effects on the aft end caused by these deviations in surface pressures were on the order of 12 aircraft drag counts (ΔC_D = 0.0012) at Mach number 1.2 but decreased at the higher and lower Mach numbers.

2. The engine bay purge flow exhaust acted as a normal jet, as expected, with significant effects on the local pressure distribution at the purge flow exit. These effects fed downstream and produced compensating effects through the expansion over the nozzle connect region so that effects on performance were minimized.

3. Changing the nozzle contour, which simulated different power settings, produced significant changes in the local surface pressure coefficients over the total aft end. This indicates that proper simulation of the nozzle contour will be required for a one-to-one pressure correlation with flight data.

4. Varying the model pitch attitude over the 0 to 6-deg range produced linear variations in the surface pressures over the total instrumented model aft end. Effects were as expected with the windward surface pressures increasing with angle of attack, whereas the lee side levels decreased. These changes produce compensating effects in the pressure area integration such that the overall effect on the axial loading is minimized.

5. The effect of varying nozzle pressure ratio (ratio of jet total to free-stream static pressure) from the design value was primarily confined to the nozzle and expansion region at the nozzle connect station. These effects on pressure and axial-force coefficients were minimal for the cruise nozzle configurations subsonically and increased as the nozzle was opened at higher Mach numbers.

6. Horizontal tail deflections (leading edge down) influenced the pressures over the total aft end, increasing the levels above the tail plane and decreasing those below. The local effects were significant but tended to cancel in the pressure-area integration such that the aft end axial loadings were not significantly affected.

7. Varying the Reynolds number over the available range of the tunnel produced significant pressure changes at the lowest Reynolds number only (1.7×10^6/ft). Data at the nominal Reynolds number of 2.8×10^6/ft should thus be directly applicable to a flight correlation attempt.

8. Parameters such as model attitude, horizontal tail position, and nozzle pressure ratio produced systematic variations that would allow linear interpolation between acquired data to provide a flight condition match for a correlation if independency of variables is assumed.

REFERENCES

1. Test Facilities Handbook (Tenth Edition). "Propulsion Wind Tunnel Facility, Vol. 4." Arnold Engineering Development Center, May, 1974.

2. Price, E. A., Jr. "Afterbody Drag Investigation of a Twin-Nozzle Fighter-Type Model at Mach Numbers 0.6 to 1.5." AEDC-TR-72-87 (AD902384L), August 1972.

3. Hines, B. G., Marsh, W. H., and Wood, R. A. "Twin Jet Installation and Test Technique Improvement Test." GE-R74AEG201, January 1974.

4. Siegfried, R. G. "Twin Jet Installation and Reynolds Number Effects Test." G.E.-T.M. No. 75-416, June 1975.

5. Galigher, L. L., Yaros, S. F., and Bauer, R. C. "Evaluation of Boattail Geometry and Exhaust Plume Temperature Effects on Nozzle Afterbody Drag at Transonic Mach Numbers." AEDC-TR-76-102 (ADA030852), October 1976.

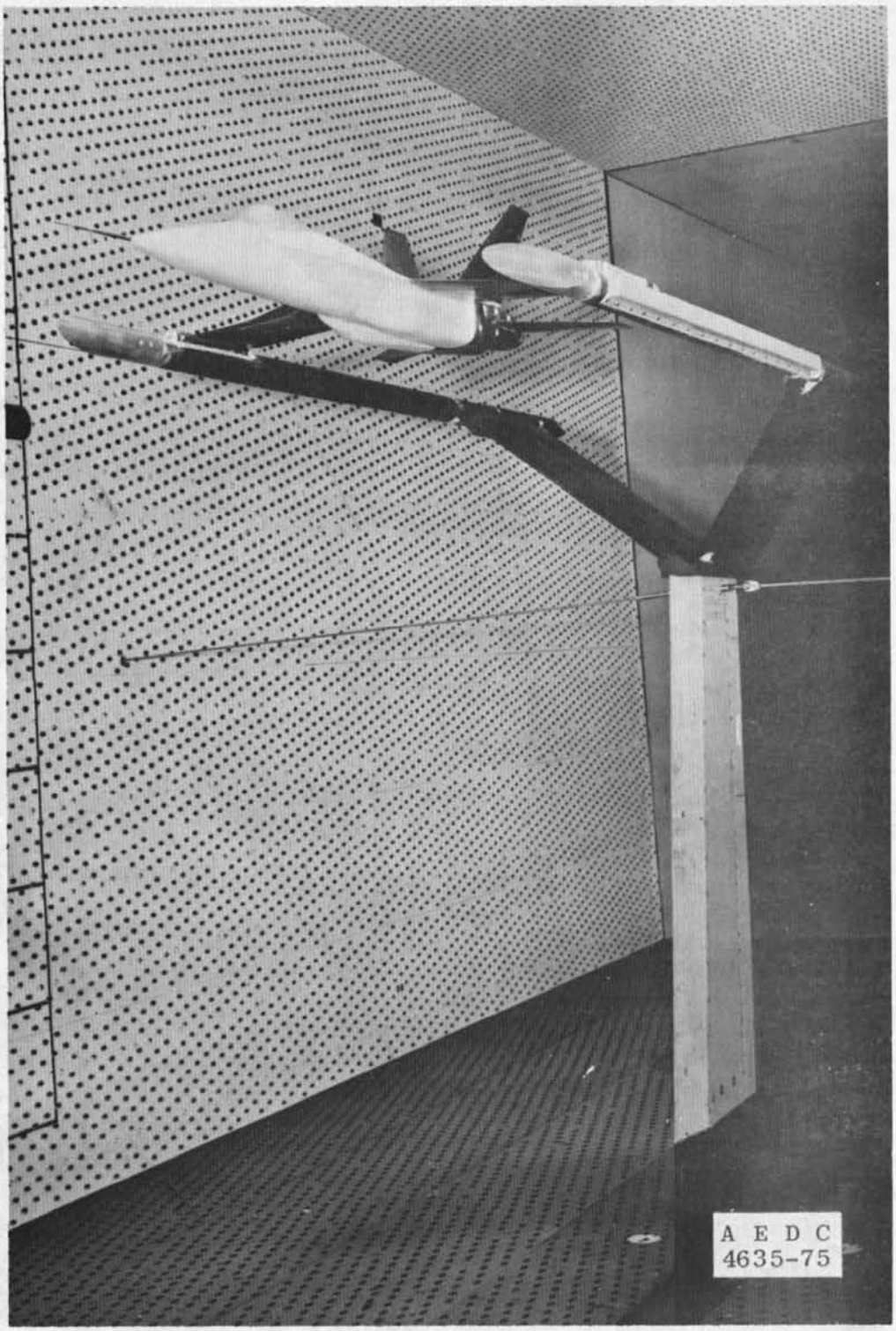

a. Model installation photograph

Figure 1. Wingtip support system.

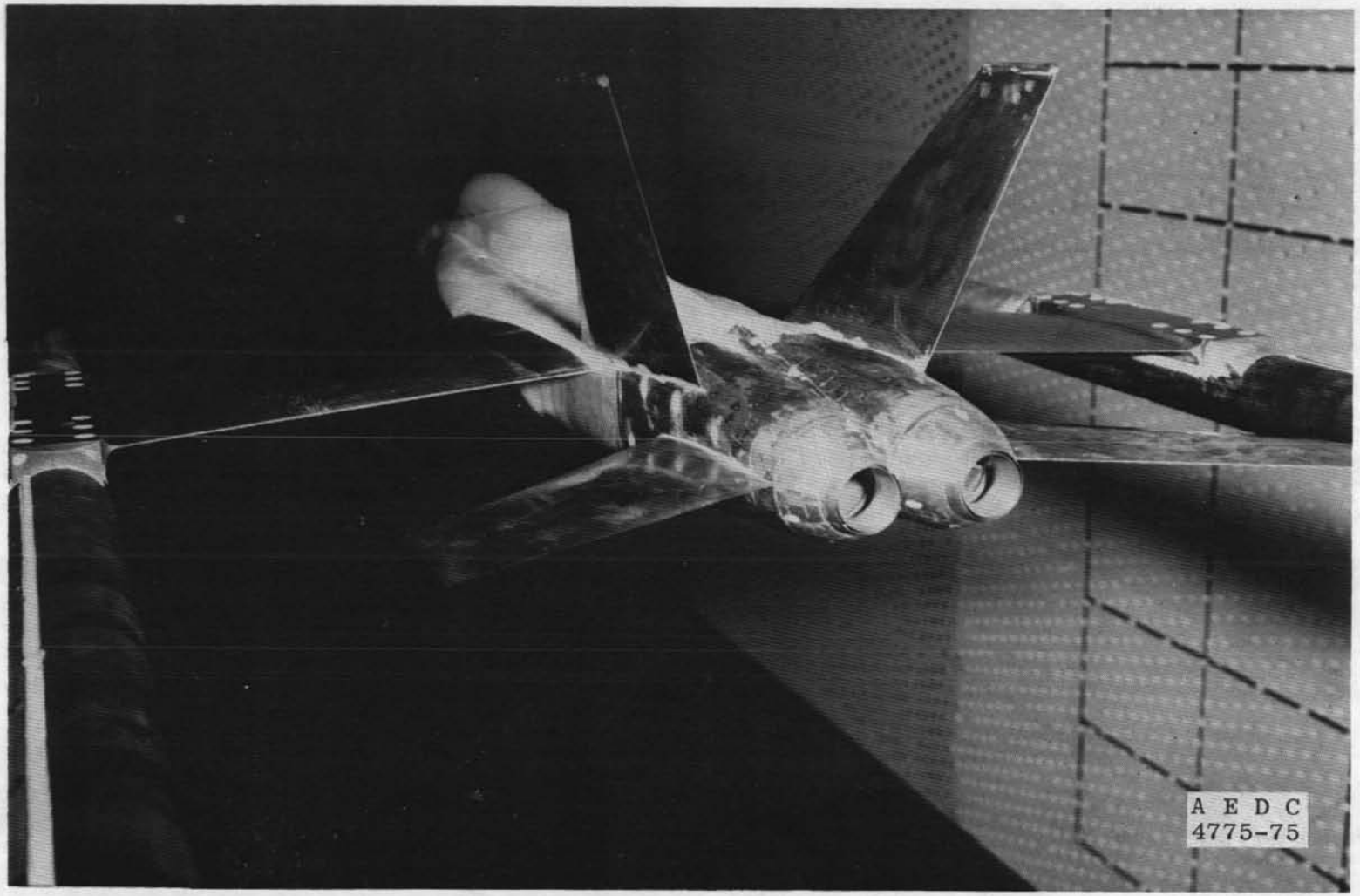

b. Cruise nozzle installation
Figure 1. Continued.

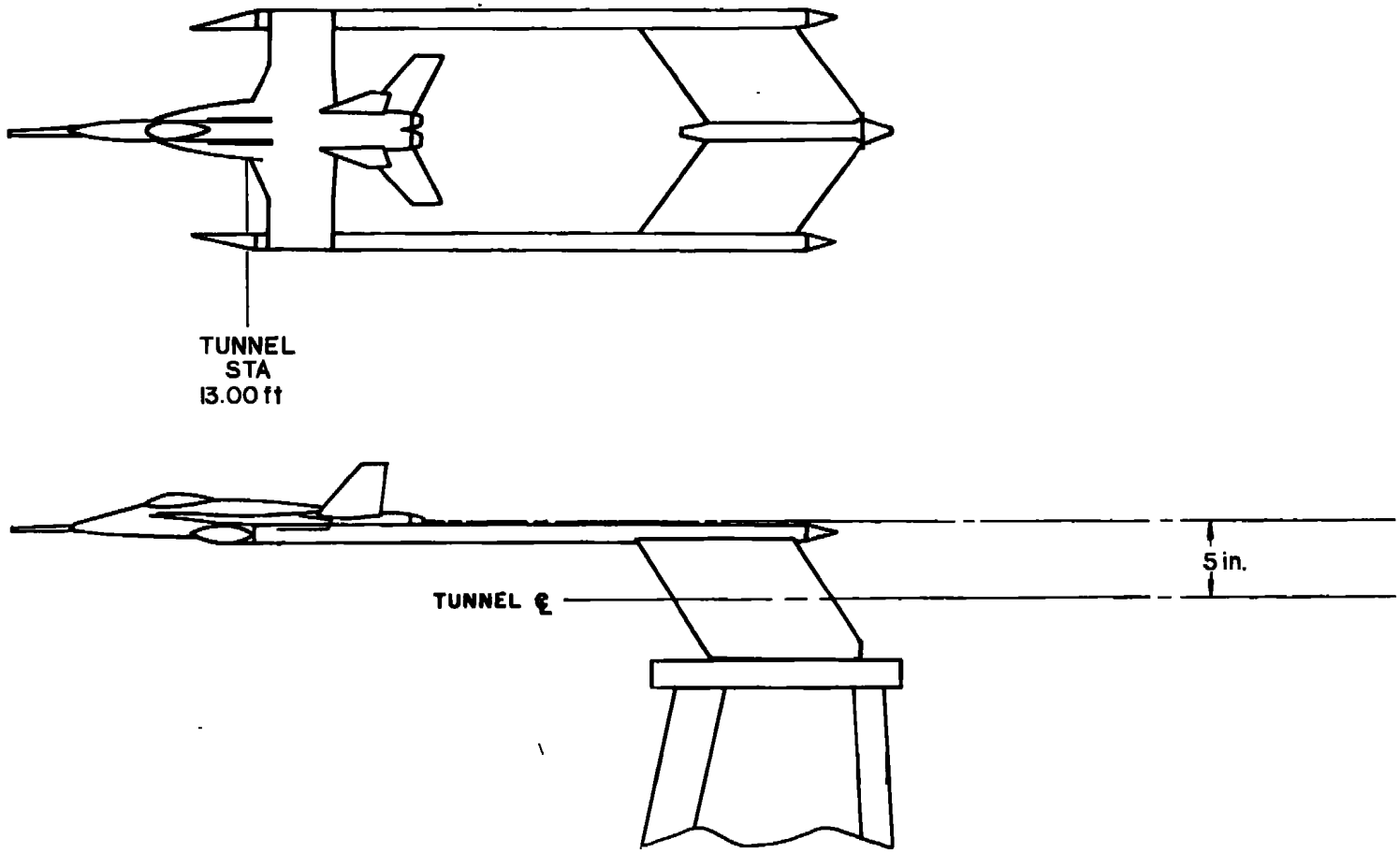

c. Test article tunnel location

Figure 1. Concluded.

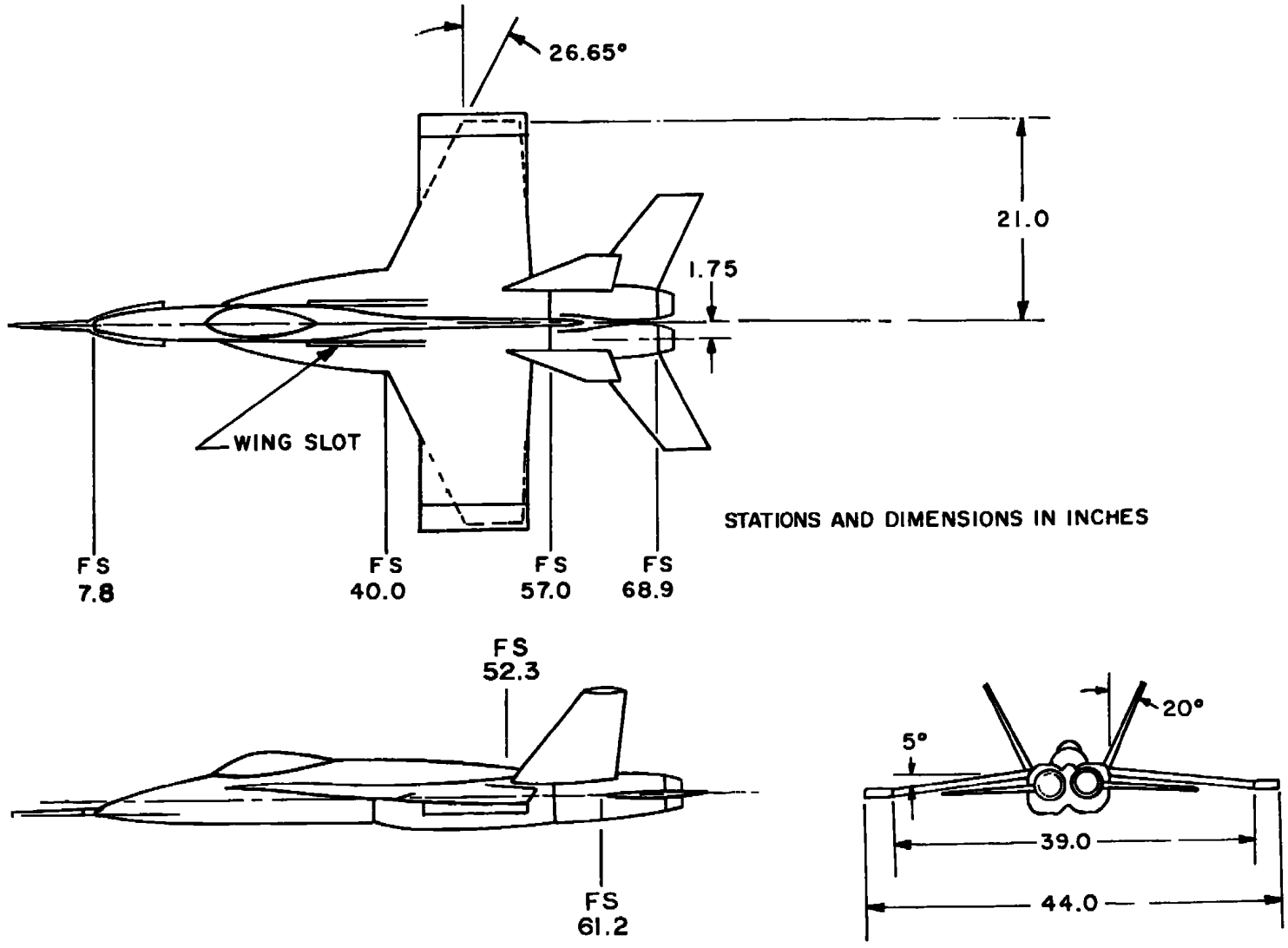

Figure 2. Dimensional sketch of model.

a. Model with dummy wingtip supports

Figure 3. Sting support system.

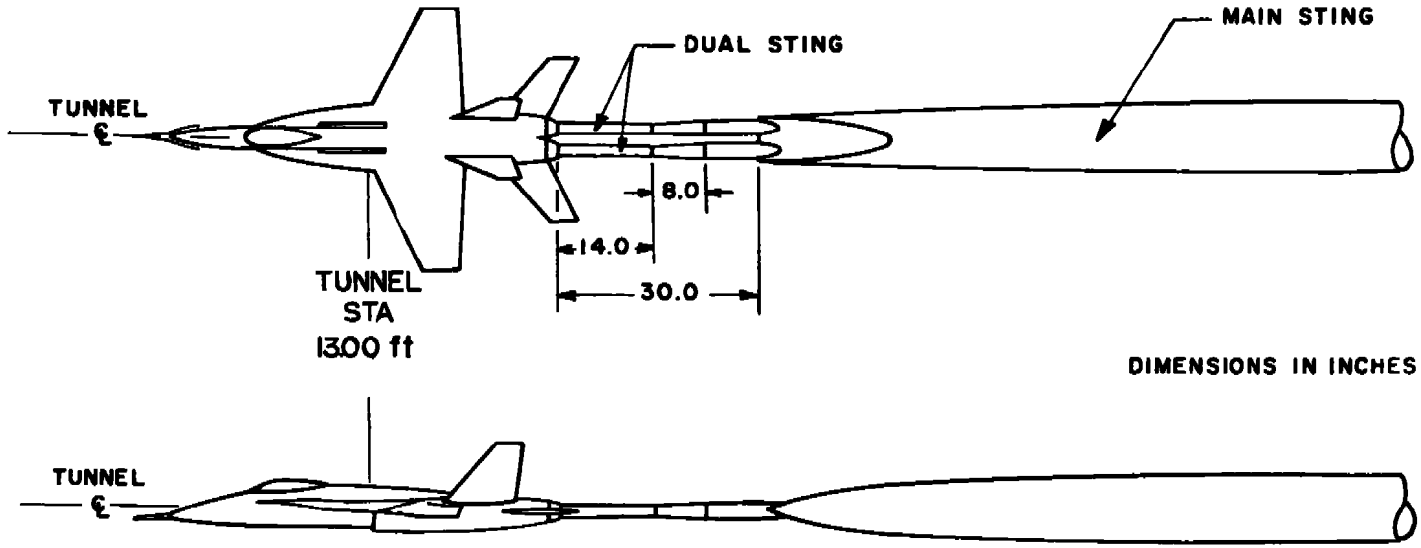

b. Model and support stings
Figure 3. Continued.

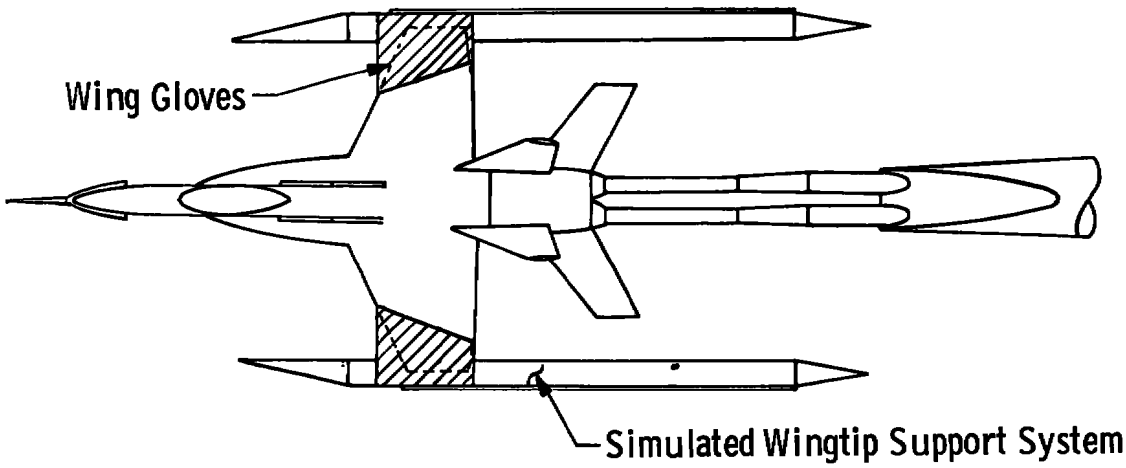

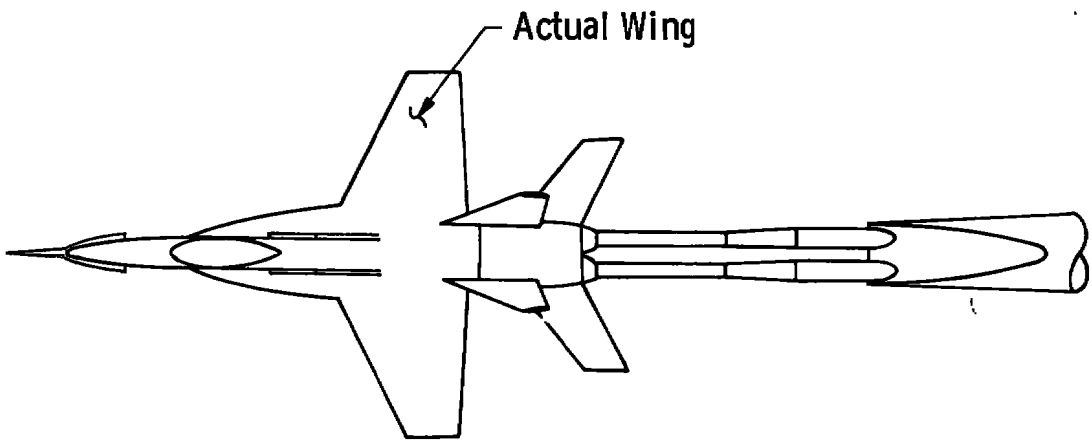

c. Wingtip support simulation sketch
Figure 3. Concluded.

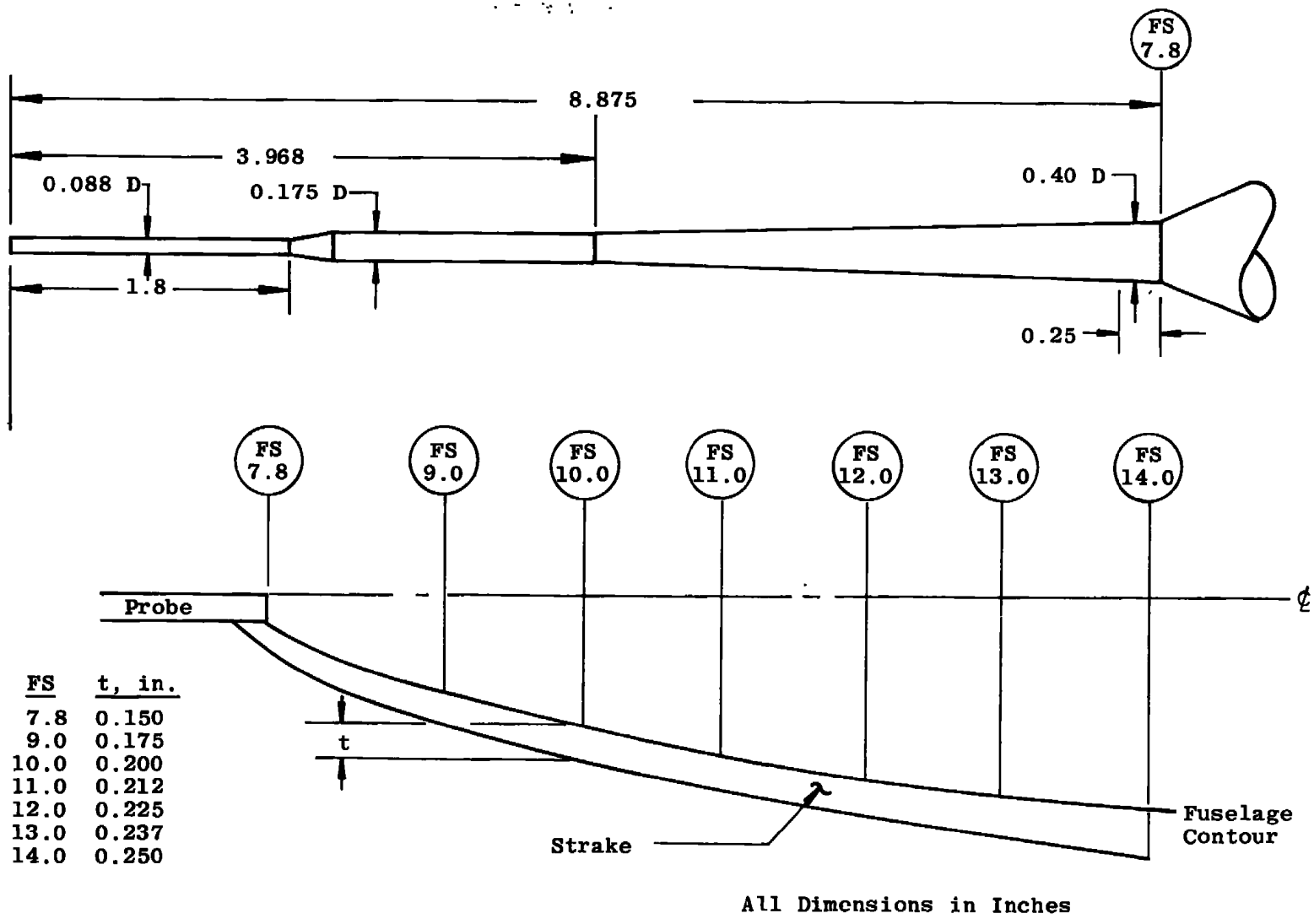

FS	t, in.
7.8	0.150
9.0	0.175
10.0	0.200
11.0	0.212
12.0	0.225
13.0	0.237
14.0	0.250

Figure 4. Nose strake and pitot boom details.

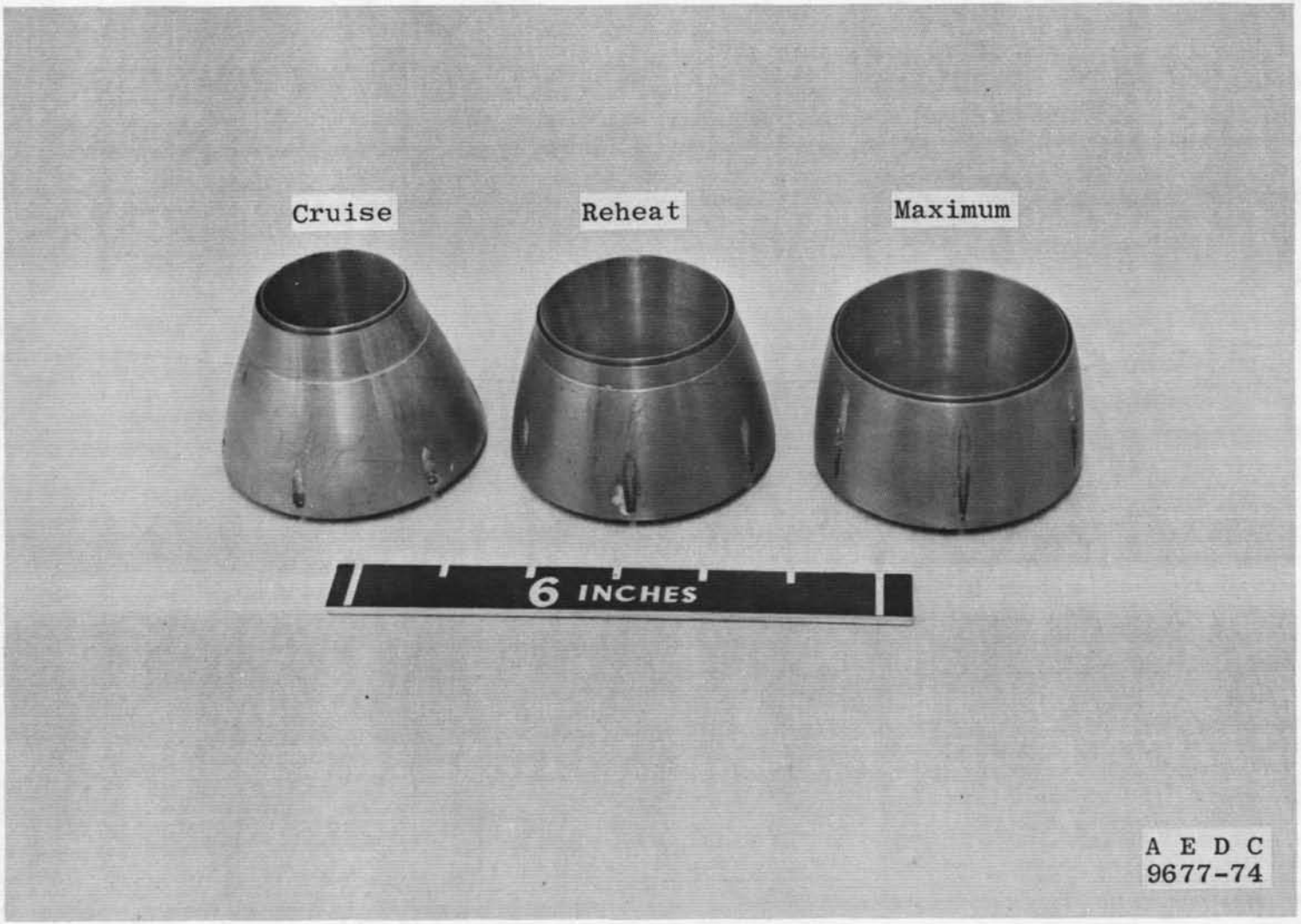

a. Comparative photograph
Figure 5. Exhaust nozzle closure.

X	R
0	1.690
0.076	1.675
0.176	1.652
0.276	1.629
0.376	1.602
0.476	1.573
0.576	1.543
0.676	1.512
0.776	1.478
0.876	1.440
0.976	1.402
1.076	1.361
1.176	1.318
1.276	1.272
1.376	1.224
1.476	1.172
1.576	1.120
1.587	1.114
1.587	1.101
2.143	0.918

X	r
0.076	1.183
0.176	1.175
0.276	1.135
0.376	1.087
0.476	1.033
0.576	0.968
0.676	0.908
0.776	0.859
0.876	0.822
0.976	0.794
1.013	0.780
1.076	0.779
1.176	0.781
1.276	0.790
1.376	0.796
1.476	0.801
1.576	0.805
1.676	0.811
1.776	0.816
1.876	0.821
1.976	0.826
2.076	0.831
2.143	0.835

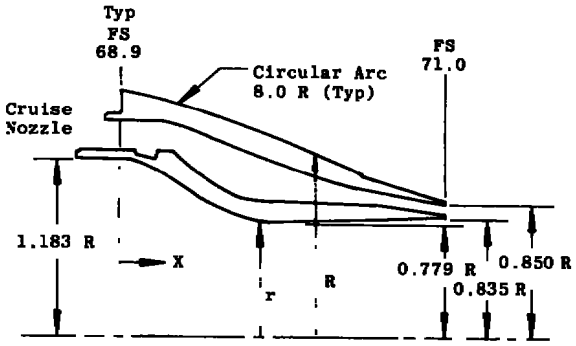

X	R
0	1.690
0.087	1.680
0.187	1.666
0.287	1.651
0.387	1.634
0.487	1.616
0.587	1.596
0.687	1.572
0.787	1.548
0.887	1.522
0.987	1.494
1.087	1.464
1.187	1.431
1.287	1.396
1.387	1.360
1.487	1.320
1.587	1.278
1.623	1.264
1.623	1.251
1.910	1.191

X	r
0	1.183
0.087	1.177
0.187	1.128
0.287	1.074
0.387	1.030
0 487	0.996
0.587	0.972
0.643	0.961
0.687	0.956
0.738	0.954
0.787	0.956
0.821	0.960
0.887	0.969
0.987	0.982
1.087	0.986
1.187	1.010
1.287	1.023
1.387	1.037
1.487	1.051
1.587	1.064
1.687	1.077
1.787	1.091
1.887	1.105
1.910	1 108

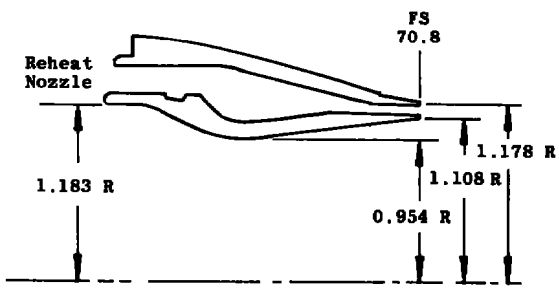

X	R
0	1.690
0.082	1.687
0.182	1.684
0.282	1.679
0.382	1.672
0.482	1.664
0.582	1.652
0.682	1.641
0.782	1.627
0.882	1.610
0.982	1.592
1.082	1.572
1.182	1.549
1.282	1.525
1.382	1.499
1.482	1.470
1.649	1.417
1.670	1.417

X	r
0	1.183
0.082	1.179
0.182	1.148
0.282	1.124
0.382	1.109
0.468	1.103
0.482	1.103
0.582	1.104
0.594	1.116
0.682	1.135
0.782	1.156
0.882	1.177
0.982	1.197
1.082	1.219
1.182	1.239
1.282	1.261
1.382	1.281
1.482	1.302
1.582	1.323
1.670	1.342

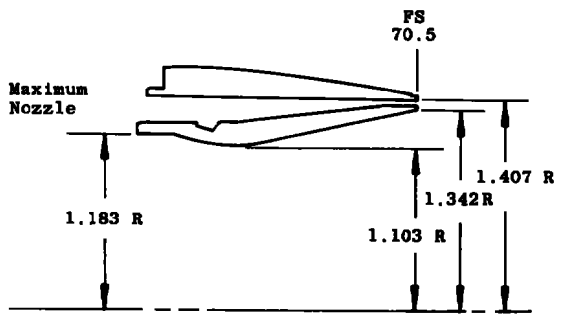

All Dimensions in Inches

b. Internal and external contours
Figure 5. Concluded.

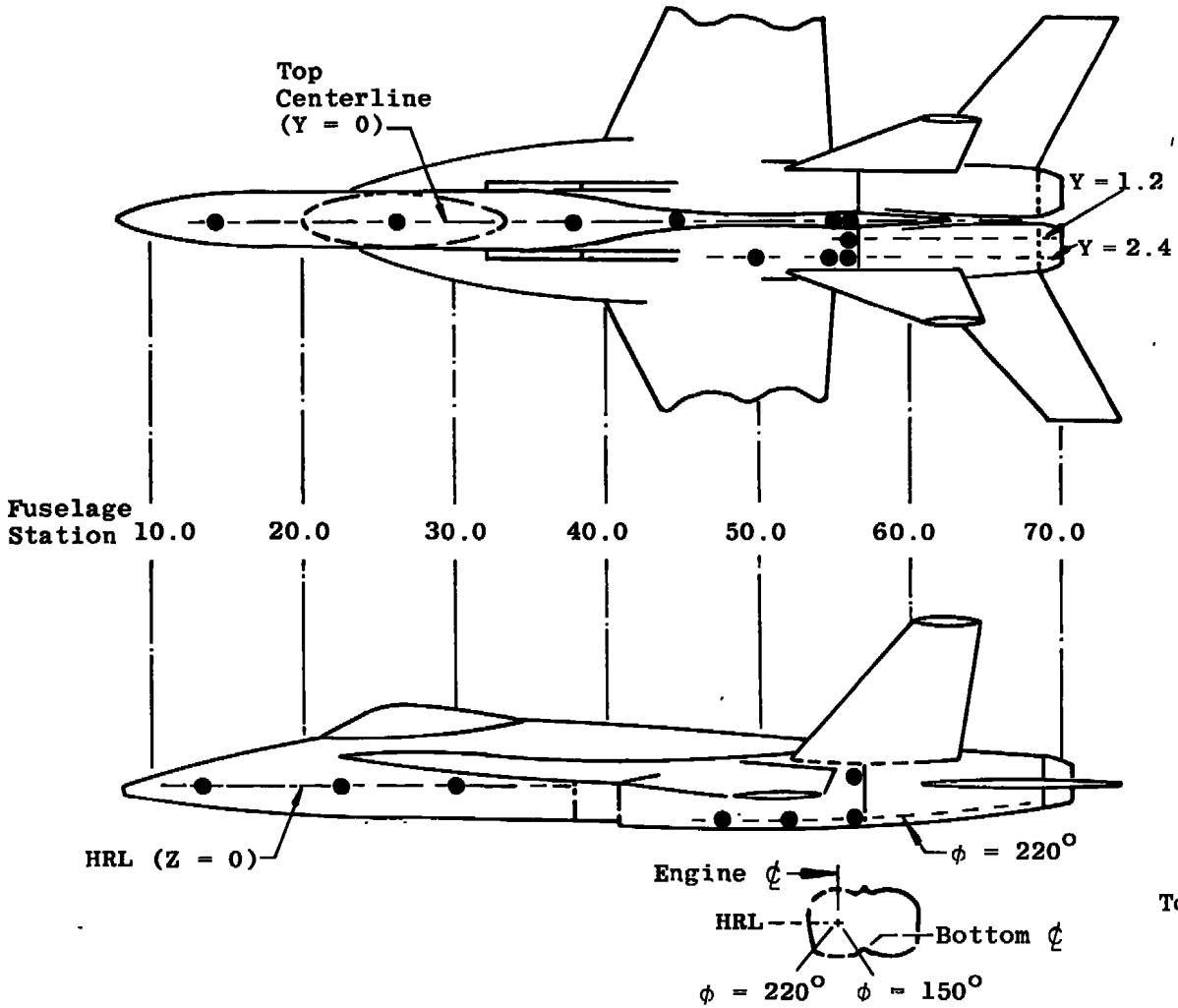

Forebody Static Taps

Tap	Station	Y, in.
502	14.0 *	0
503	26.5	
504	38.0	
505	45.0	
506	55.0	
507	56.5	
508	56.5	1.2
511	50.0	2.4
510	55.0	
509	56.5	
520	56.5 **	0

Tap	Station	Z, in.
512	14.0	0
513	22.0	
514	30.0	
518	56.5	0.4

Tap	Station	ϕ, deg
515	47.6	220
516	52.0	
517	56.5	
519	56.5	150

* Top Centerline
** Bottom Centerline

Total Forebody Taps = 19

a. Forebody

Figure 6. Surface pressure instrumentation location.

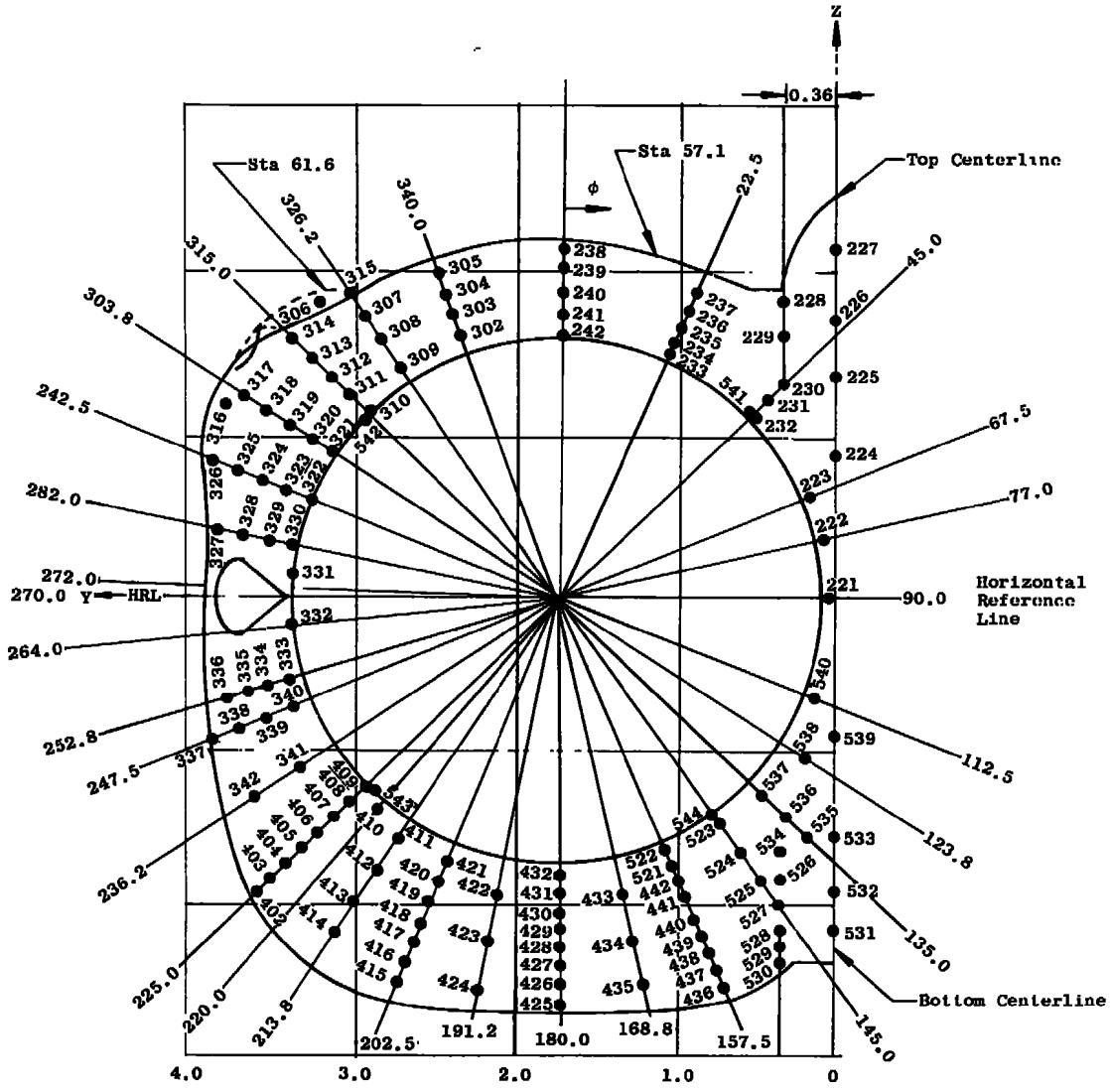

b. Afterbody

Figure 6. Continued.

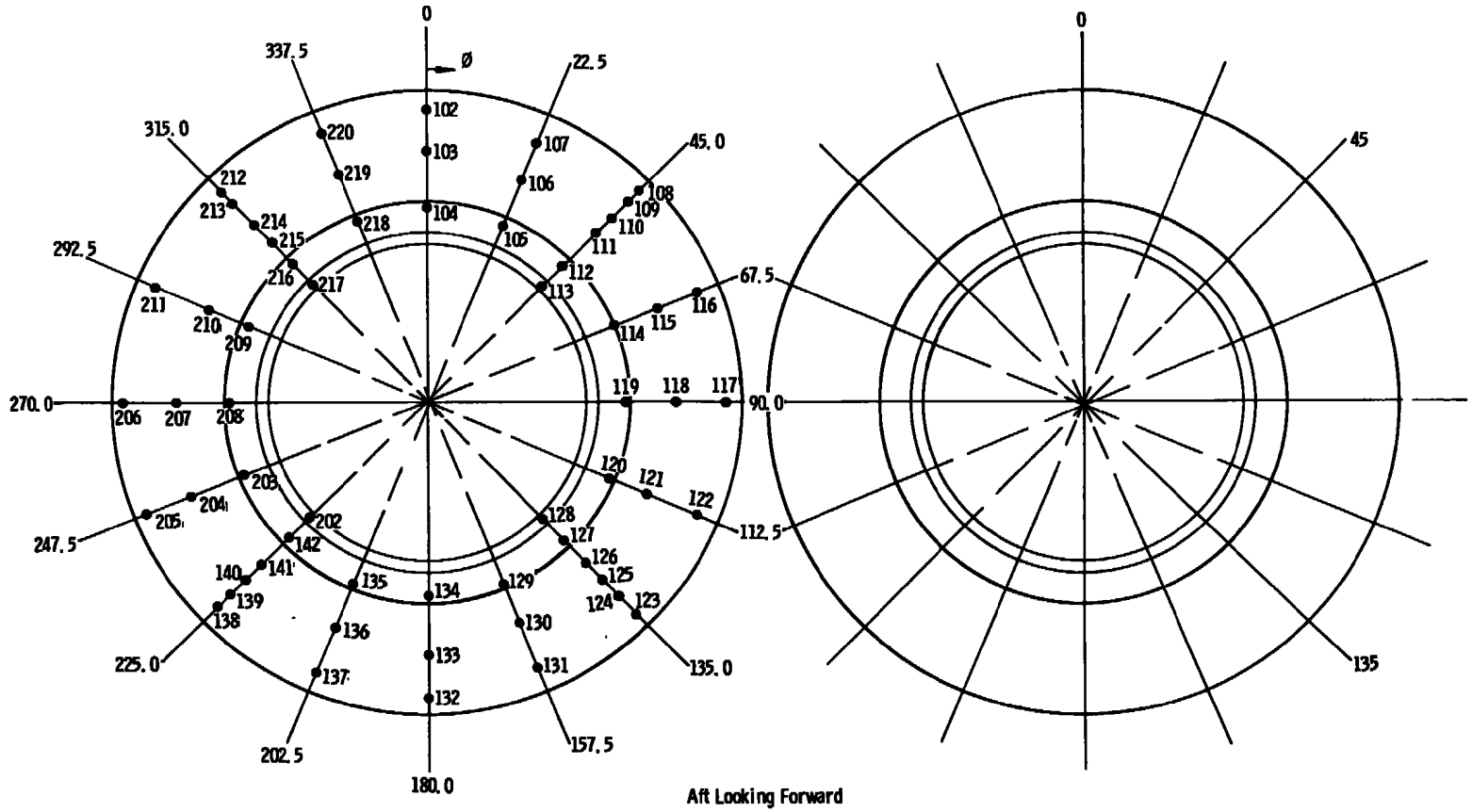

Aft Looking Forward

c. Cruise nozzle

Figure 6. Continued.

Note: Taps numbered same as cruise nozzle (Fig. 6c).

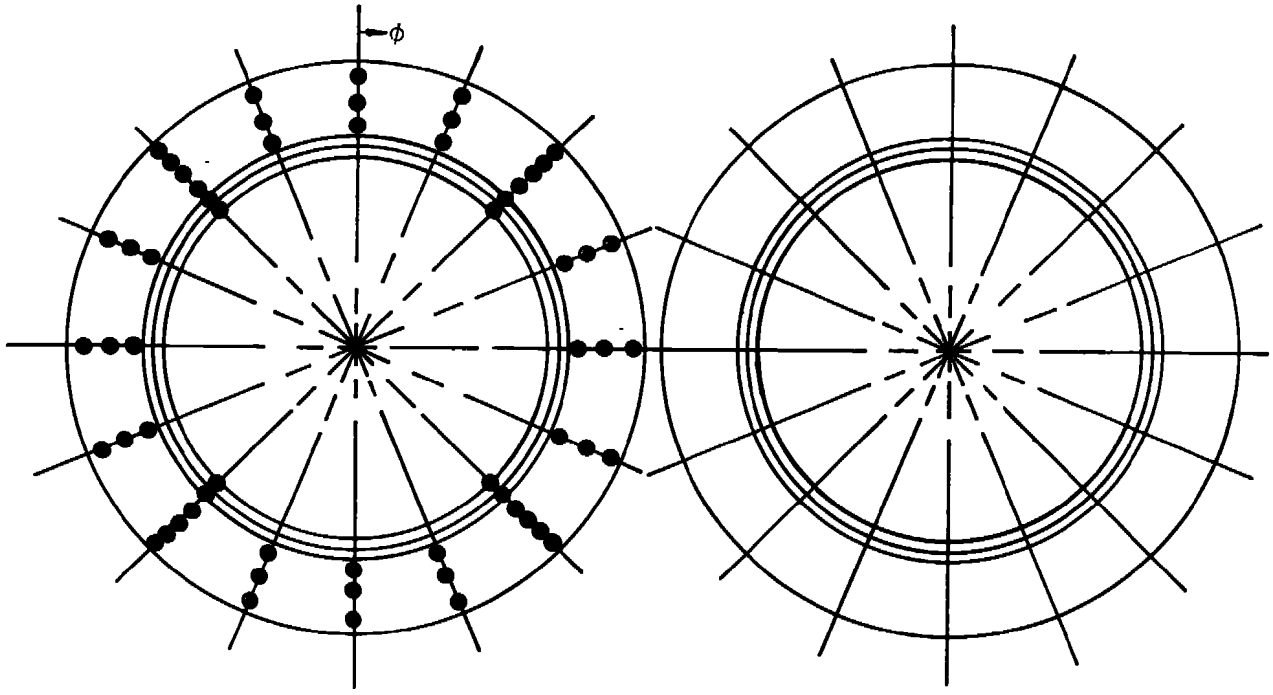

Aft Looking Forward

d. Reheat nozzle
Figure 6. Continued.

Note: Taps numbered same as cruise nozzle (Fig. 6c)

e. Maximum nozzle

Figure 6. Concluded.

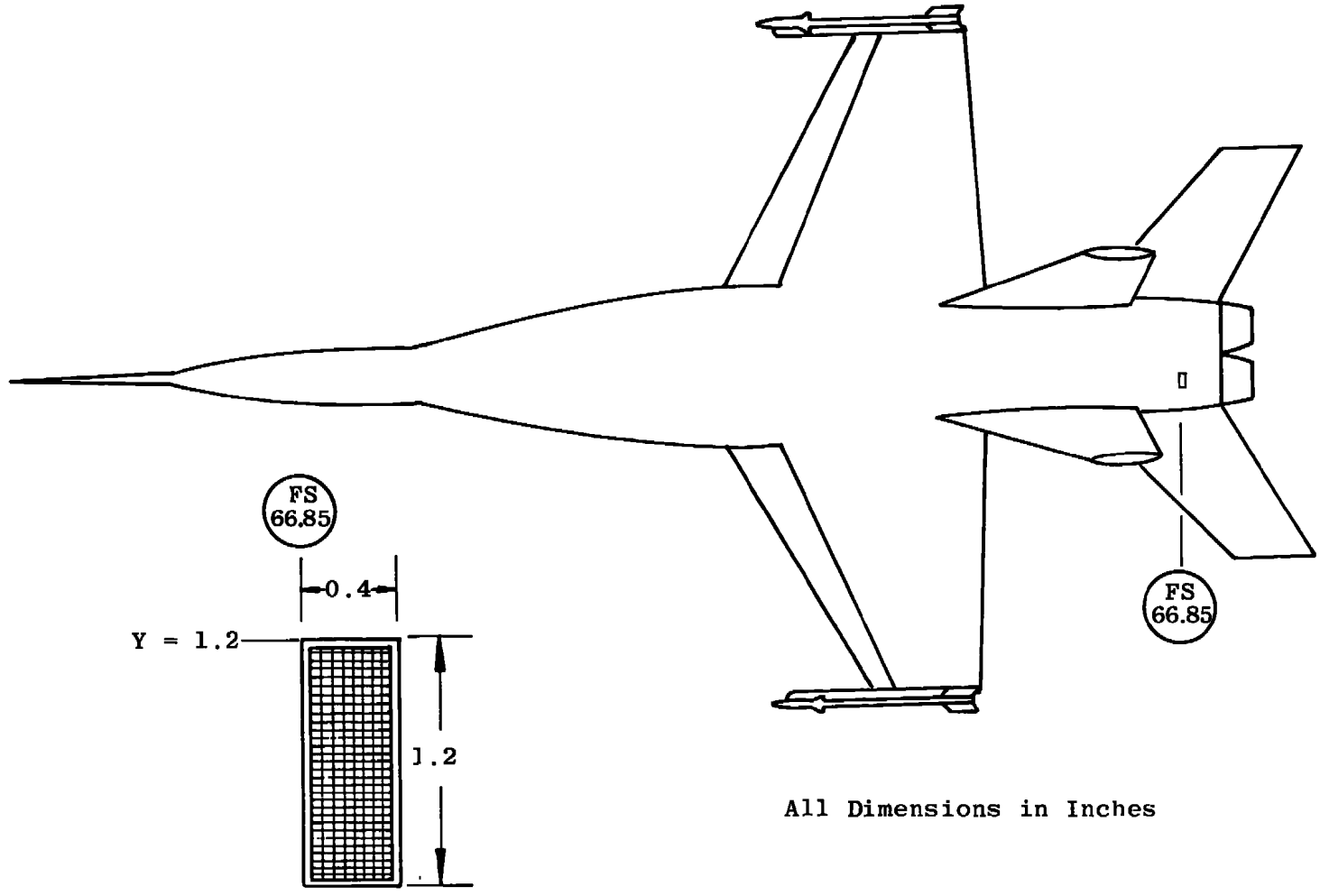

Engine Bay Purge Exit (Typ Top and Bottom, Left-Hand Side)

Figure 7. Auxiliary flow exhaust.

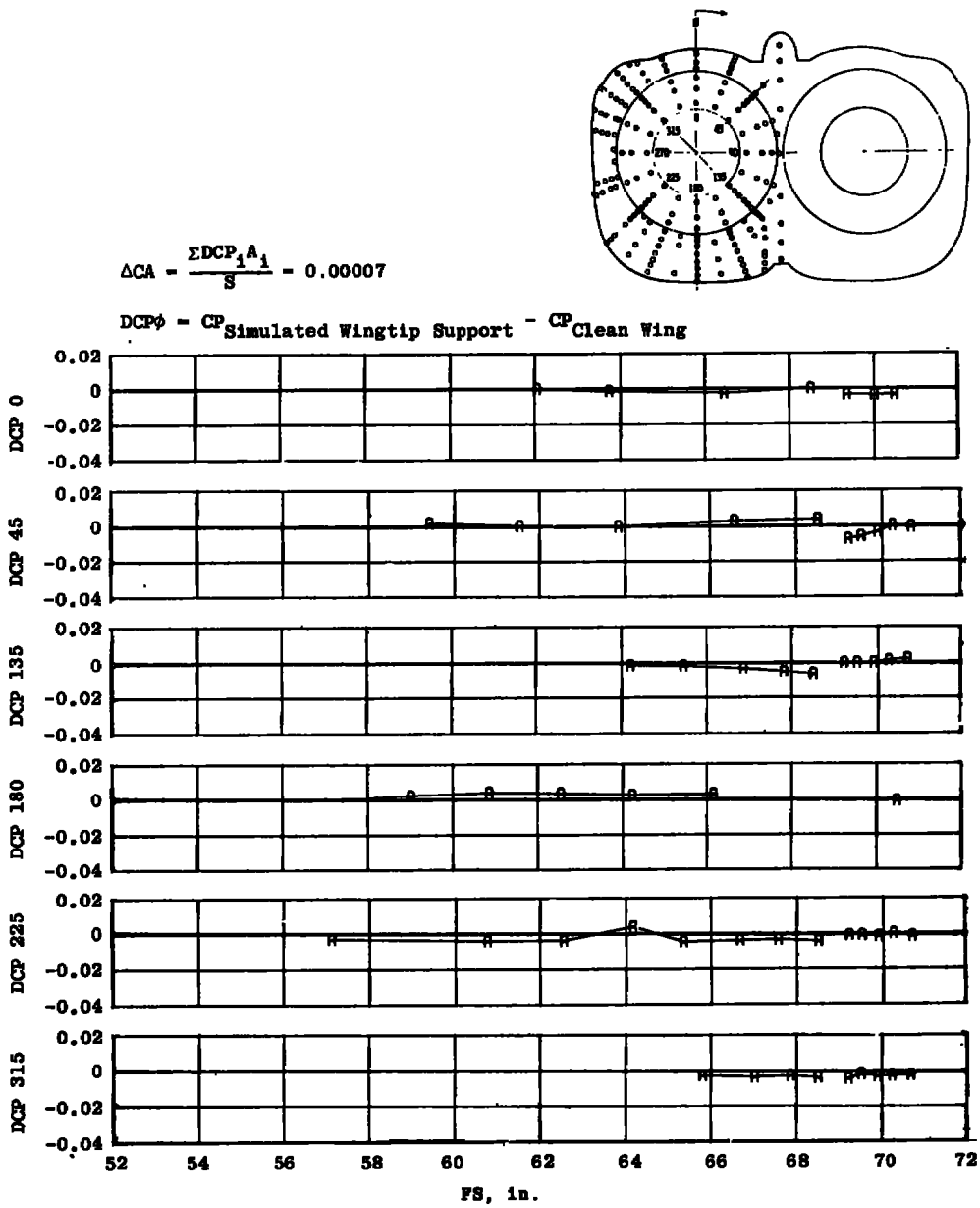

a. Cruise nozzle, $M_\infty = 0.6$

Figure 8. Wingtip support system interference on surface pressure distributions, $\delta_H = 0$, $\alpha = 4$ deg, and Re = 2.8 x 10^6/ft.

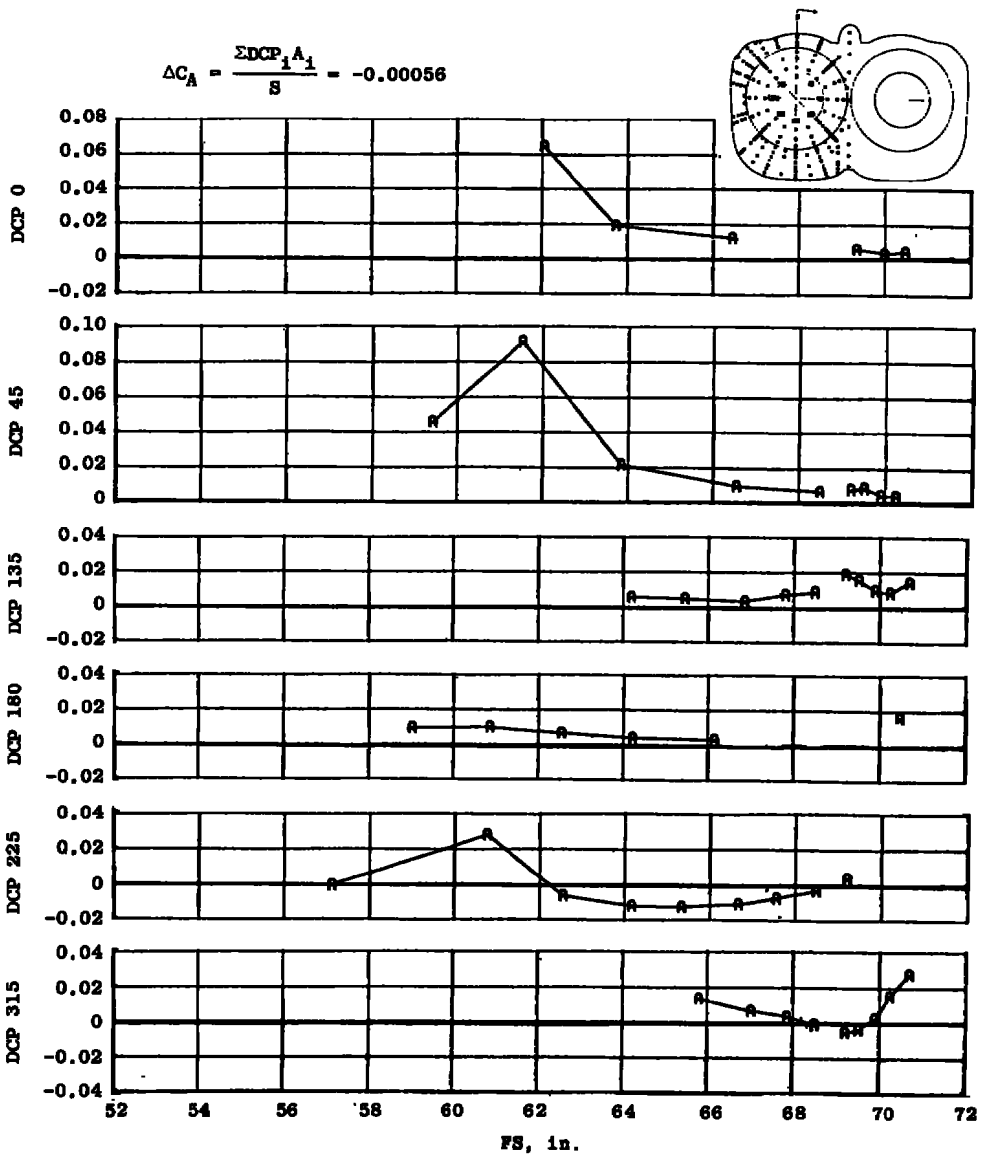

b. Reheat nozzle, $M_\infty = 0.9$
Figure 8. Continued.

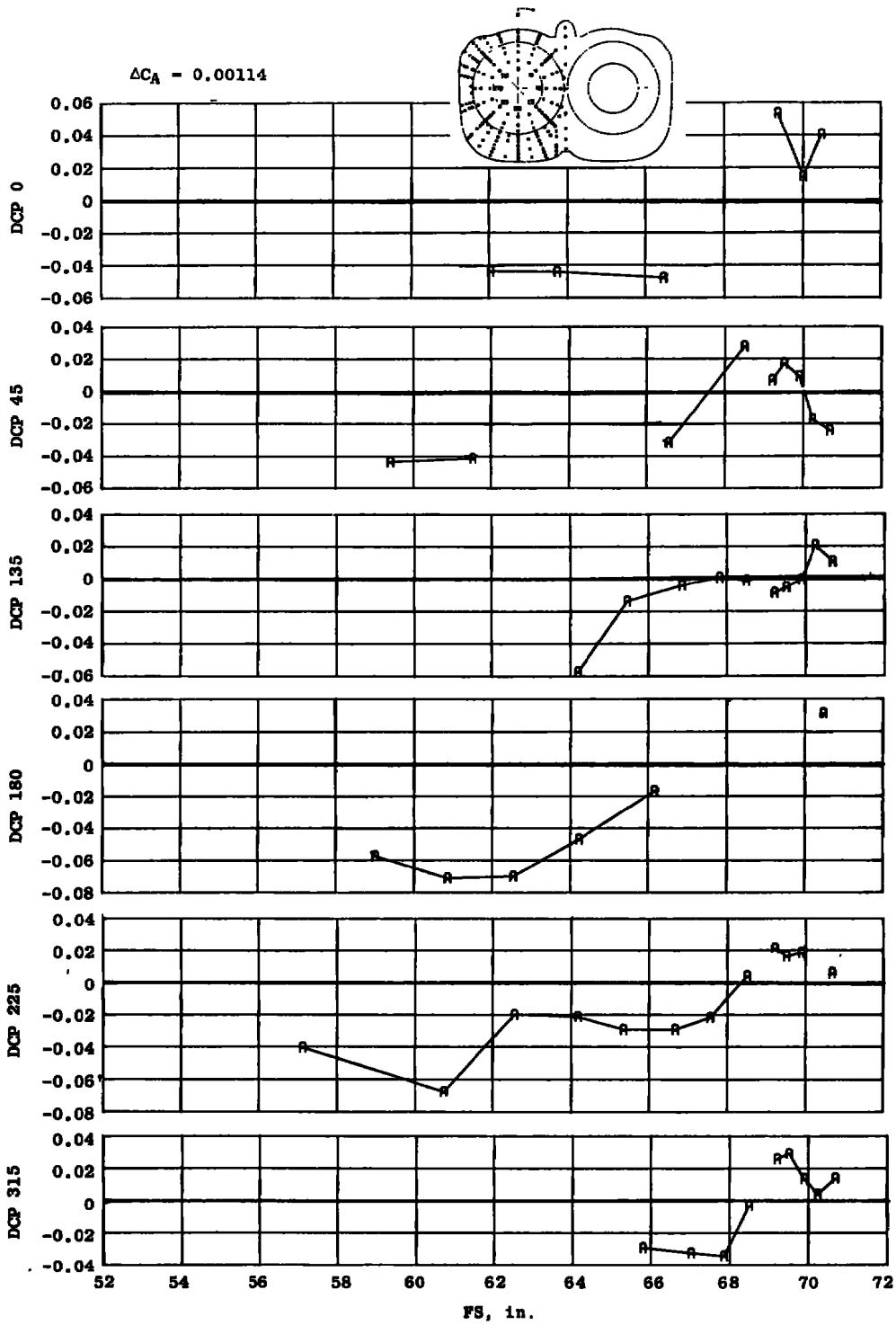

c. Maximum nozzle, M_∞ = 1.2

Figure 8. Concluded.

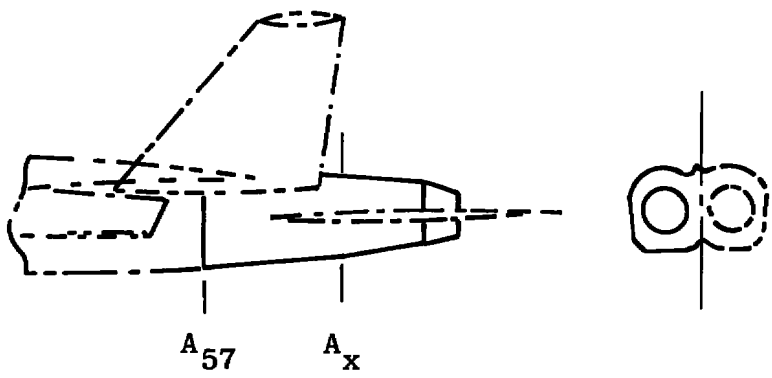

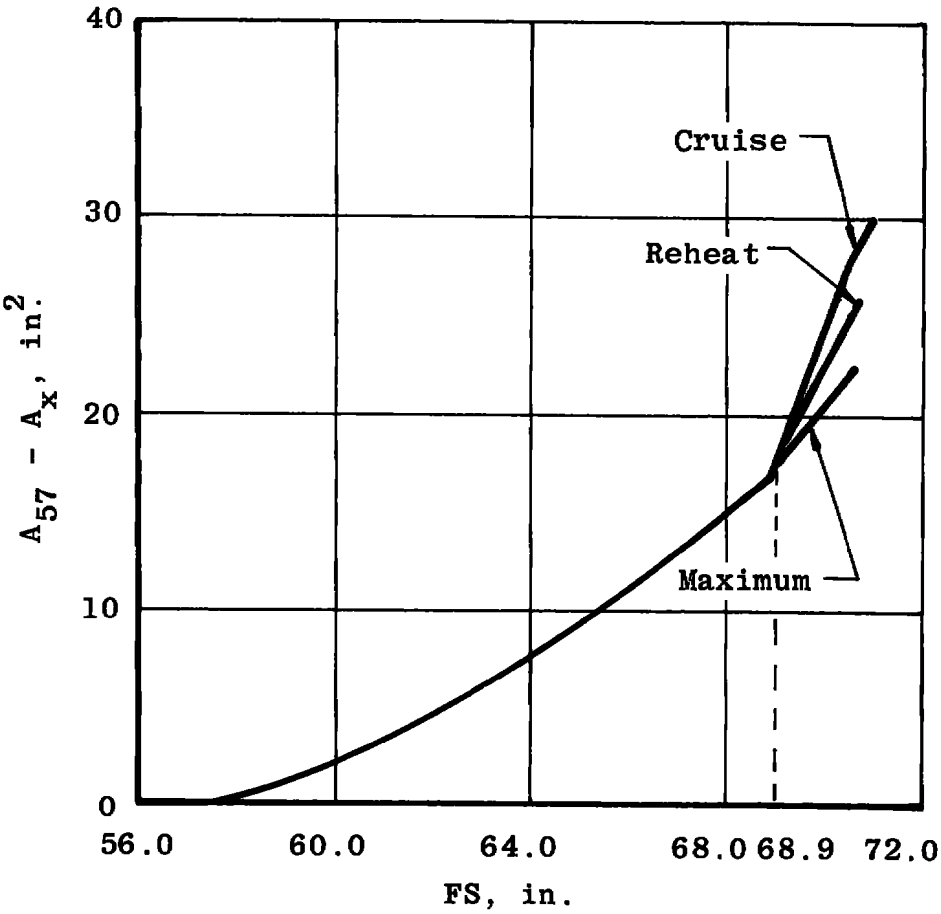

Figure 9. Projected axial area of fuselage and nozzles.

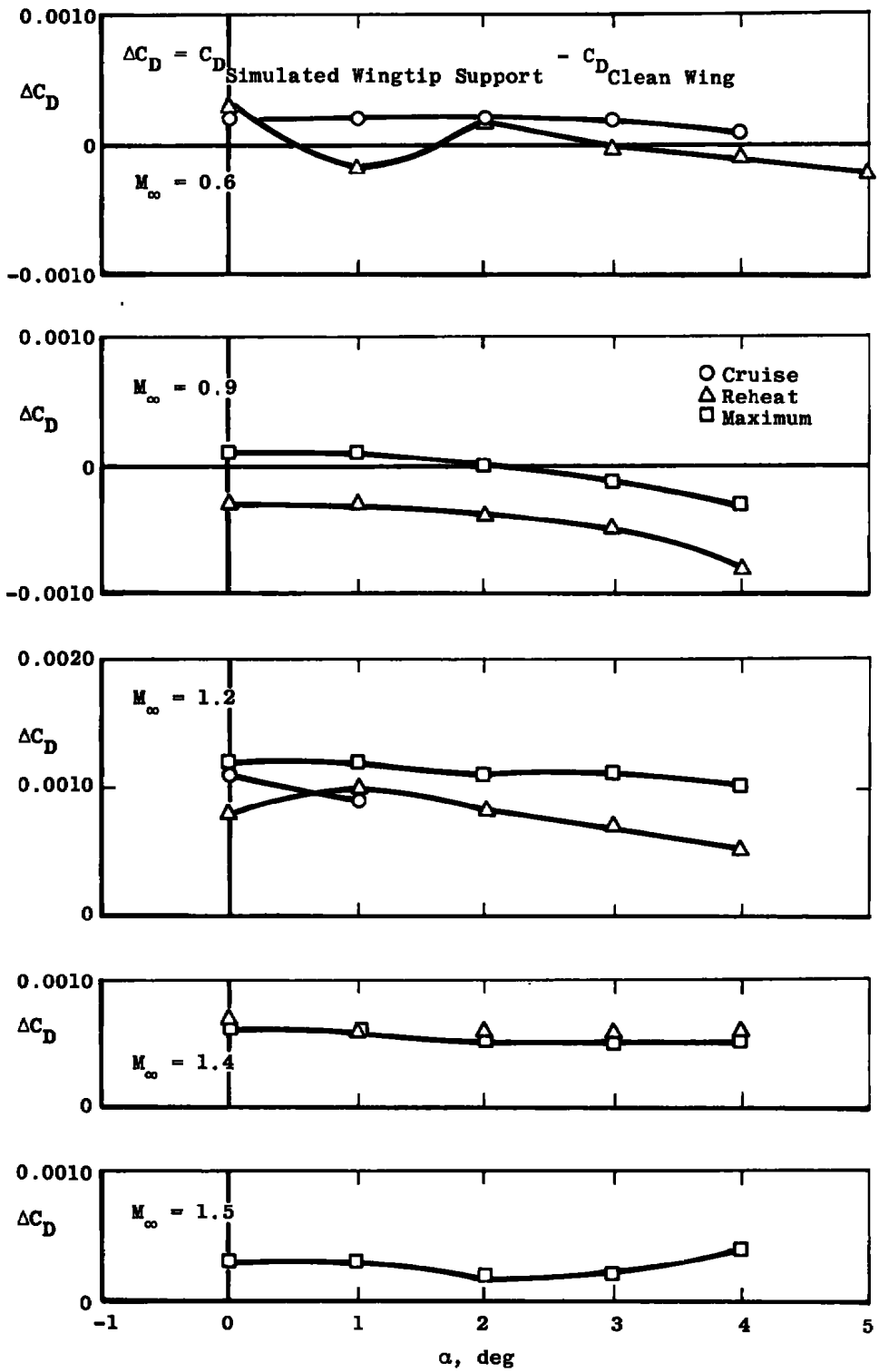

Figure 10. Wingtip support system drag interference.

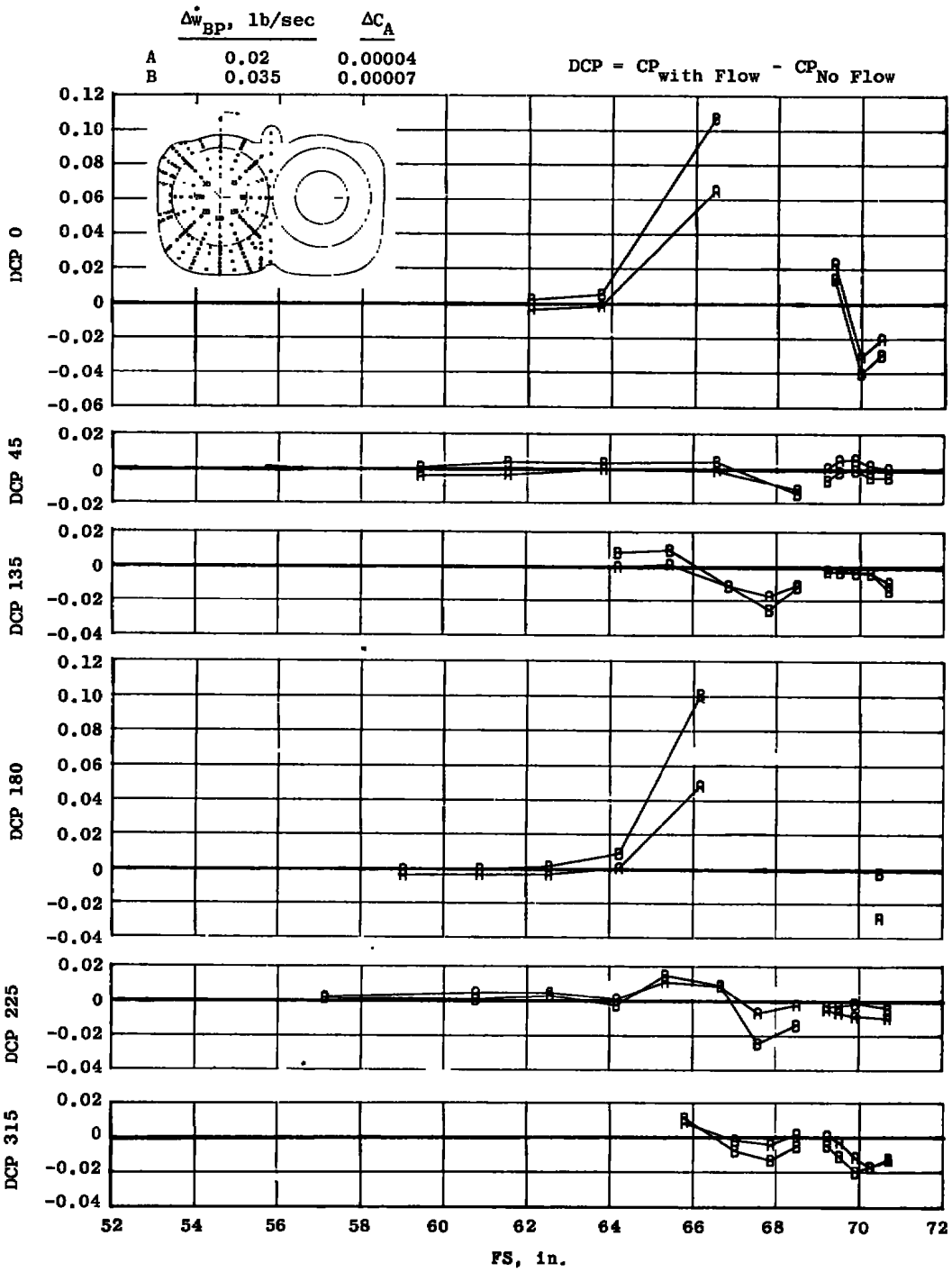

a. Cruise nozzle, M_∞ = 0.6, α = 4 deg with dummy wingtip supports

Figure 11. Bay purge exhaust effects on the surface pressure distribution, δ_H = 0 and Re = 2.8 x 10^6/ft.

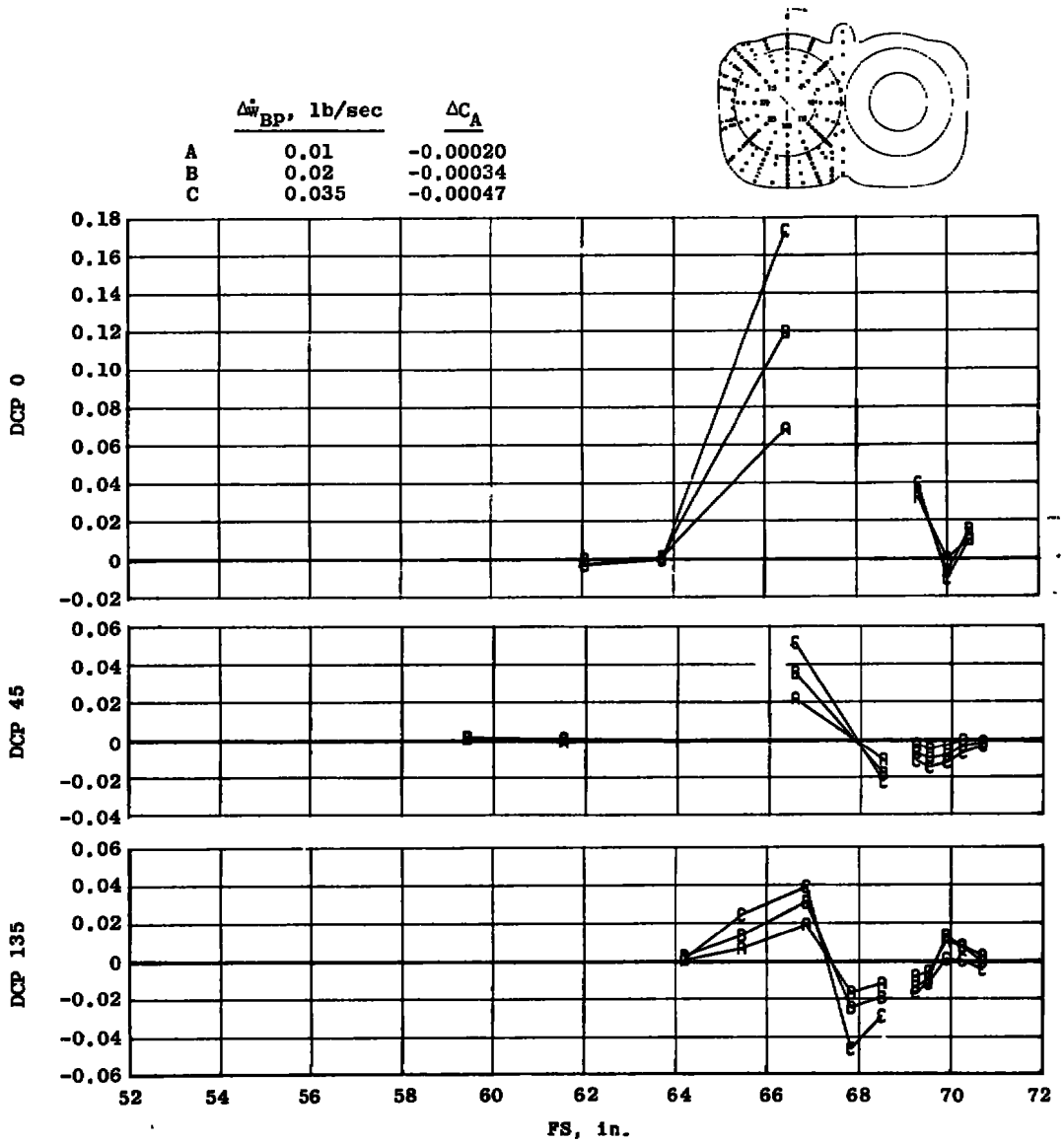

b. Maximum nozzle, M_∞ = 1.2, α = 1 deg with clean wing
Figure 11. Continued.

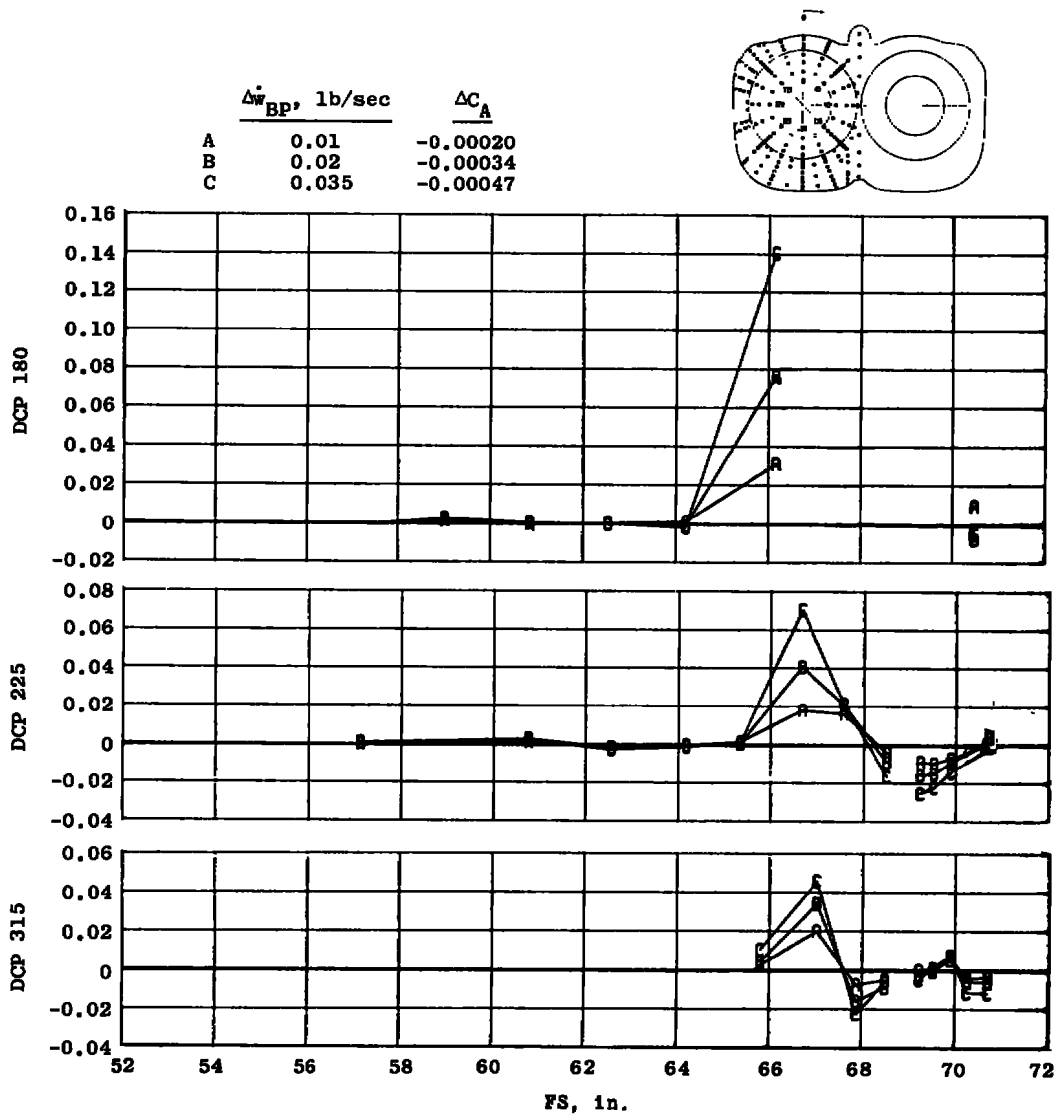

b. Concluded

Figure 11. Concluded.

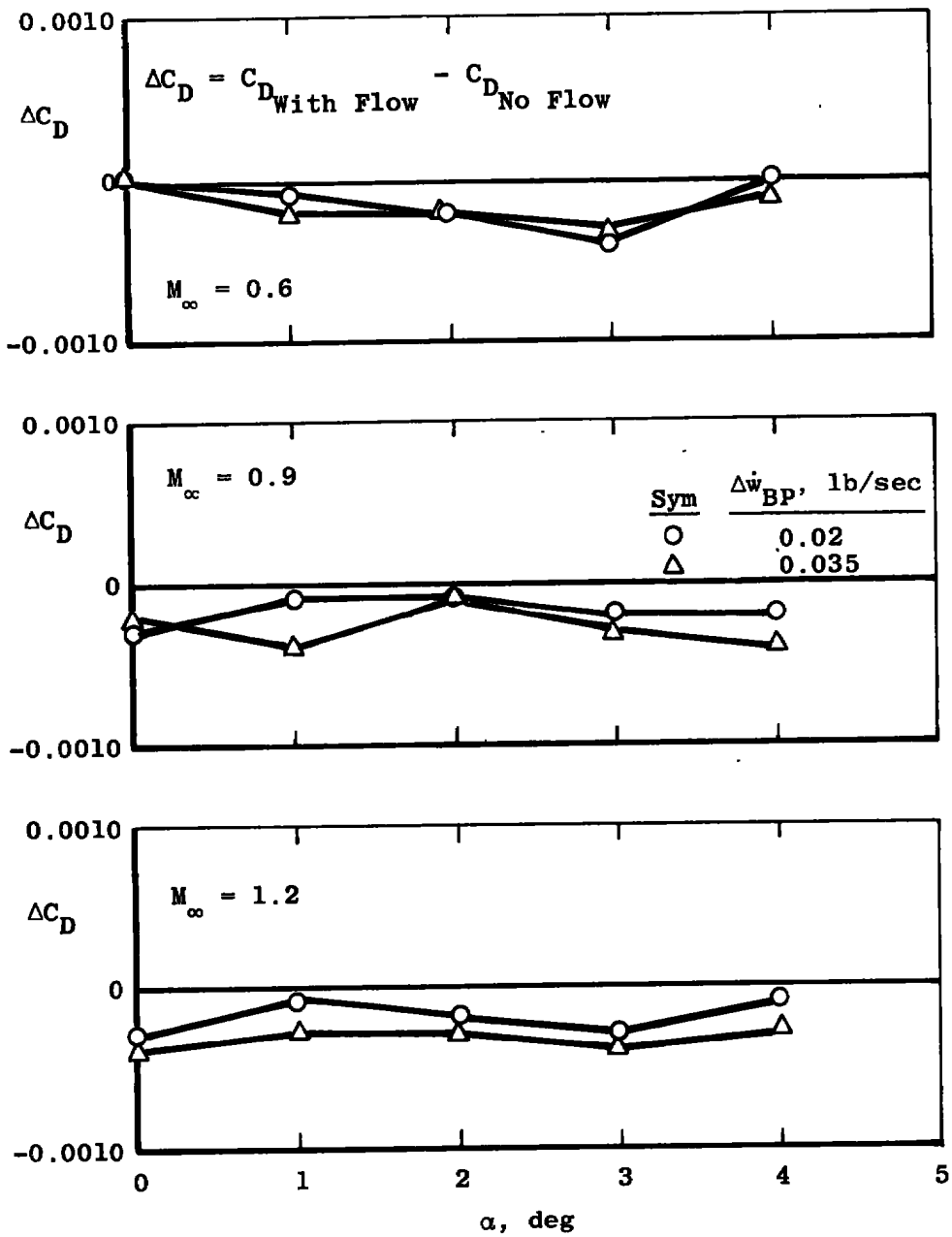

a. Cruise nozzle with dummy wingtip supports

Figure 12. Bay purge exhaust drag effects, $\delta_H = 0$.

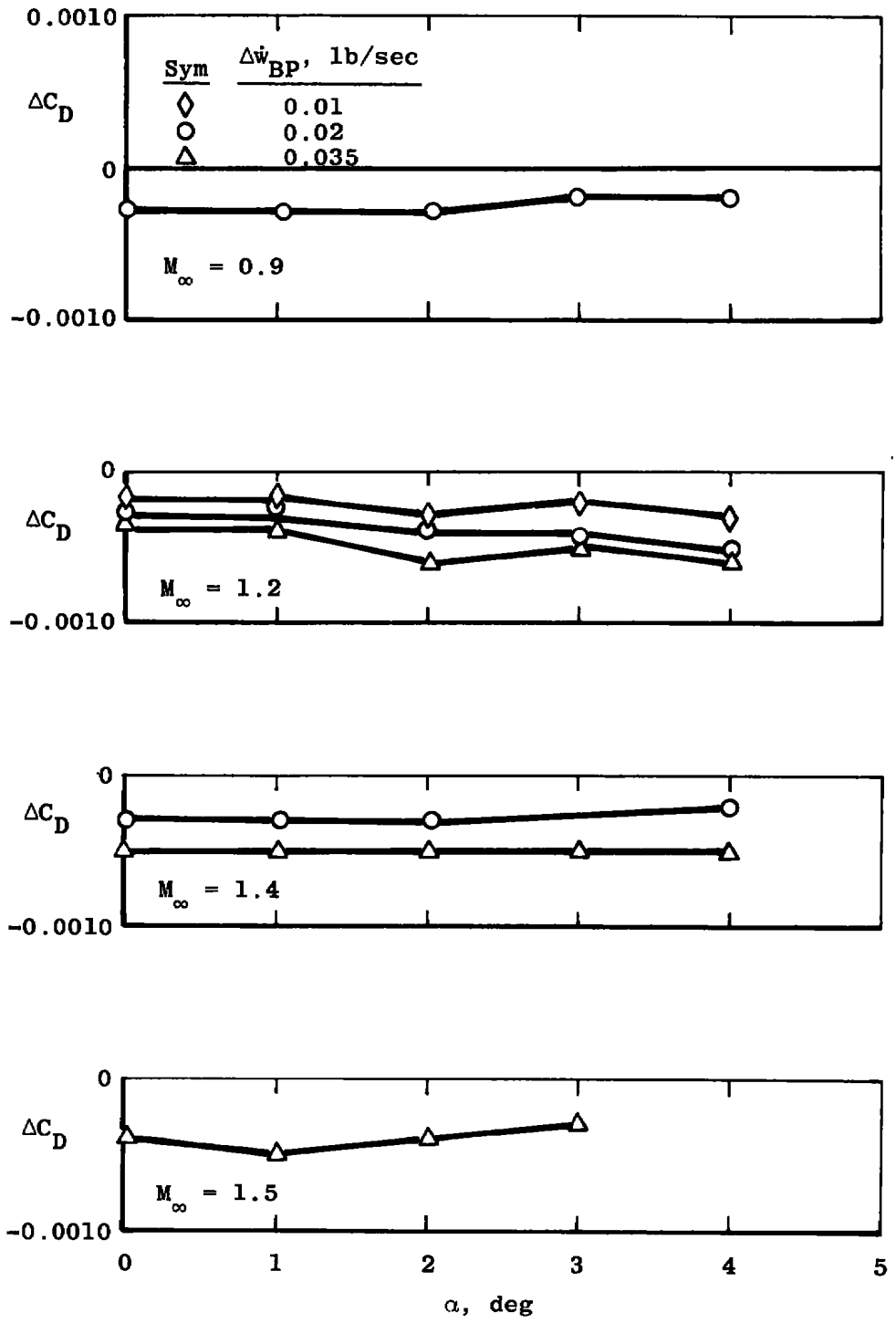

b. Maximum nozzle with clean wing
Figure 12. Concluded.

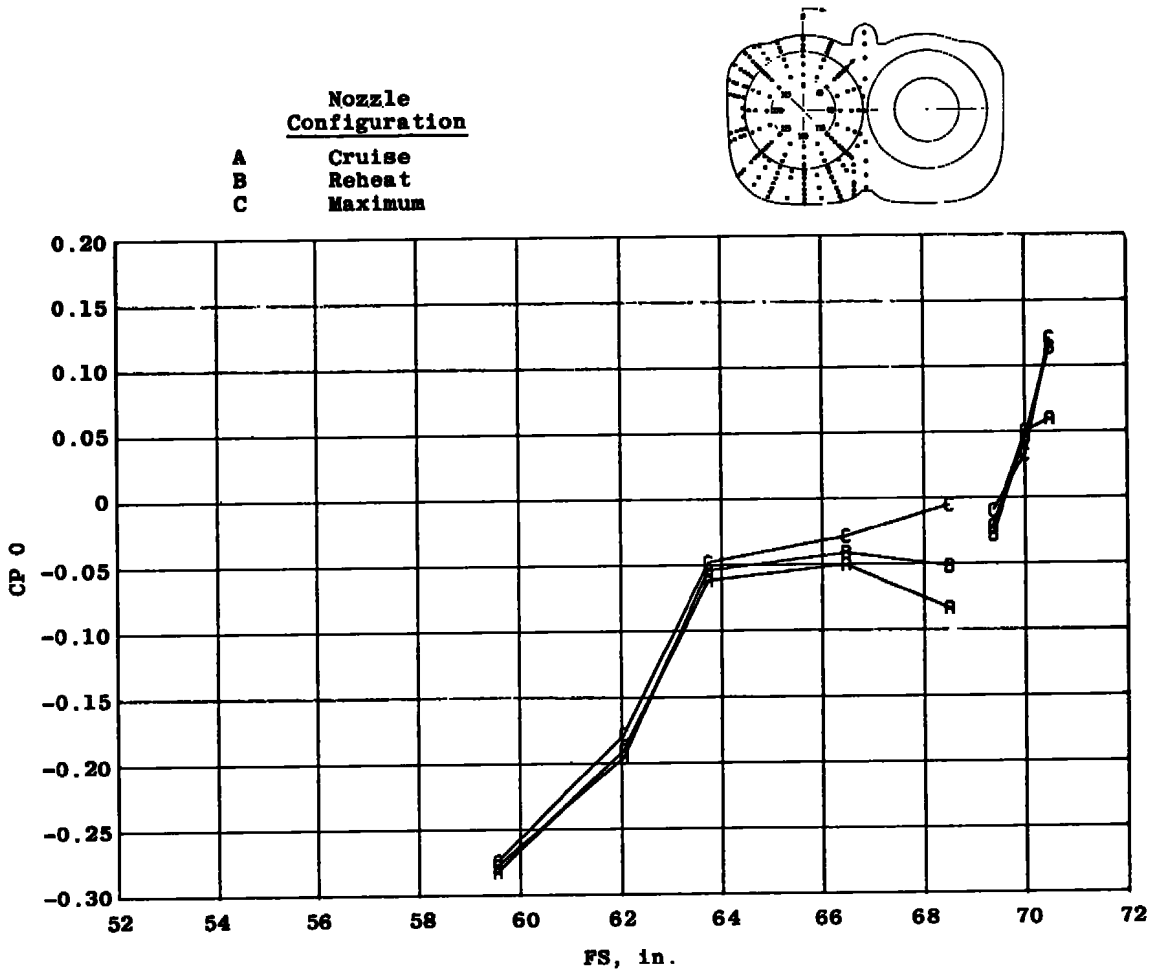

a. $\phi = 0$

Figure 13. Effect of nozzle closure on the surface pressure distribution, $M_\infty = 0.9$, Re = 2.8 x 10^6/ft, $\alpha = 4$ deg, NPR = 5.0, and $\delta = 0$.

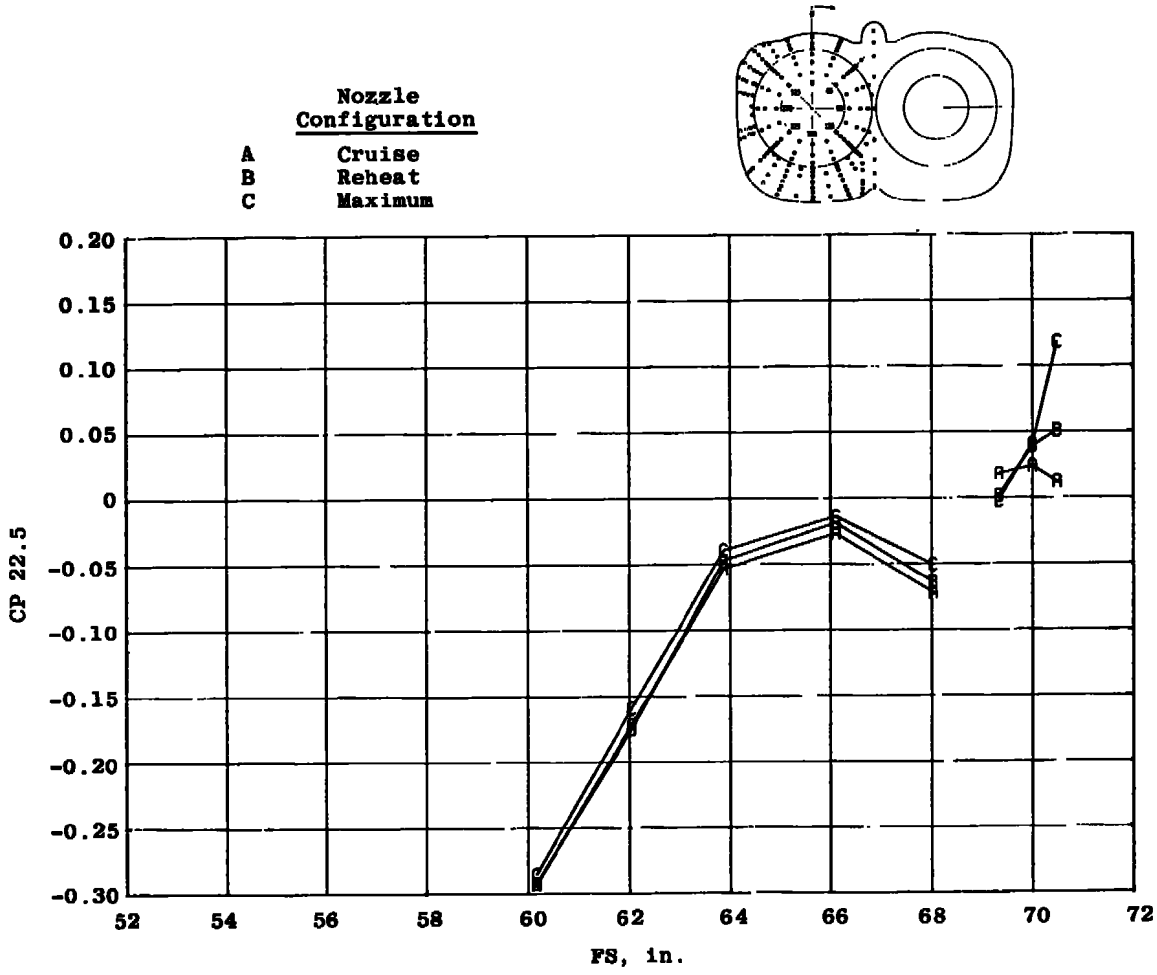

b. ϕ = 22.5 deg

Figure 13. Continued.

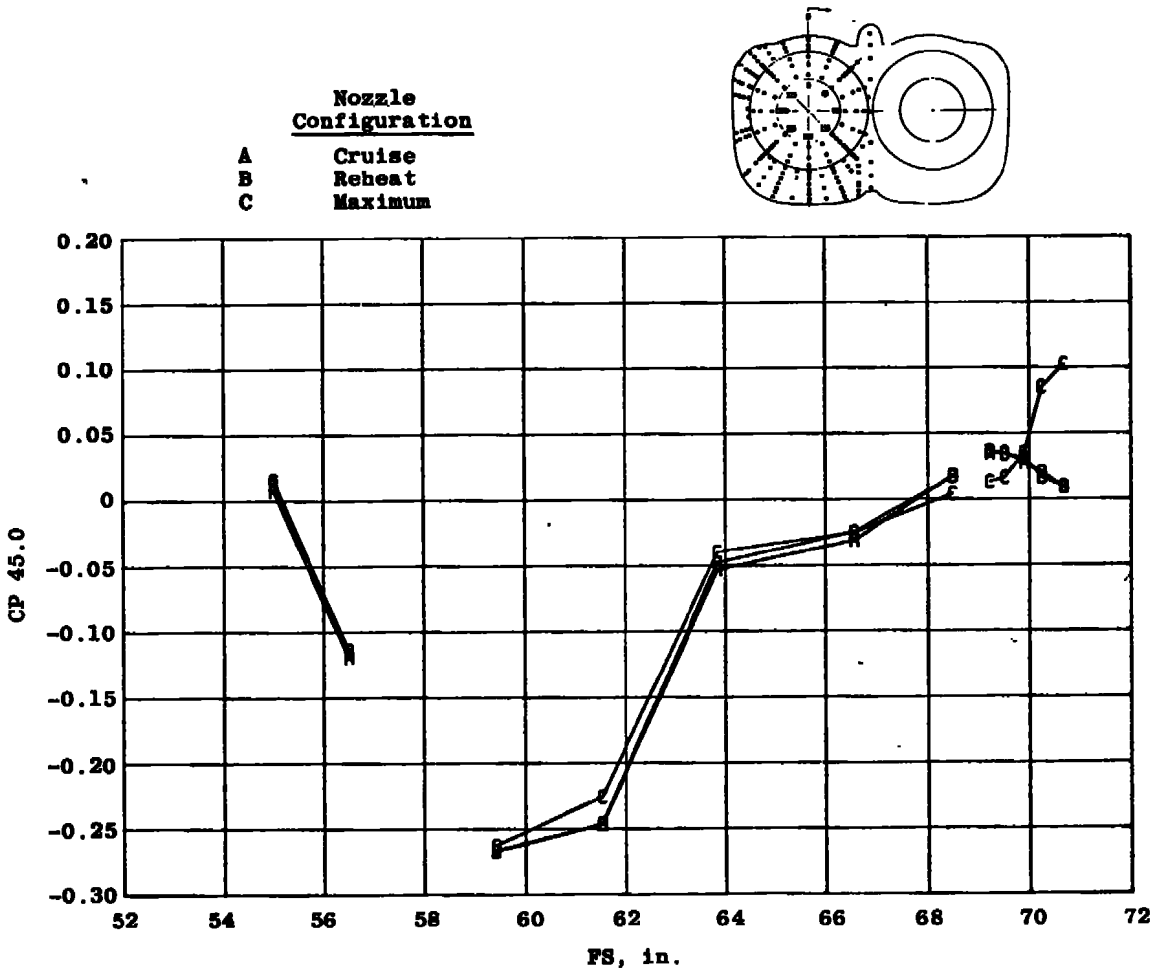

c. ϕ = 45.0 deg

Figure 13. Continued.

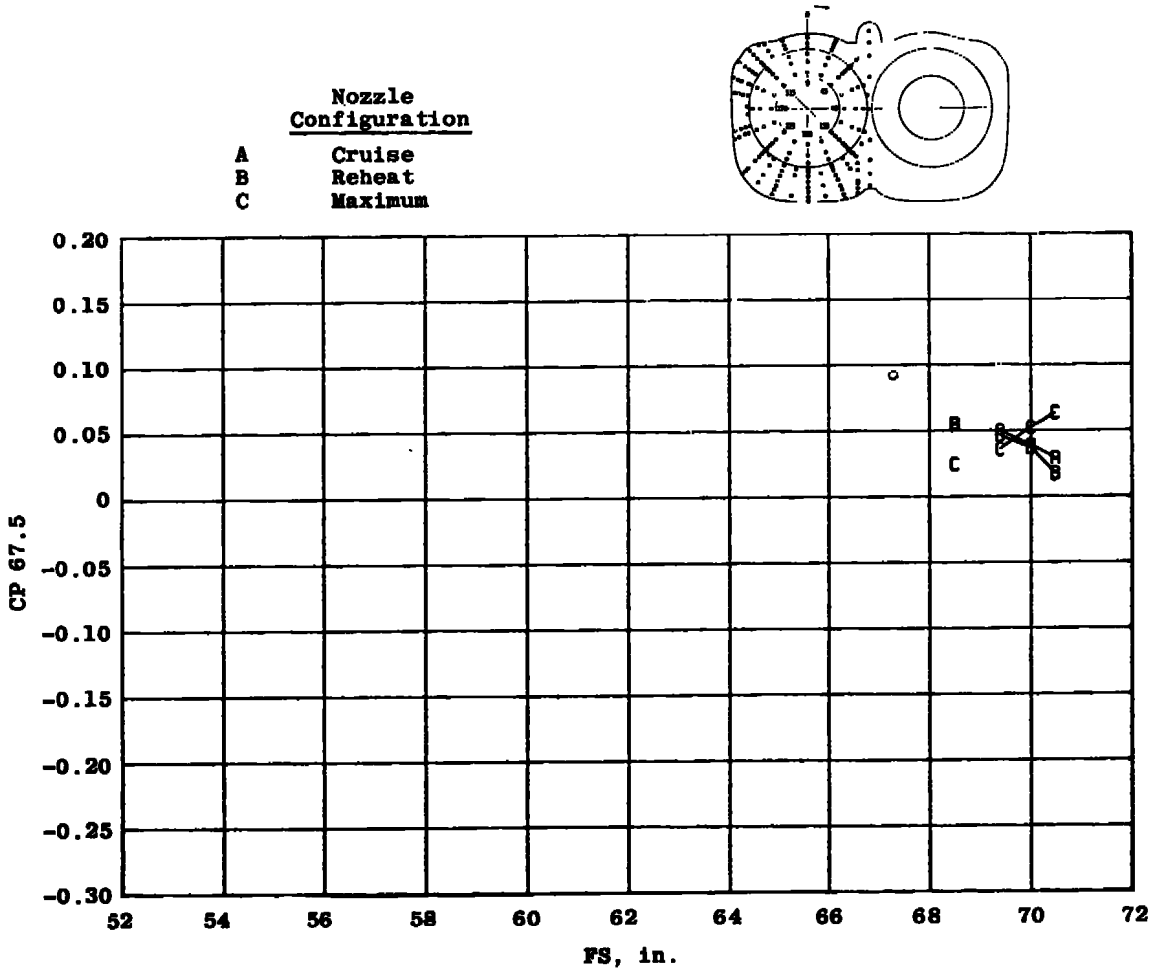

d. ϕ = 67.5 deg

Figure 13. Continued.

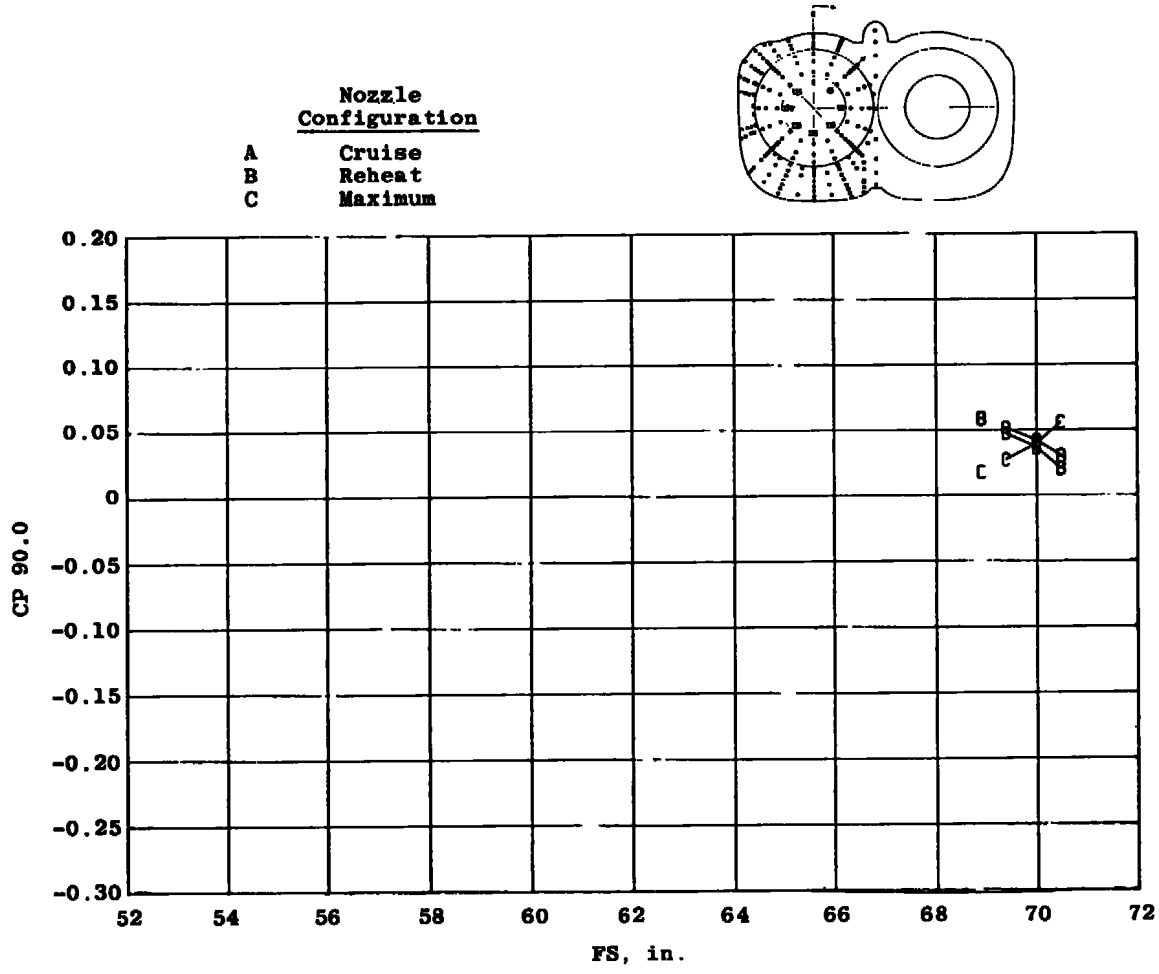

e. ϕ = 90.0 deg

Figure 13. Continued.

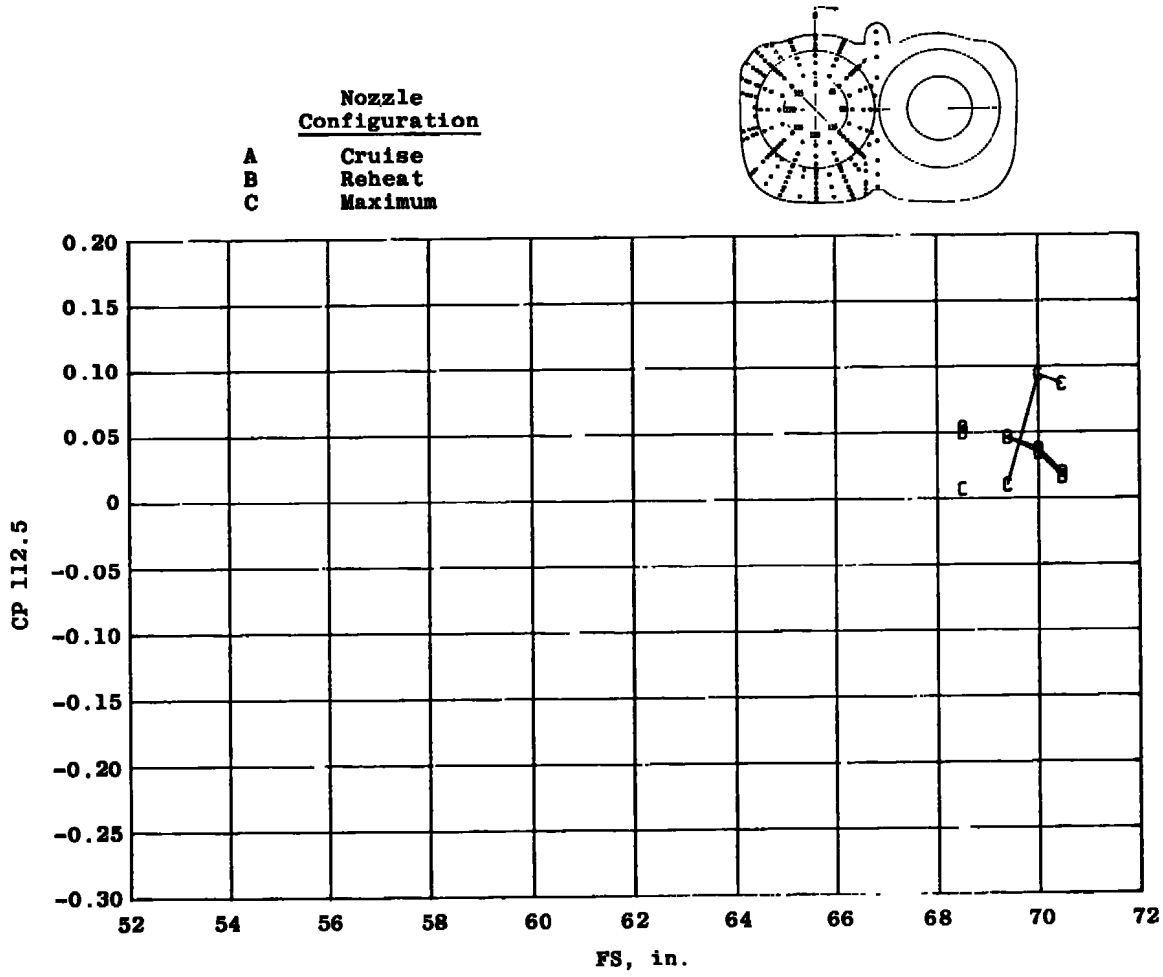

f. ϕ = 112.5 deg

Figure 13. Continued.

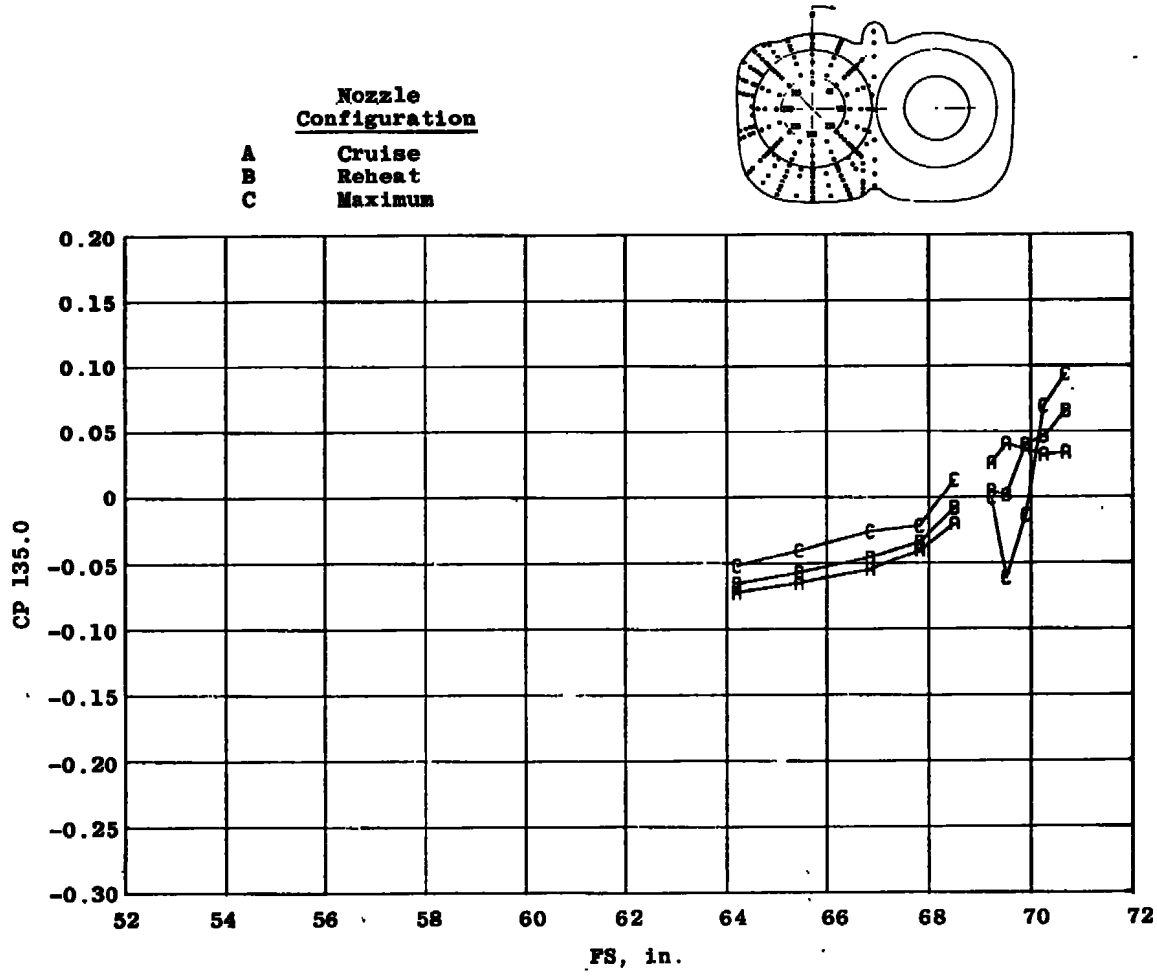

g. ϕ = 135.0 deg

Figure 13. Continued.

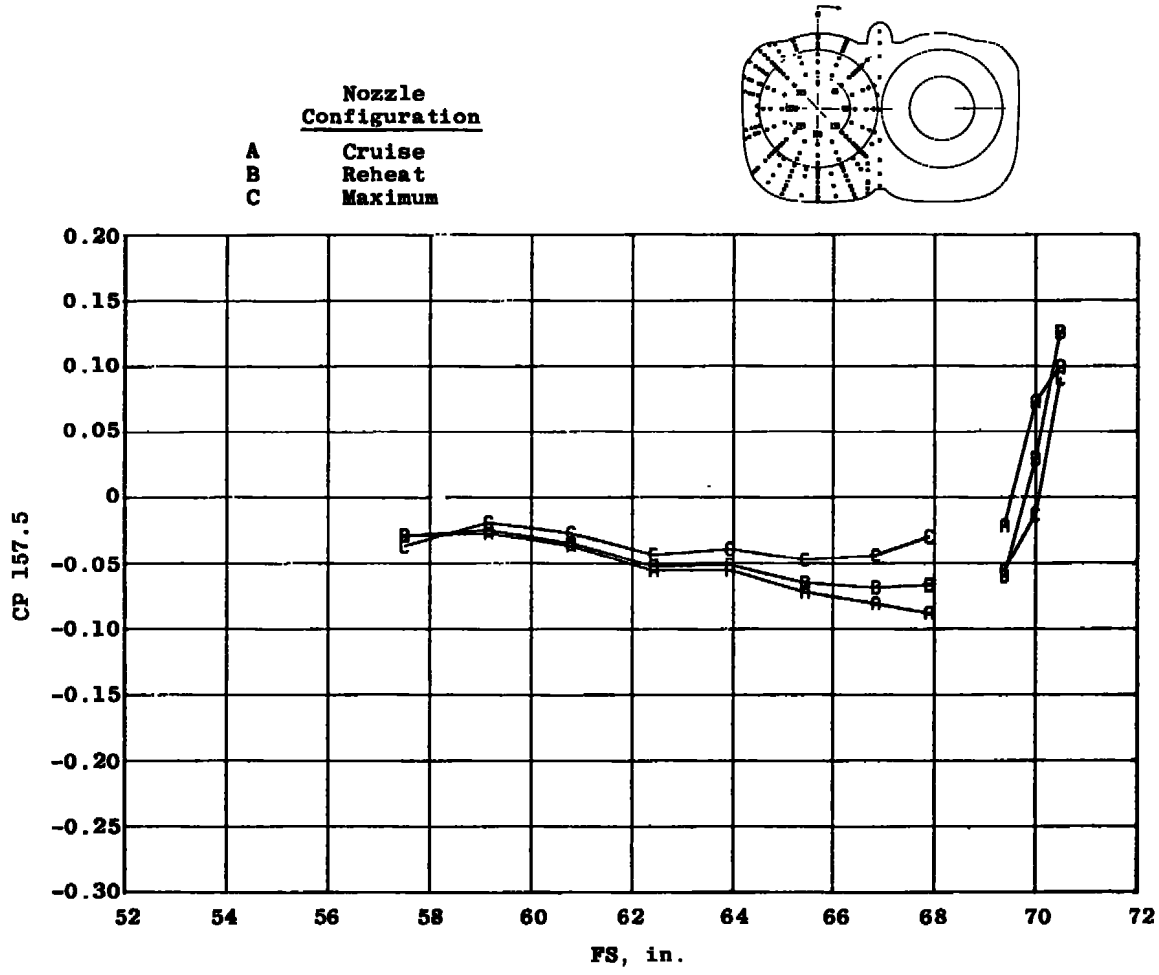

h. ϕ = 157.5 deg

Figure 13. Continued.

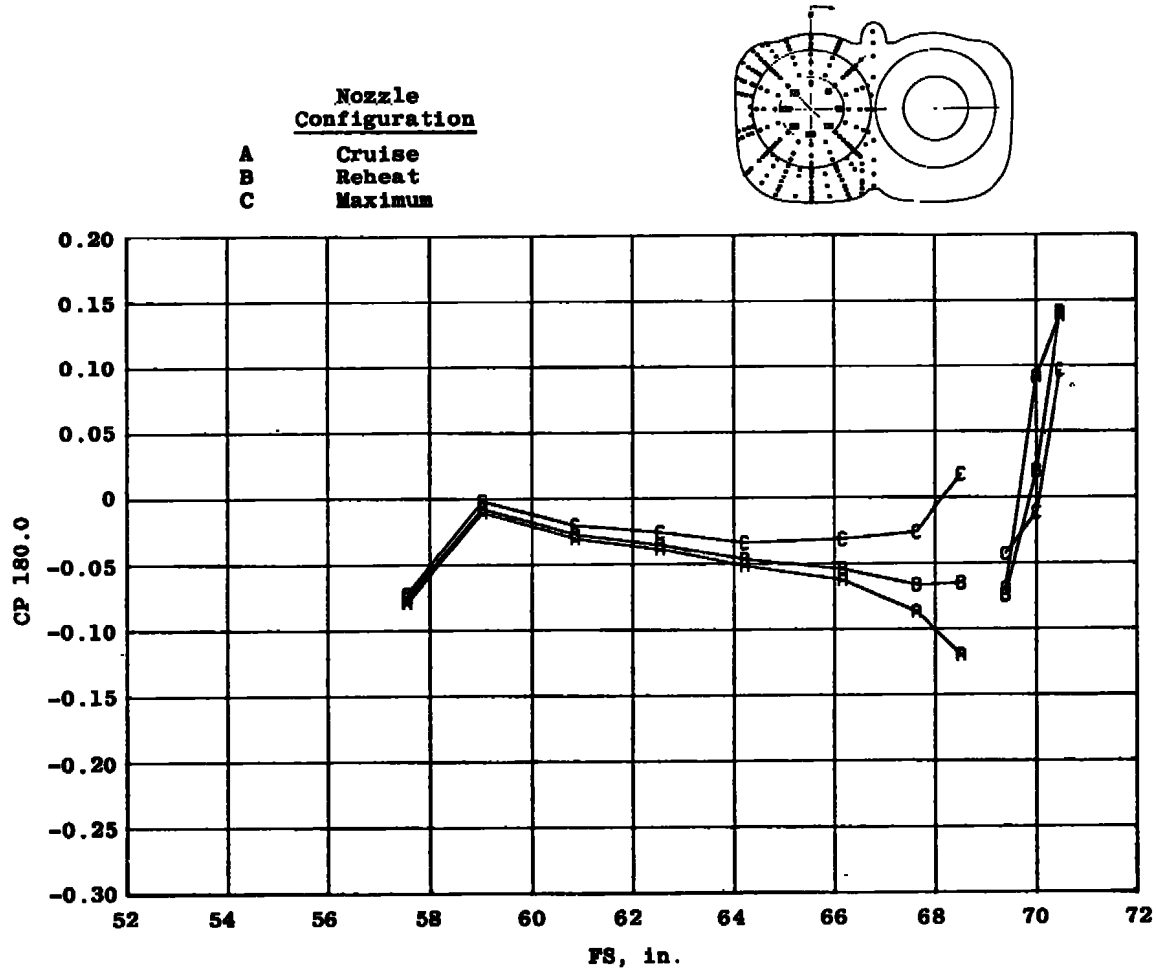

i. ϕ = 180.0 deg

Figure 13. Continued.

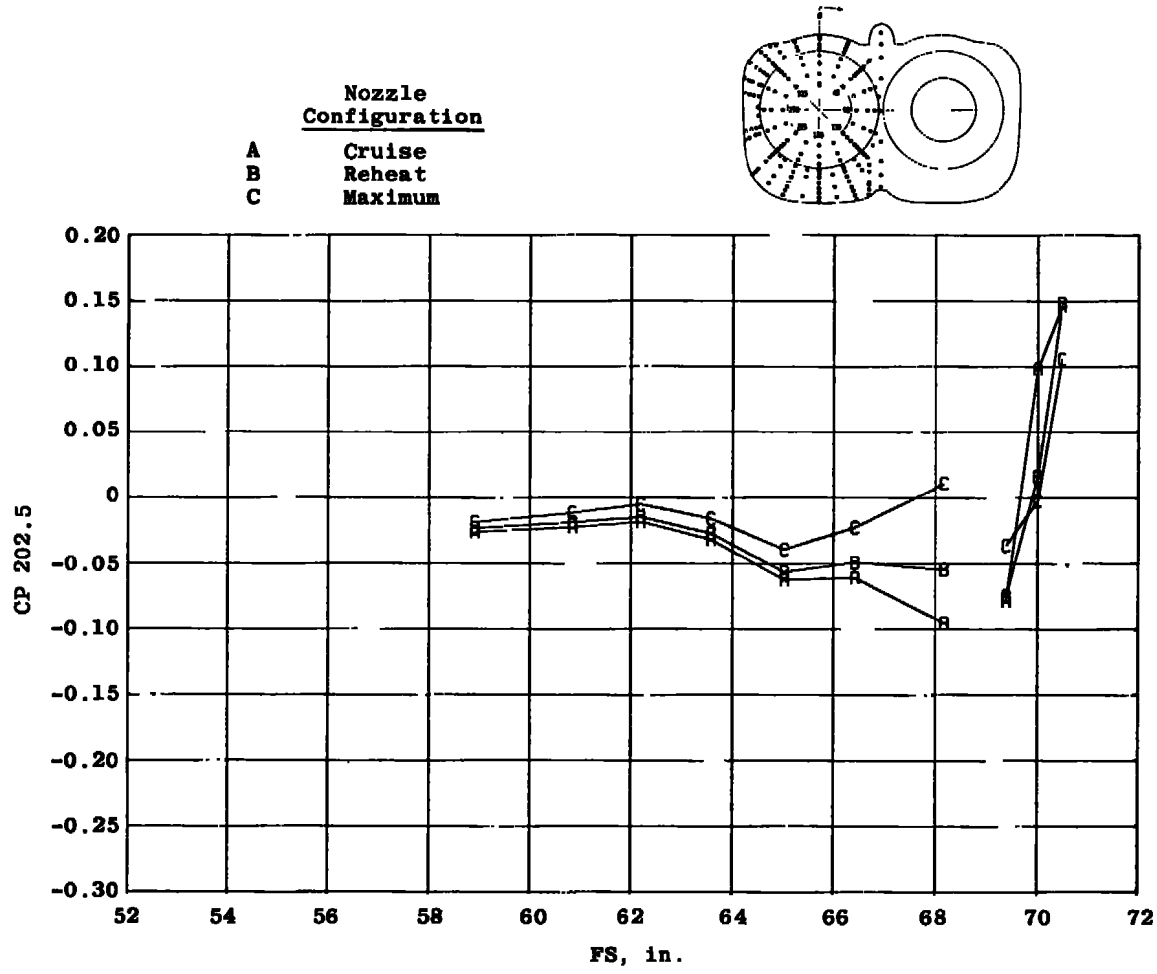

j. ϕ = 202.5 deg

Figure 13. Continued.

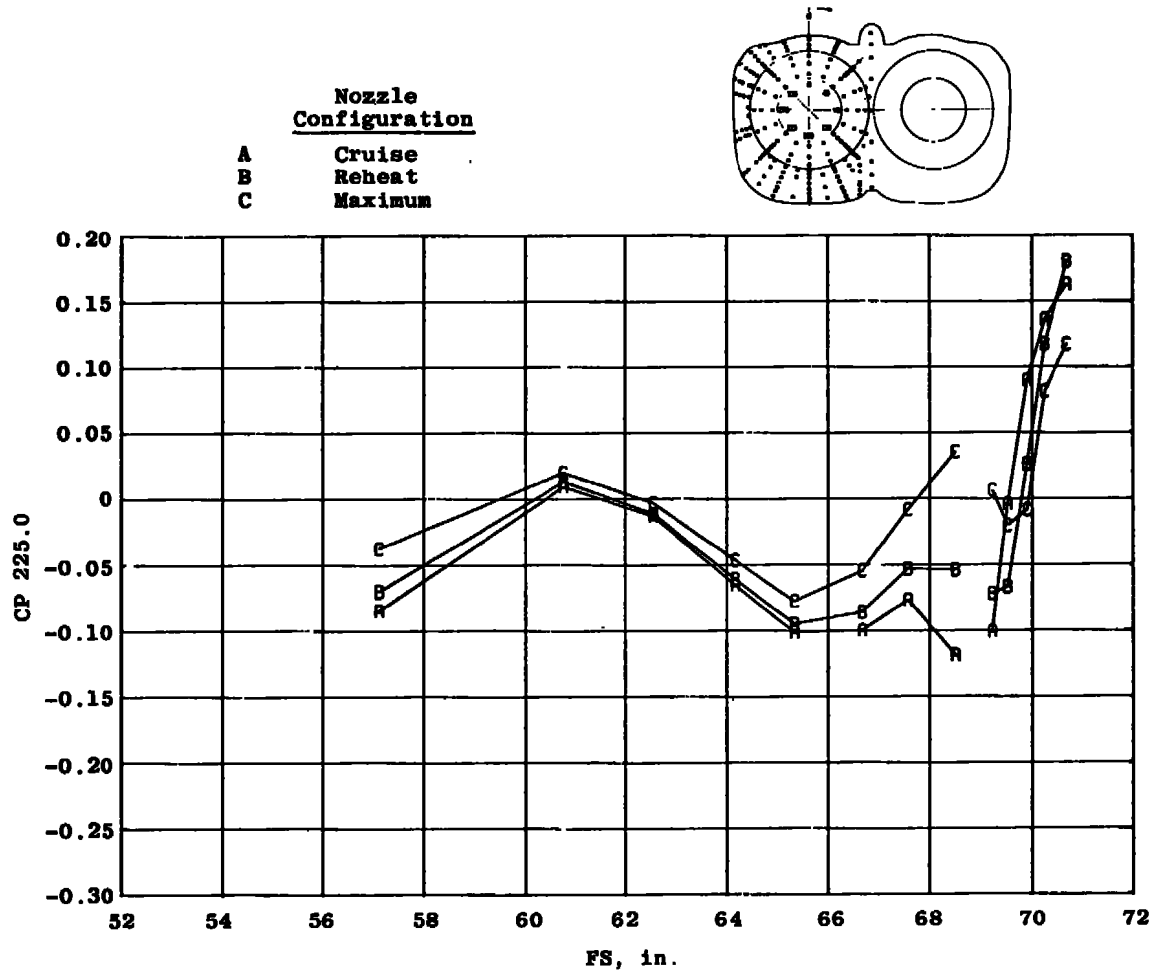

k. ϕ = 225.0 deg

Figure 13. Continued.

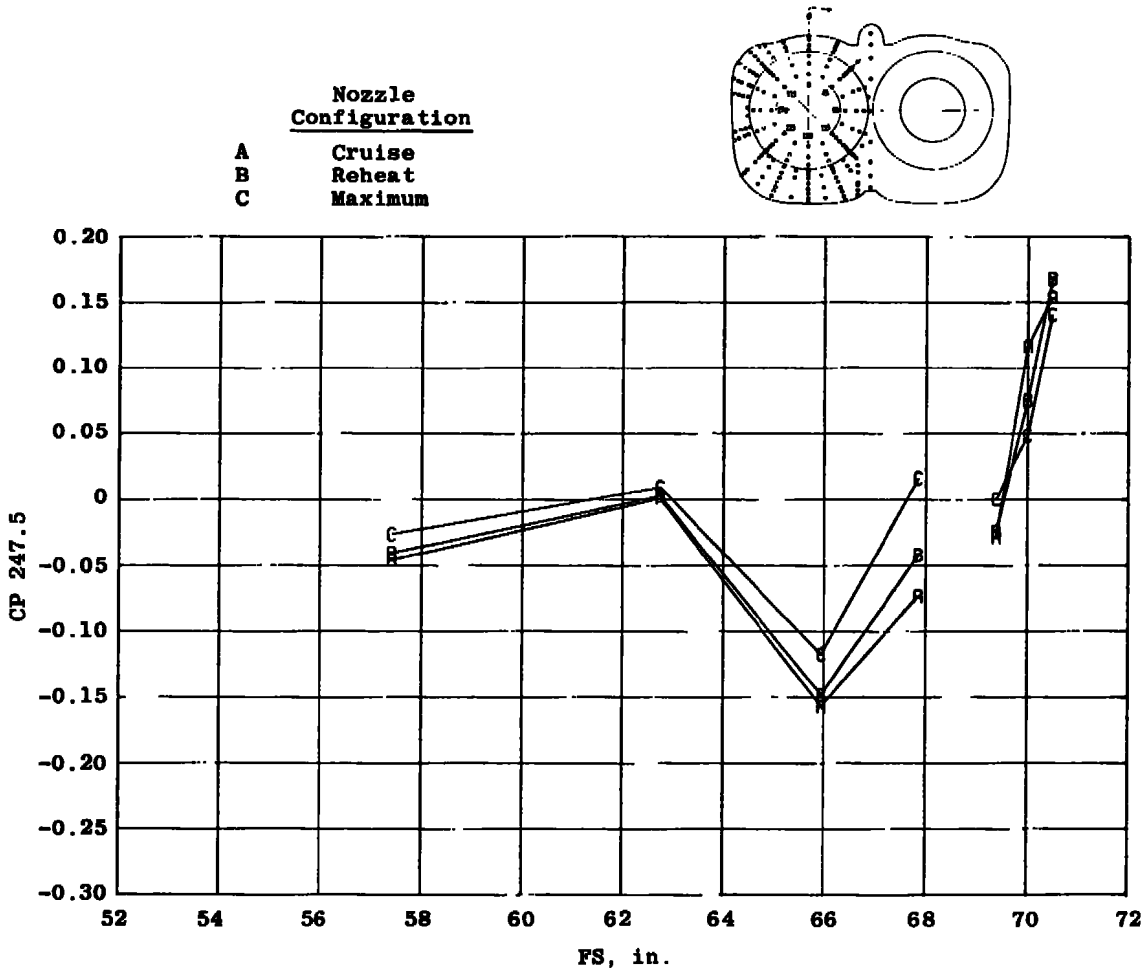

l. ϕ = 247.5 deg

Figure 13. Continued.

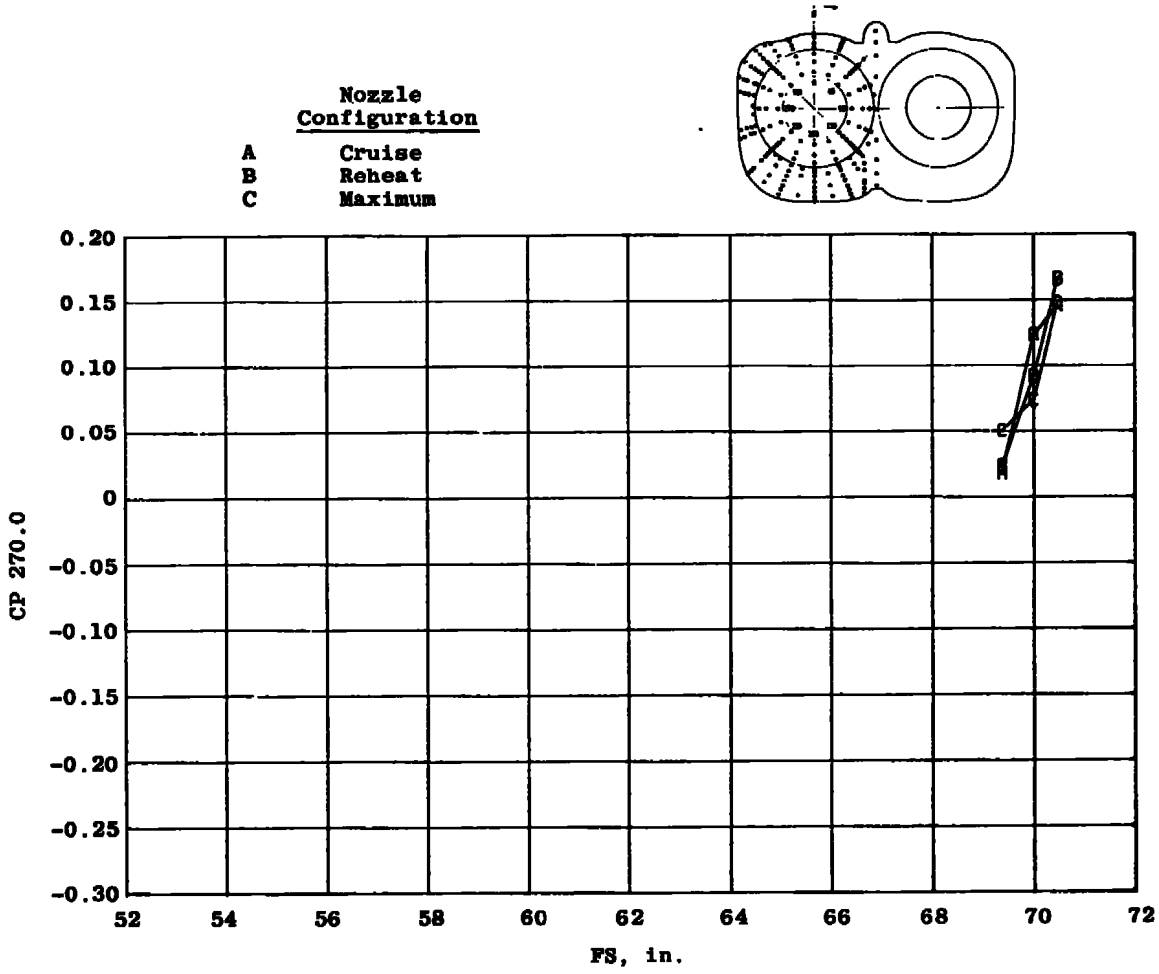

m. ϕ = 270.0 deg

Figure 13. Continued.

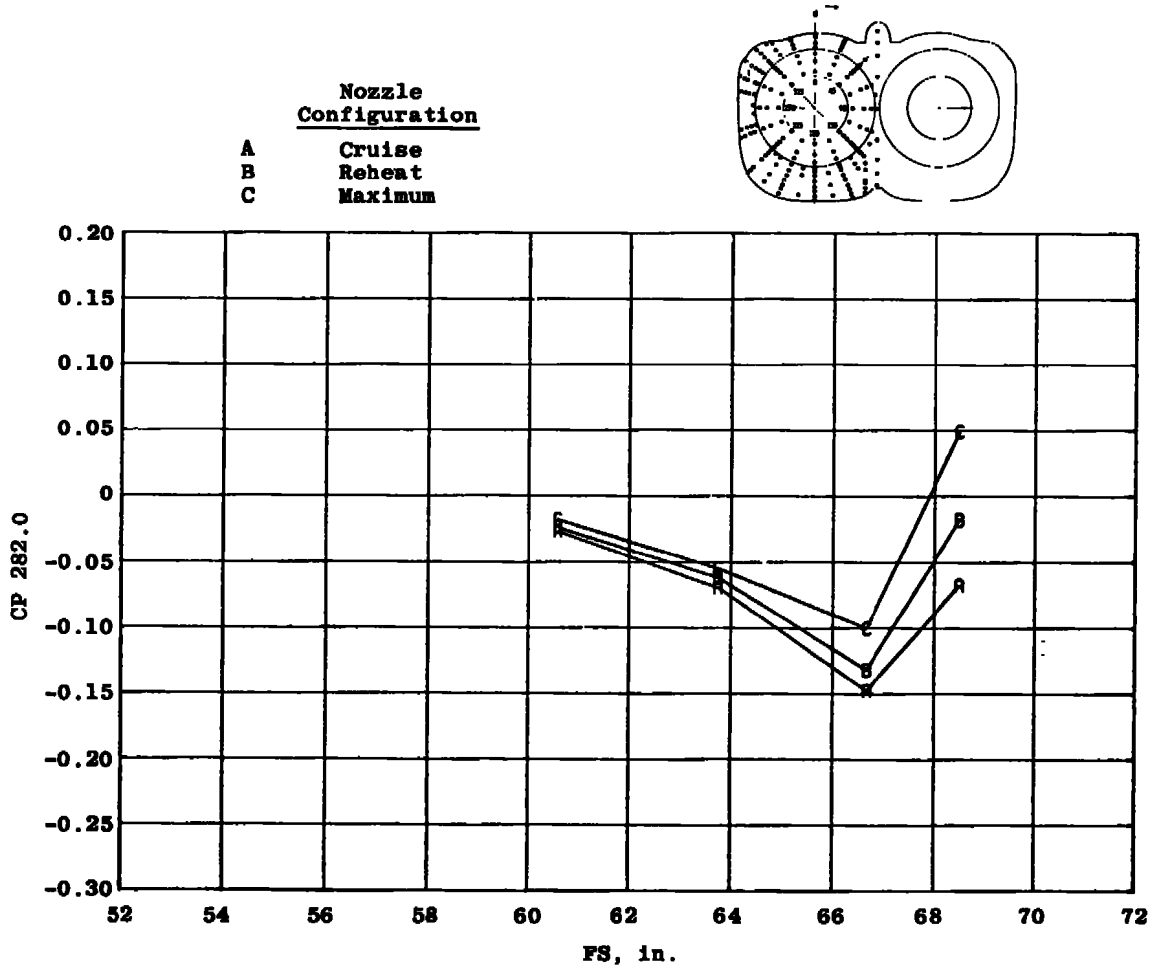

n. ϕ = 282.0 deg

Figure 13. Continued.

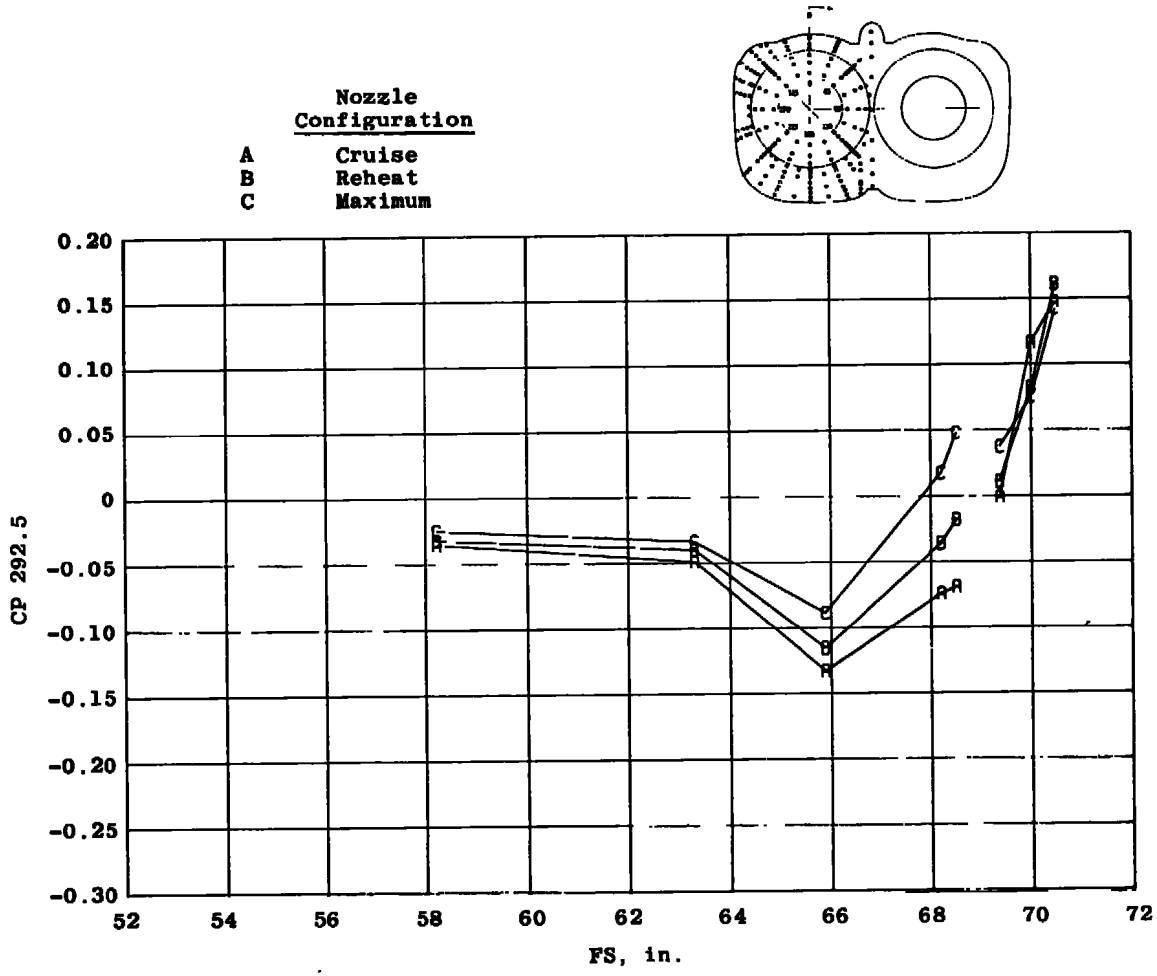

o. ϕ = 292.5 deg

Figure 13. Continued.

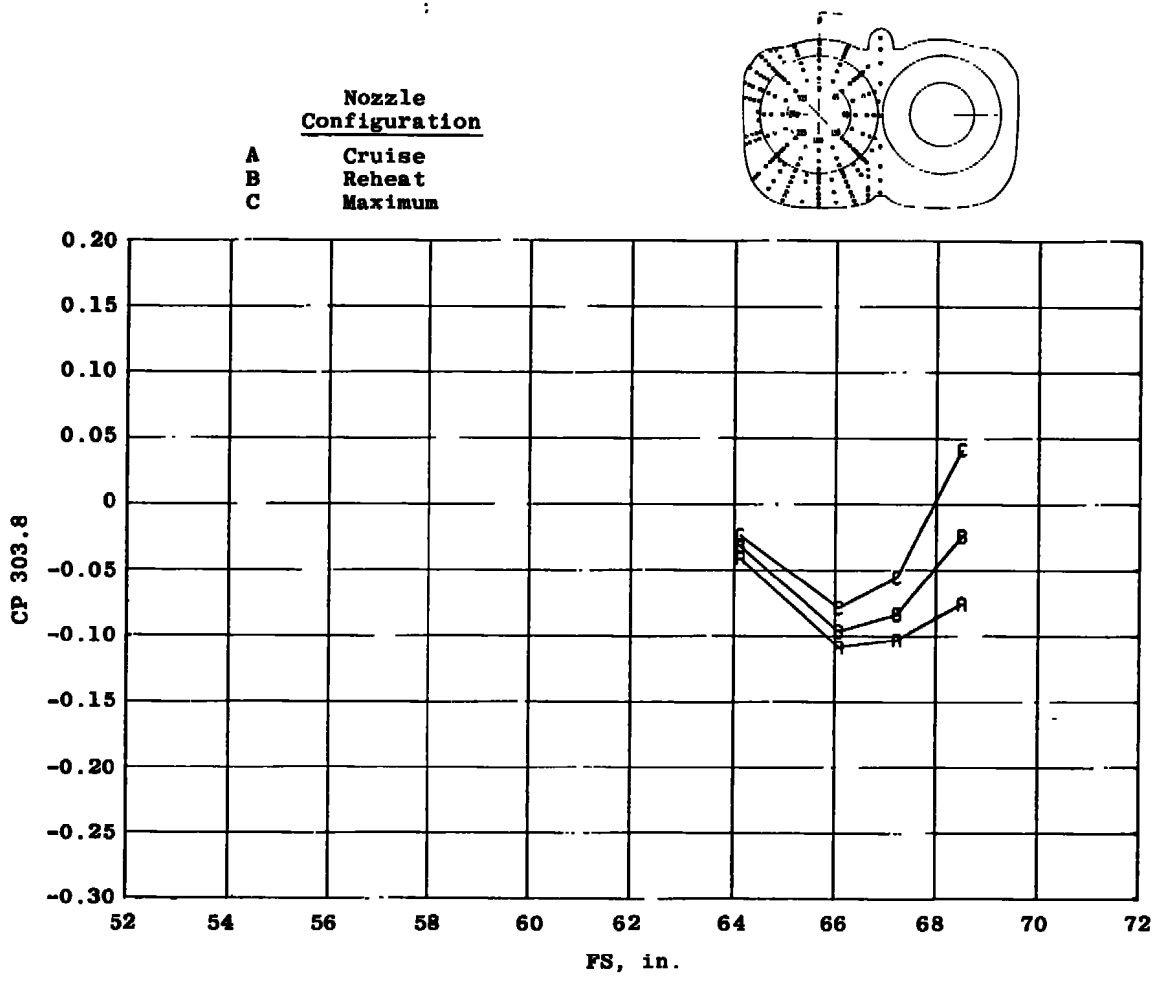

p. ϕ = 303.8 deg

Figure 13. Continued.

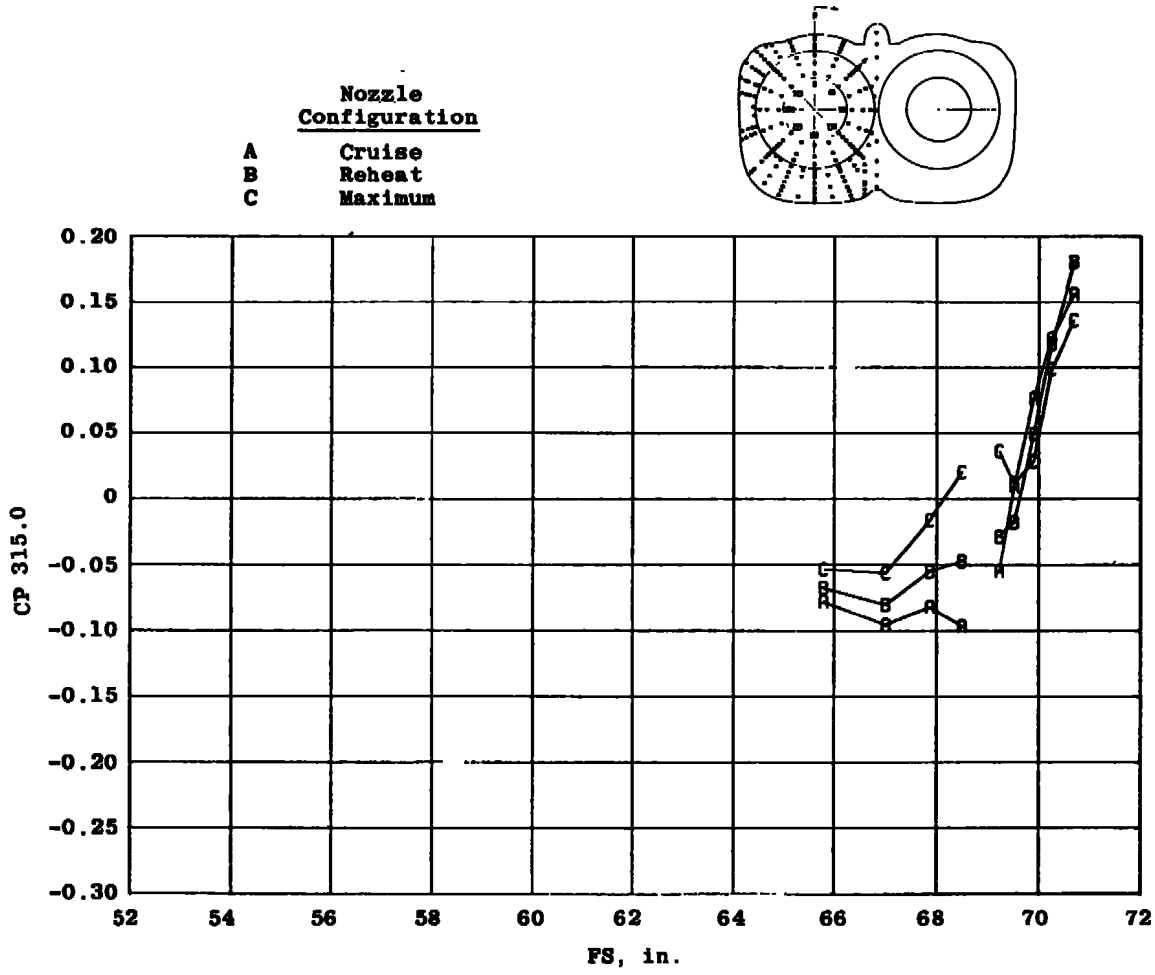

q. ϕ = 315.0 deg

Figure 13. Continued.

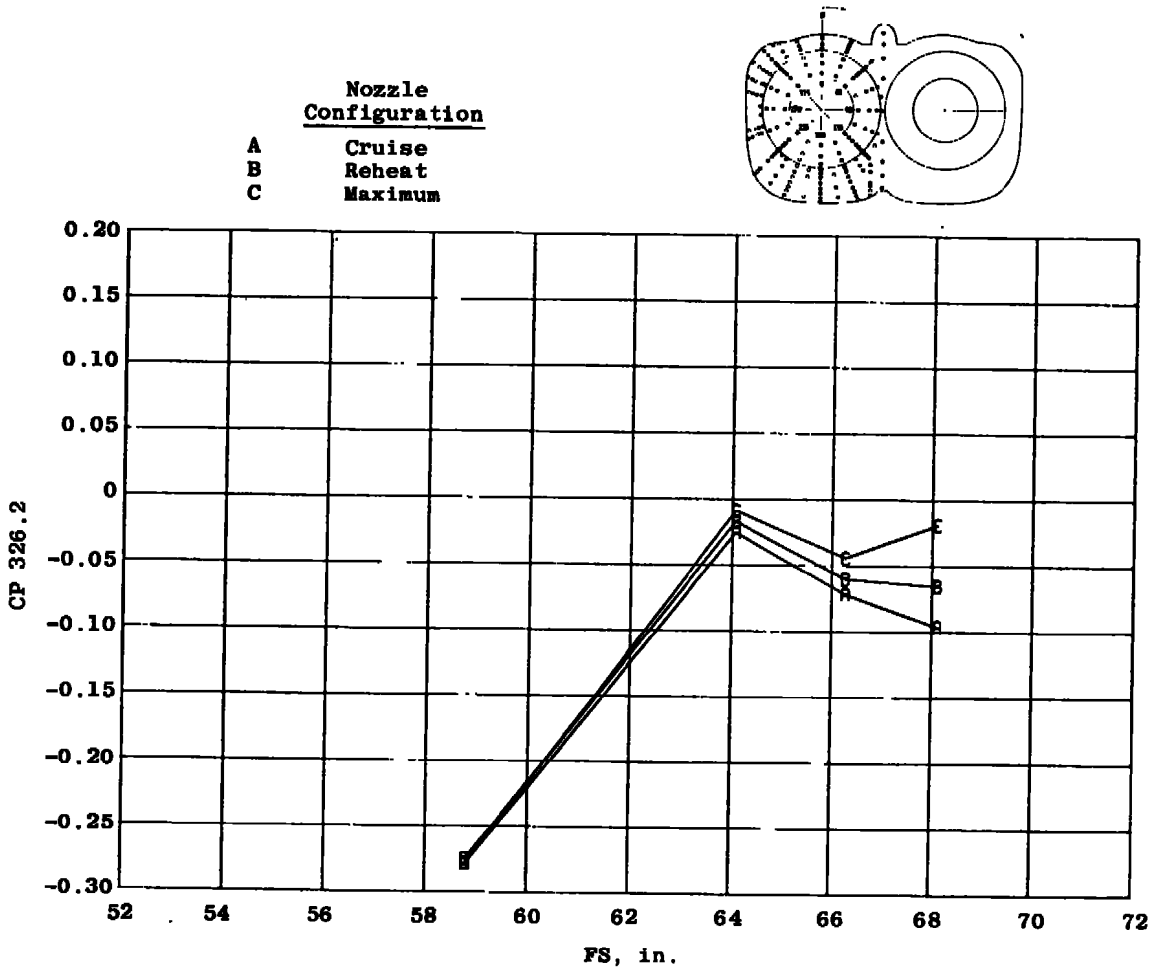

r. ϕ = 326.2 deg

Figure 13. Continued.

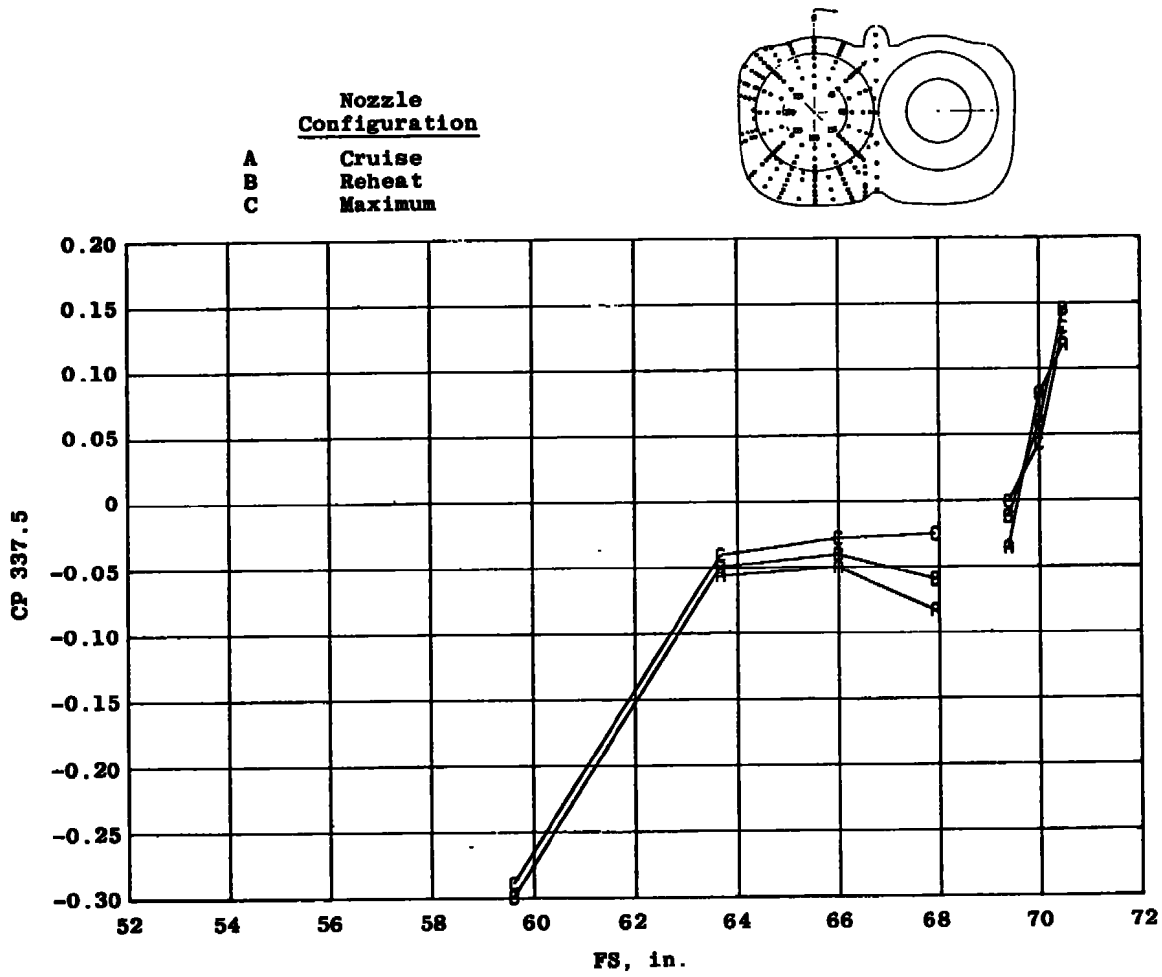

s. ϕ = 337.5 deg

Figure 13. Concluded.

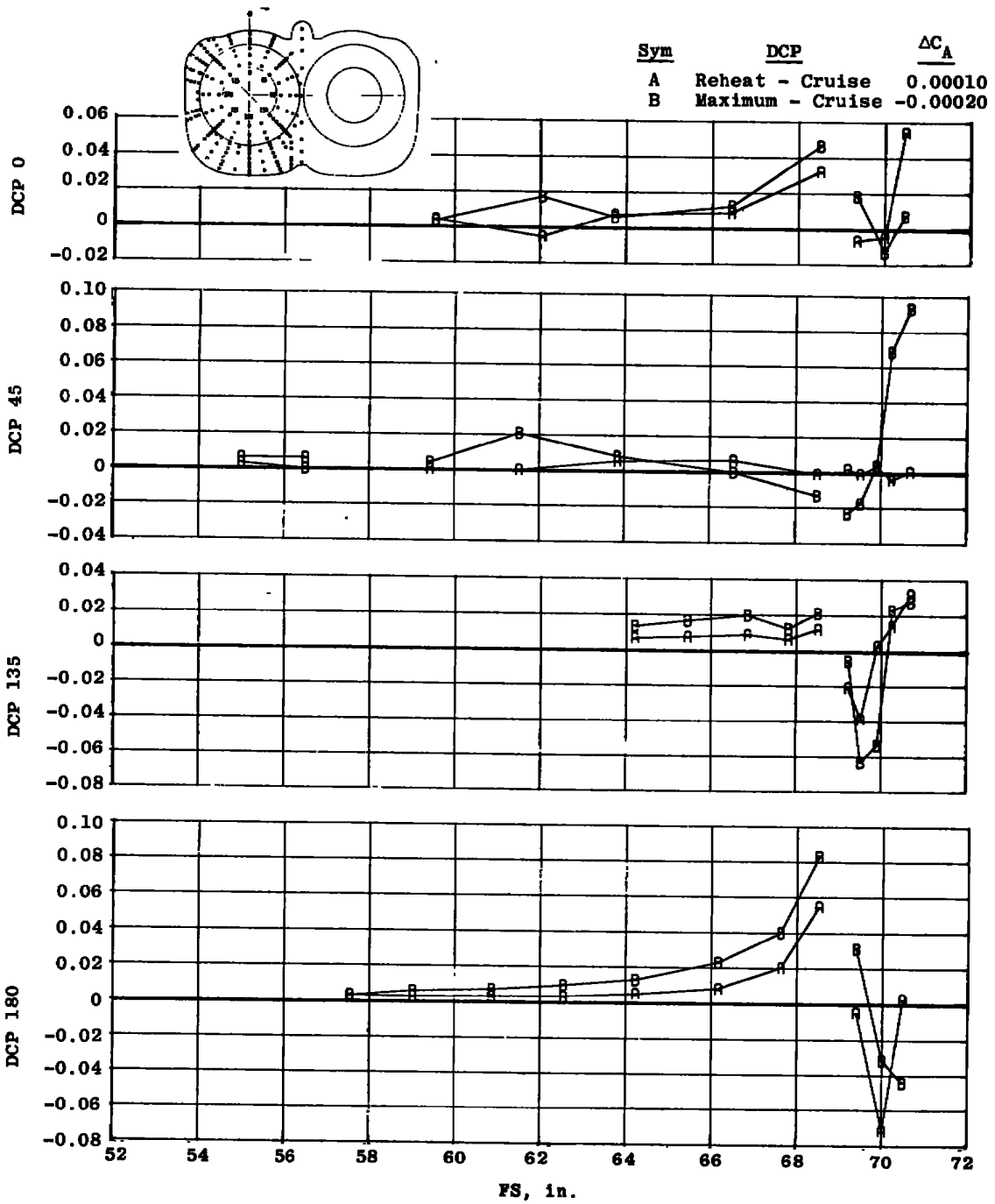

Figure 14. Surface pressure changes with nozzle closure, M_∞ = 0.9, Re = 2.8 x 10^6/ft, α = 4 deg, δ_H = 0, and NPR = 5.

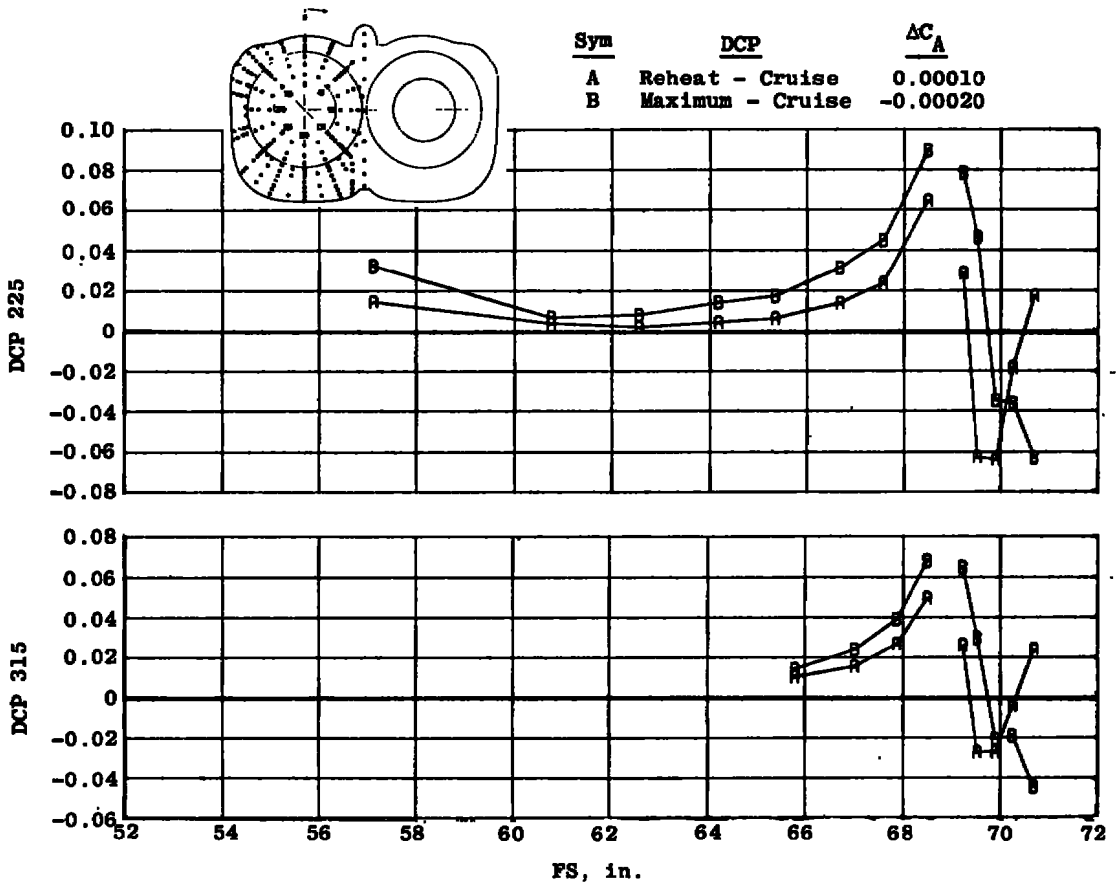

Figure 14. Concluded.

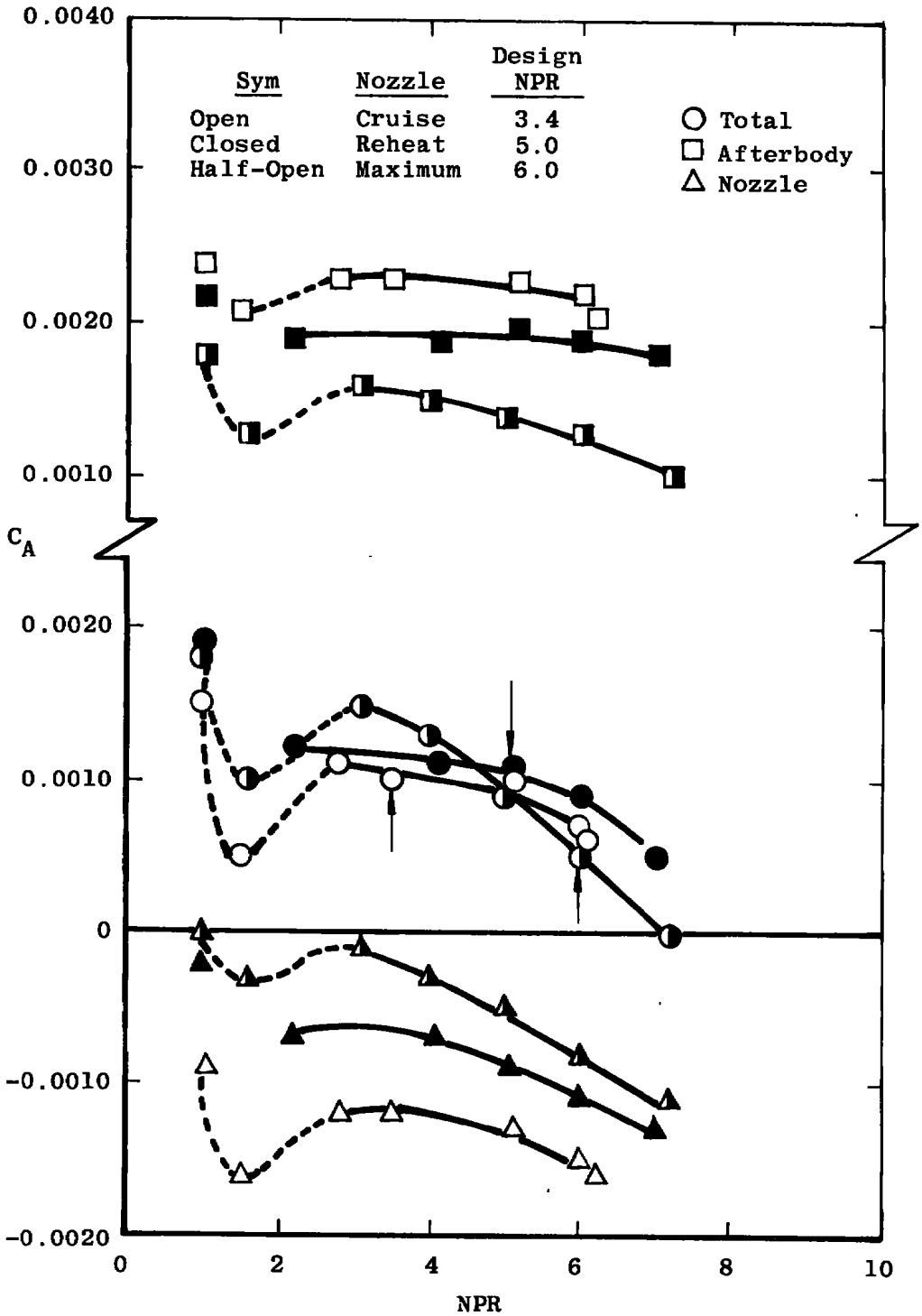

Figure 15. Nozzle closure effects on the aft end axial loads, M_∞ = 0.9, α = 4.2 deg, and δ_H = 0.

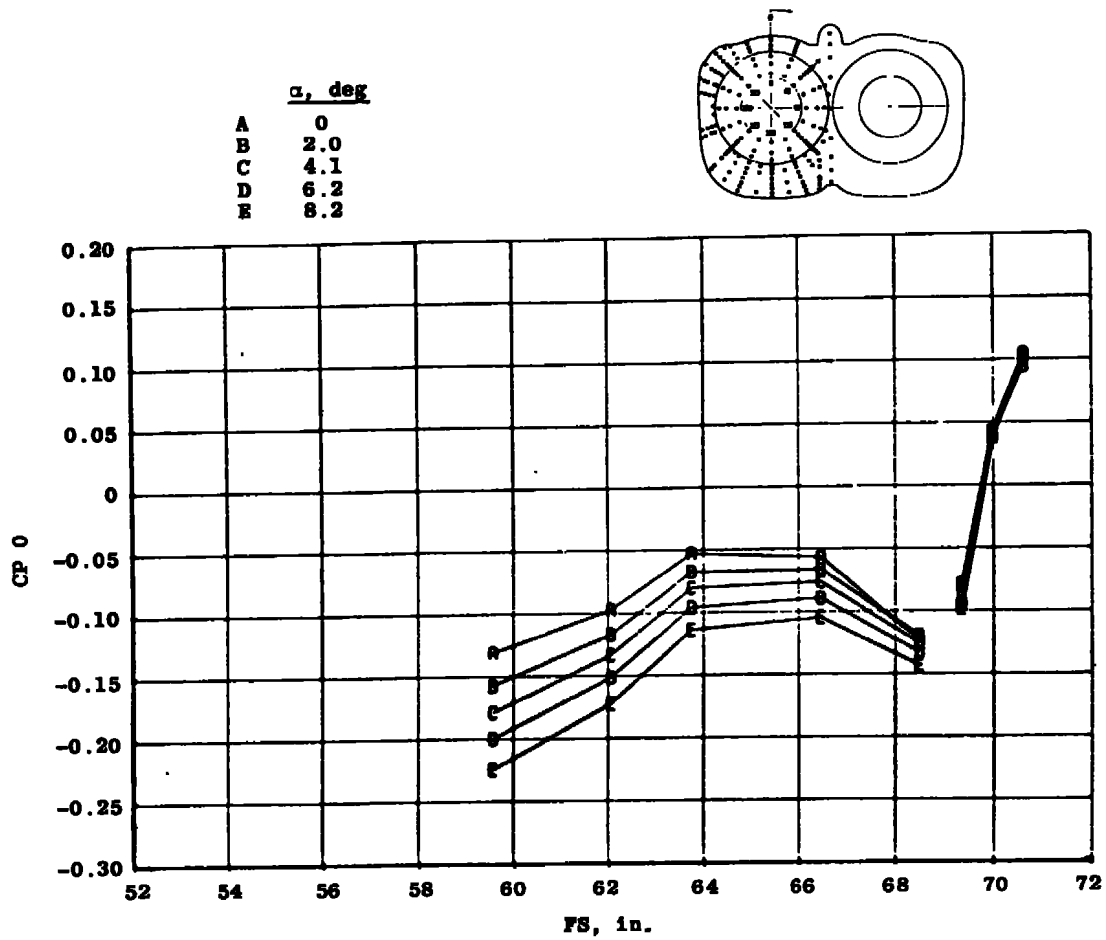

a. $\phi = 0$

Figure 16. Model attitude effects on the surface pressure distribution of the cruise nozzle configuration, $M_\infty = 0.6$, Re = 2.8 x 10^6/ft, $\delta_H = -2$ deg, and NPR = 3.

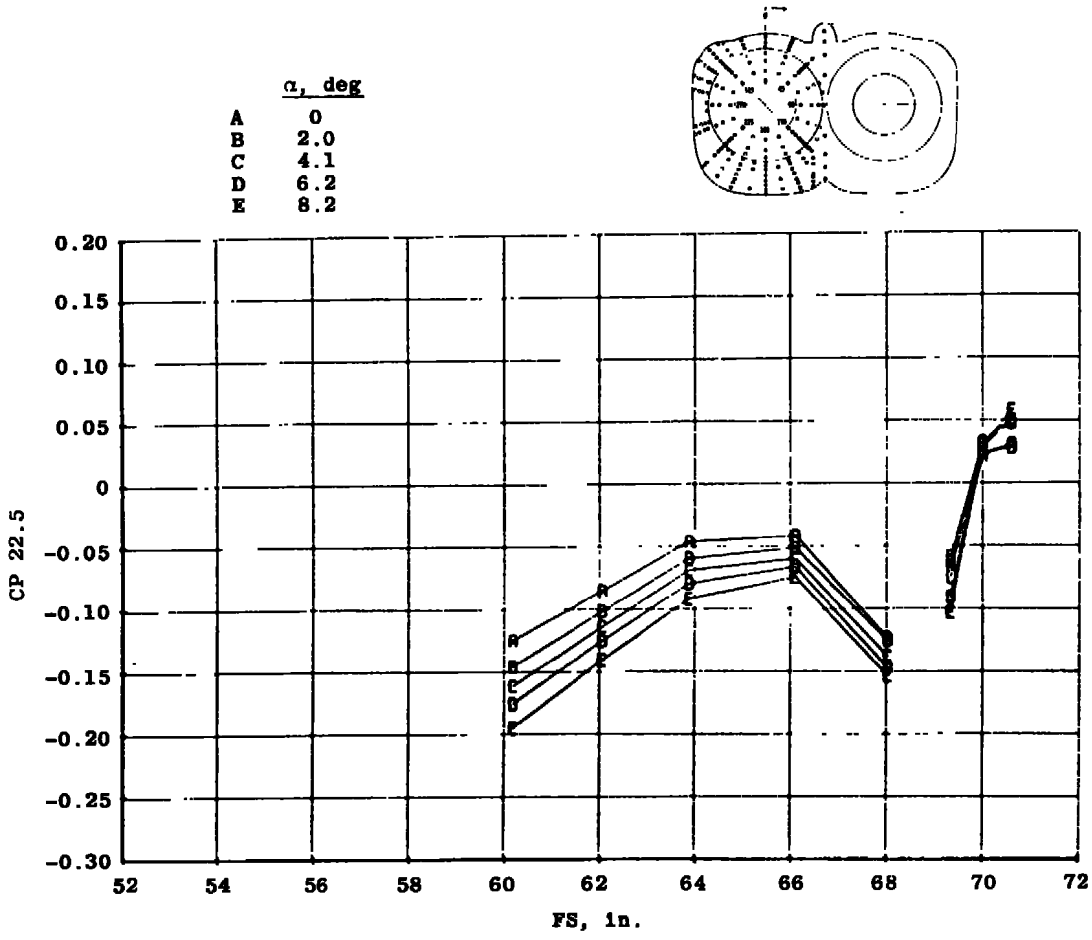

b. ϕ = 22.5 deg

Figure 16. Continued.

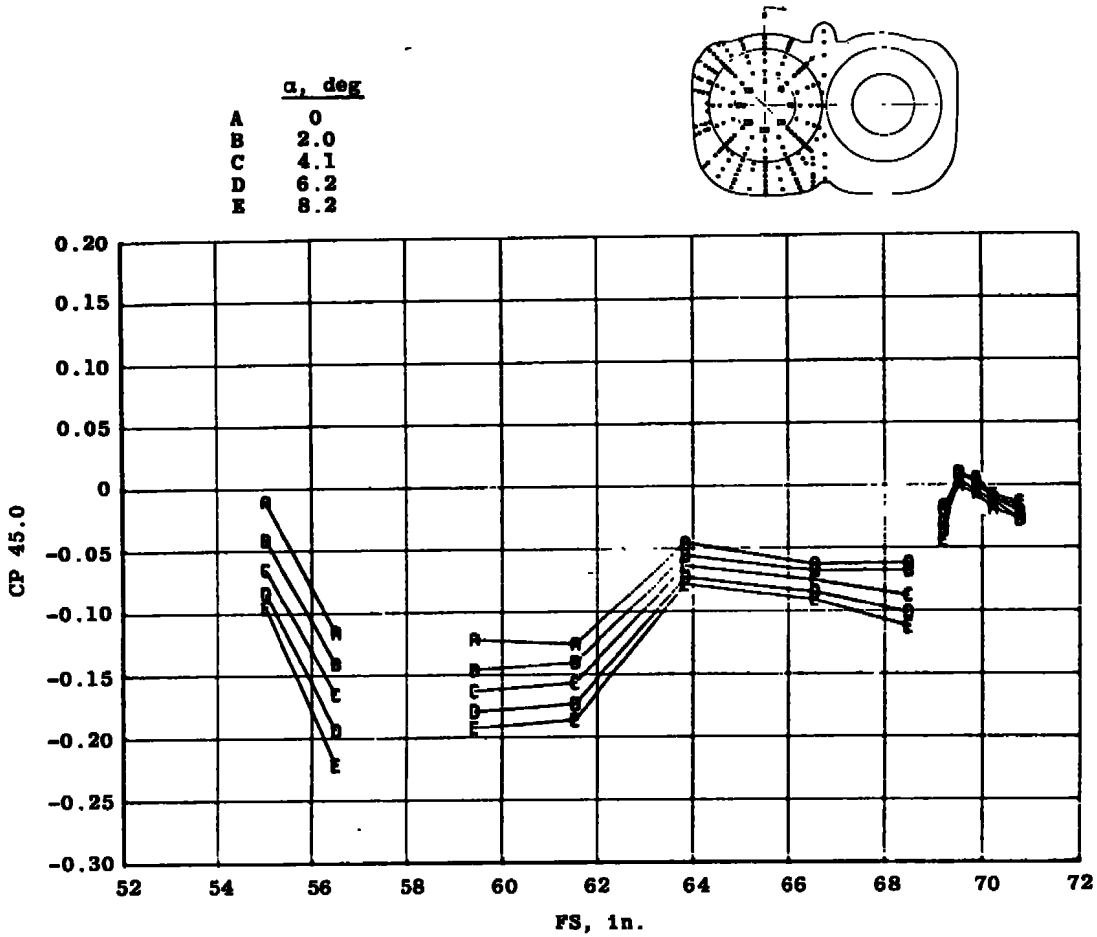

c. ϕ = 45.0 deg

Figure 16. Continued.

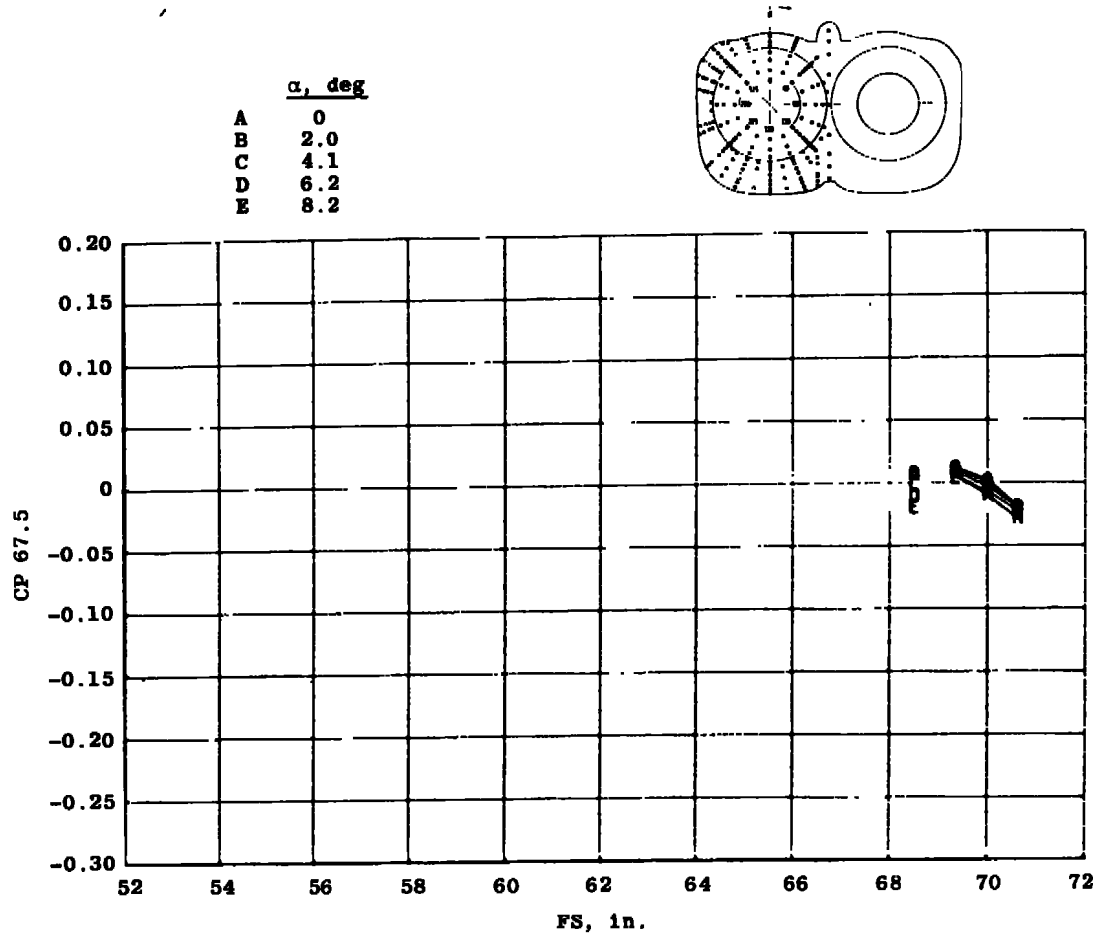

d. ϕ = 67.5 deg

Figure 16. Continued.

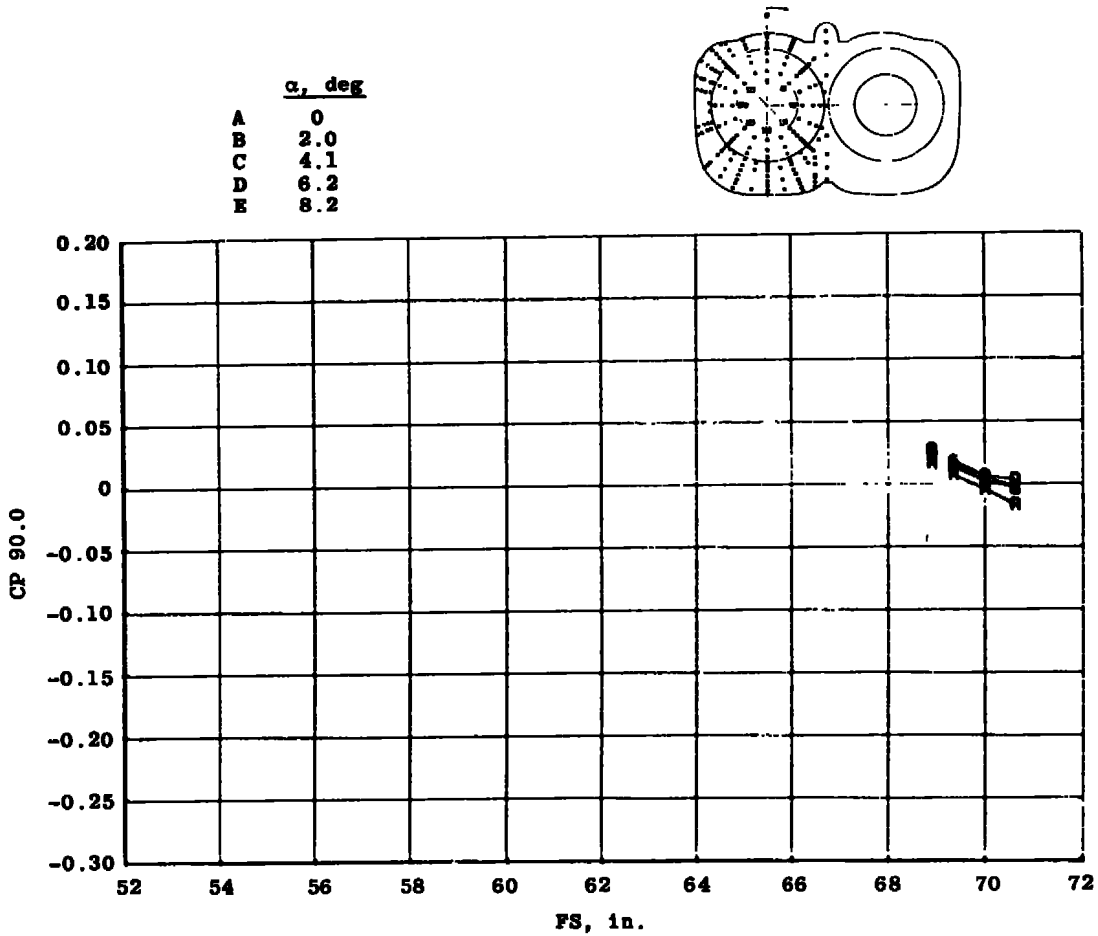

e. ϕ = 90.0 deg

Figure 16. Continued.

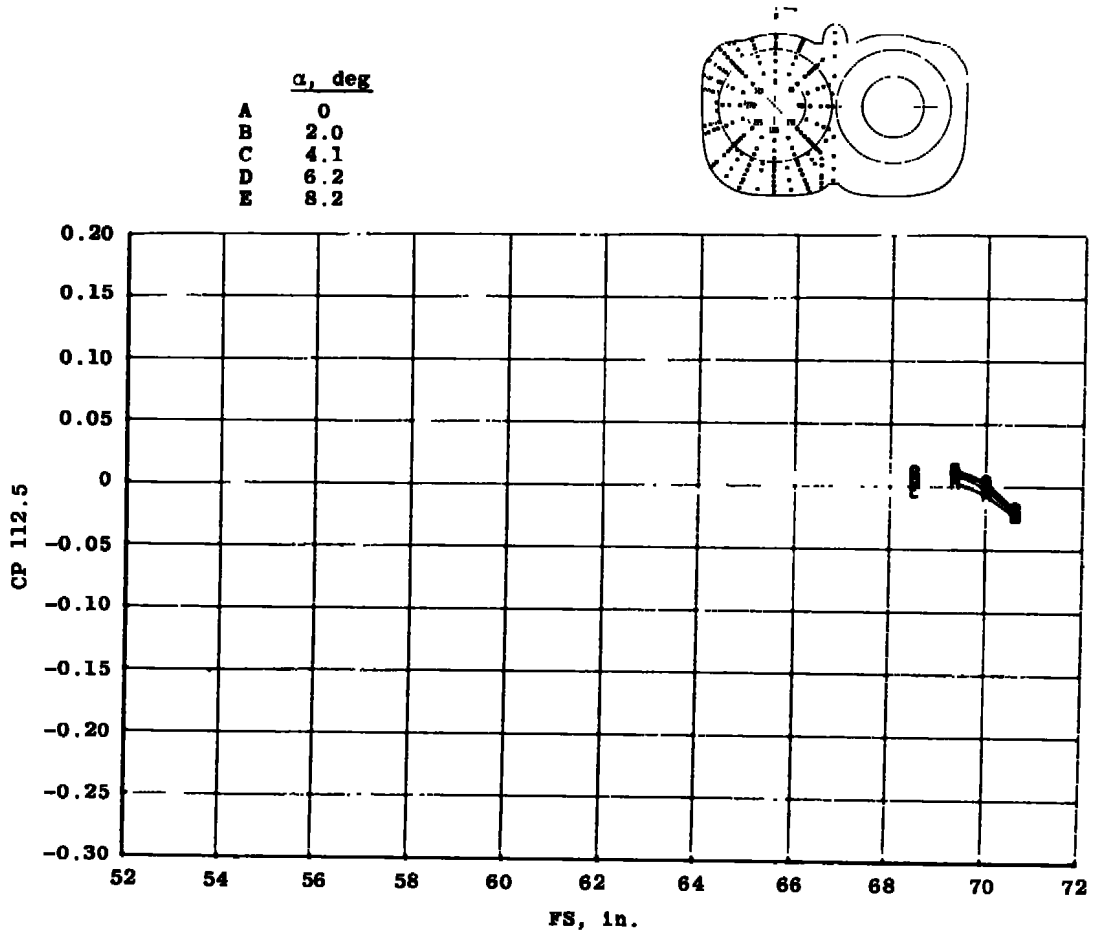

f. ϕ = 112.5 deg

Figure 16. Continued.

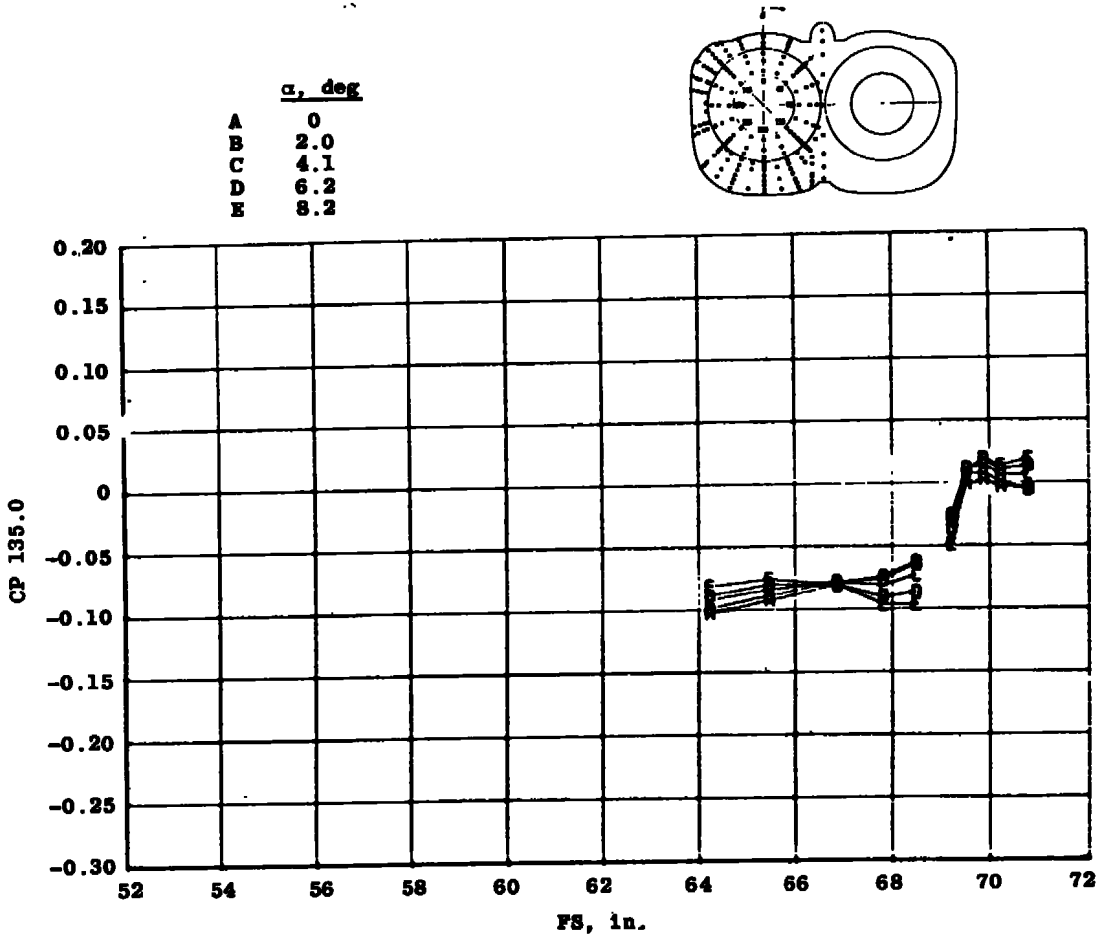

g. ϕ = 135.0 deg

Figure 16. Continued.

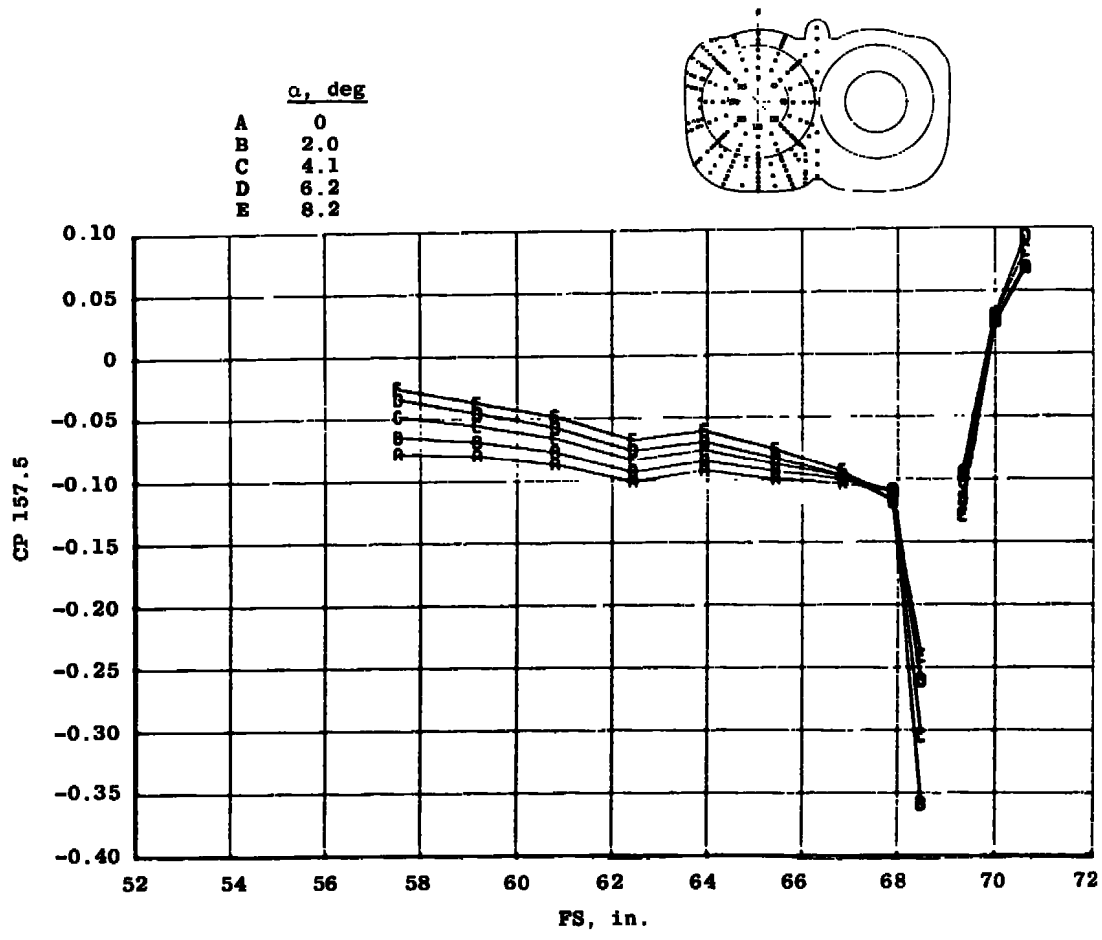

h. ϕ = 157.5 deg

Figure 16. Continued.

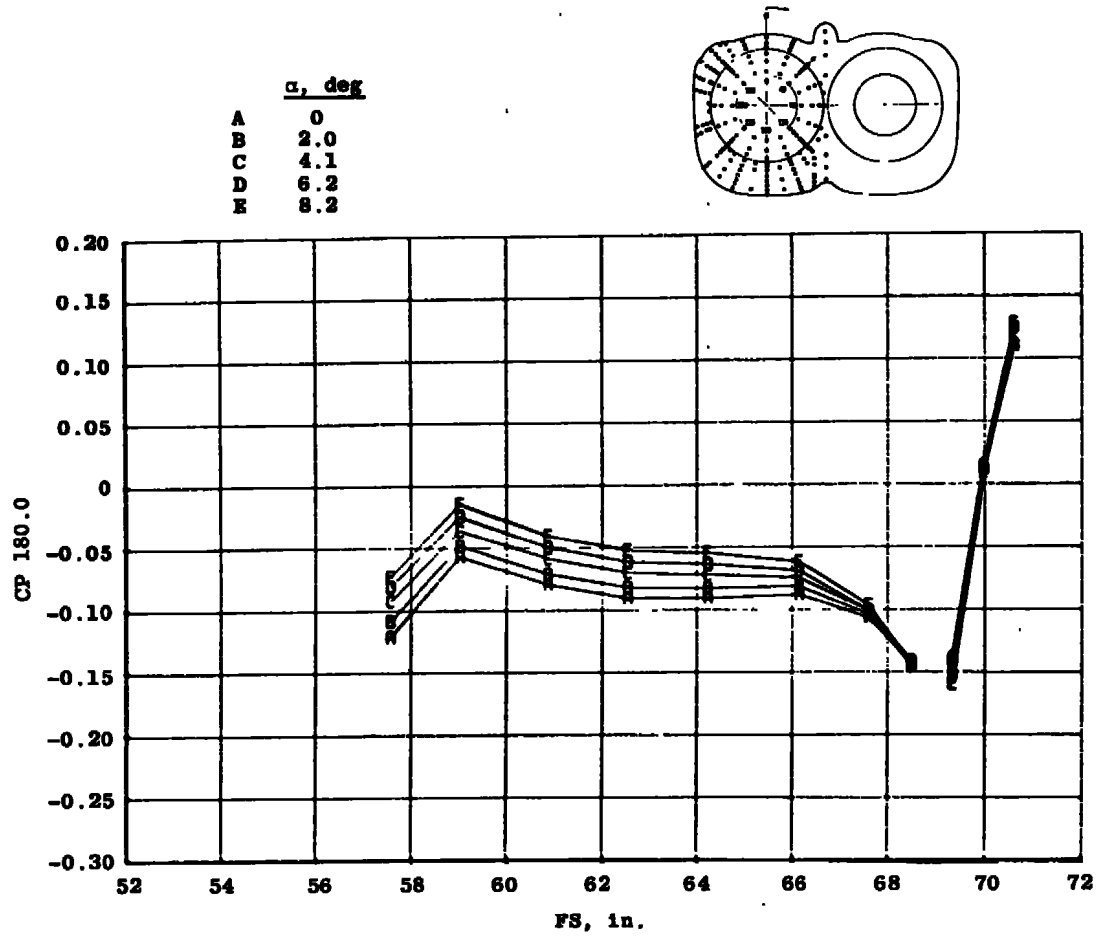

i. ϕ = 180.0 deg

Figure 16. Continued.

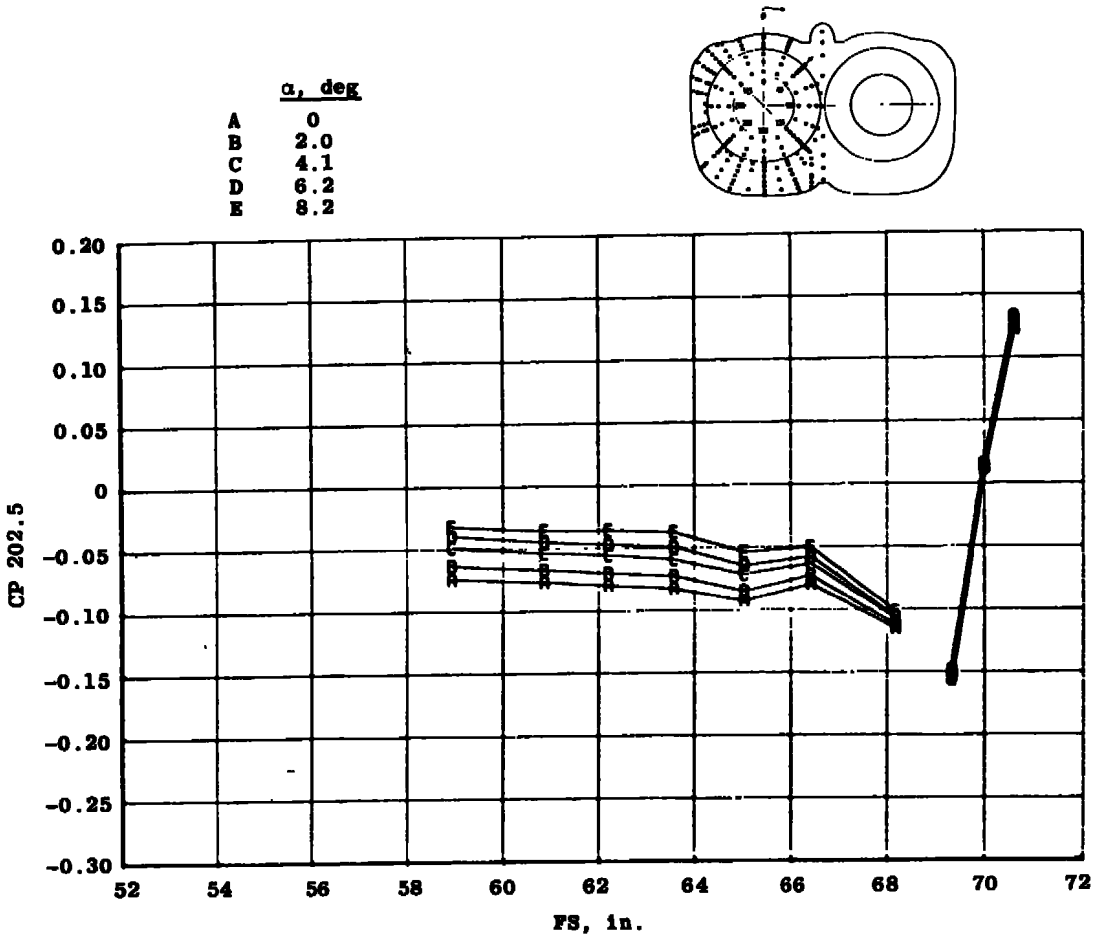

j. ϕ = 202.5 deg

Figure 16. Continued.

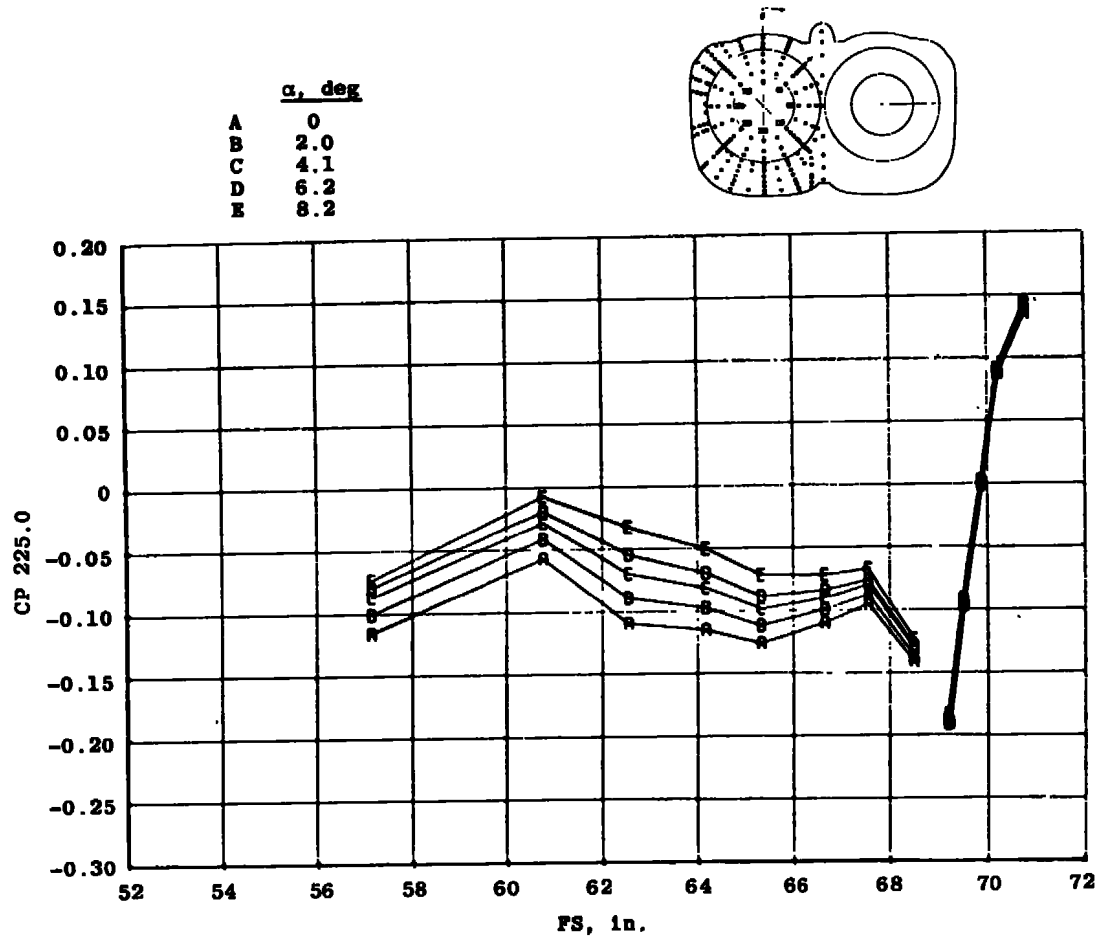

k. ϕ = 225.0 deg

Figure 16. Continued.

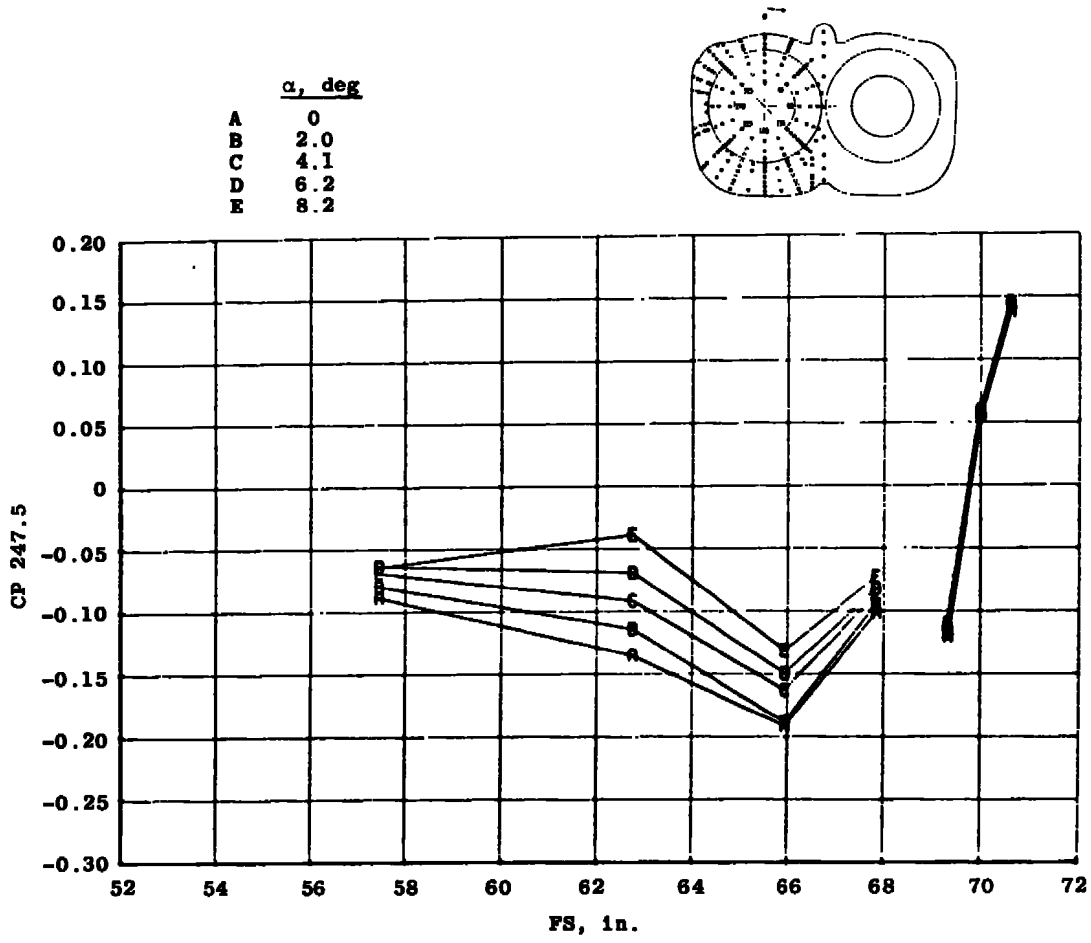

l. ϕ = 247.5 deg

Figure 16. Continued.

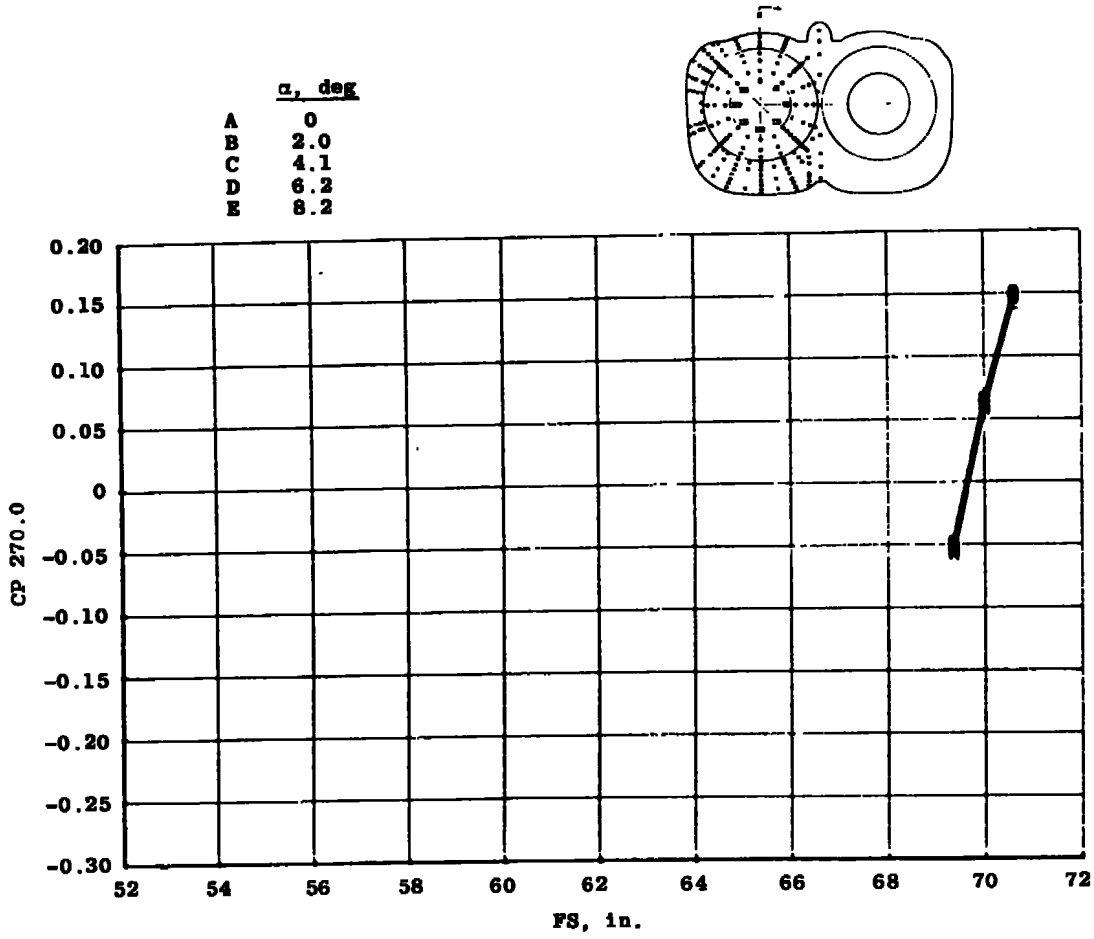

m. ϕ = 270.0 deg

Figure 16. Continued.

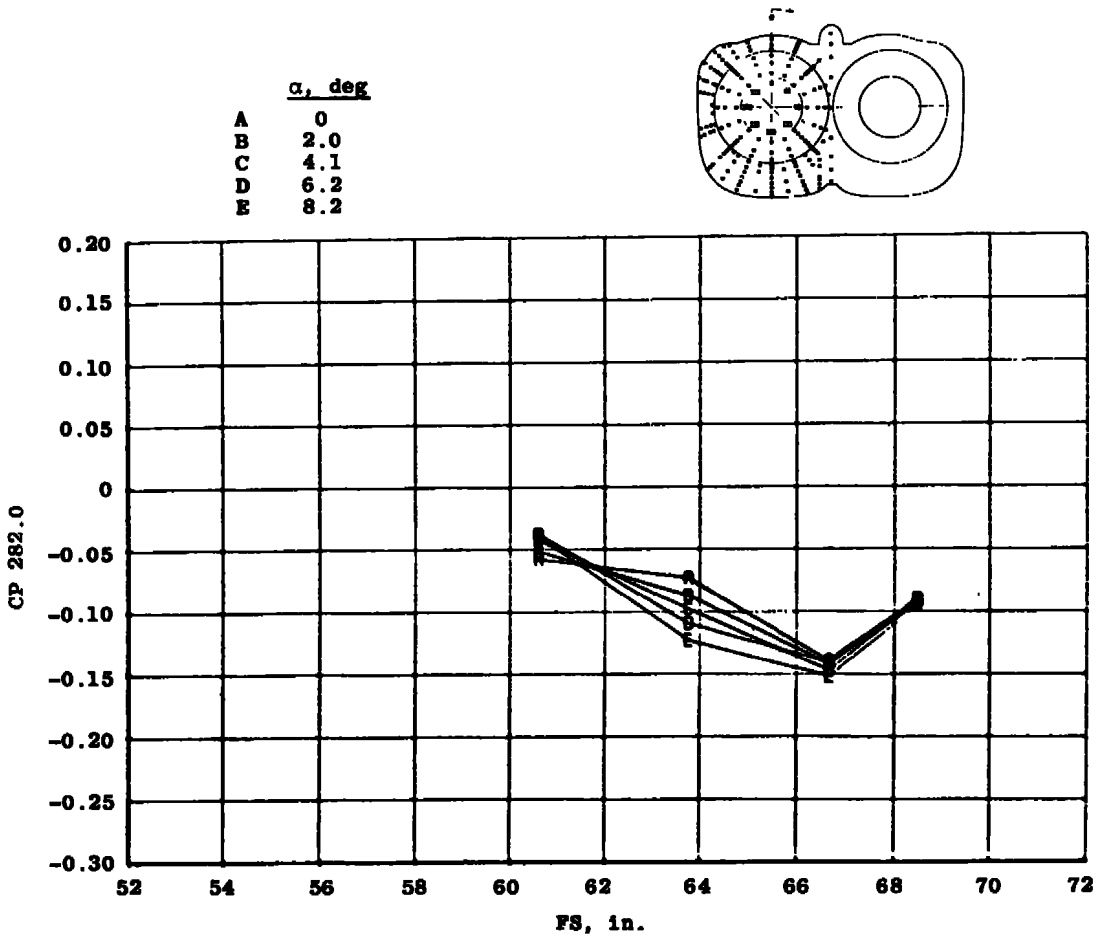

n. ϕ = 282.0 deg

Figure 16. Continued.

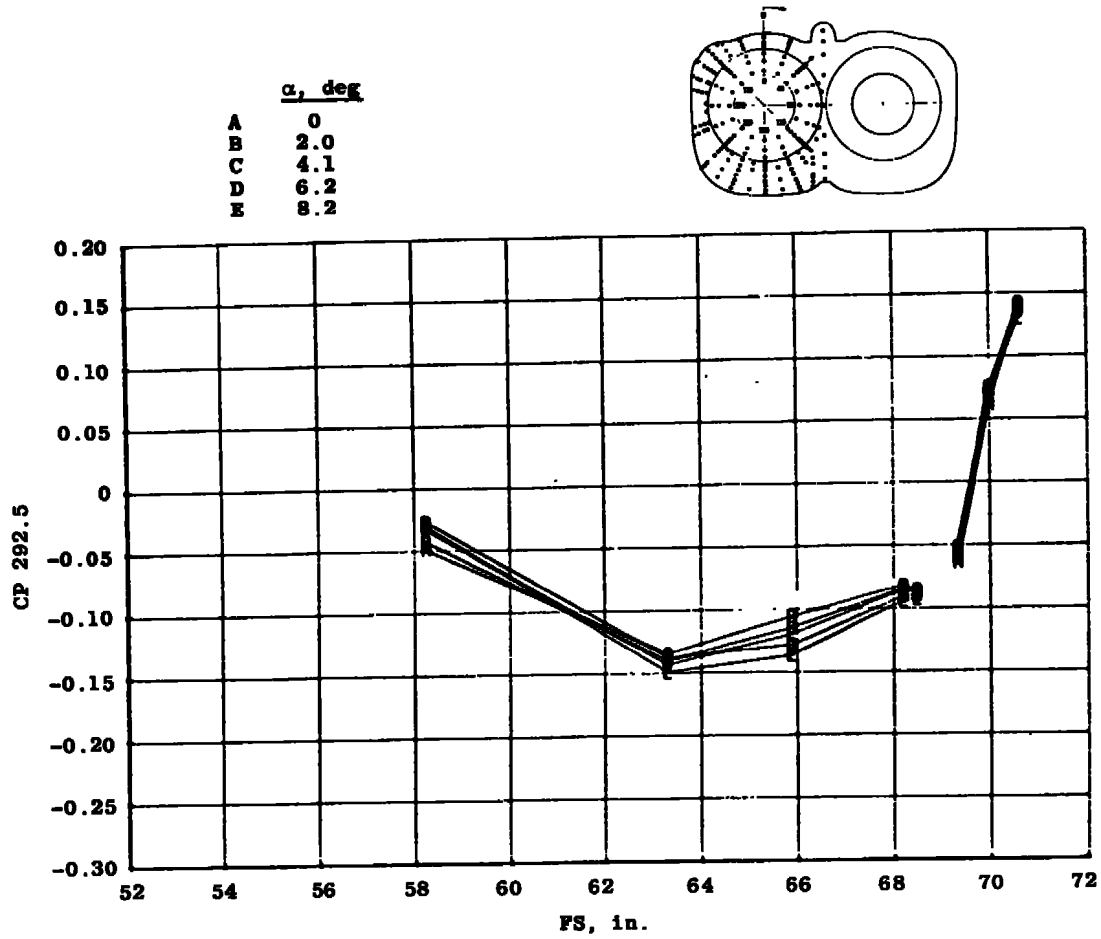

o. ϕ = 292.5 deg

Figure 16. Continued.

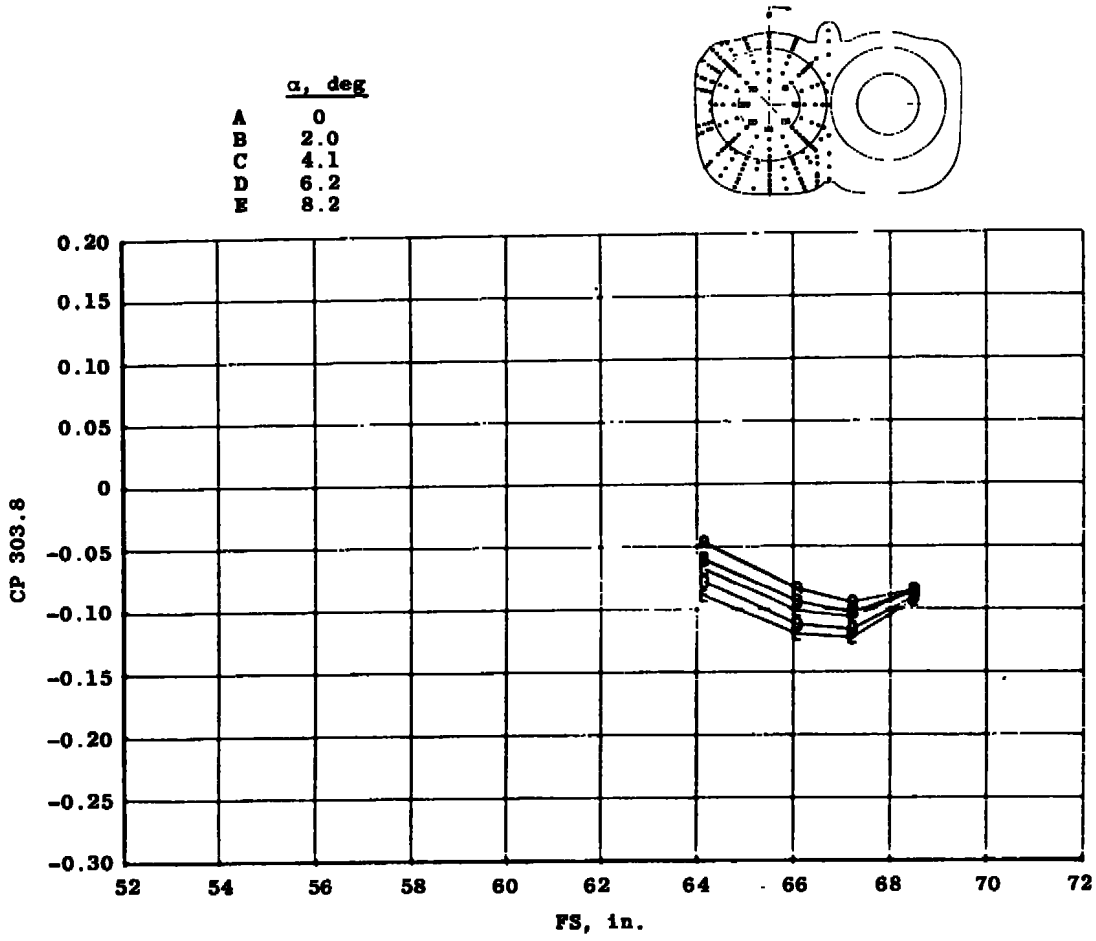

p. ϕ = 303.8 deg

Figure 16. Continued.

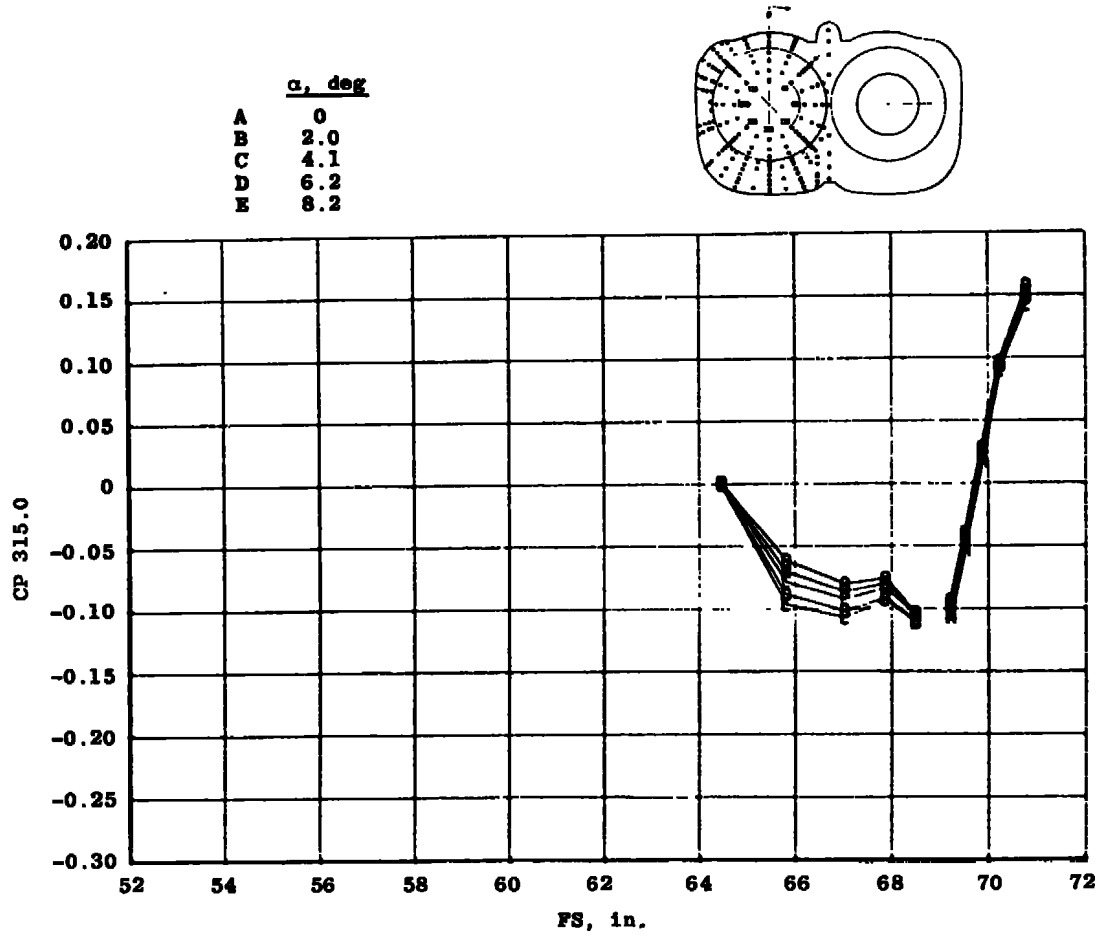

q. ϕ = 315.0 deg

Figure 16. Continued.

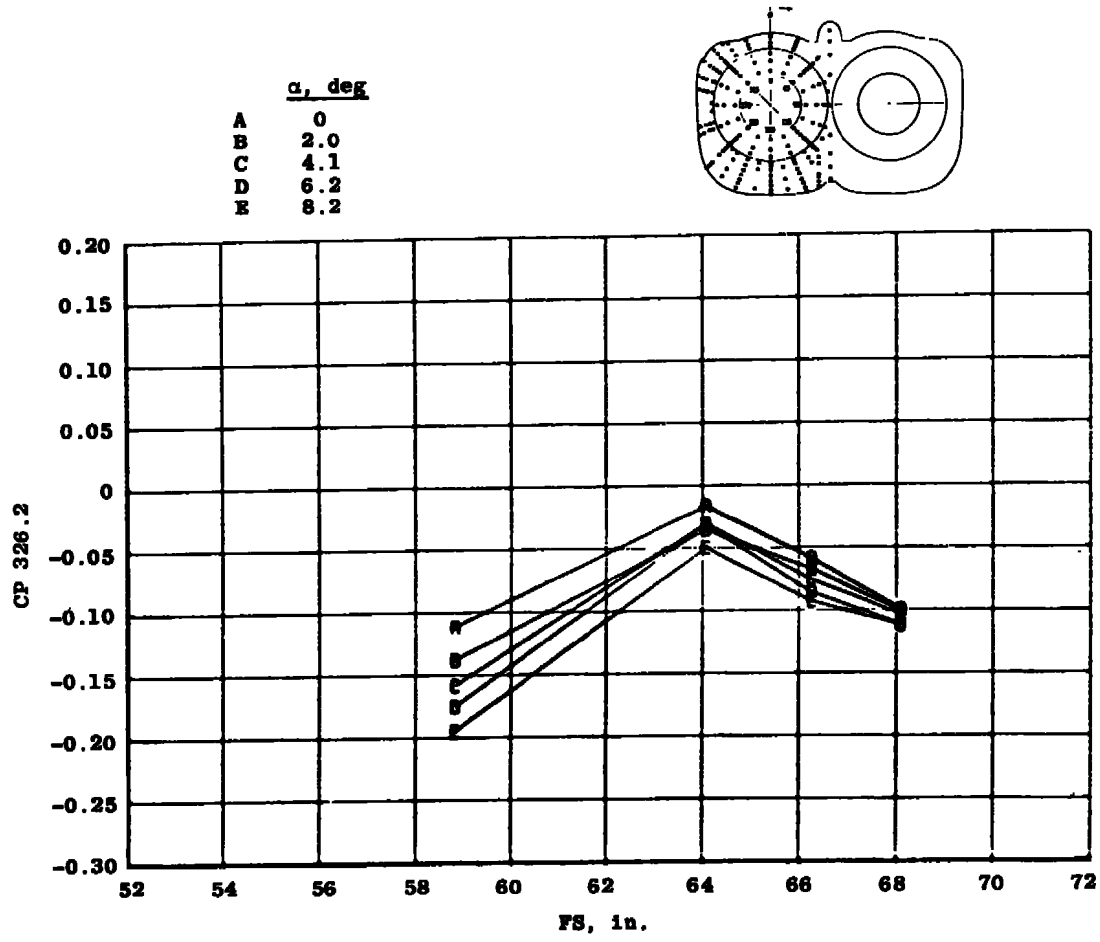

r. ϕ = 326.2 deg

Figure 16. Continued.

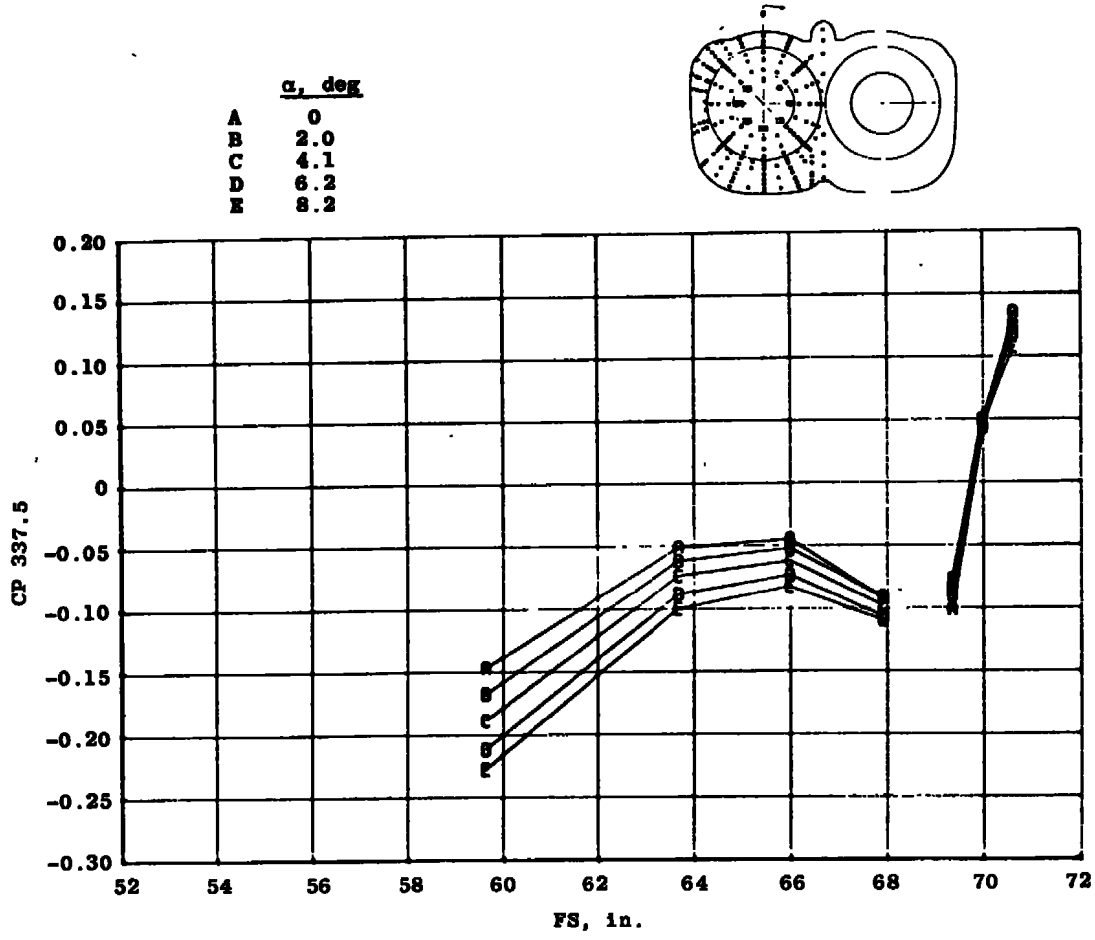

s. ϕ = 337.5 deg

Figure 16. Continued.

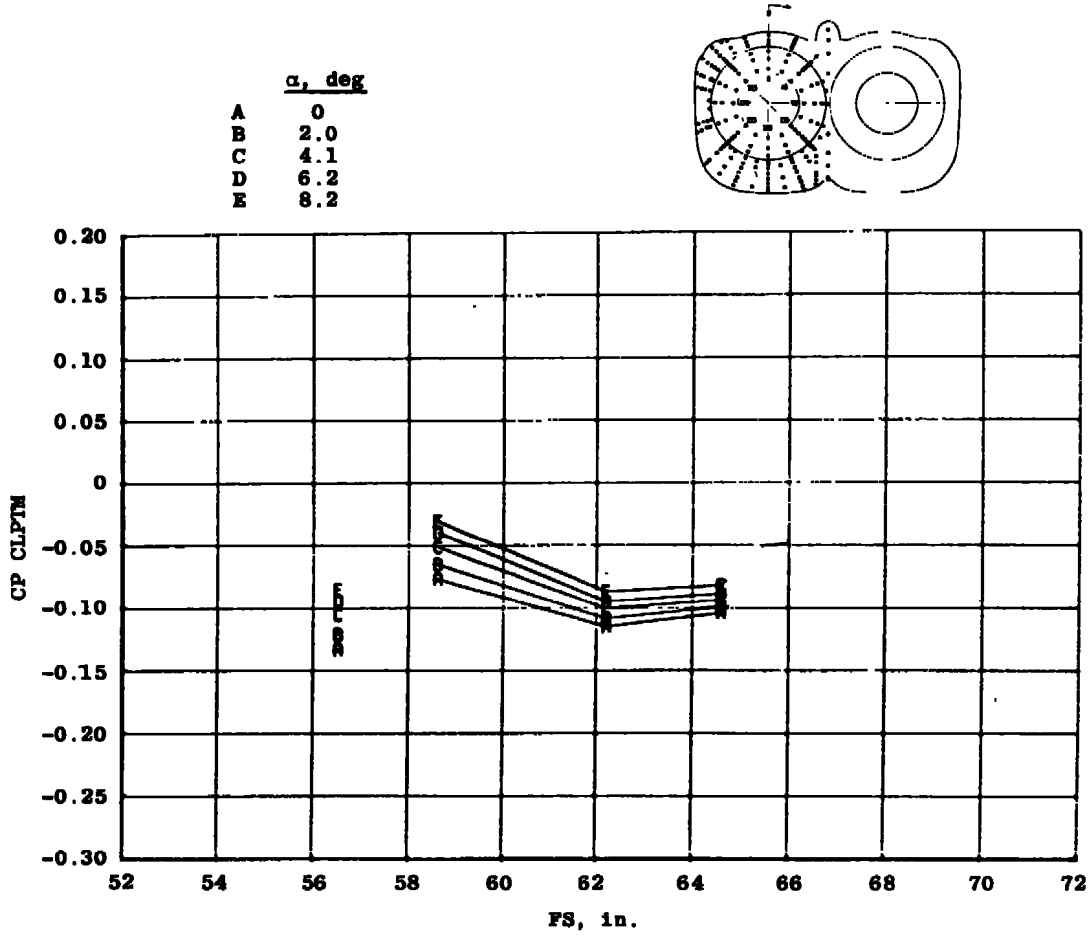

t. Aircraft bottom centerline

Figure 16. Continued.

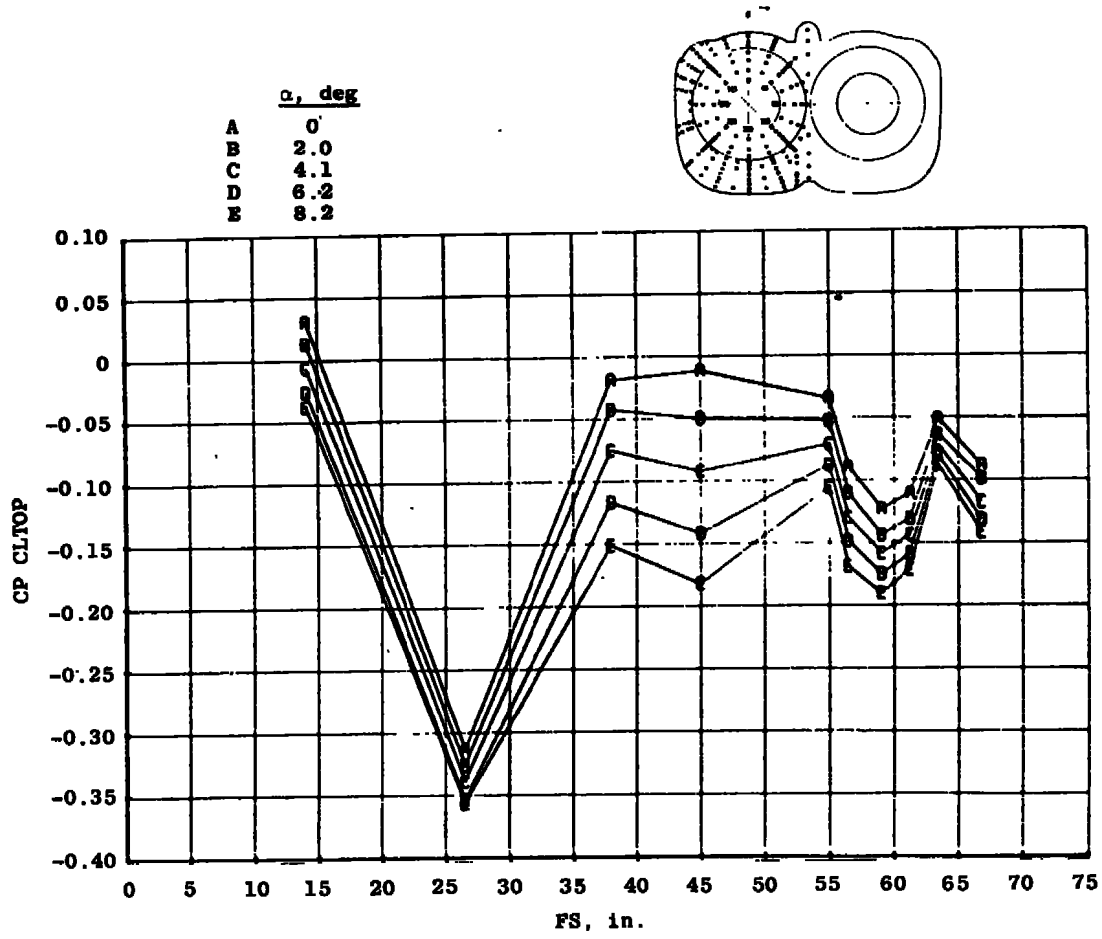

u. Aircraft top centerline

Figure 16. Concluded.

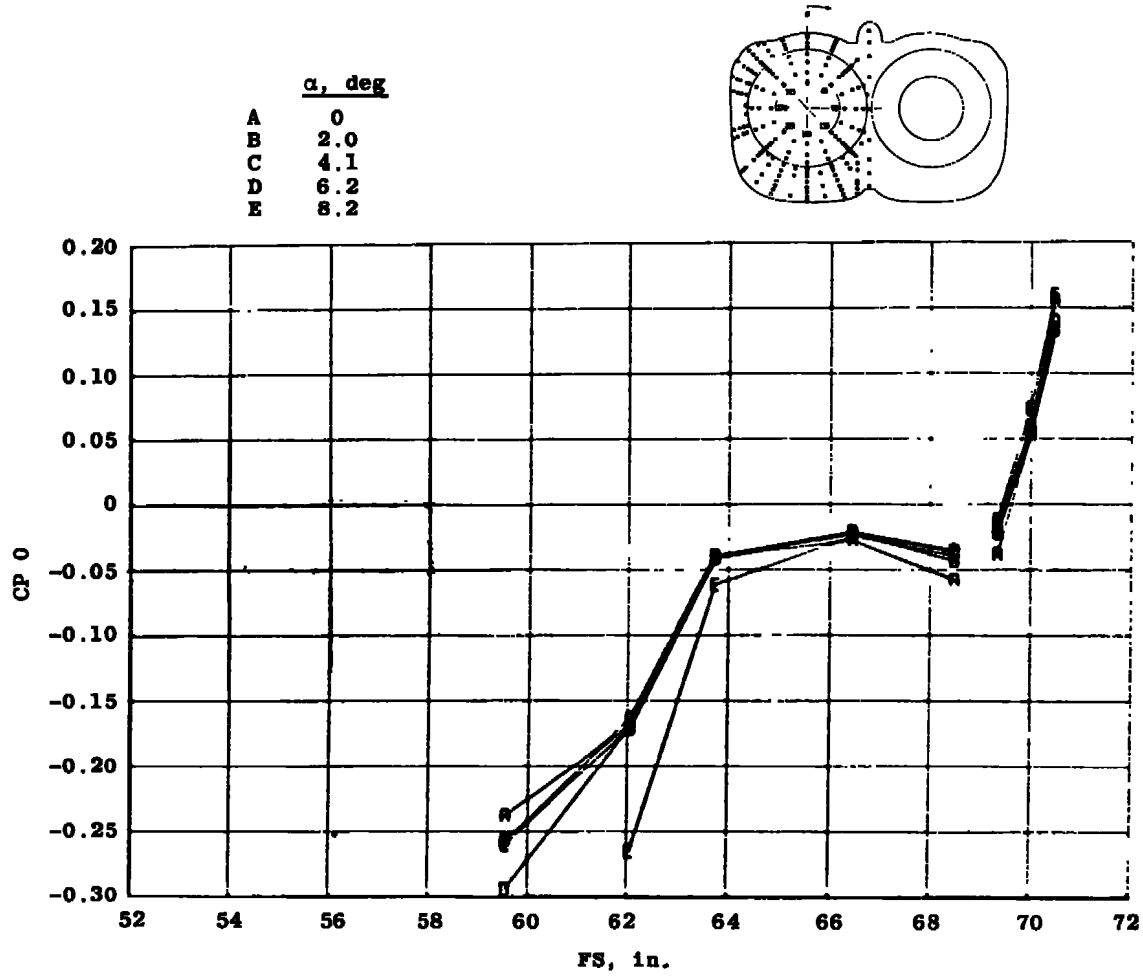

a. $\phi = 0$

Figure 17. Model attitude effects on the surface pressure distribution of the reheat nozzle configuration, $M_\infty = 0.9$, Re = 2.8 x 10^6/ft, δ_H = -2 deg, and NPR = 5.

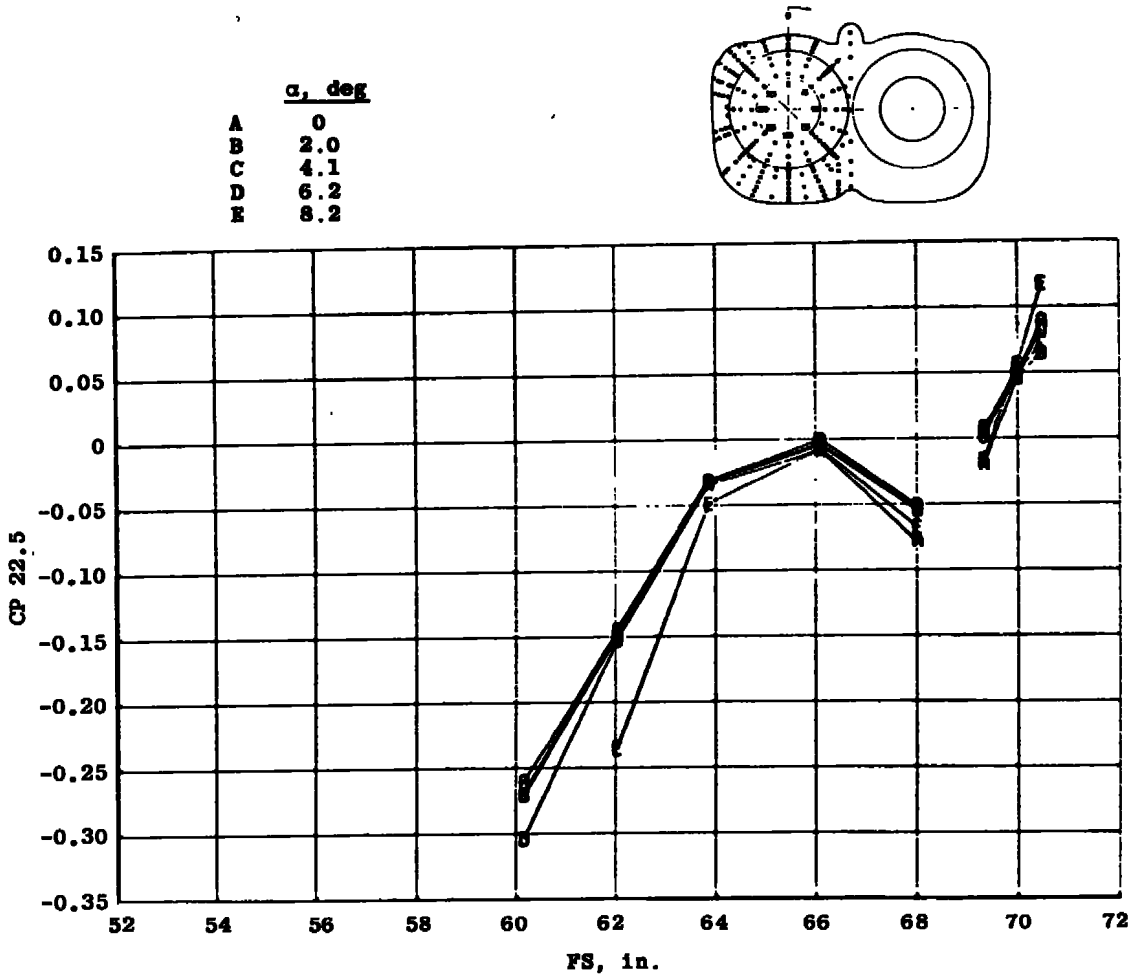

b. ϕ = 22.5 deg

Figure 17. Continued.

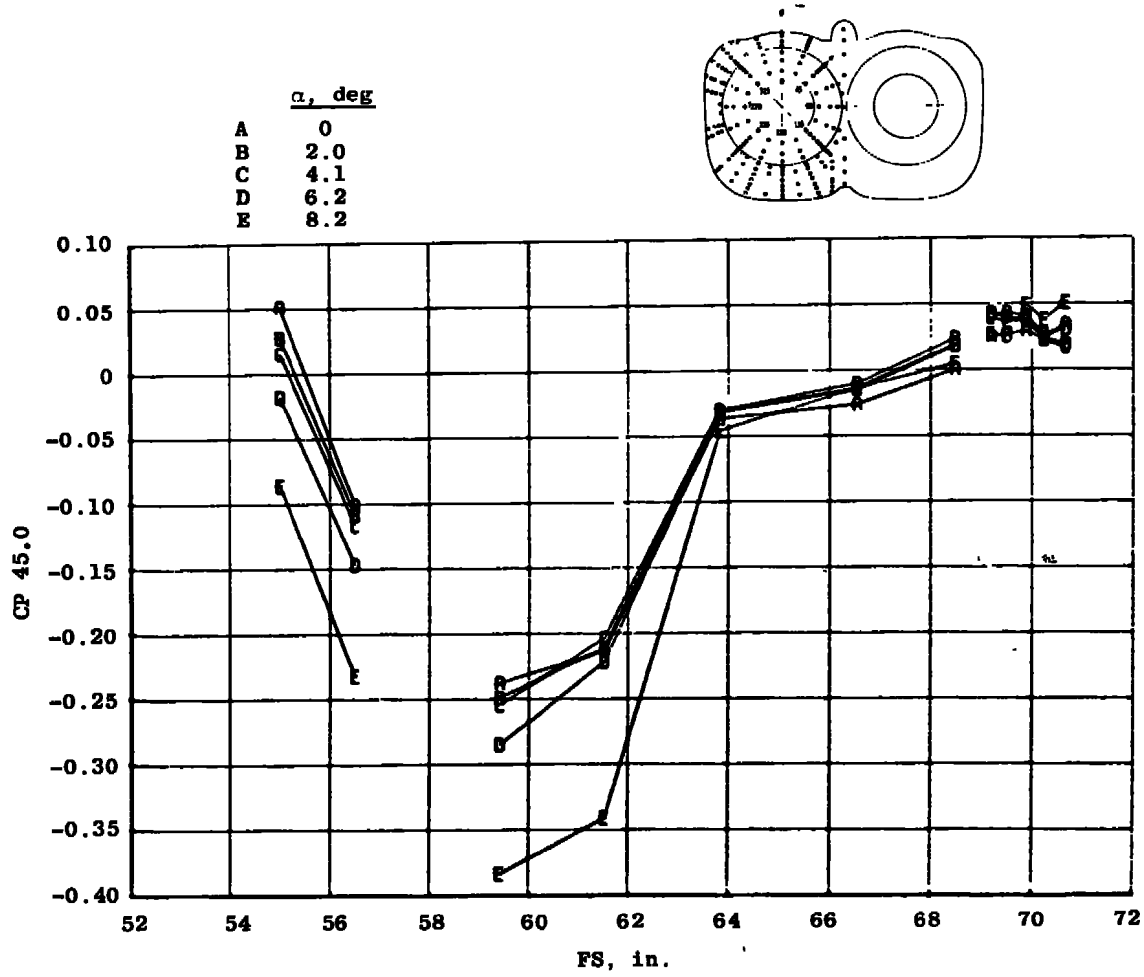

c. ϕ = 45.0 deg

Figure 17. Continued.

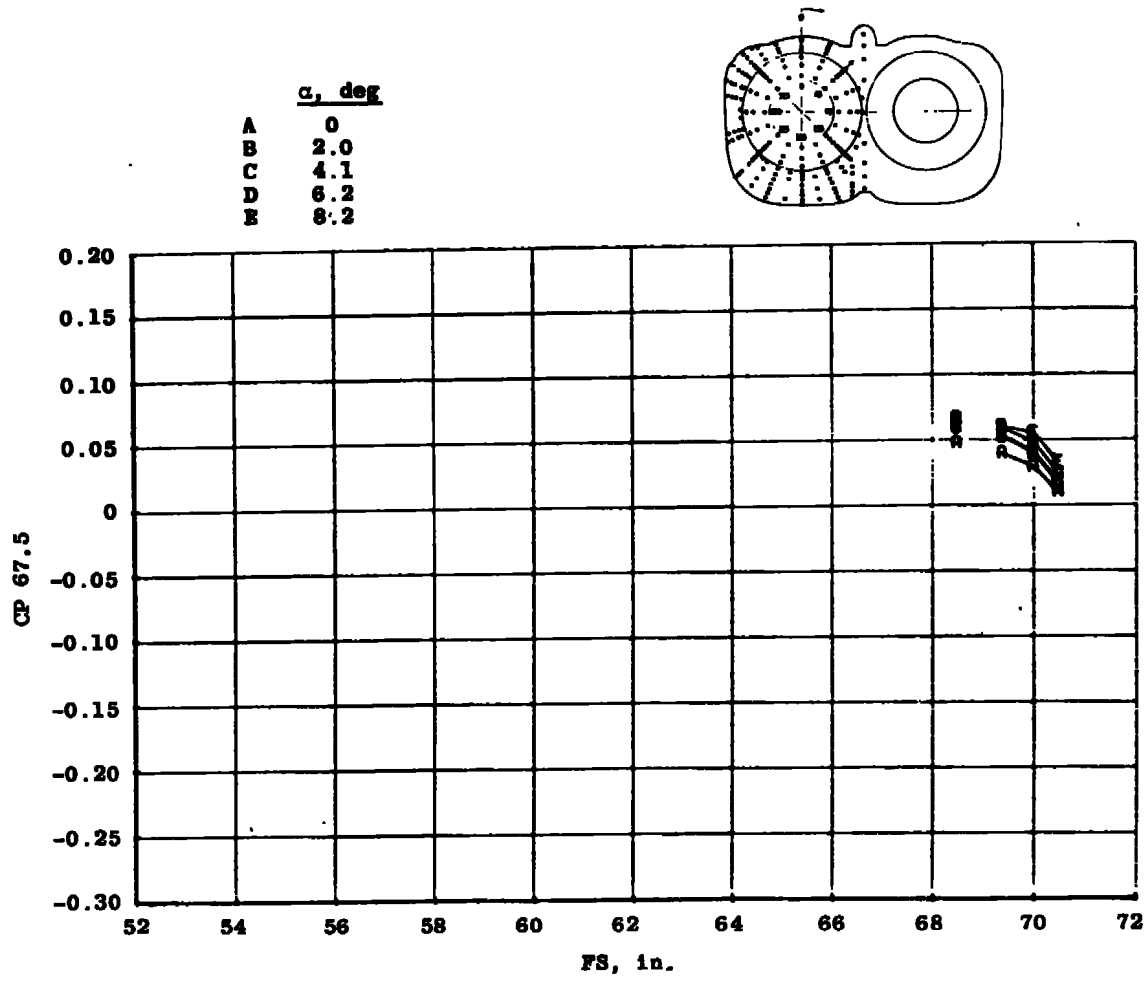

d. ϕ = 67.5 deg

Figure 17. Continued.

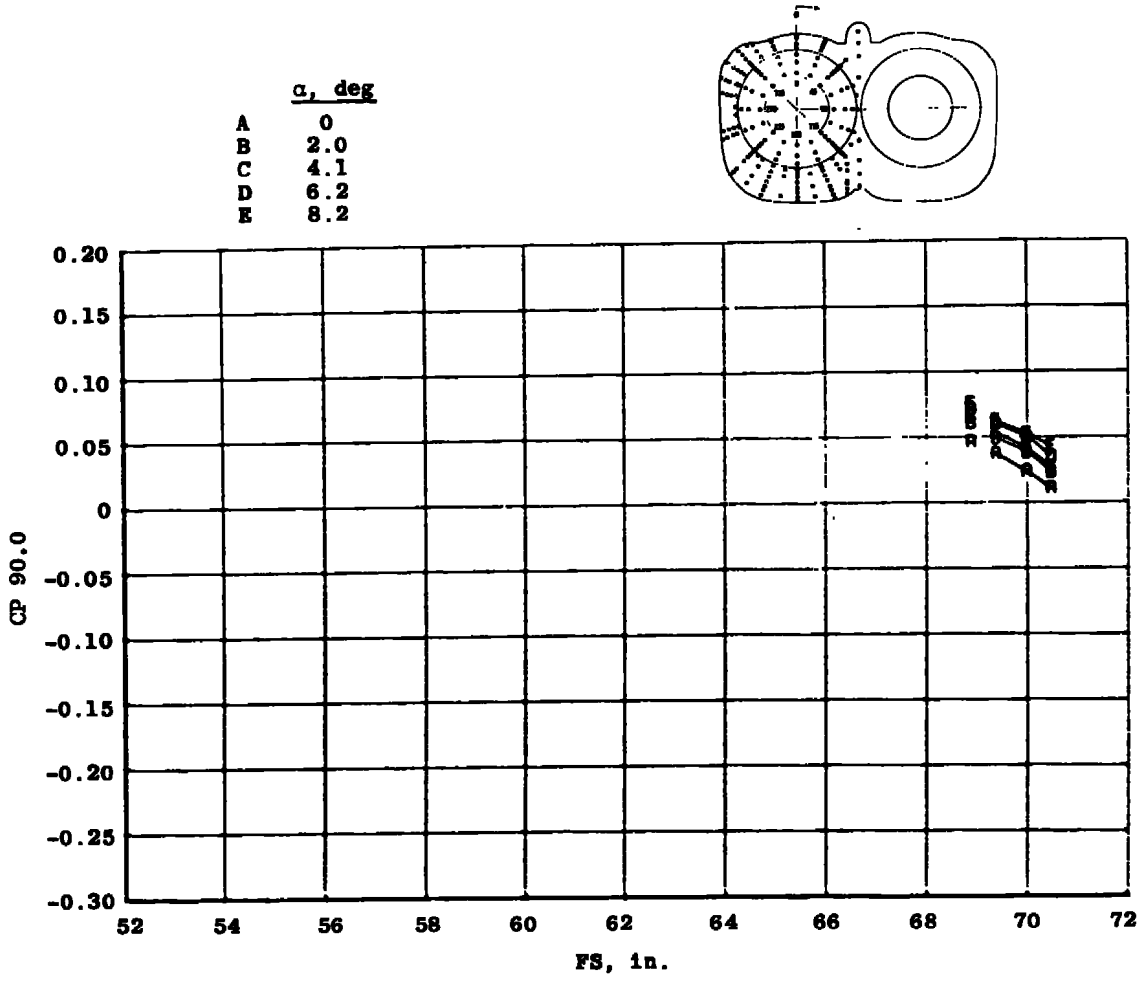

e. ϕ = 90.0 deg

Figure 17. Continued.

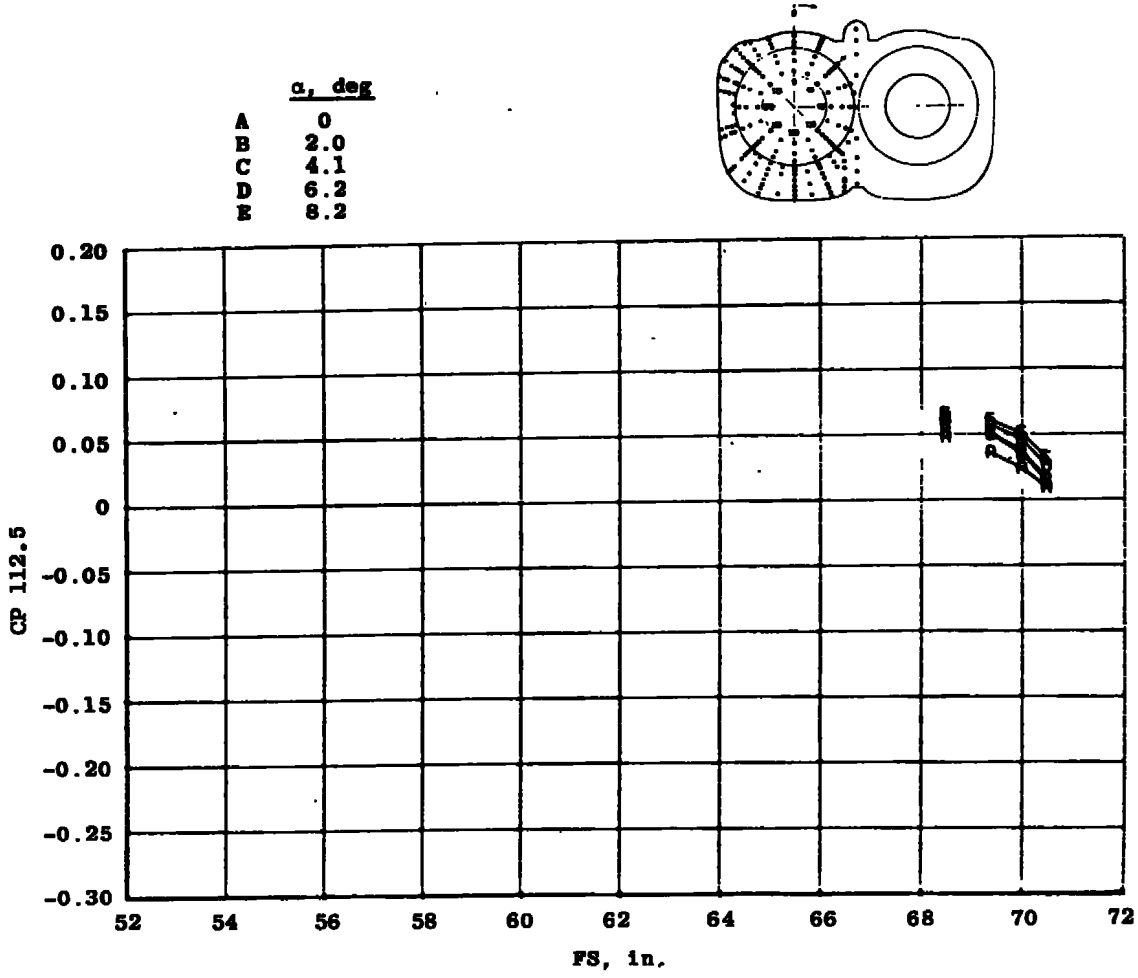

f. ϕ = 112.5 deg

Figure 17. Continued.

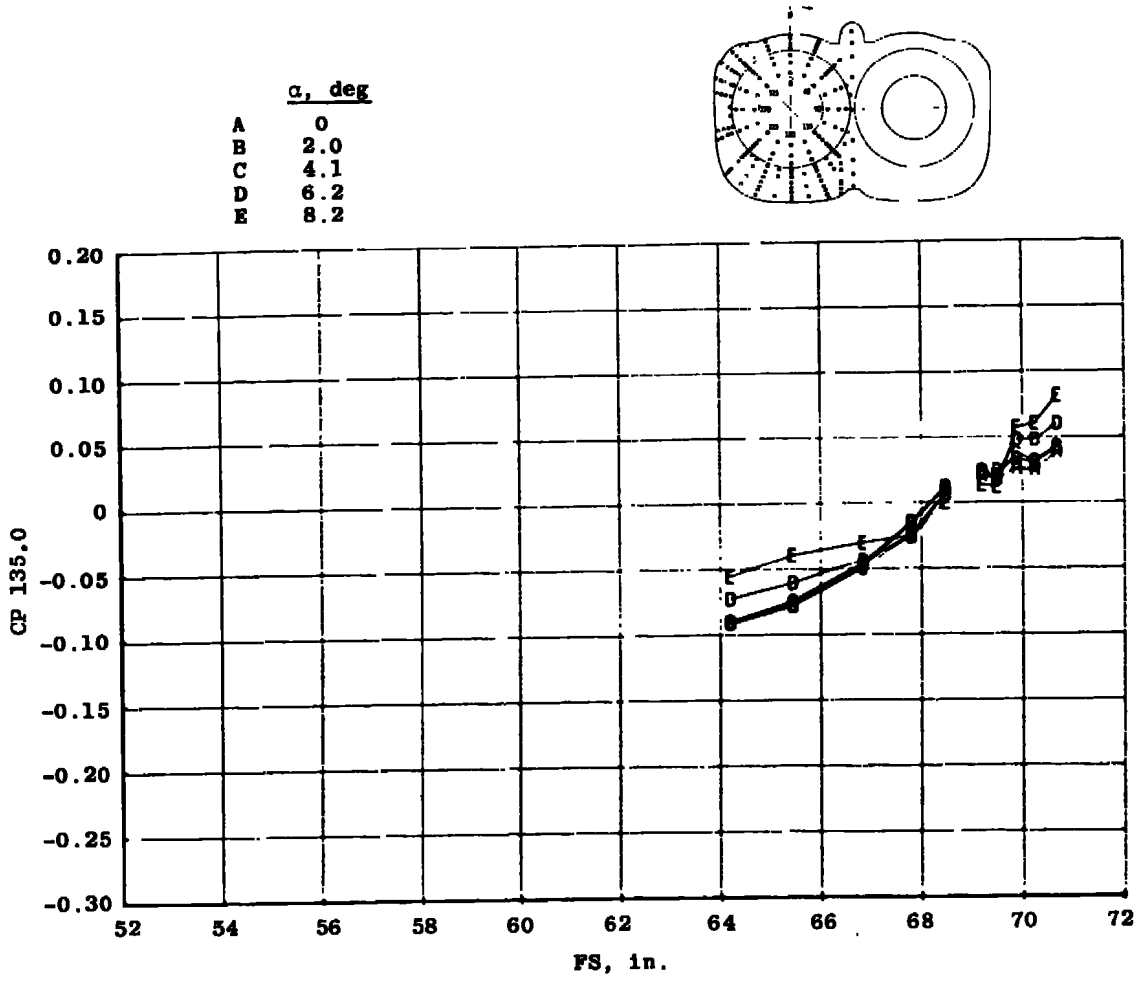

g. ϕ = 135.0 deg

Figure 17. Continued.

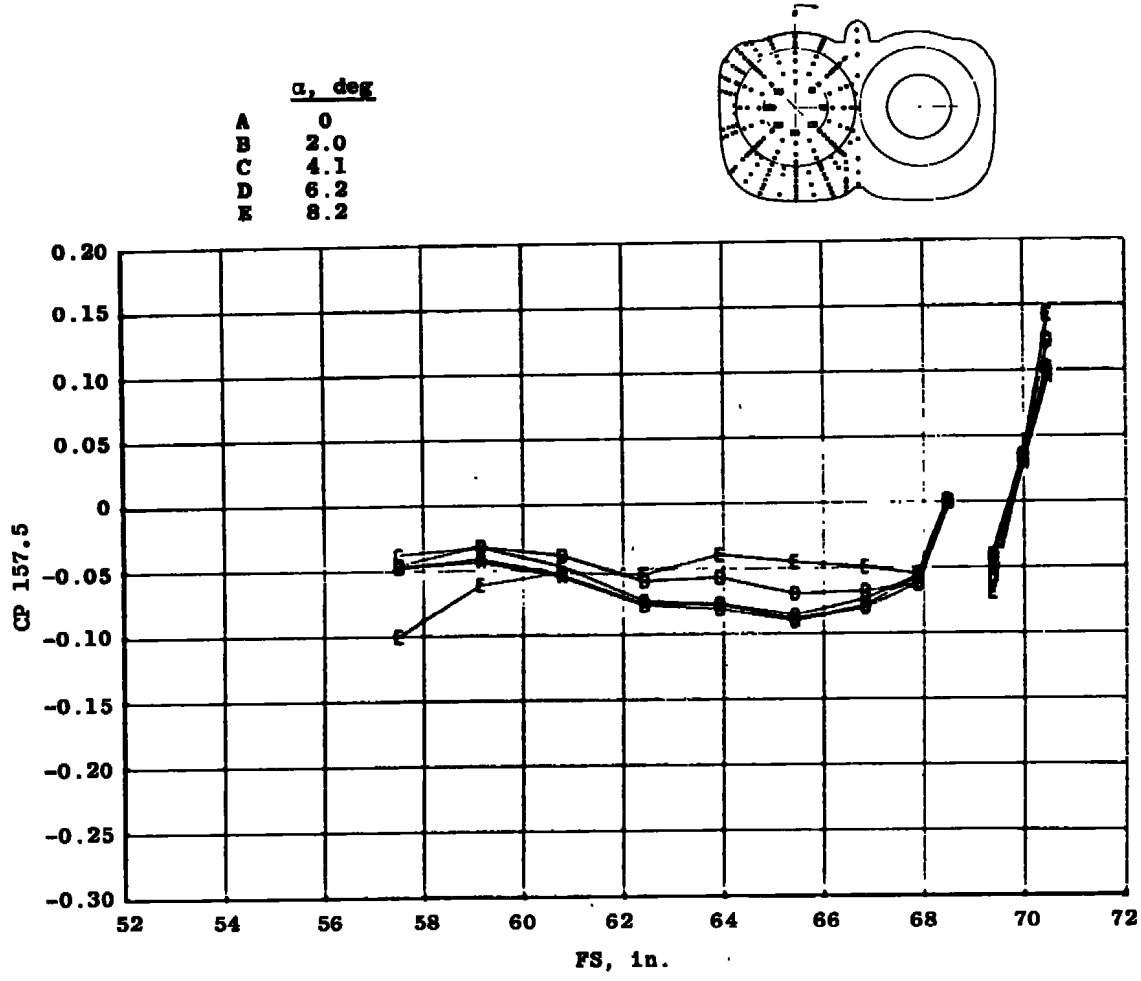

h. ϕ = 157.5 deg

Figure 17. Continued.

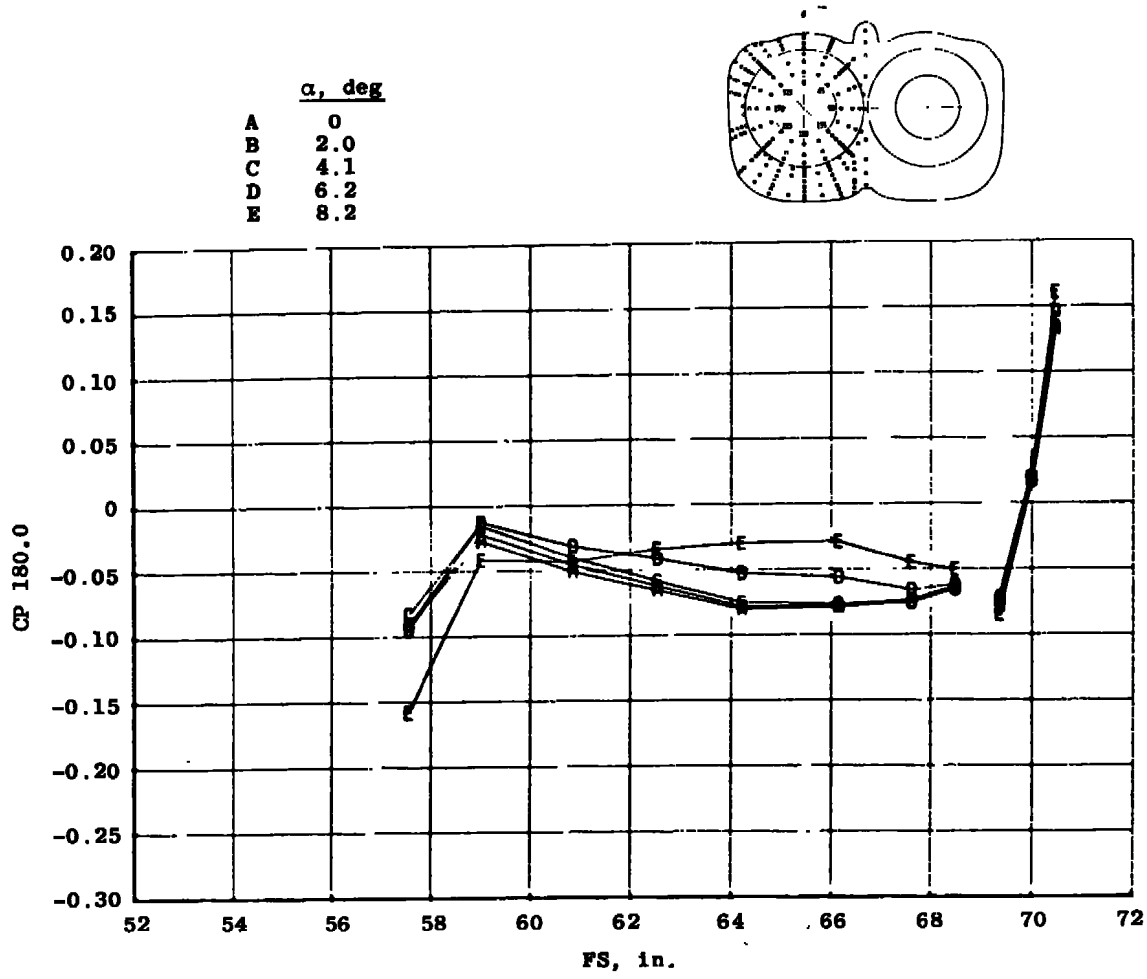

i. ϕ = 180.0 deg

Figure 17. Continued.

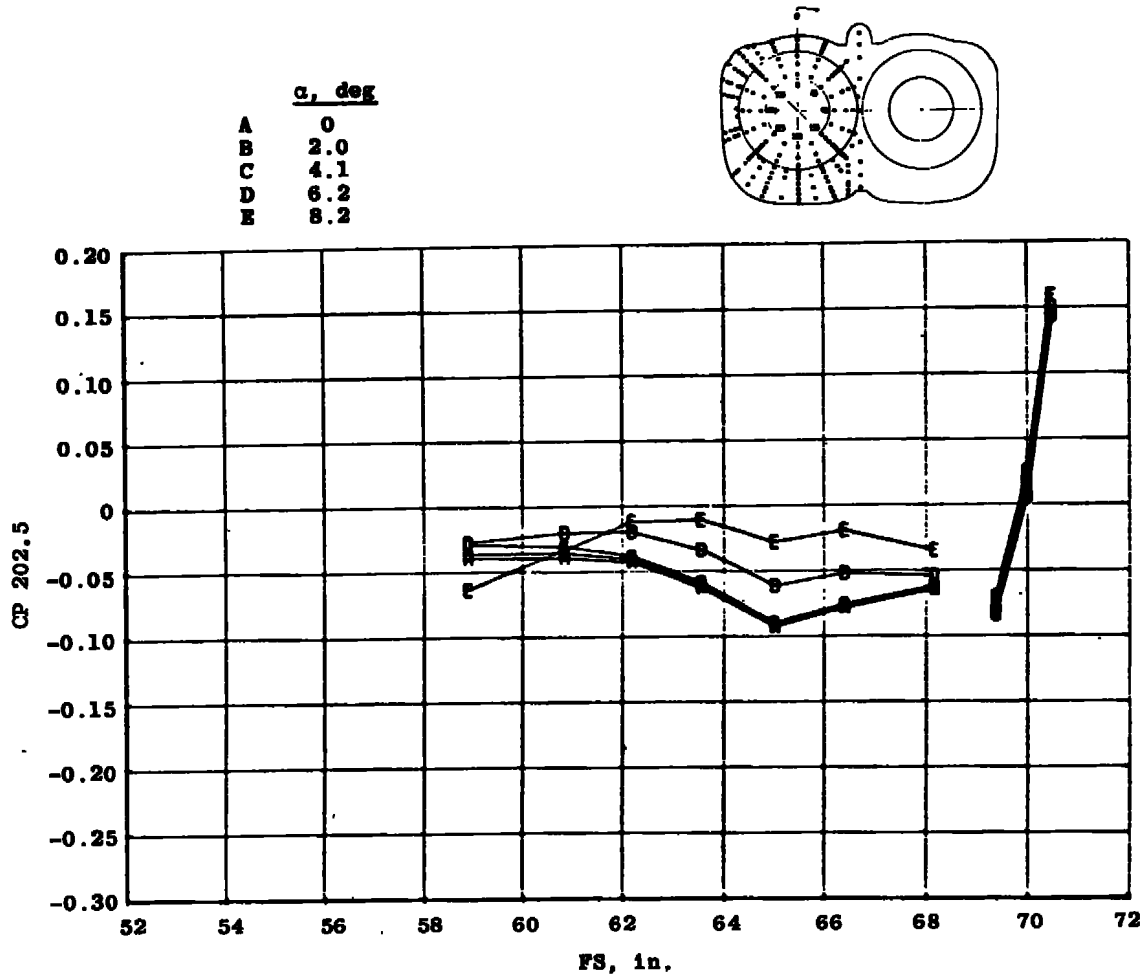

j. ϕ = 202.5 deg
Figure 17. Continued.

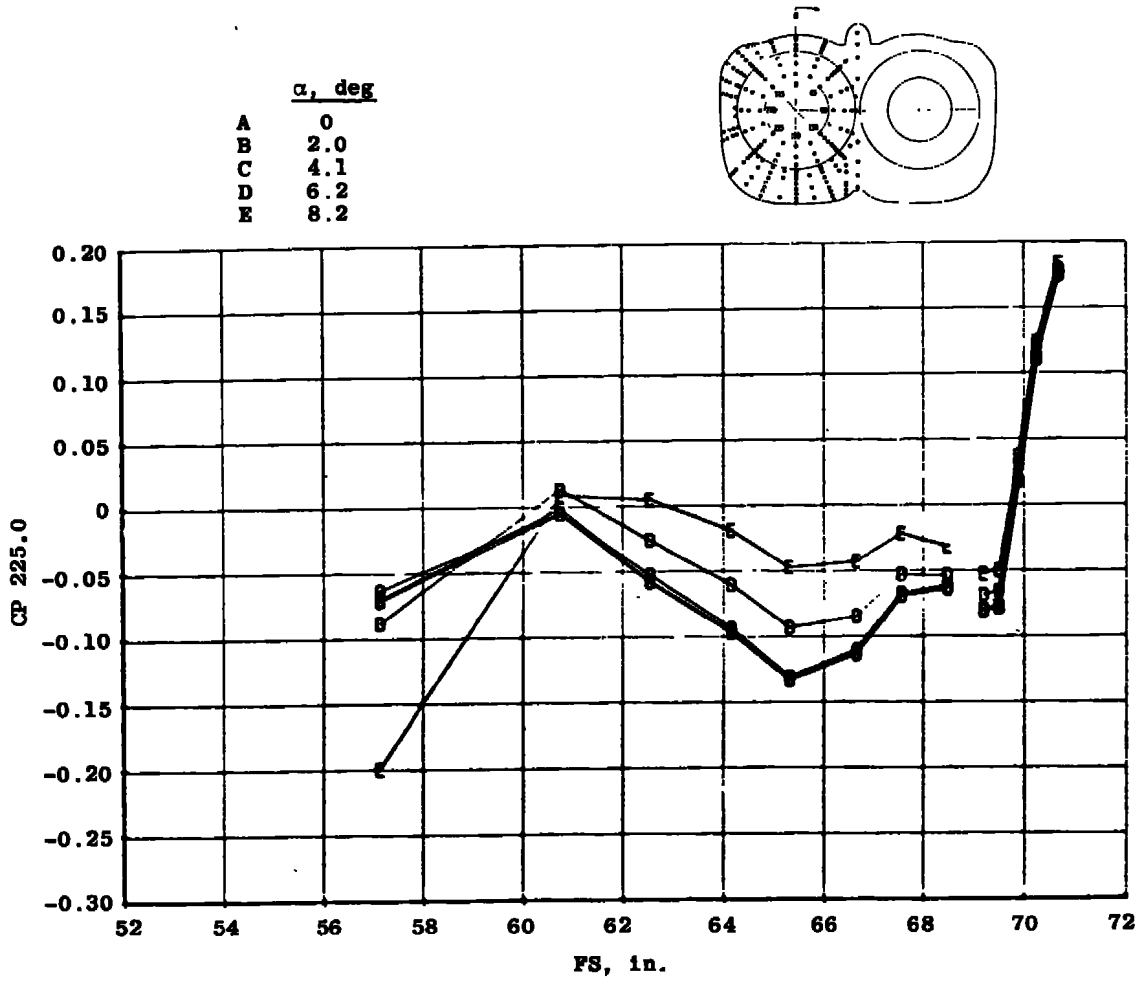

k. ϕ = 225.0 deg

Figure 17. Continued.

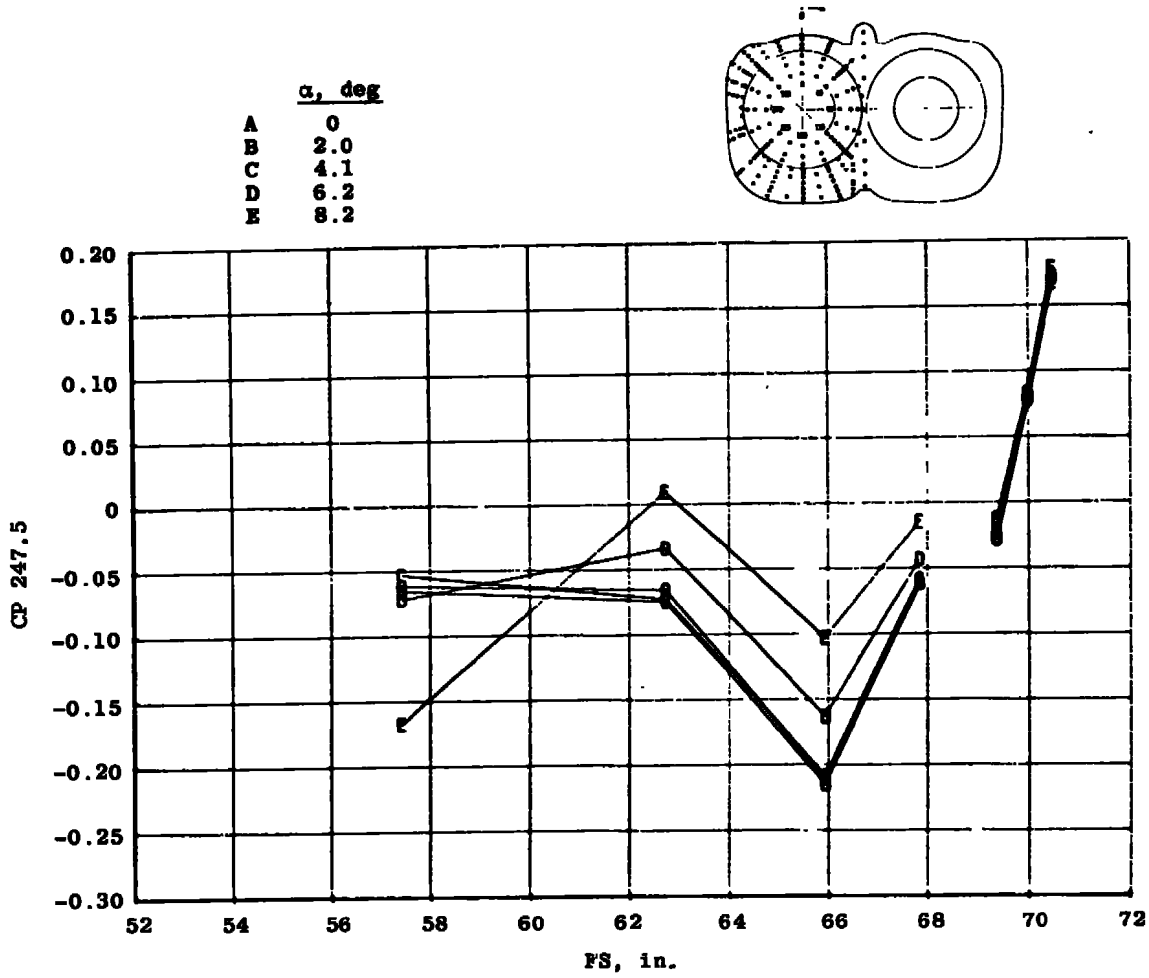

l. ϕ = 247.5 deg

Figure 17. Continued.

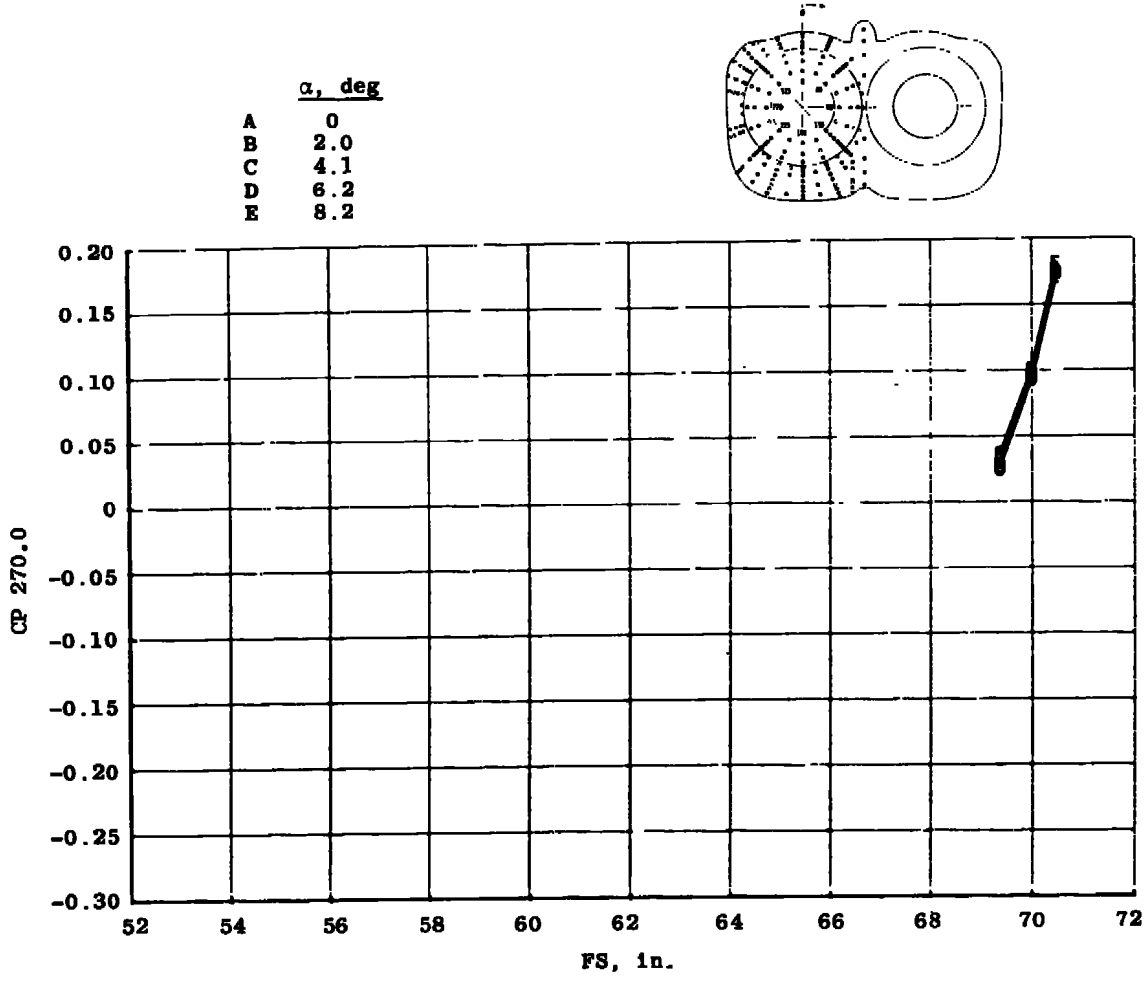

m. ϕ = 270.0 deg

Figure 17. Continued.

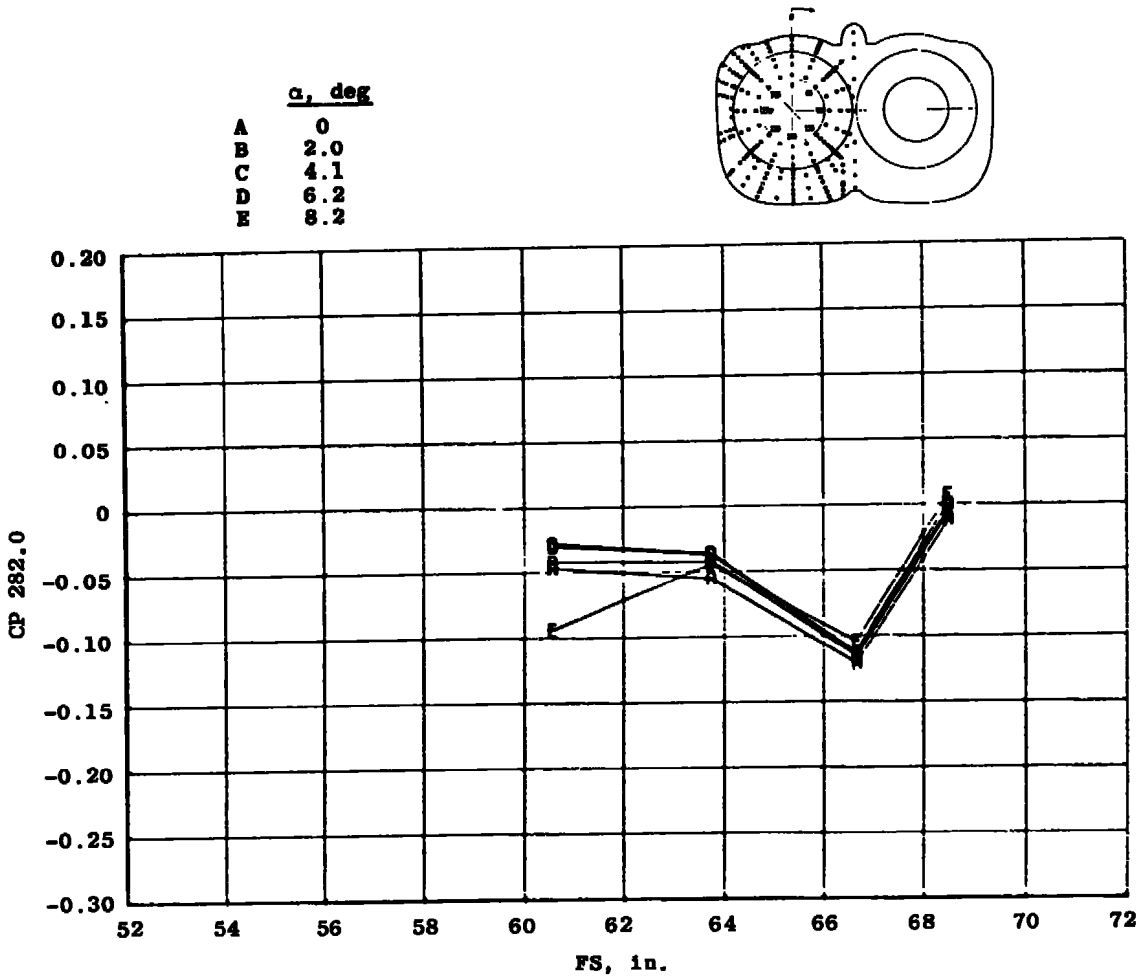

n. ϕ = 282.0 deg

Figure 17. Continued.

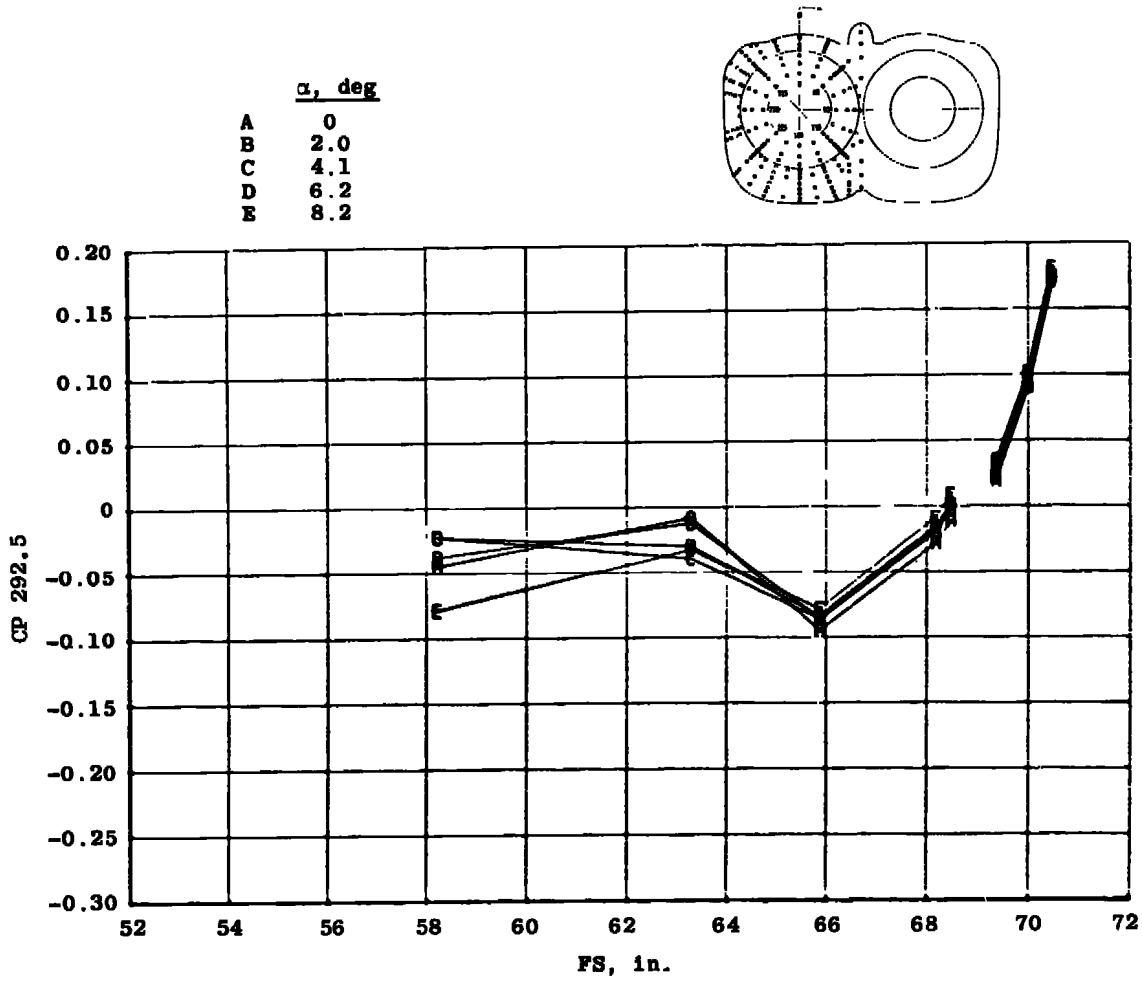

o. ϕ = 292.5 deg

Figure 17. Continued.

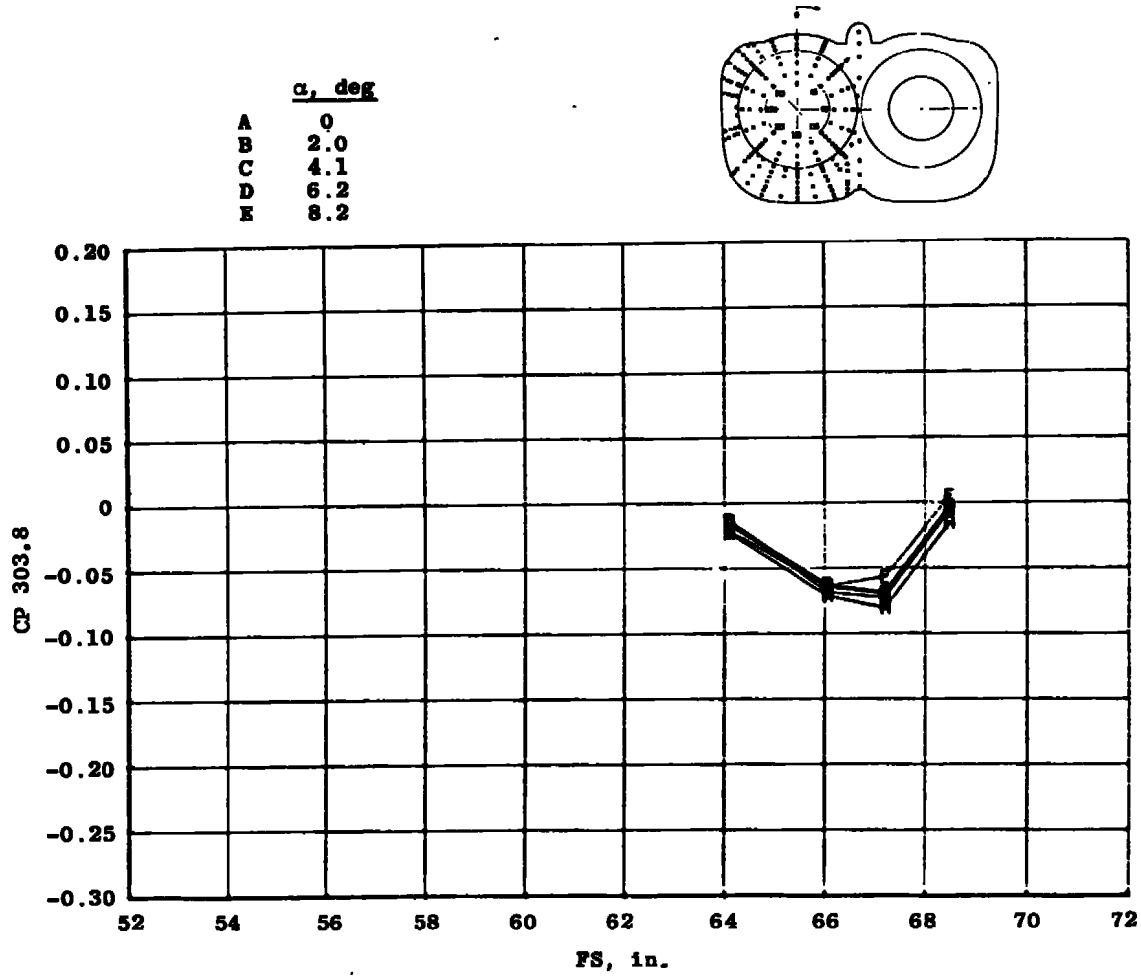

p. ϕ = 303.8 deg

Figure 17. Continued.

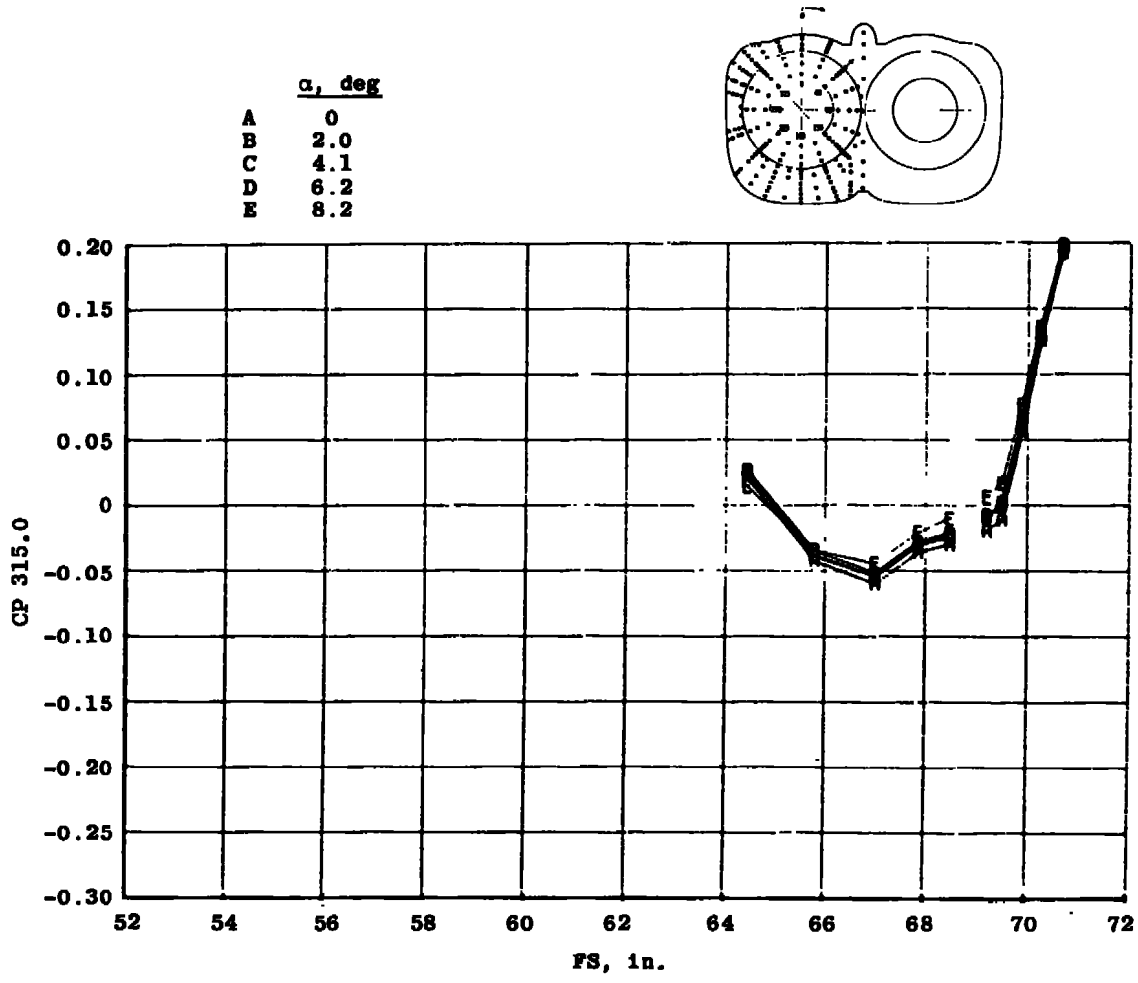

q. ϕ = 315.0 deg

Figure 17. Continued.

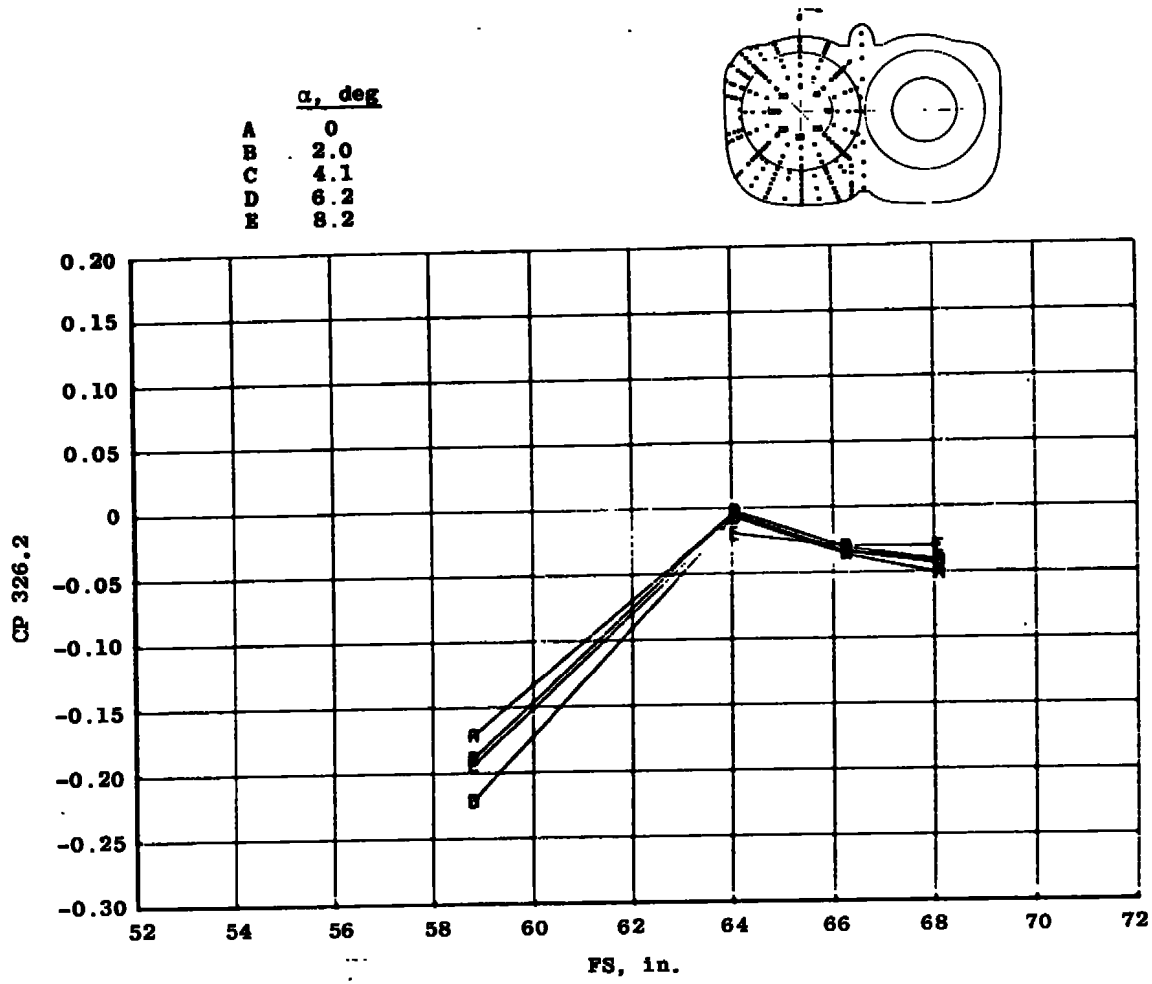

r. ϕ = 326.2 deg

Figure 17. Continued.

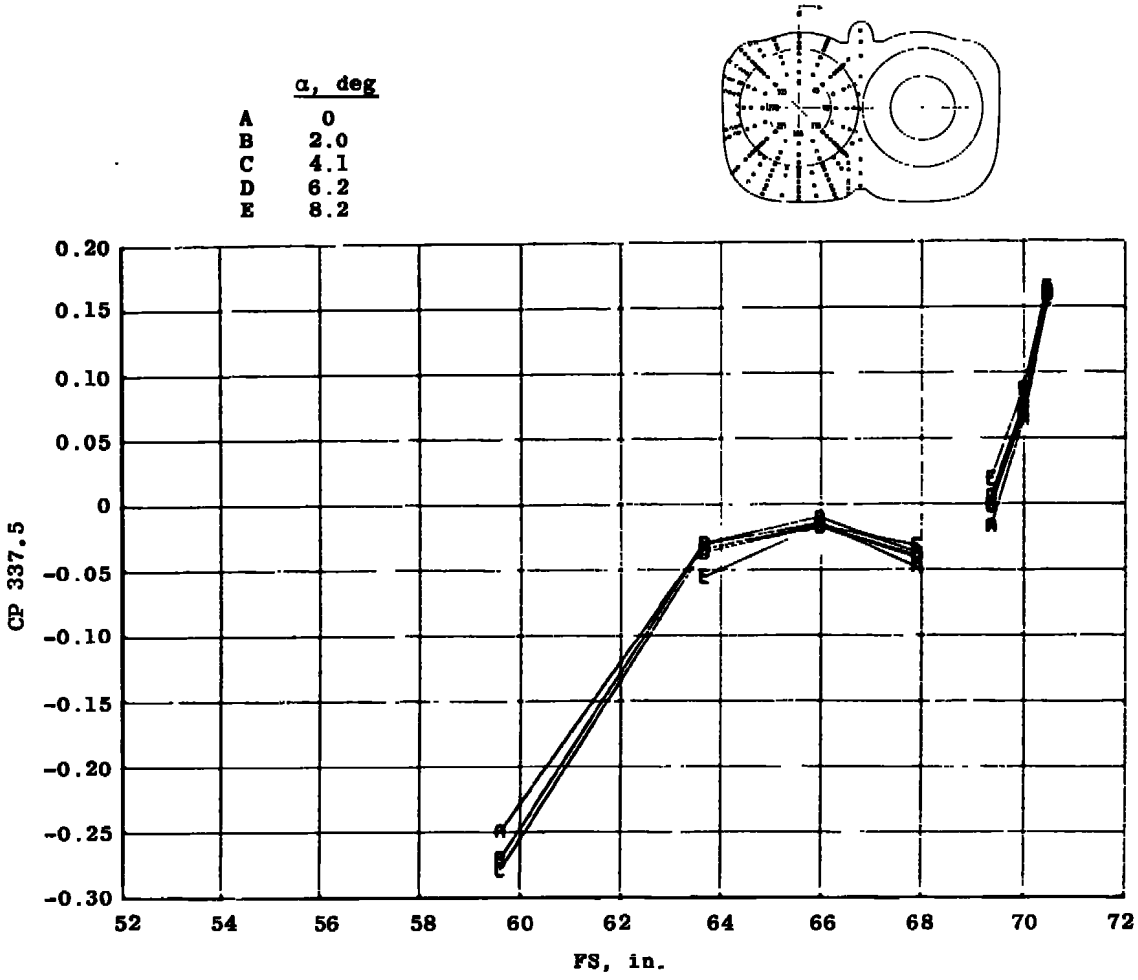

s. ϕ = 337.5 deg

Figure 17. Continued.

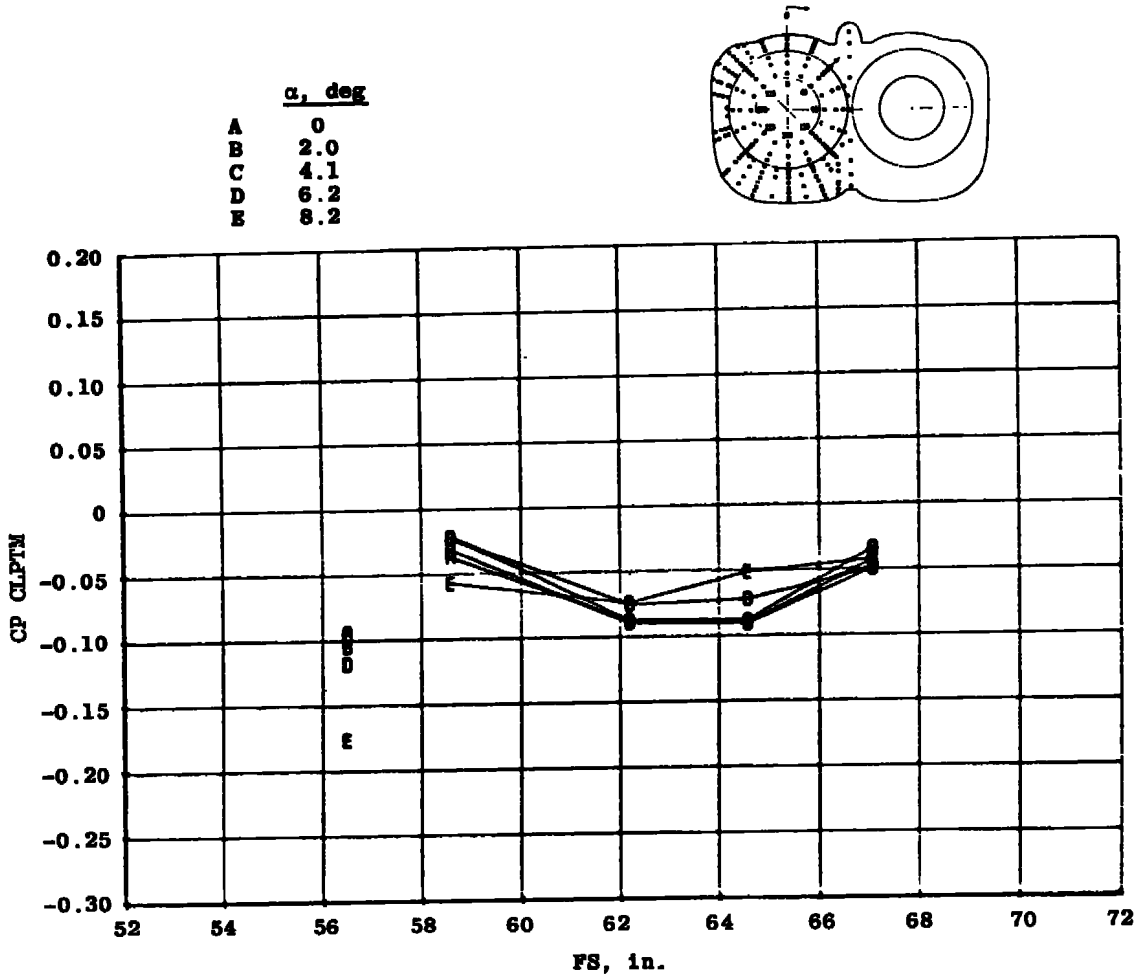

t. Aircraft bottom centerline

Figure 17. Continued.

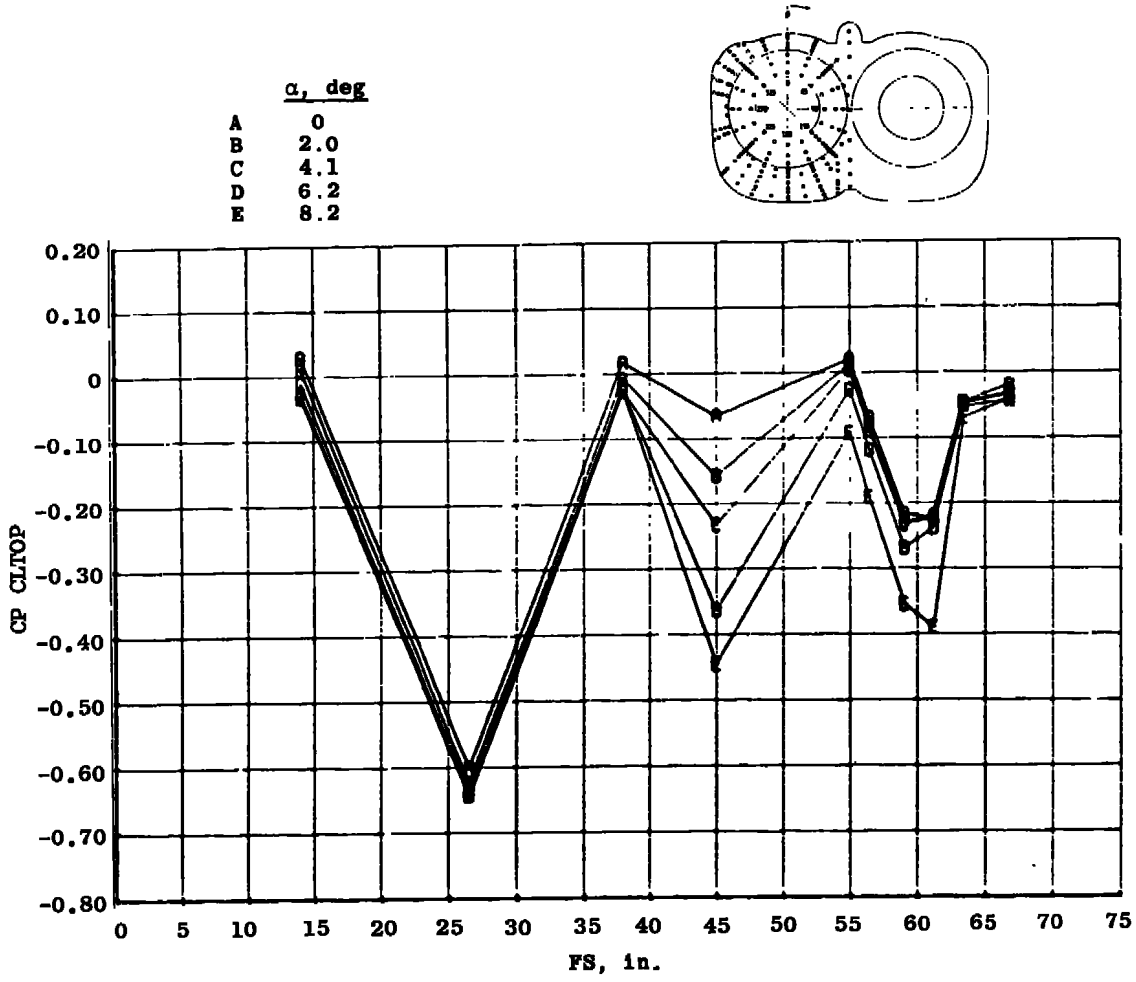

u. Aircraft top centerline

Figure 17. Concluded.

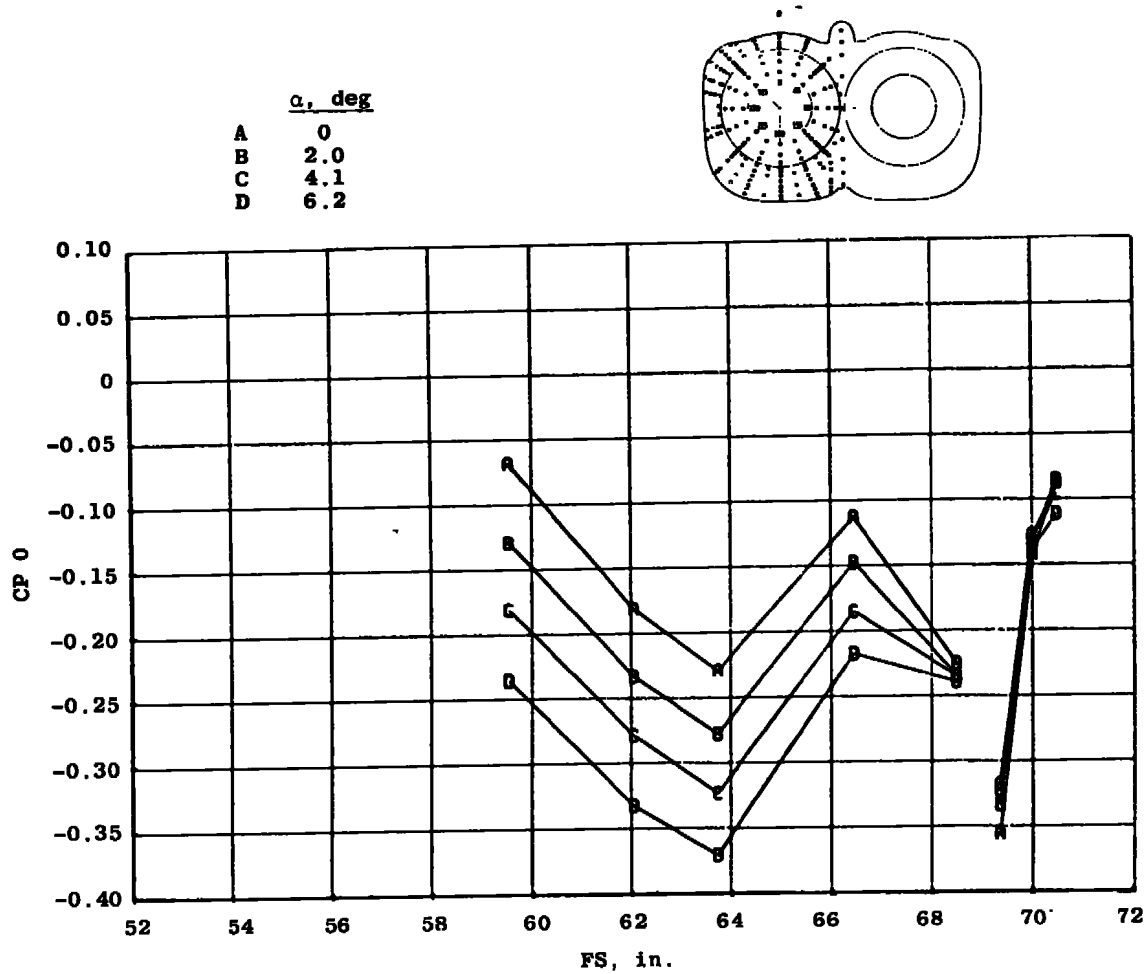

a. $\phi = 0$

Figure 18. Model attitude effects on the surface pressure distribution of the reheat nozzle configuration, M_∞ = 1.2, Re = 2.8 x 10^6/ft, δ_H = -2 deg, and NPR = 6.

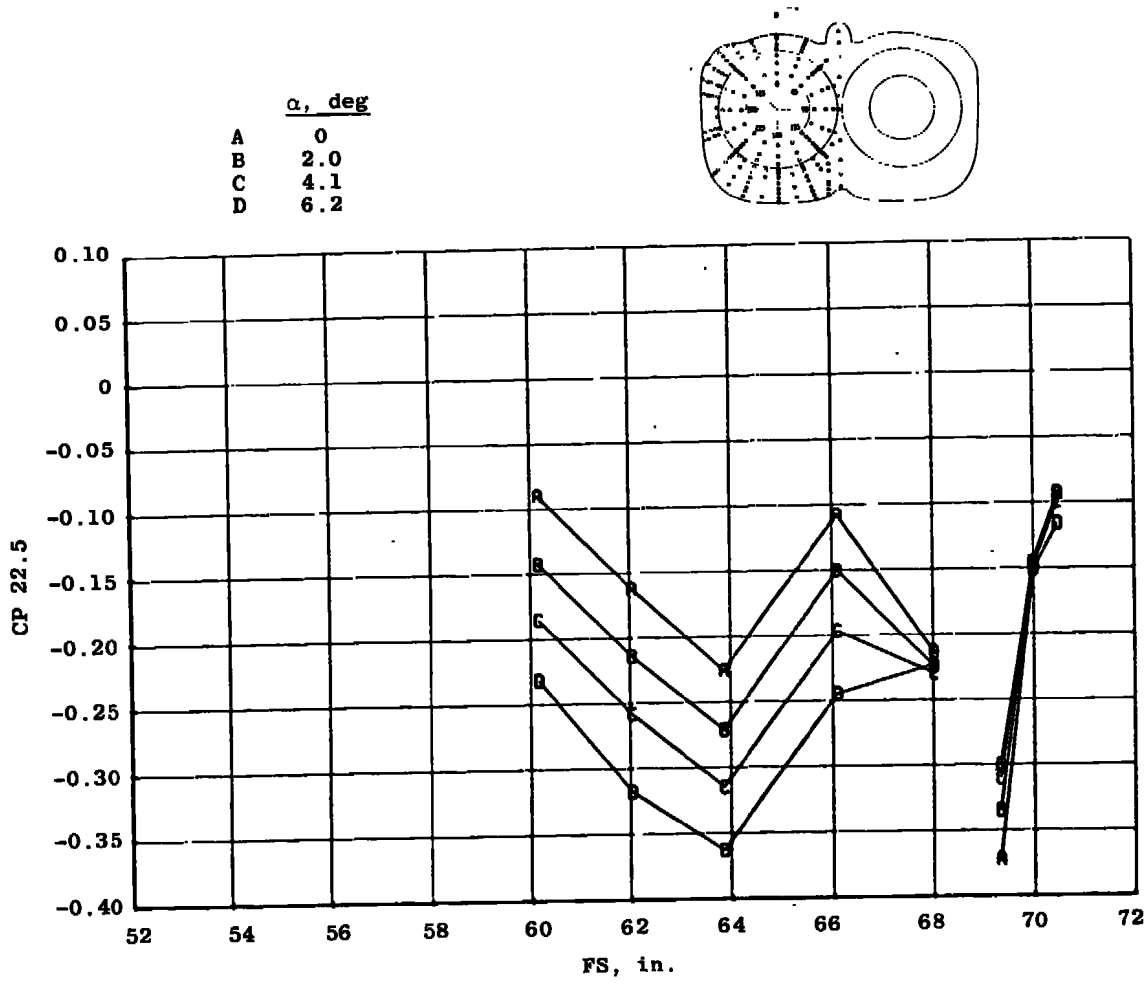

b. ϕ = 22.5 deg

Figure 18. Continued.

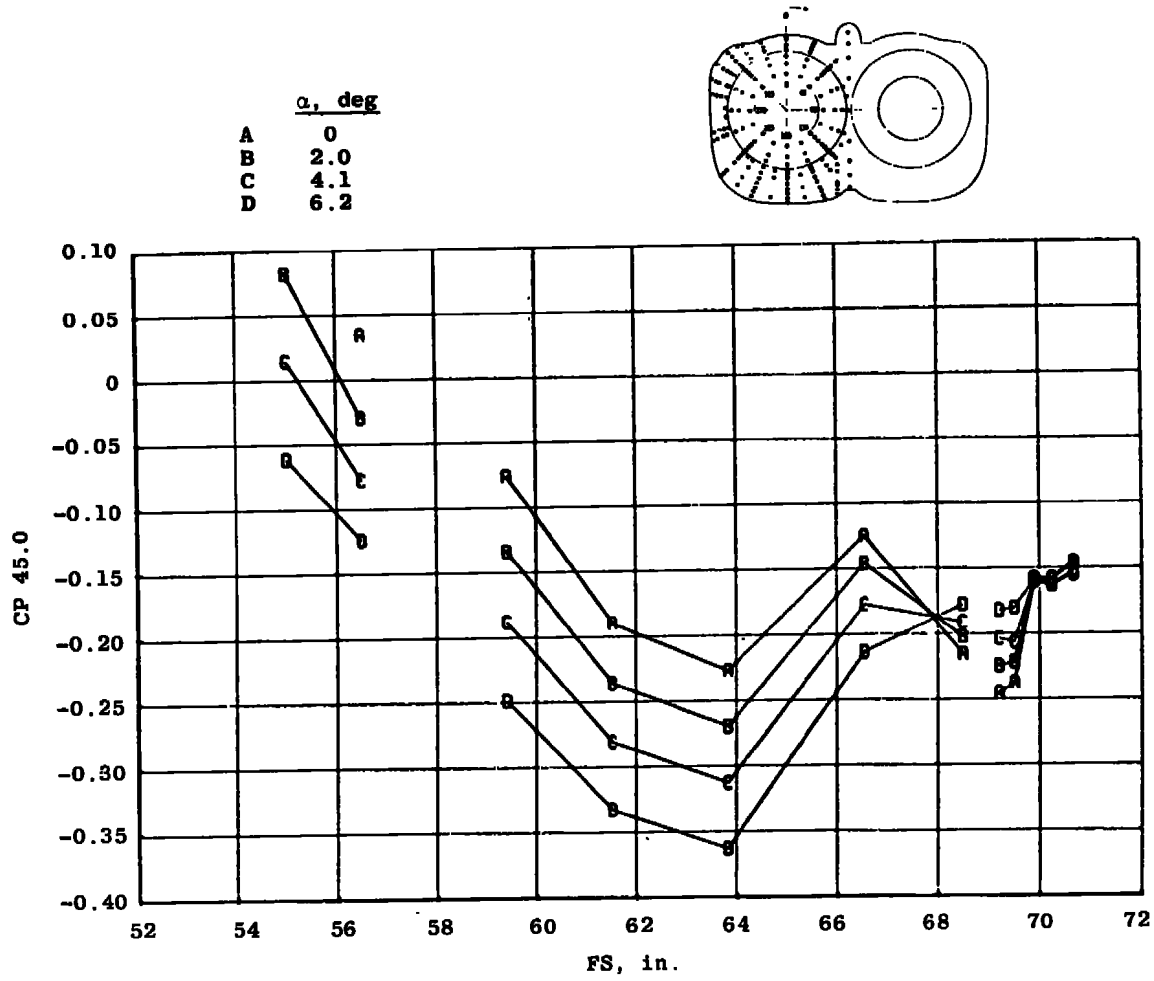

c. ϕ = 45.0 deg

Figure 18. Continued.

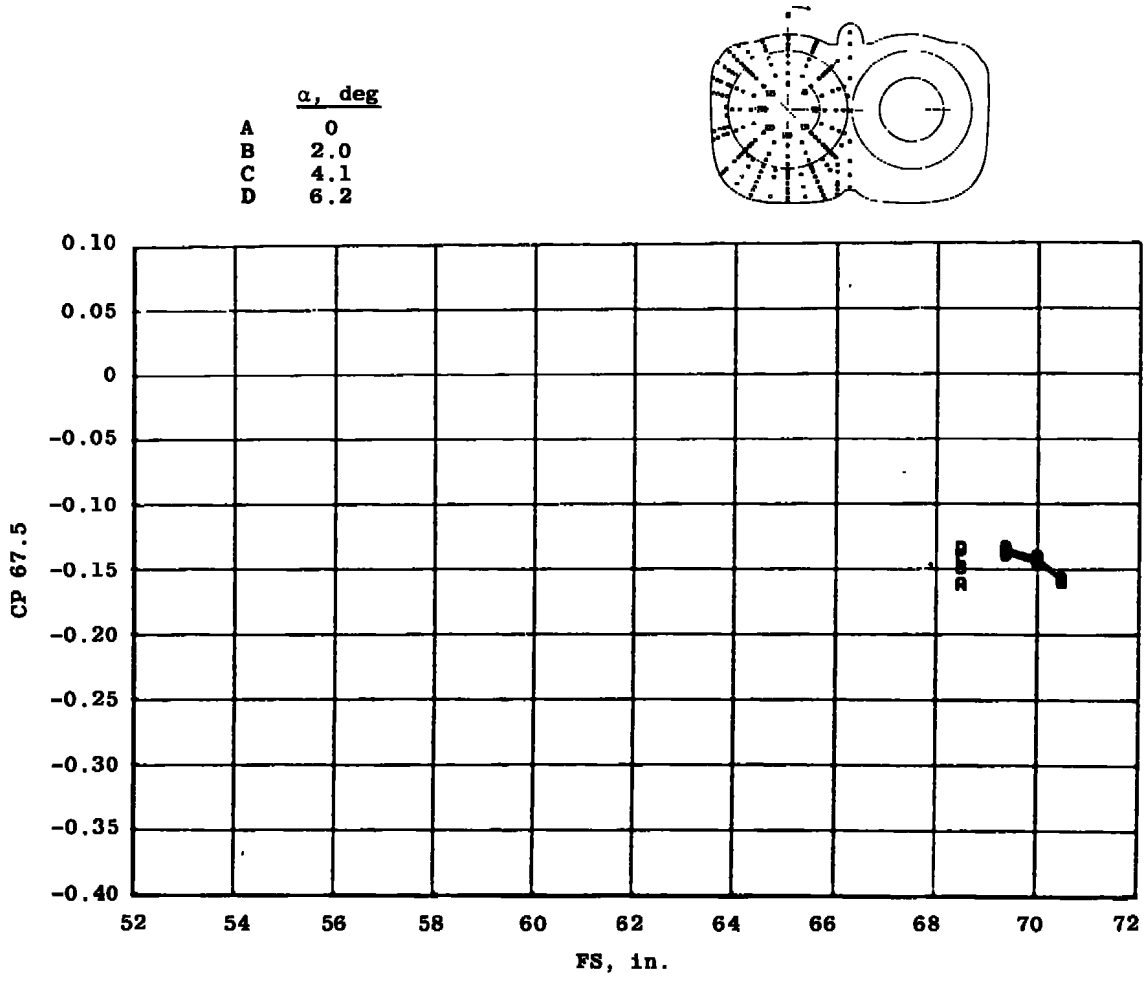

d. ϕ = 67.5 deg

Figure 18. Continued.

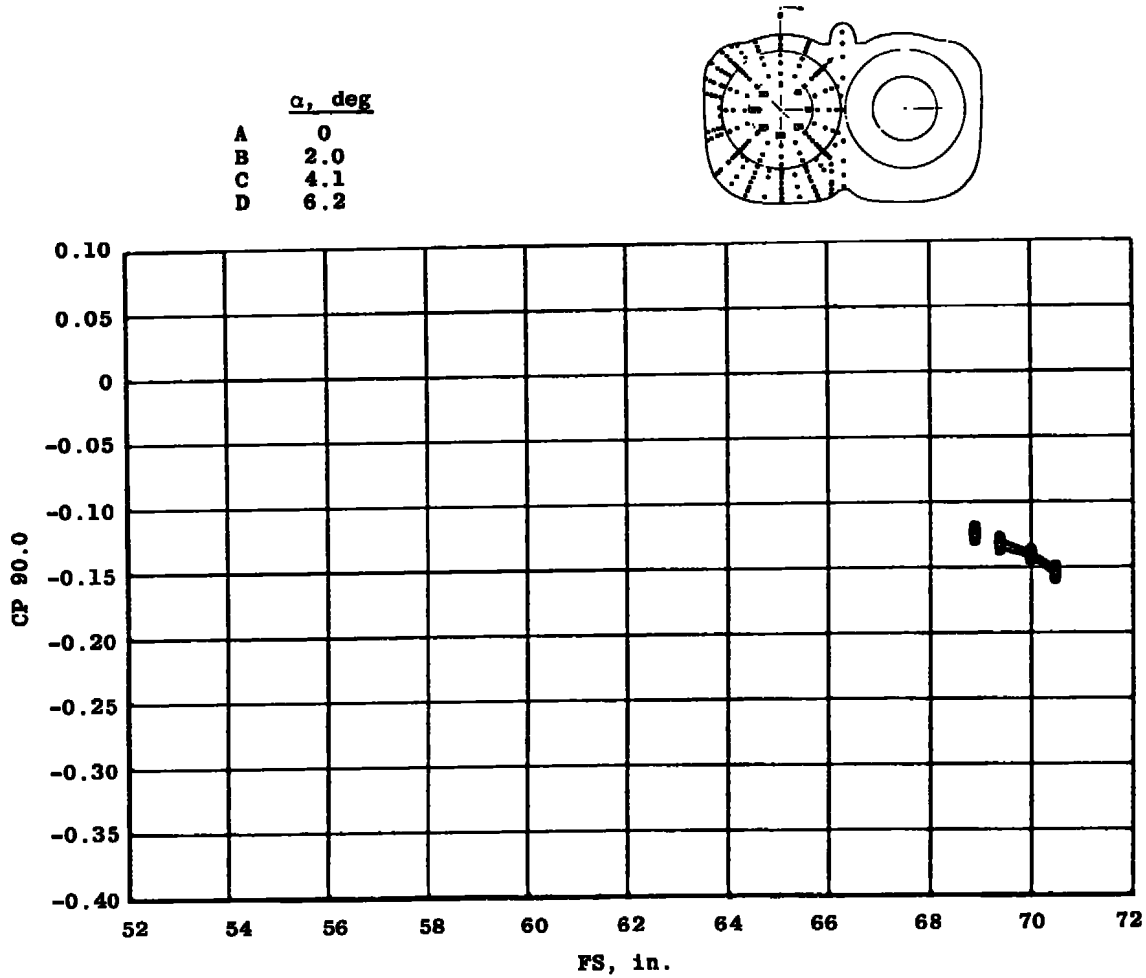

e. ϕ = 90.0 deg

Figure 18. Continued.

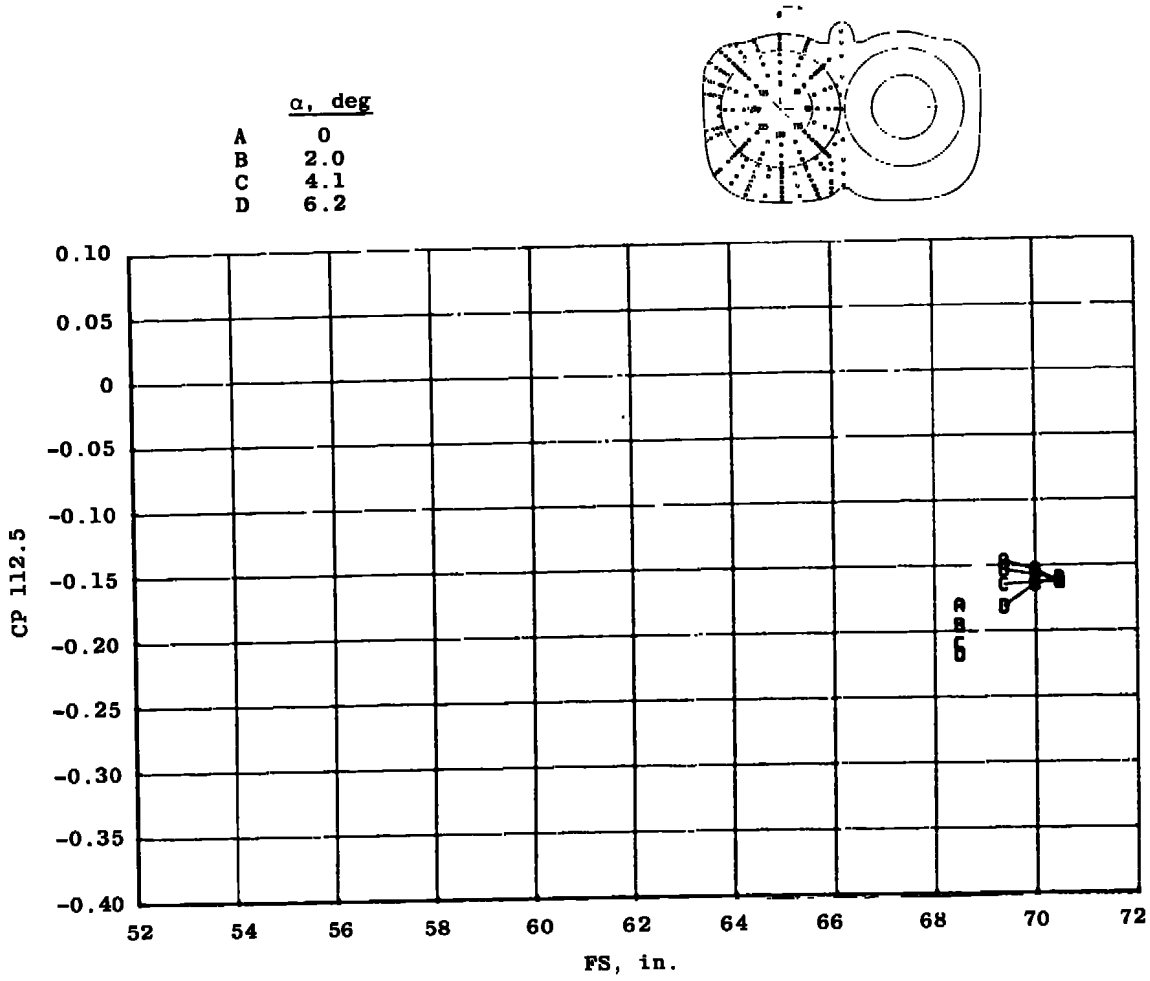

f. ϕ = 112.5 deg

Figure 18. Continued.

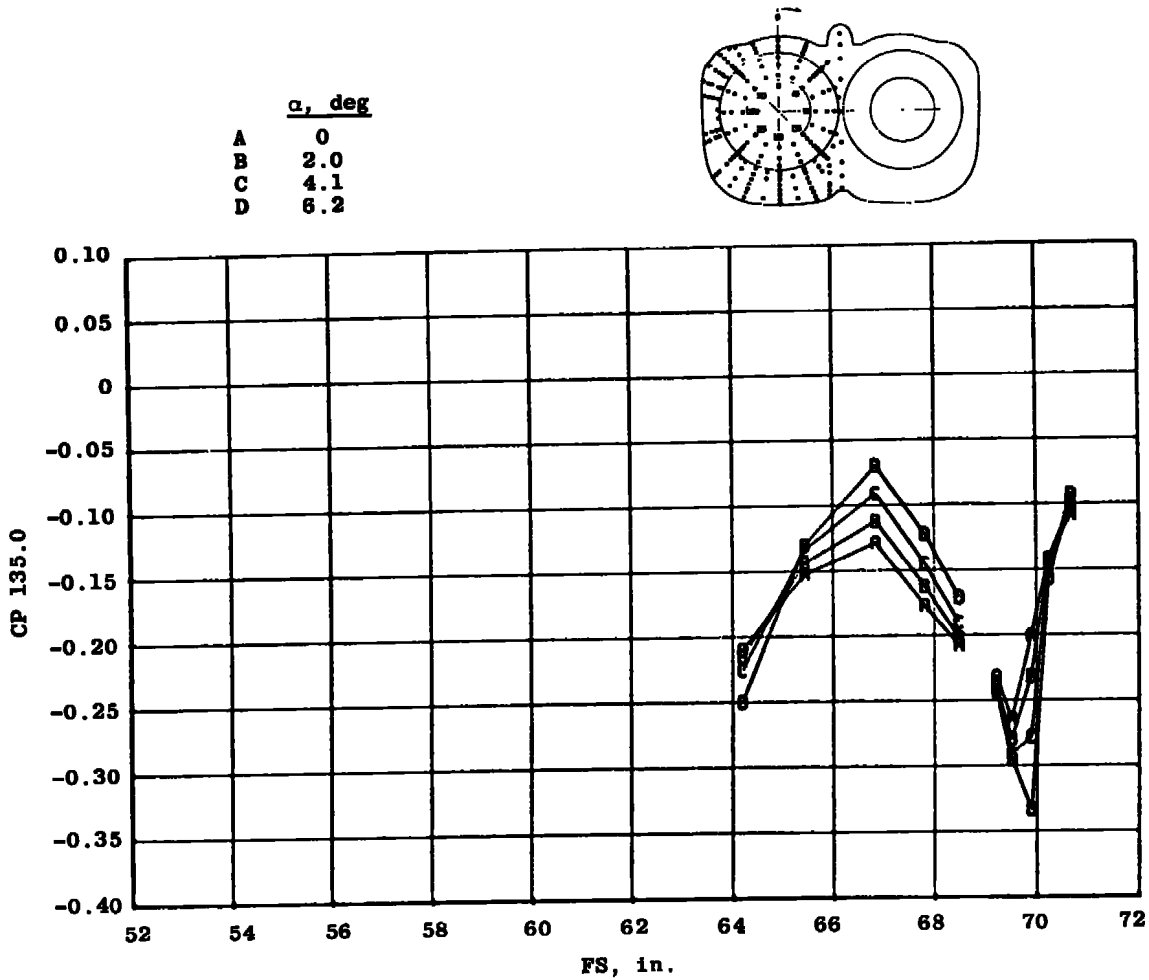

g. ϕ = 135.0 deg

Figure 18. Continued.

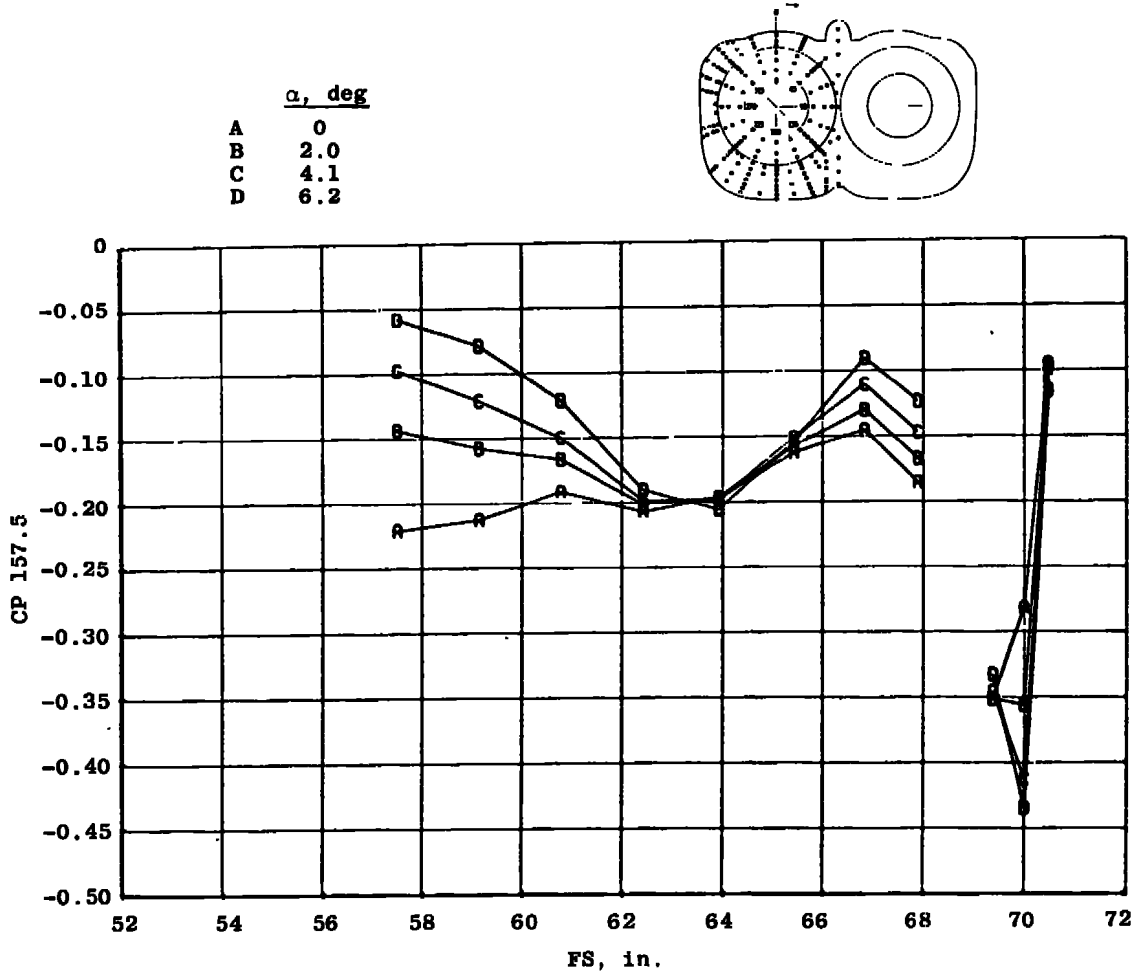

h. ϕ = 157.5 deg

Figure 18. Continued.

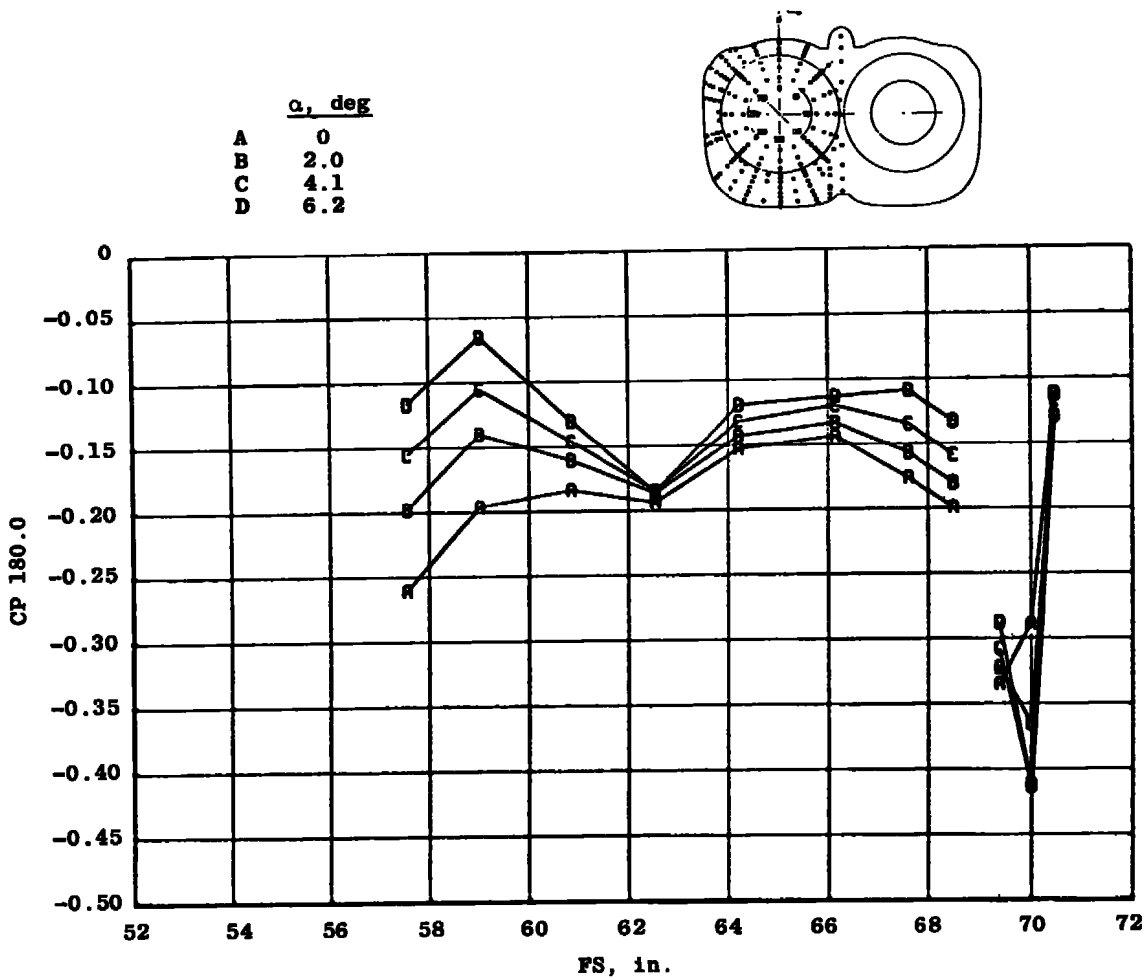

i. ϕ = 180.0 deg

Figure 18. Continued.

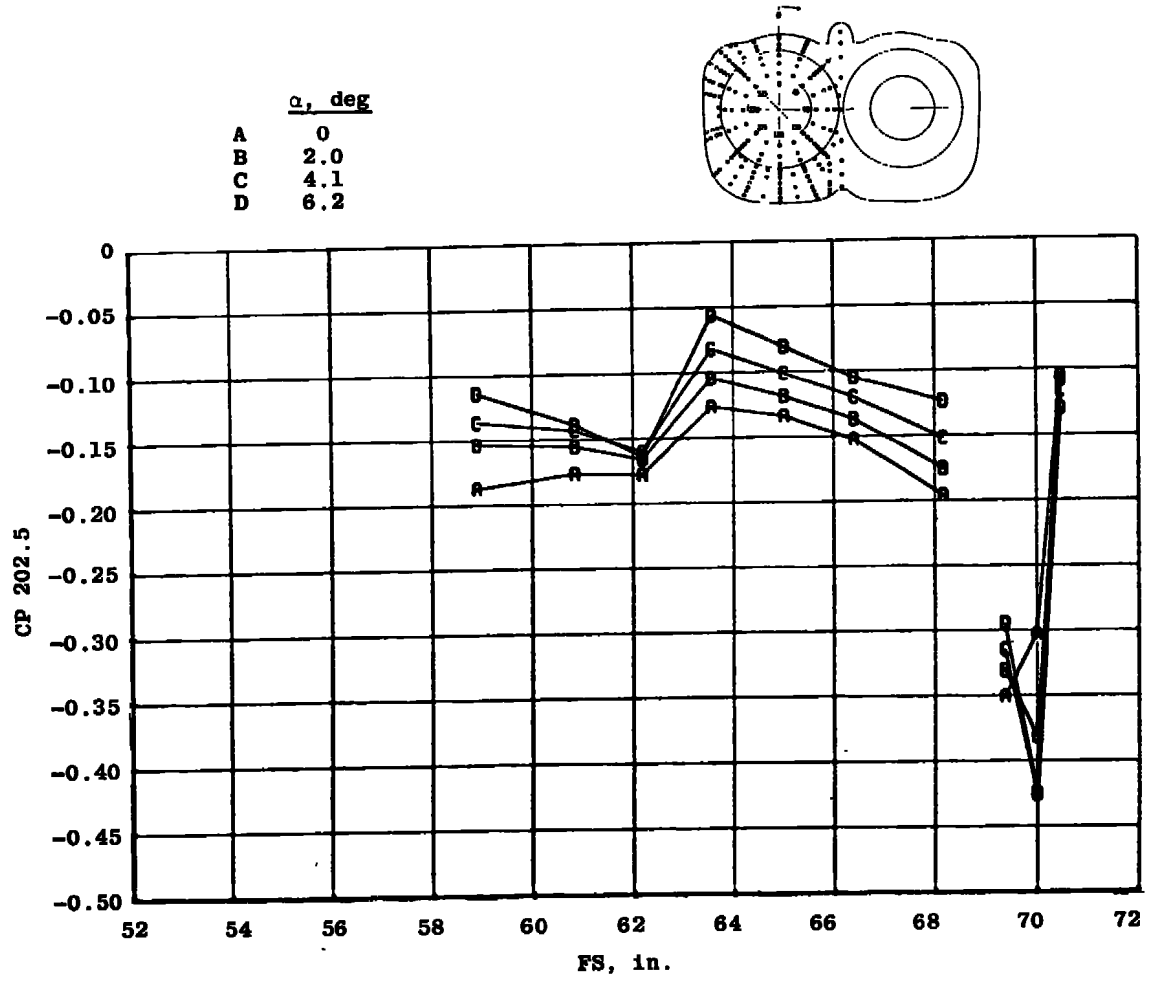

j. ϕ = 202.5 deg

Figure 18. Continued.

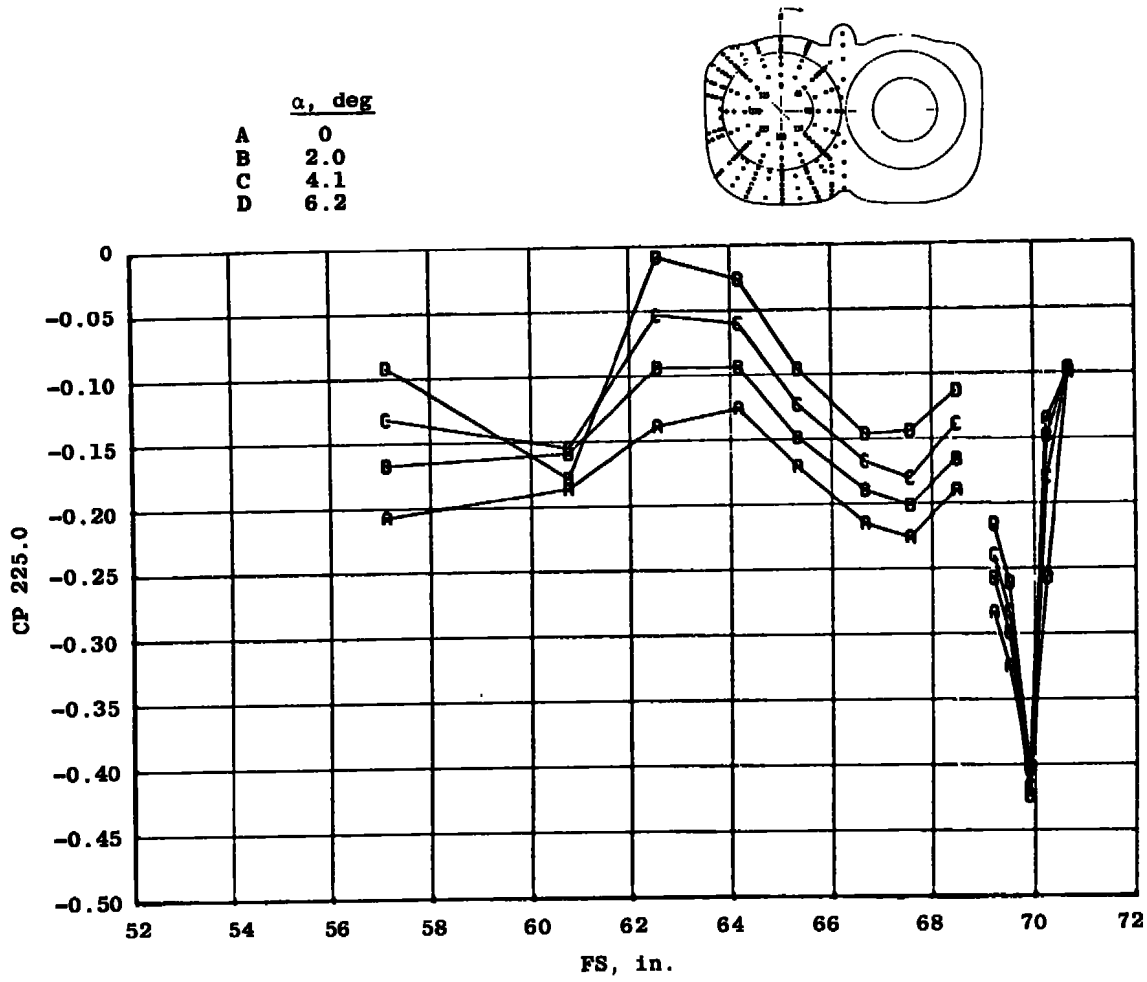

k. ϕ = 225.0 deg

Figure 18. Continued.

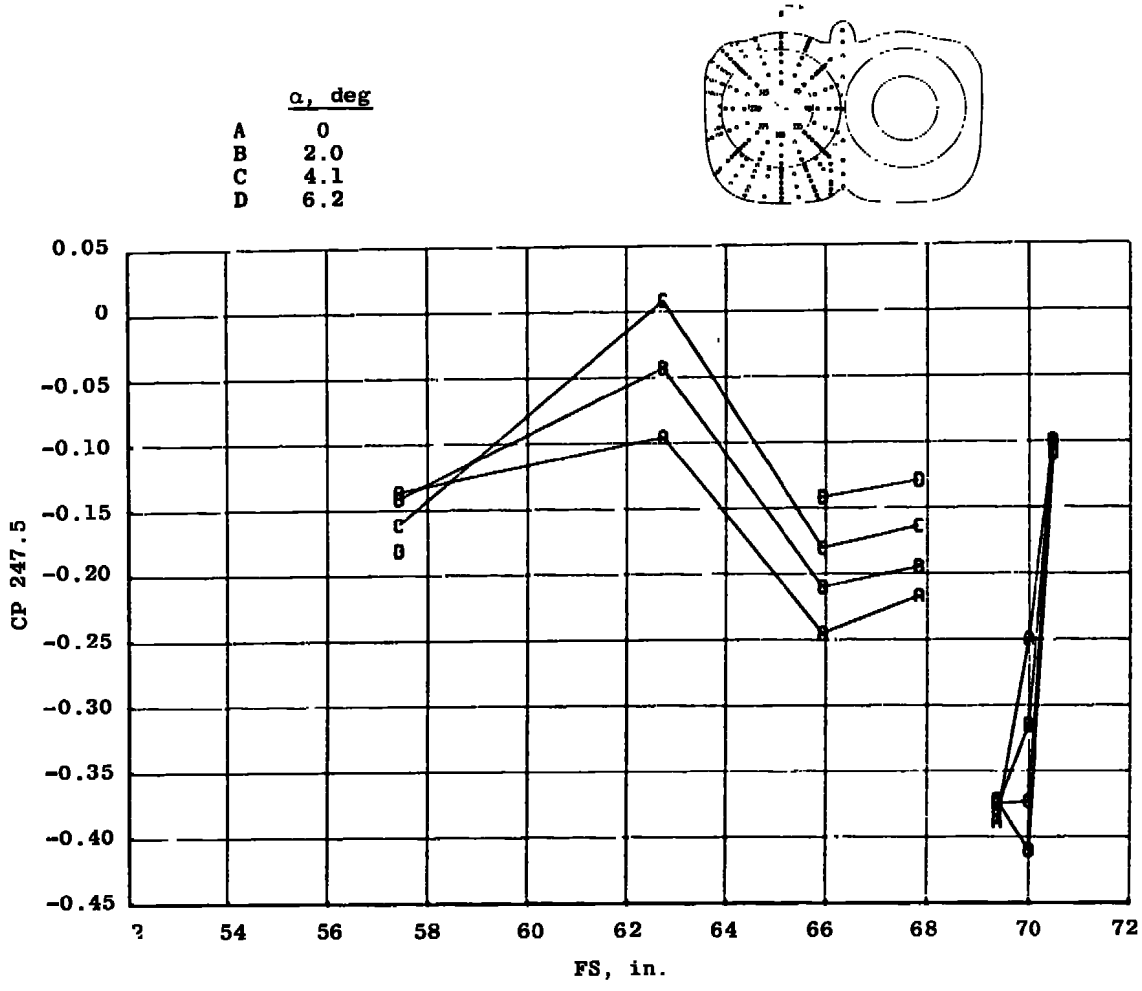

l. ϕ = 247.5 deg

Figure 18. Continued.

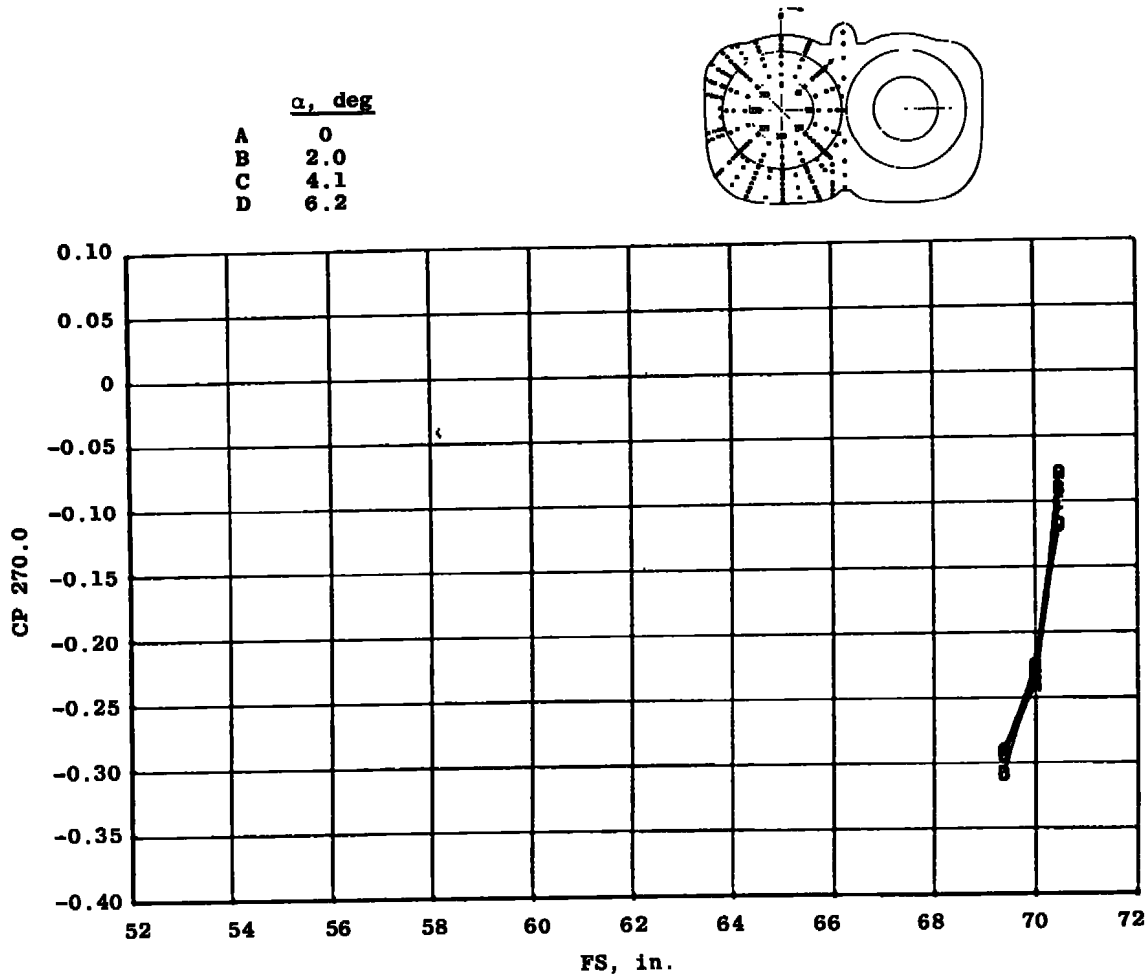

m. ϕ = 270.0 deg

Figure 18. Continued.

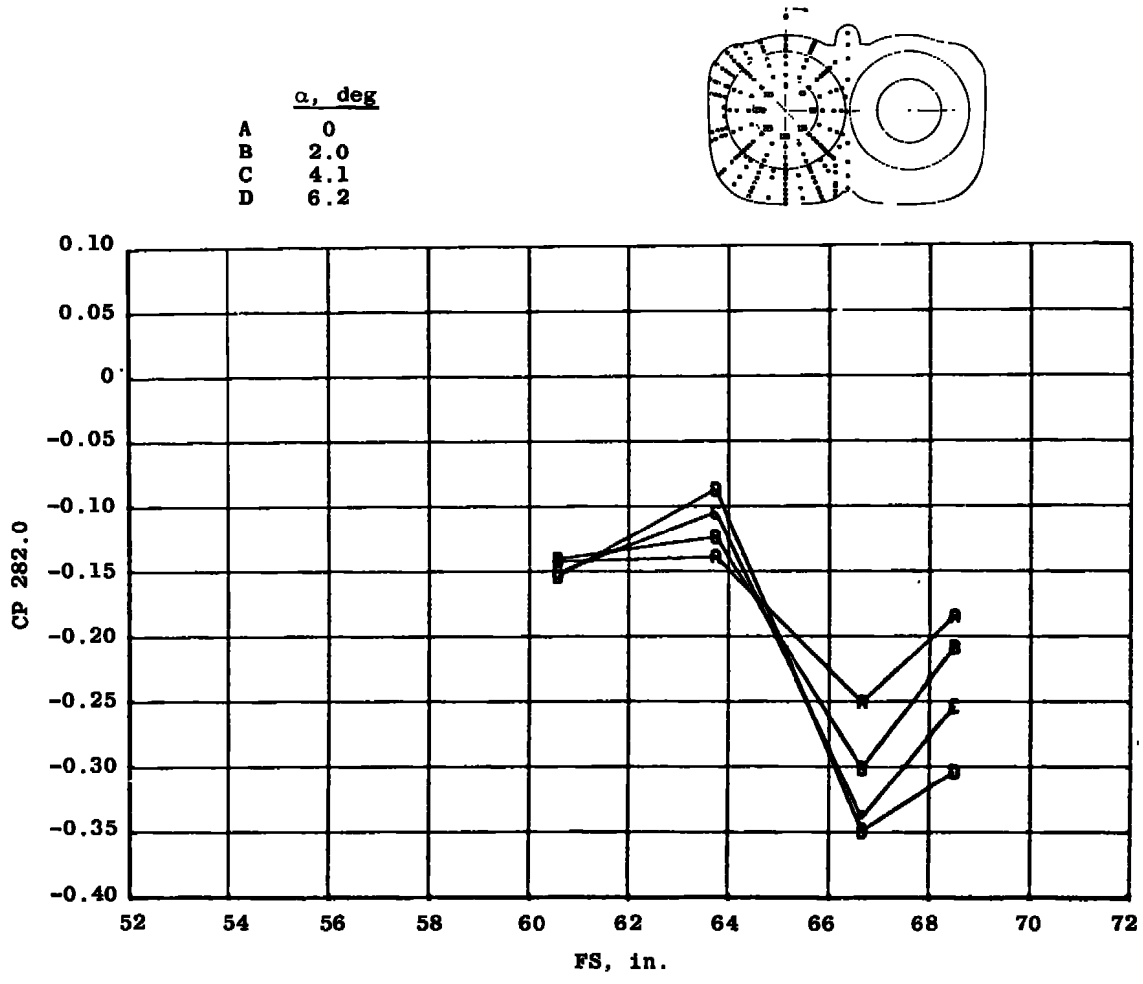

n. ϕ = 282.0 deg

Figure 18. Continued.

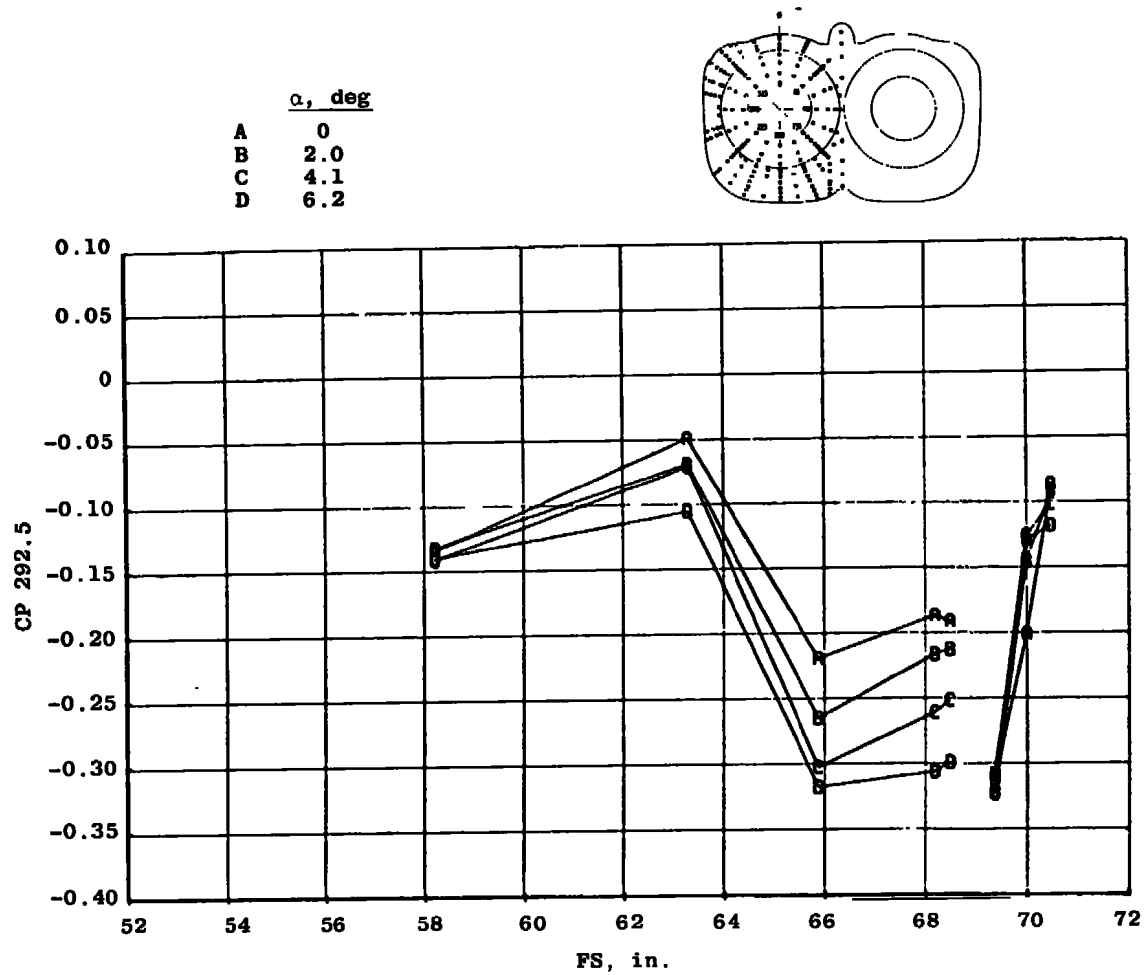

o. ϕ = 292.5 deg

Figure 18. Continued.

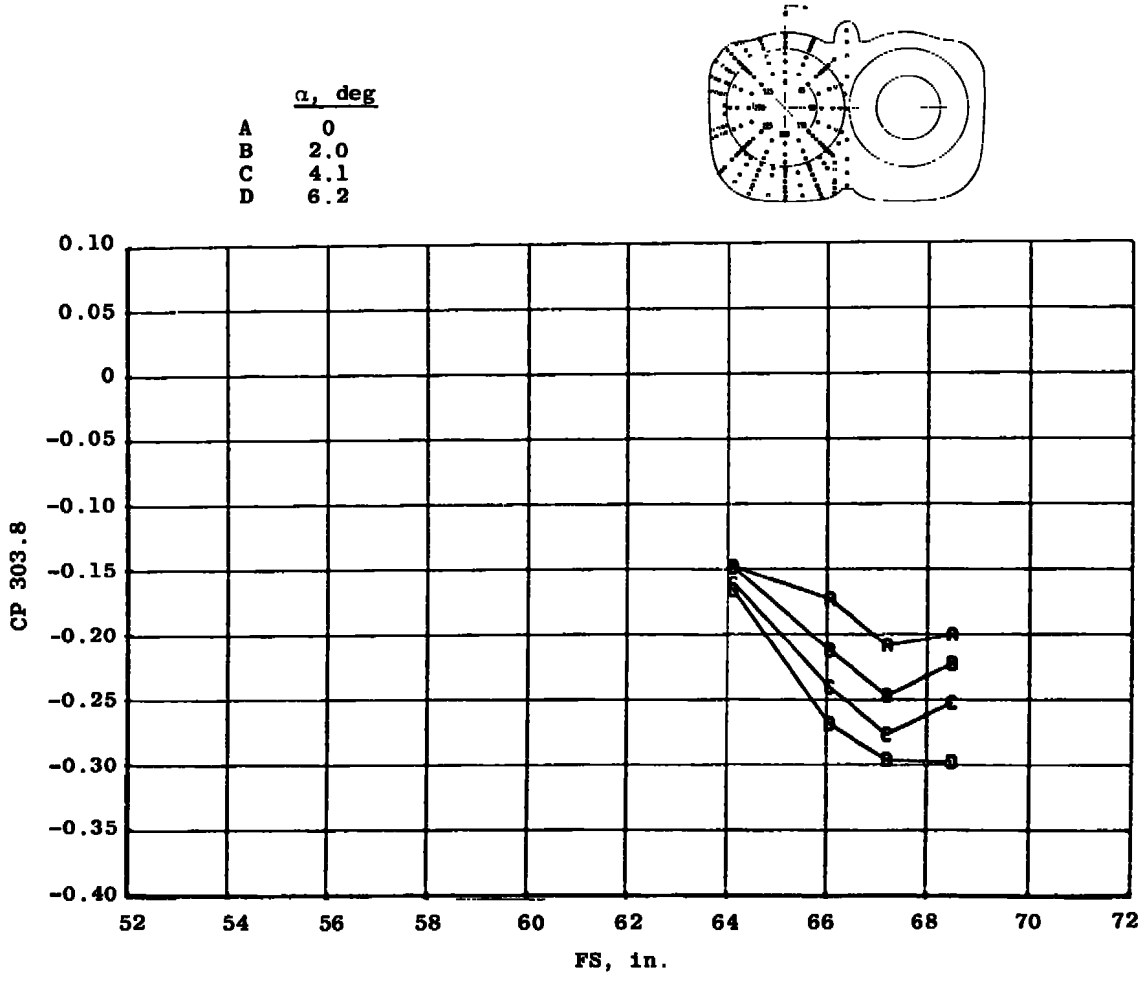

p. ϕ = 303.8 deg

Figure 18. Continued.

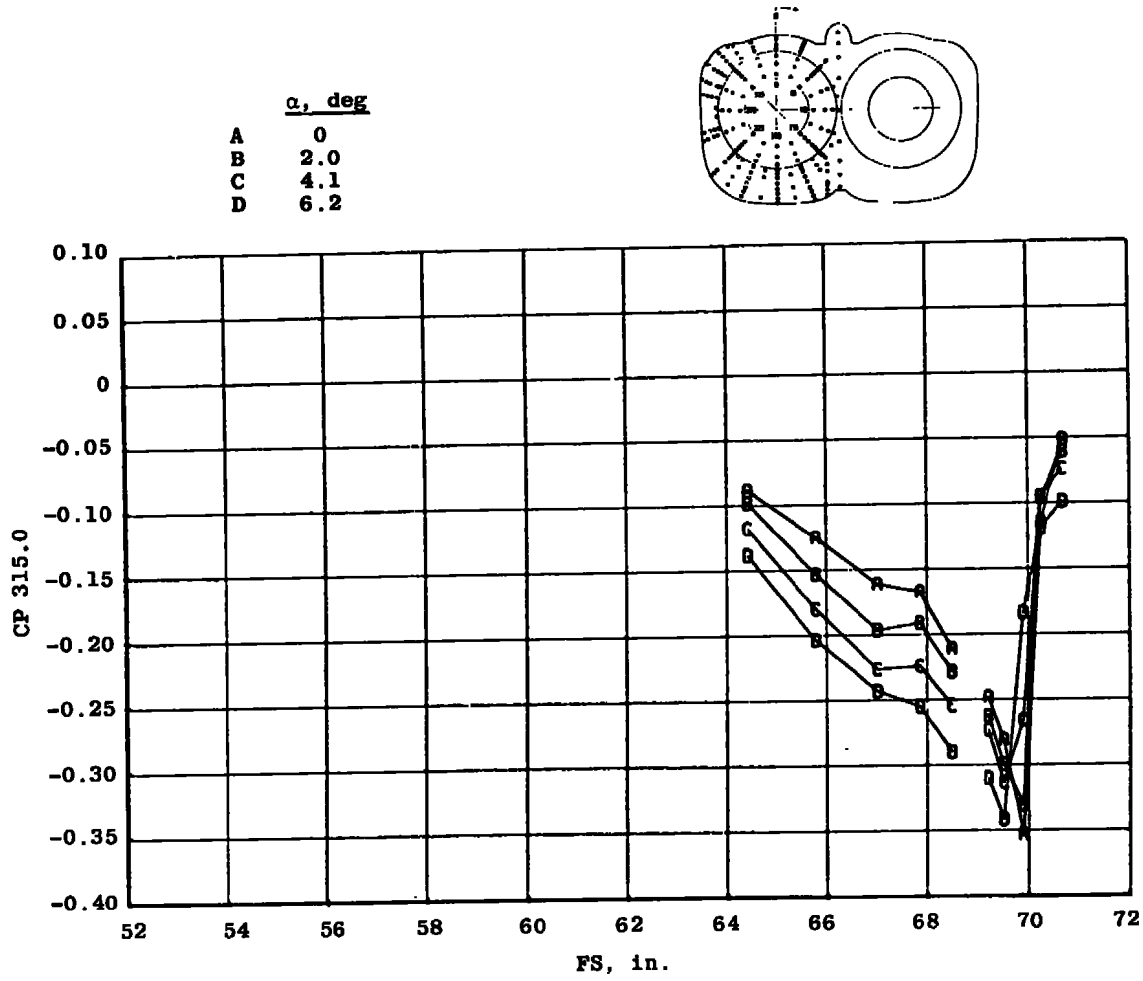

q. ϕ = 315.0 deg

Figure 18. Continued.

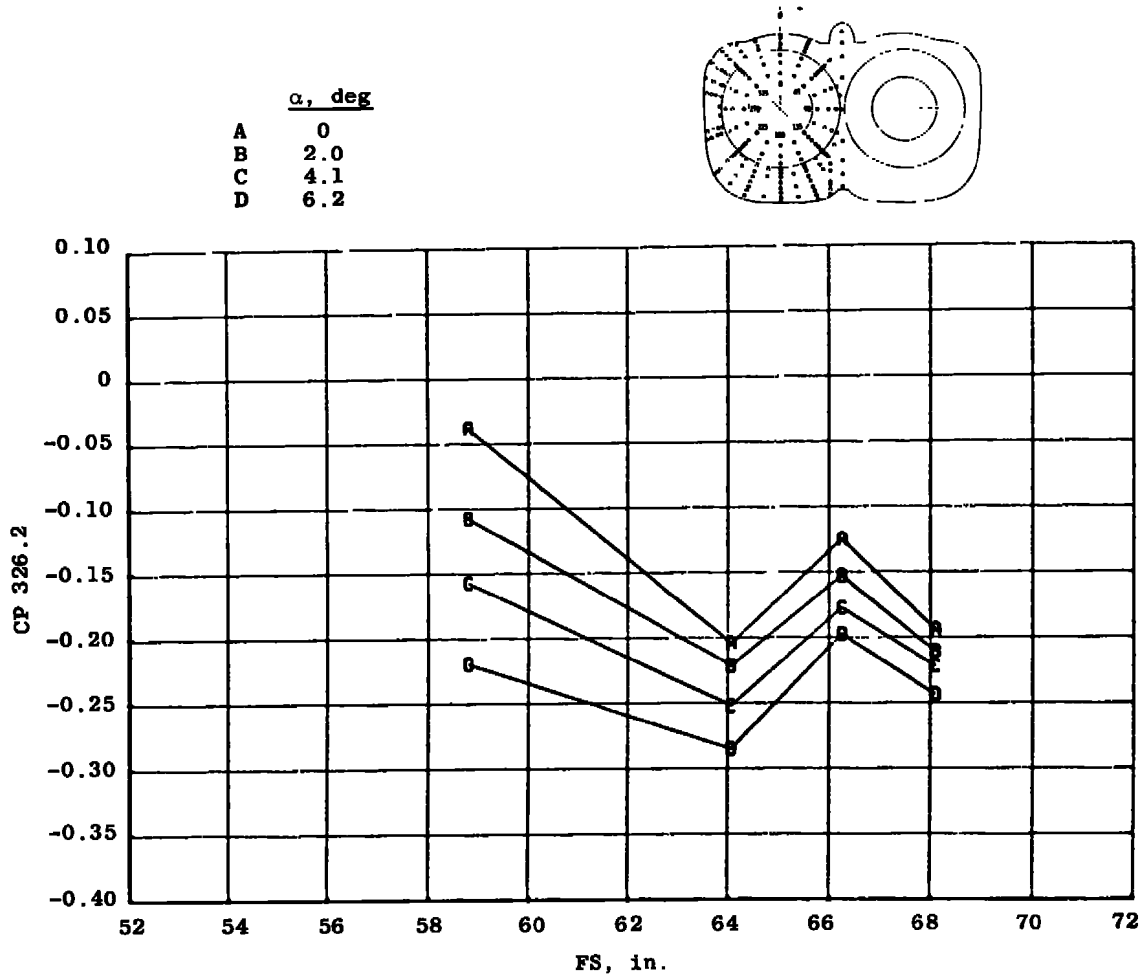

r. ϕ = 326.2 deg

Figure 18. Continued.

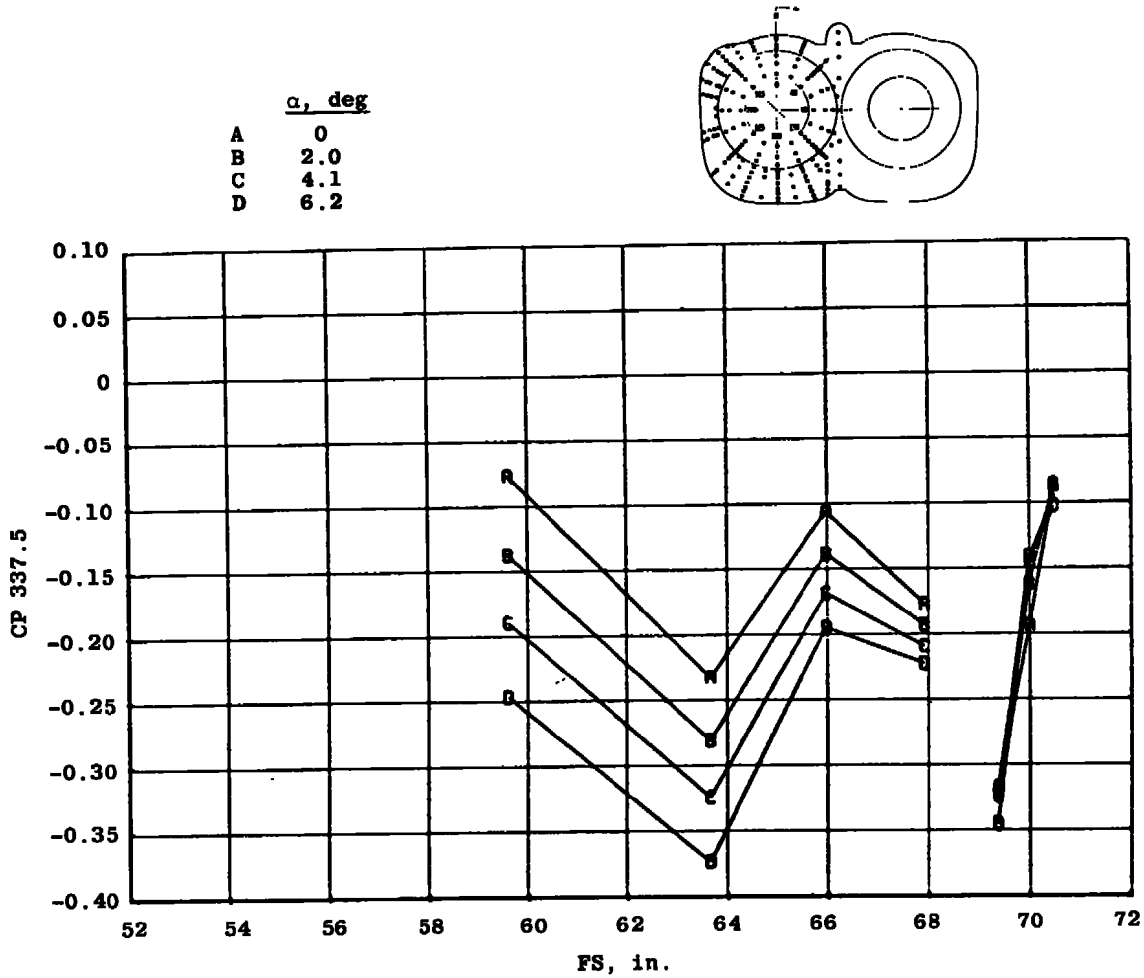

s. ϕ = 337.5 deg

Figure 18. Continued.

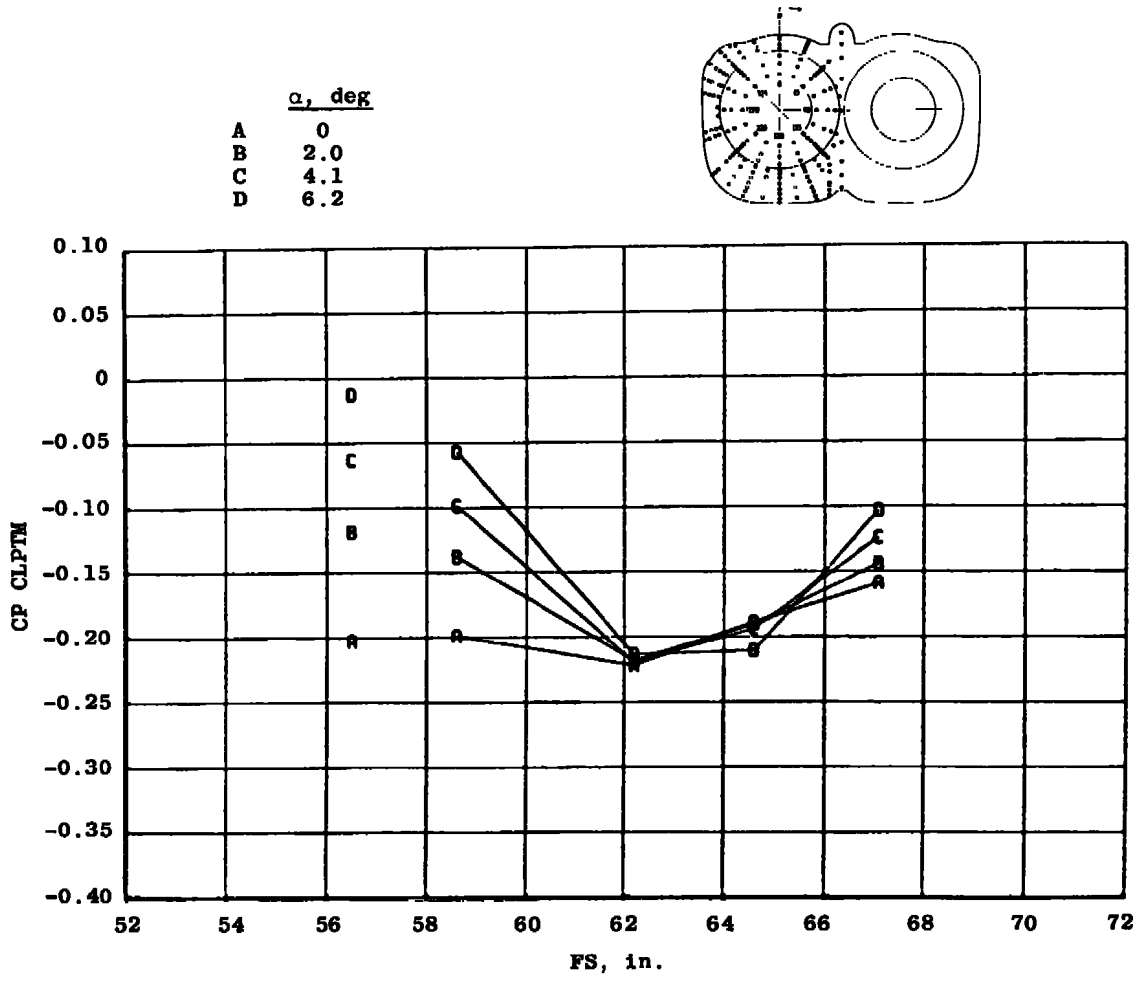

t. Aircraft bottom centerline
Figure 18. Continued.

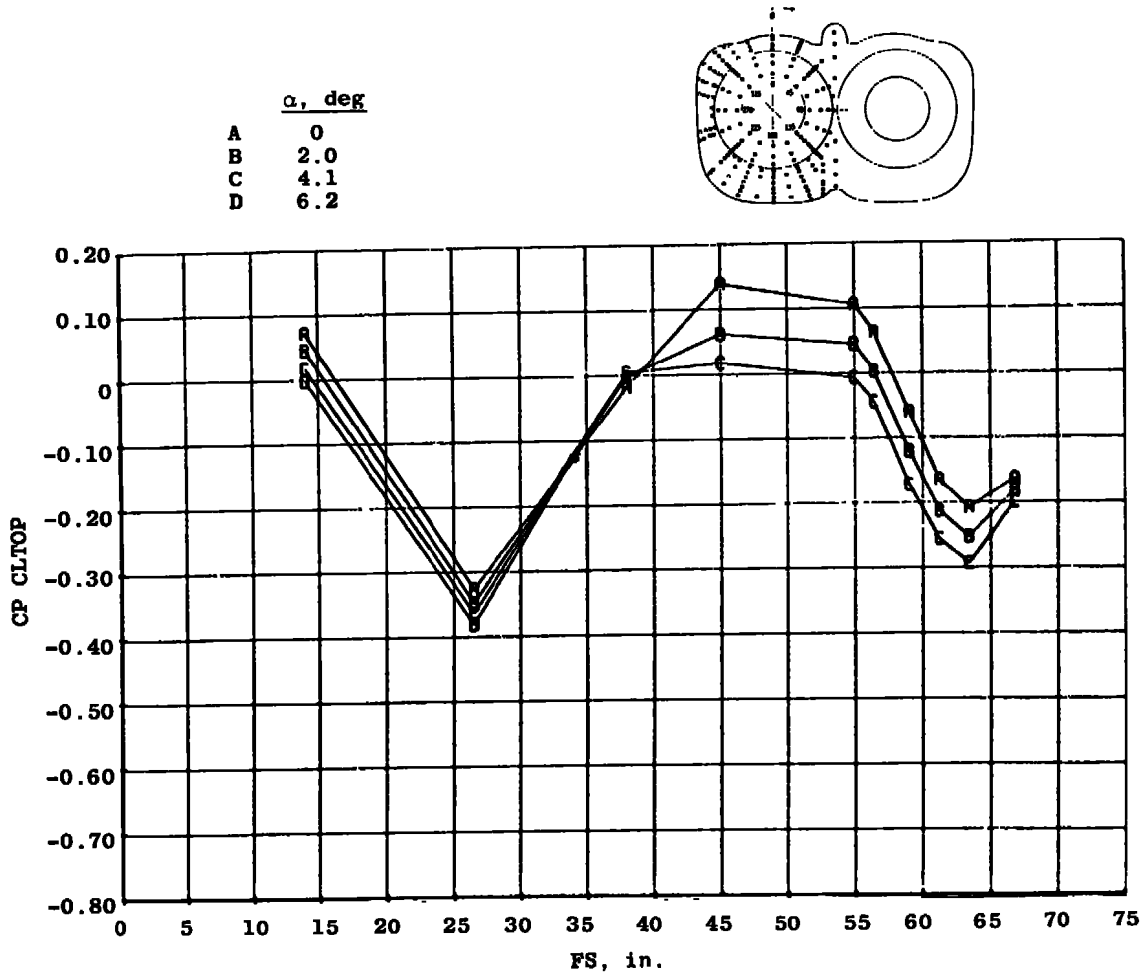

u. Aircraft top centerline

Figure 18. Concluded.

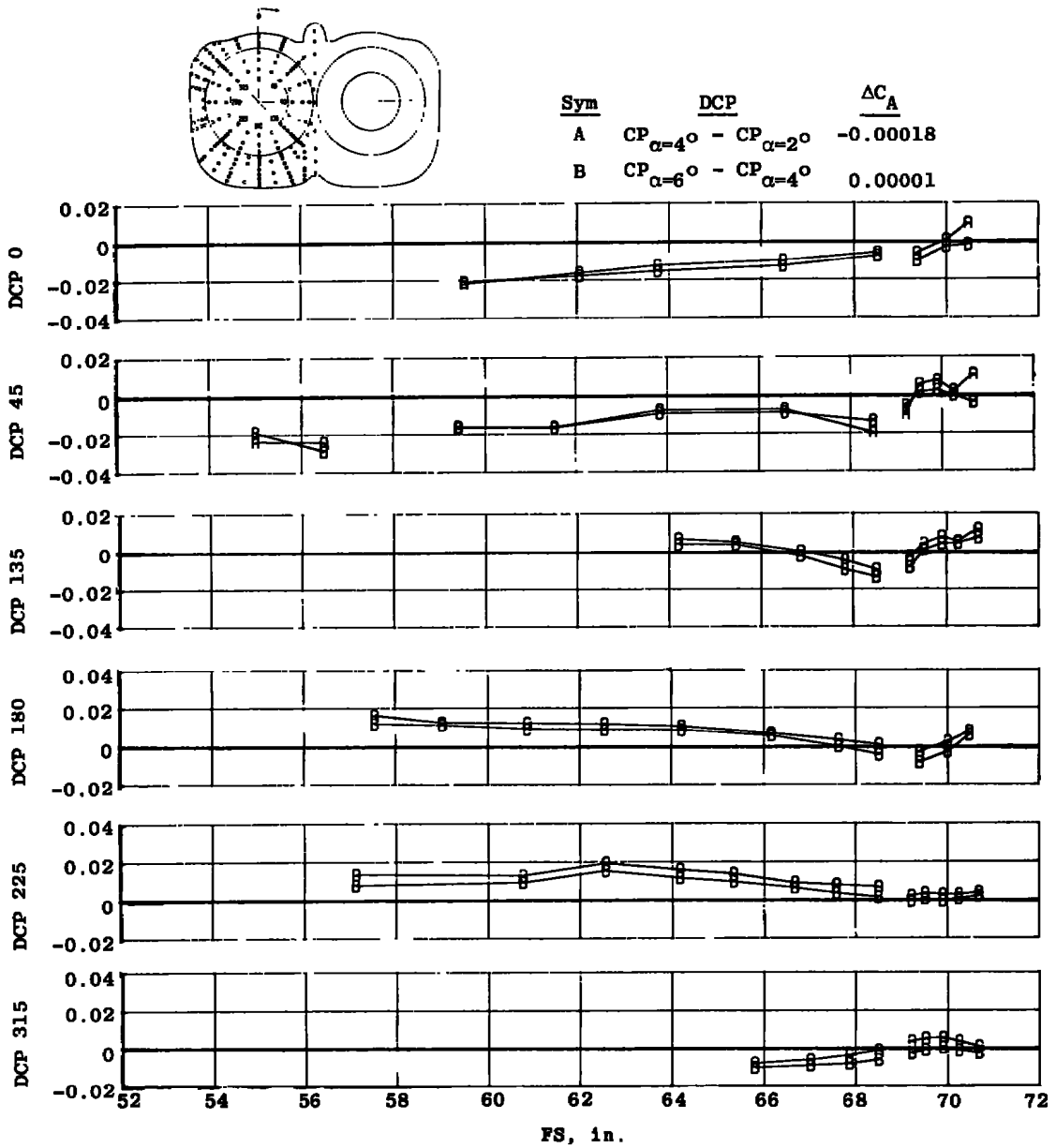

a. Cruise nozzle, M_∞ = 0.6, NPR = 3

Figure 19. Effect of incremental angle-of-attack changes on surface pressure distributions, Re = 2.8 x 10^6/ft, δ_H = -2 deg.

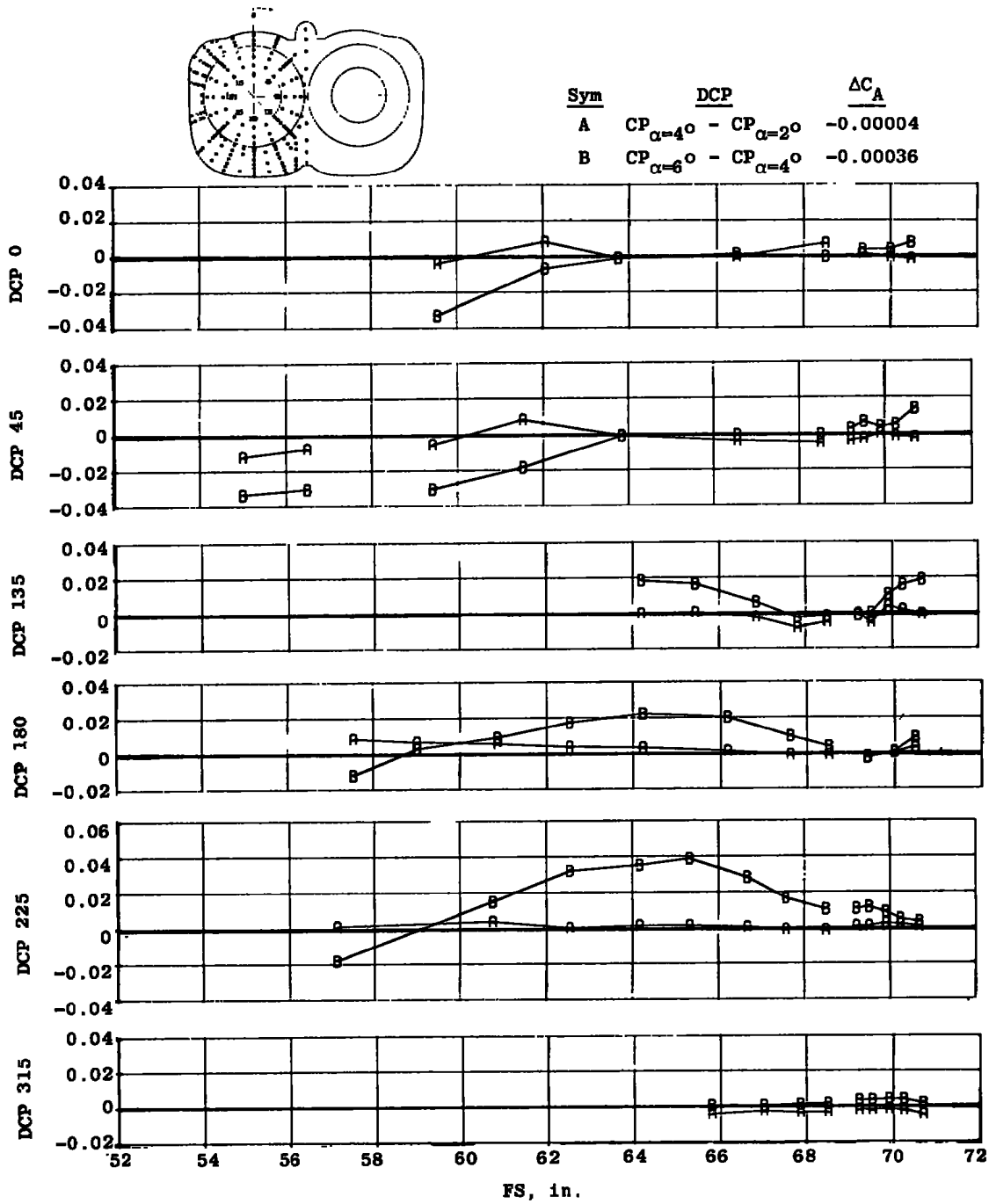

b. Reheat nozzle, M_∞ = 0.9, NPR = 5
Figure 19. Continued.

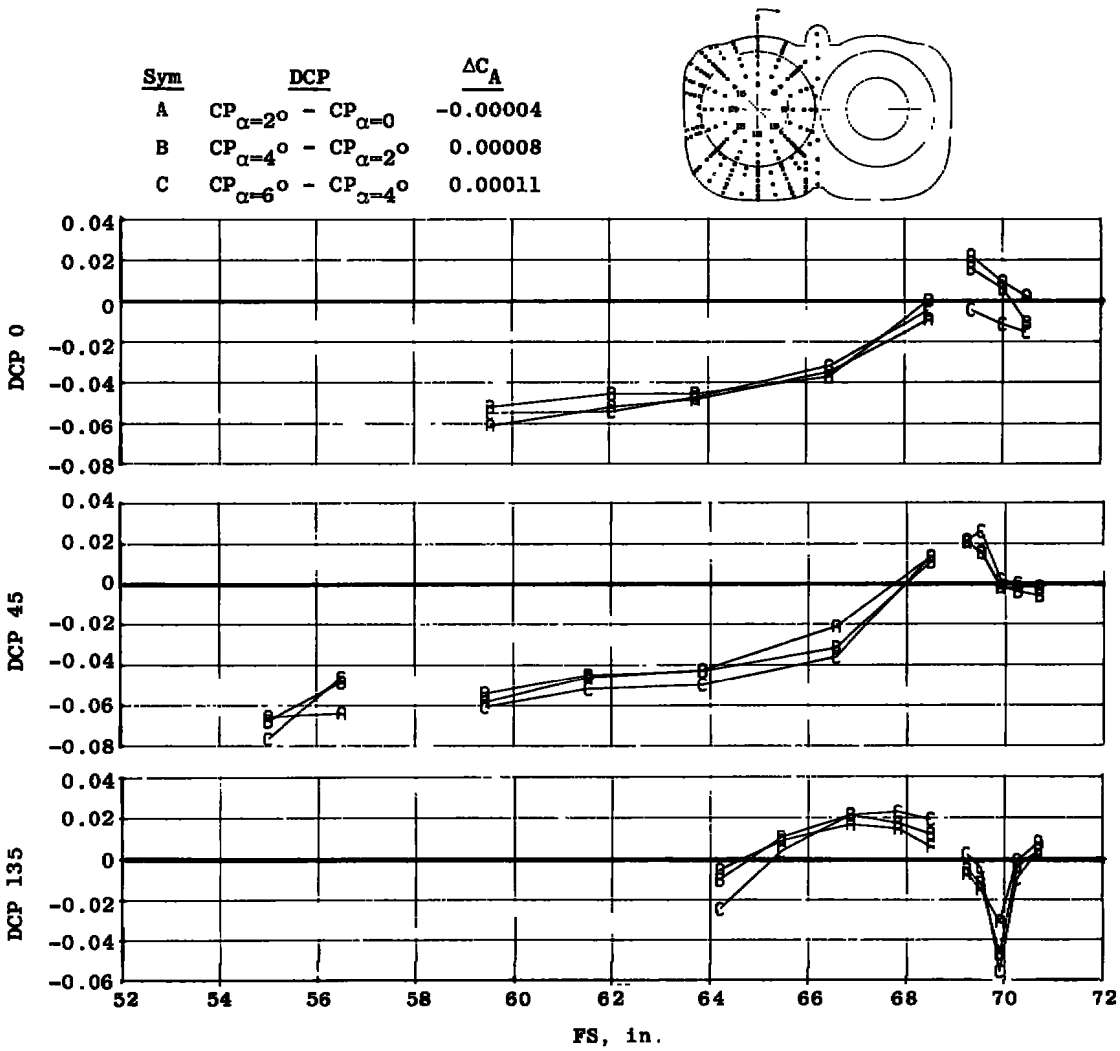

c. Reheat nozzle, M_∞ = 1.2, NPR = 6
Figure 19. Continued.

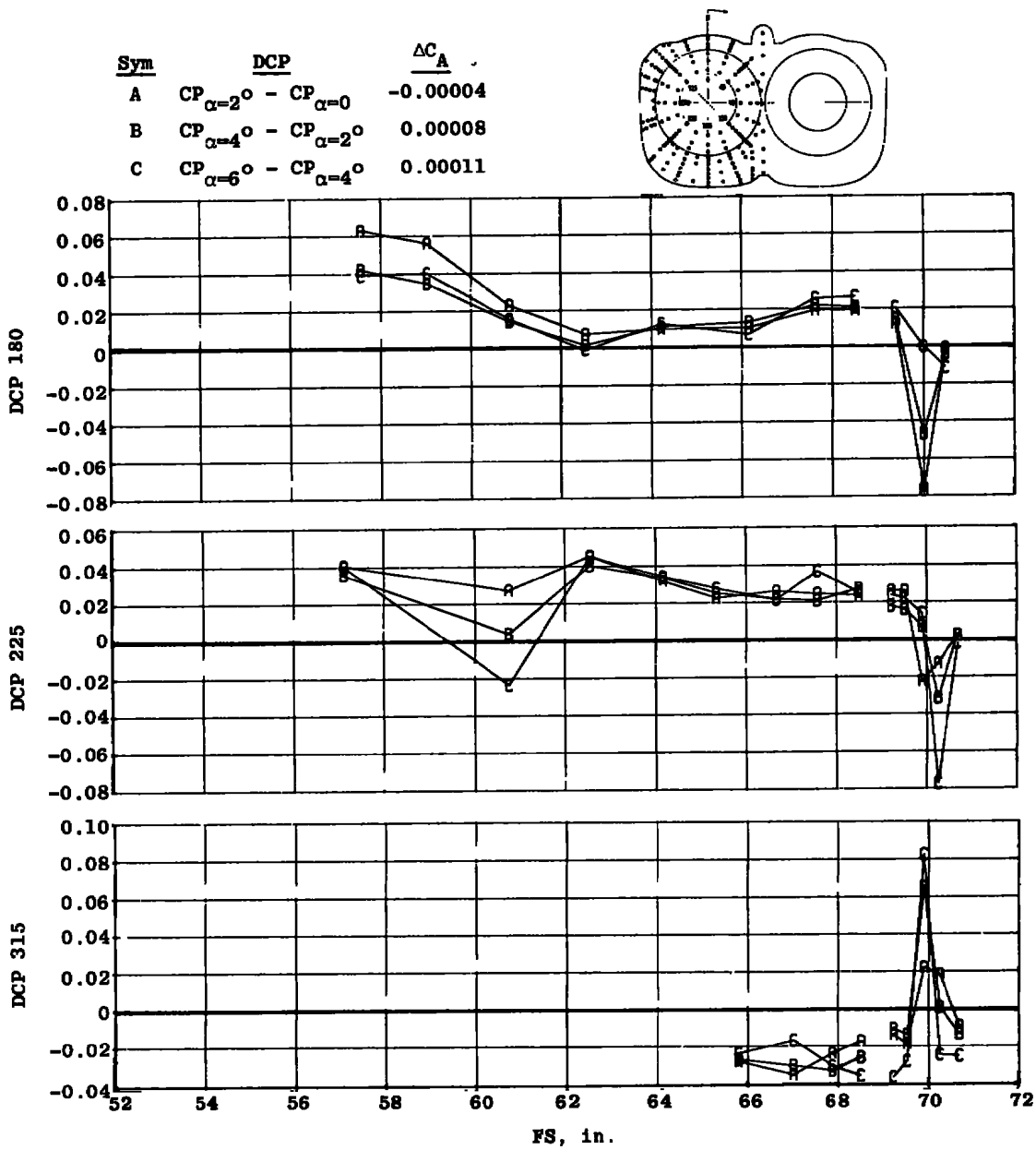

c. Concluded

Figure 19. Concluded.

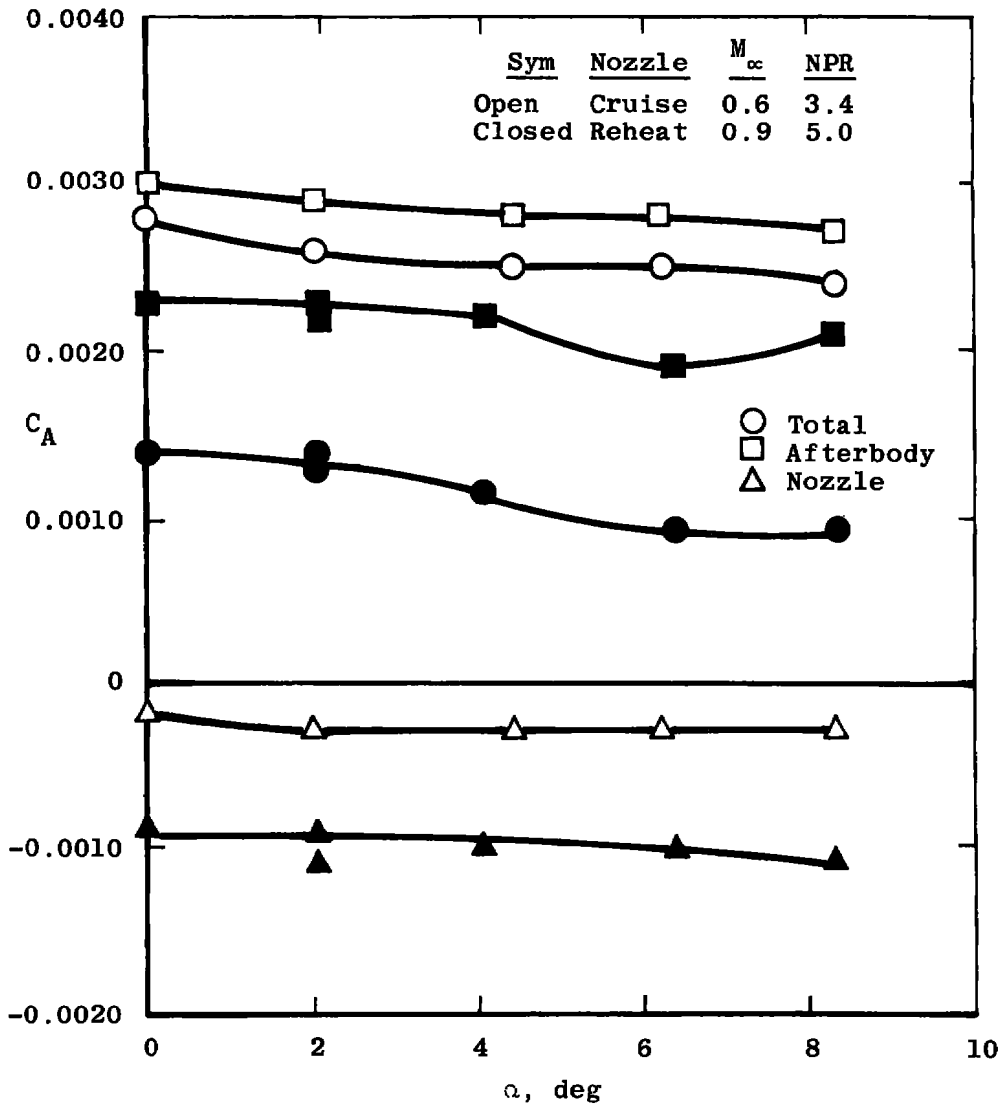

a. Subsonic Mach numbers

Figure 20. Model attitude effect on pressure integrated axial loads, Re = 2.8 x 10^6/ft, δ_H = -2 deg.

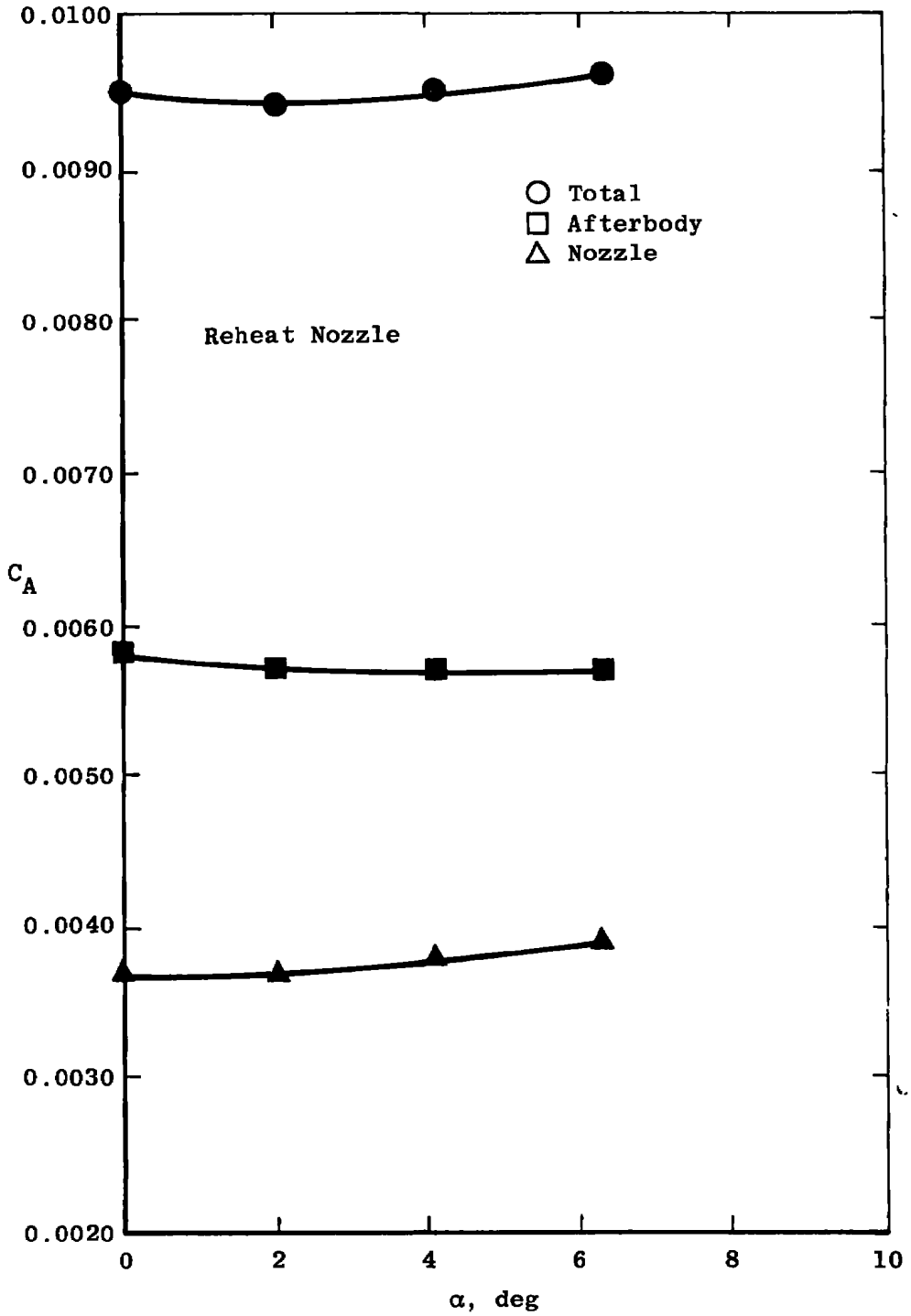

b. M_∞ = 1.2, NPR = 6
Figure 20. Concluded.

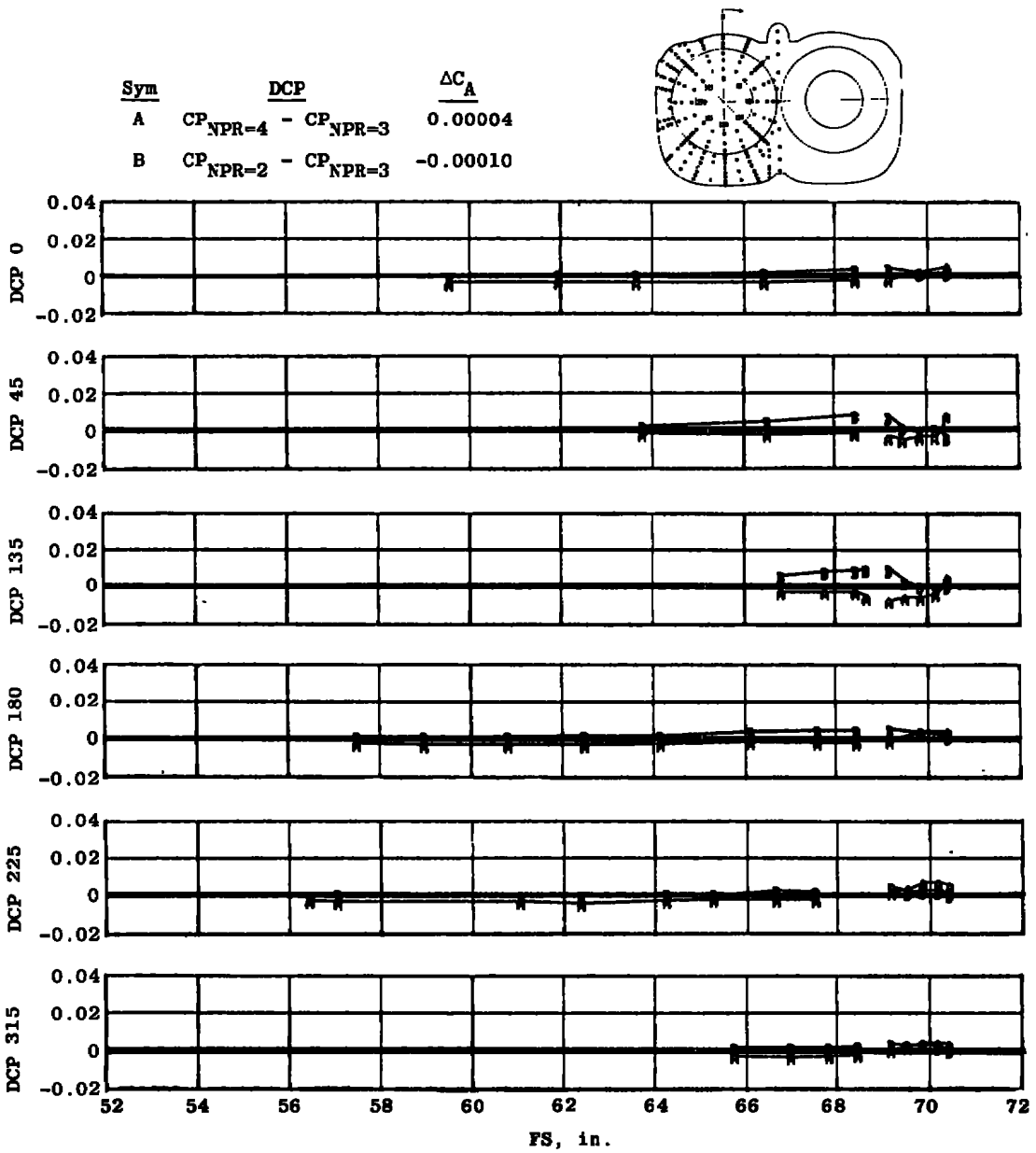

a. Cruise nozzle configuration, $M_\infty = 0.6$

Figure 21. Effect of incremental NPR changes on surface pressure distributions, Re = 2.8 x 10^6/ft, δ_H = -2 deg, and α = 4 deg.

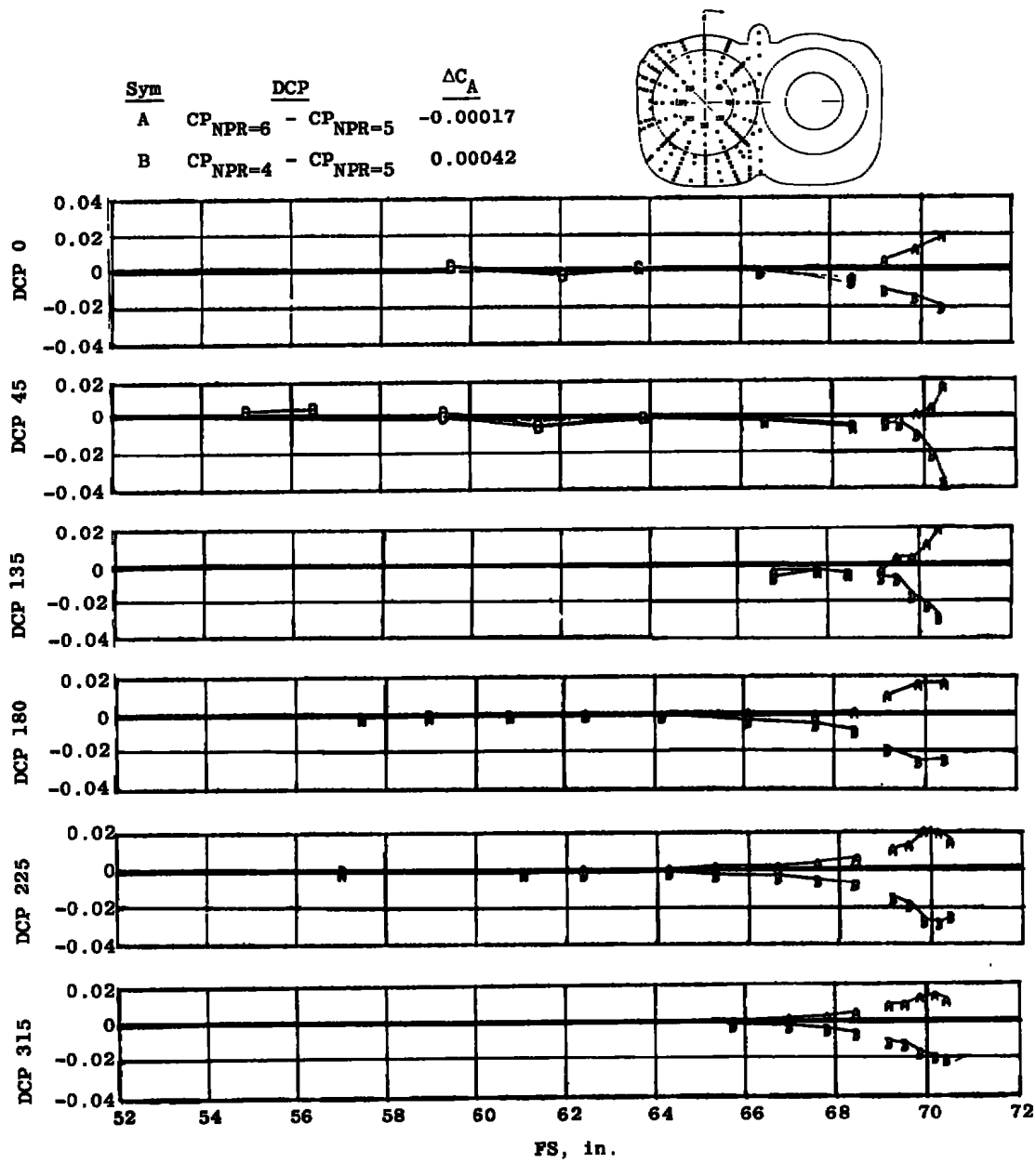

b. Reheat nozzle configuration, M_∞ = 0.9
Figure 21. Continued.

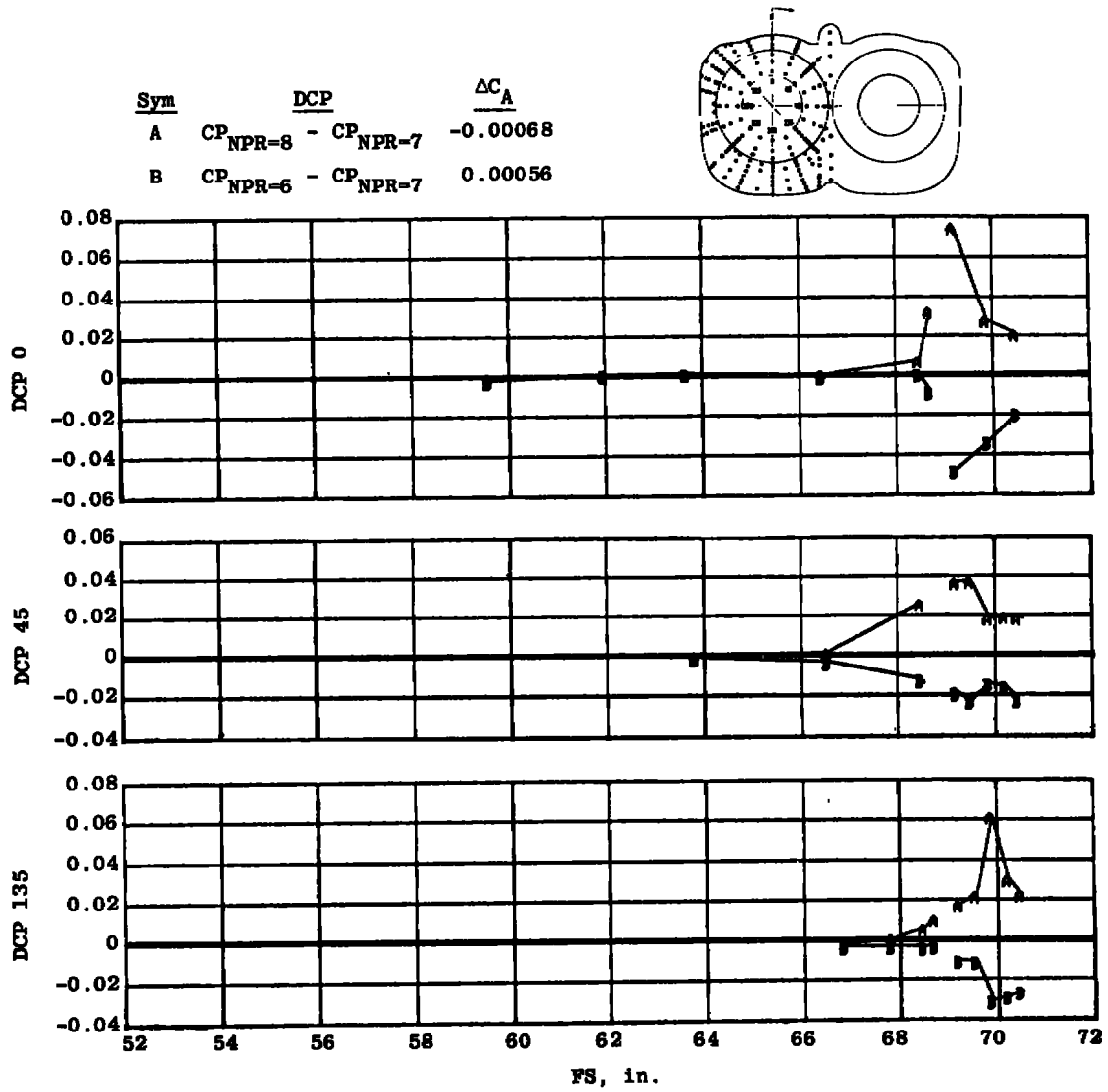

c. Reheat nozzle configuration, M_∞ = 1.2

Figure 21. Continued.

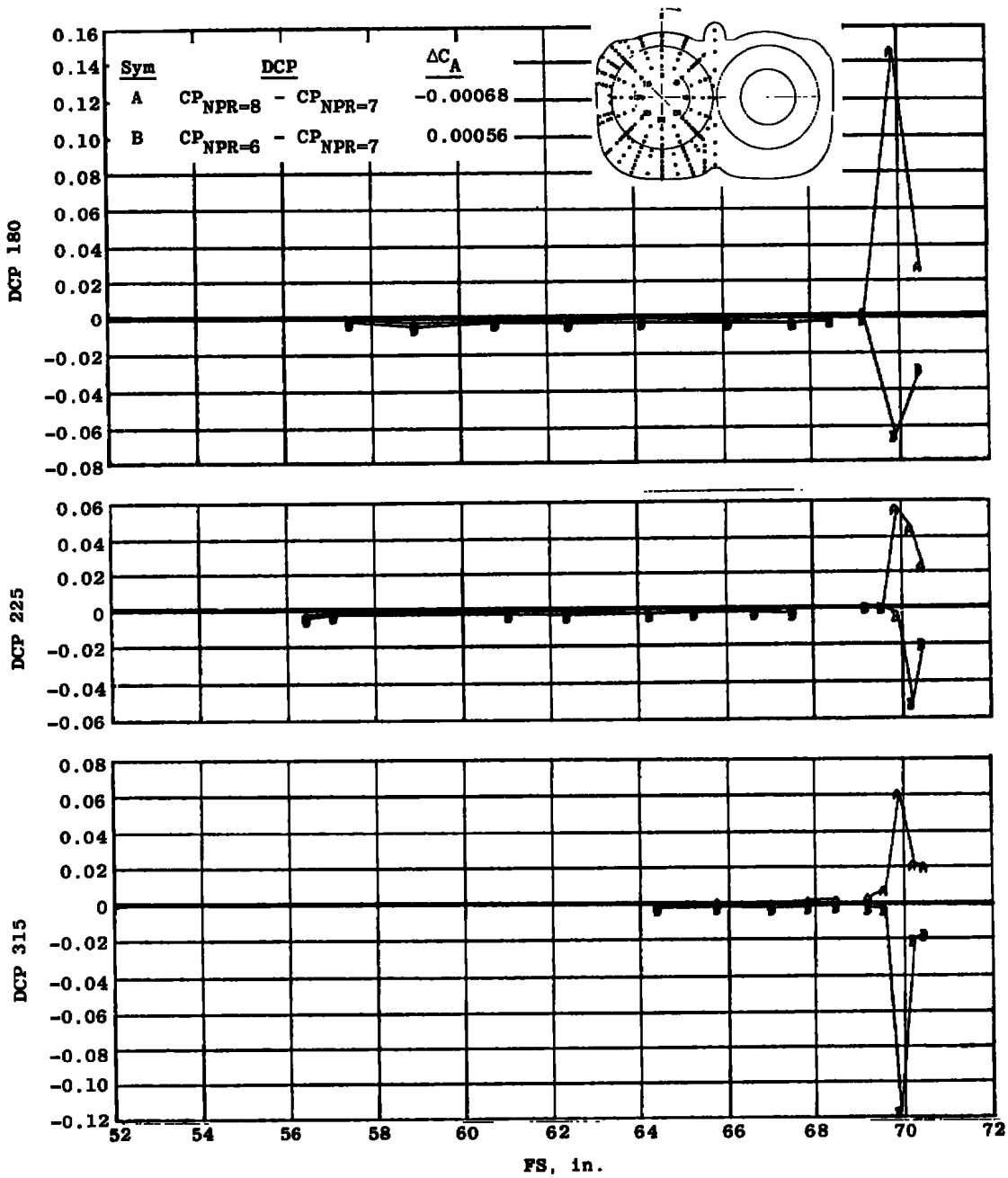

c. Concluded
Figure 21. Continued.

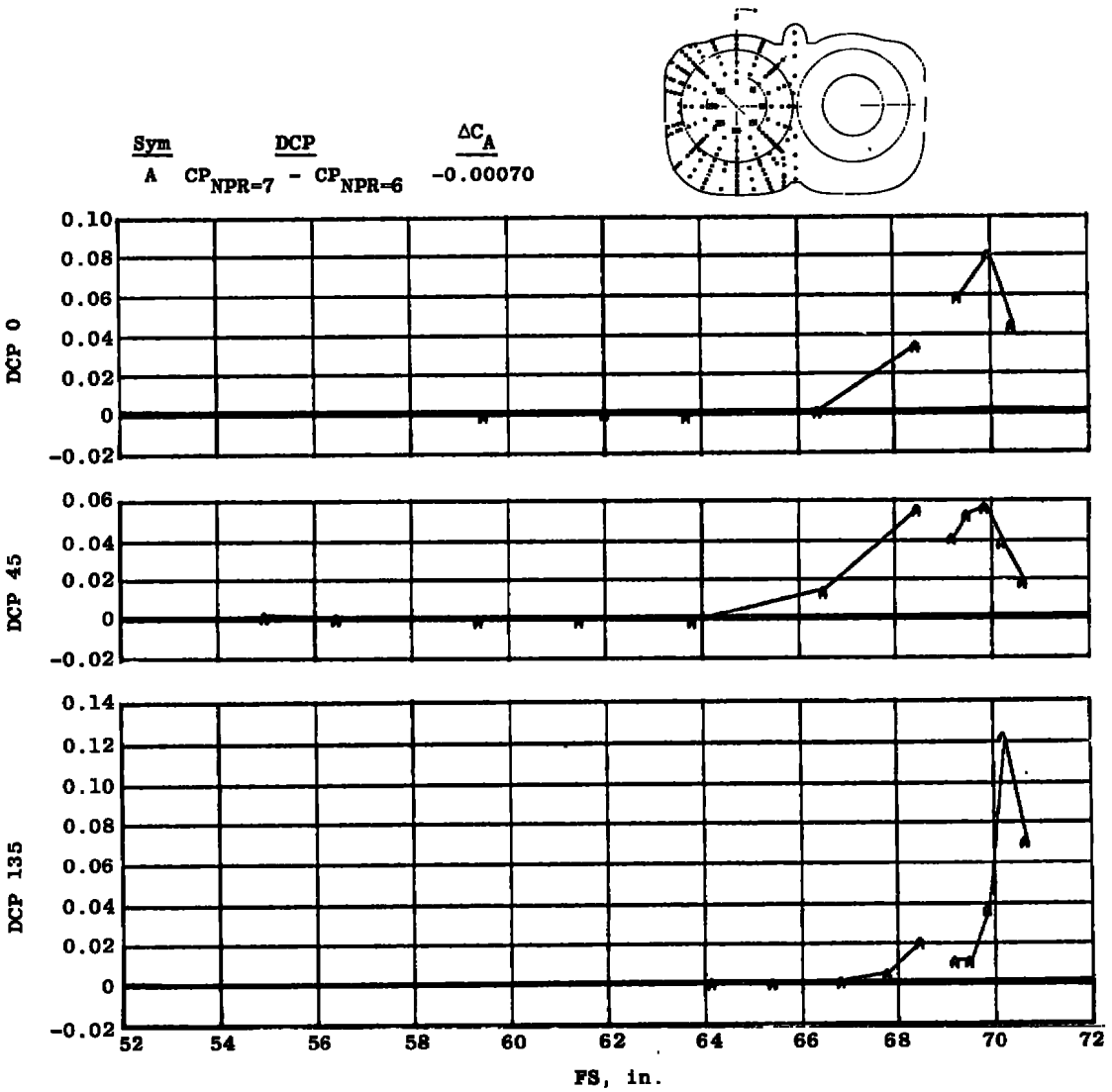

d. Maximum nozzle configuration, M_∞ = 1.2

Figure 21. Continued.

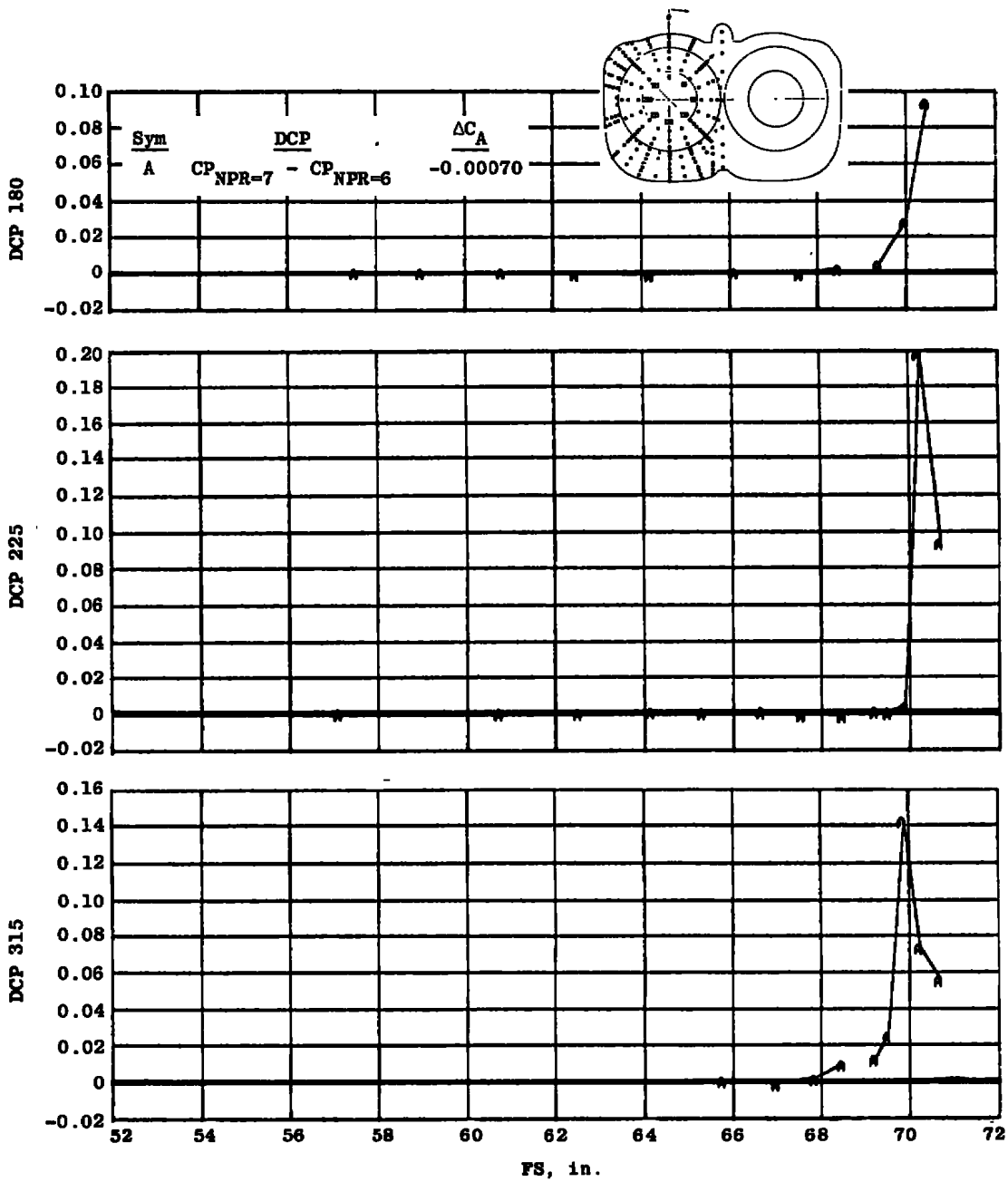

d. Concluded.

Figure 21. Concluded.

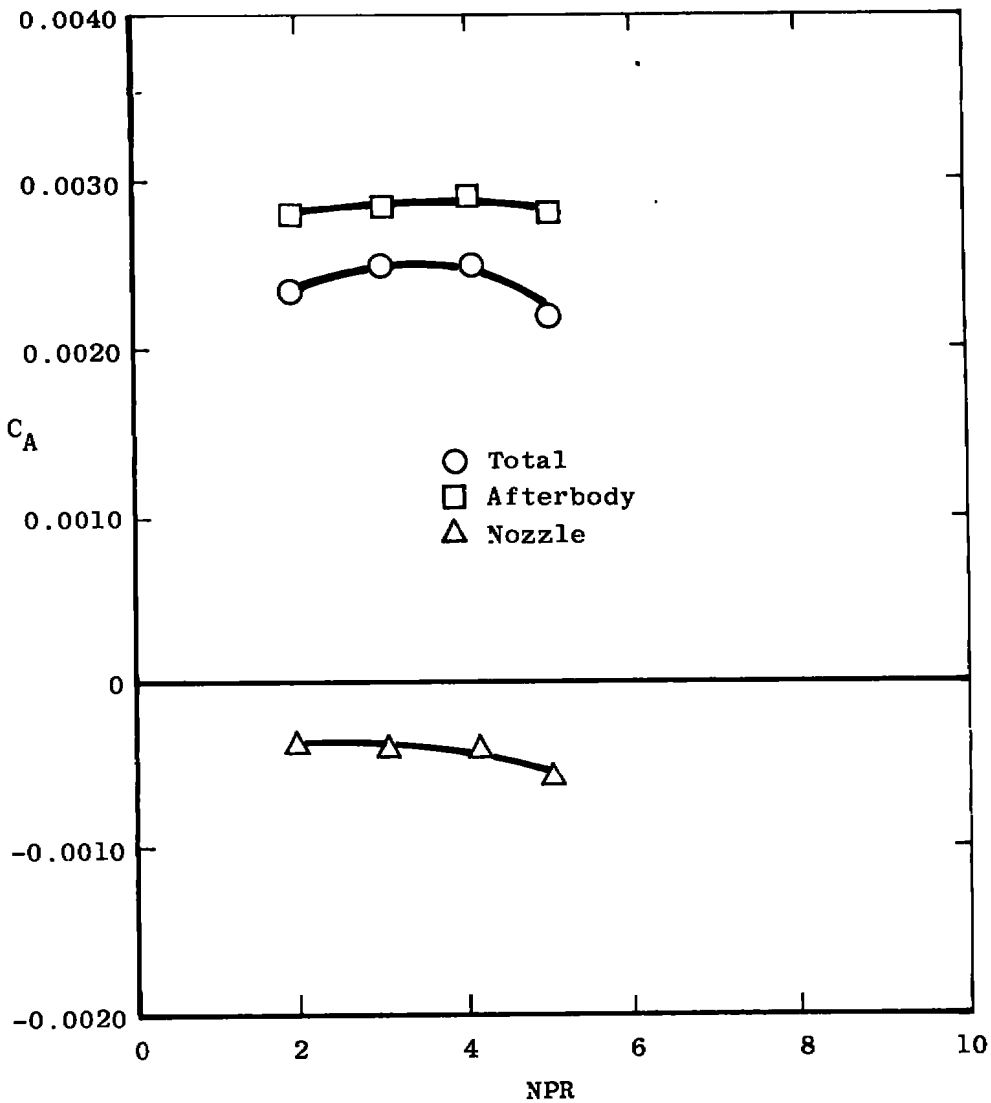

a. Cruise nozzle configuration, M_∞ = 0.6

Figure 22. Nozzle pressure ratio effects on the aft end axial loads, Re = 2.8 x 10^6/ft, δ_H = -2 deg, and α = 4 deg.

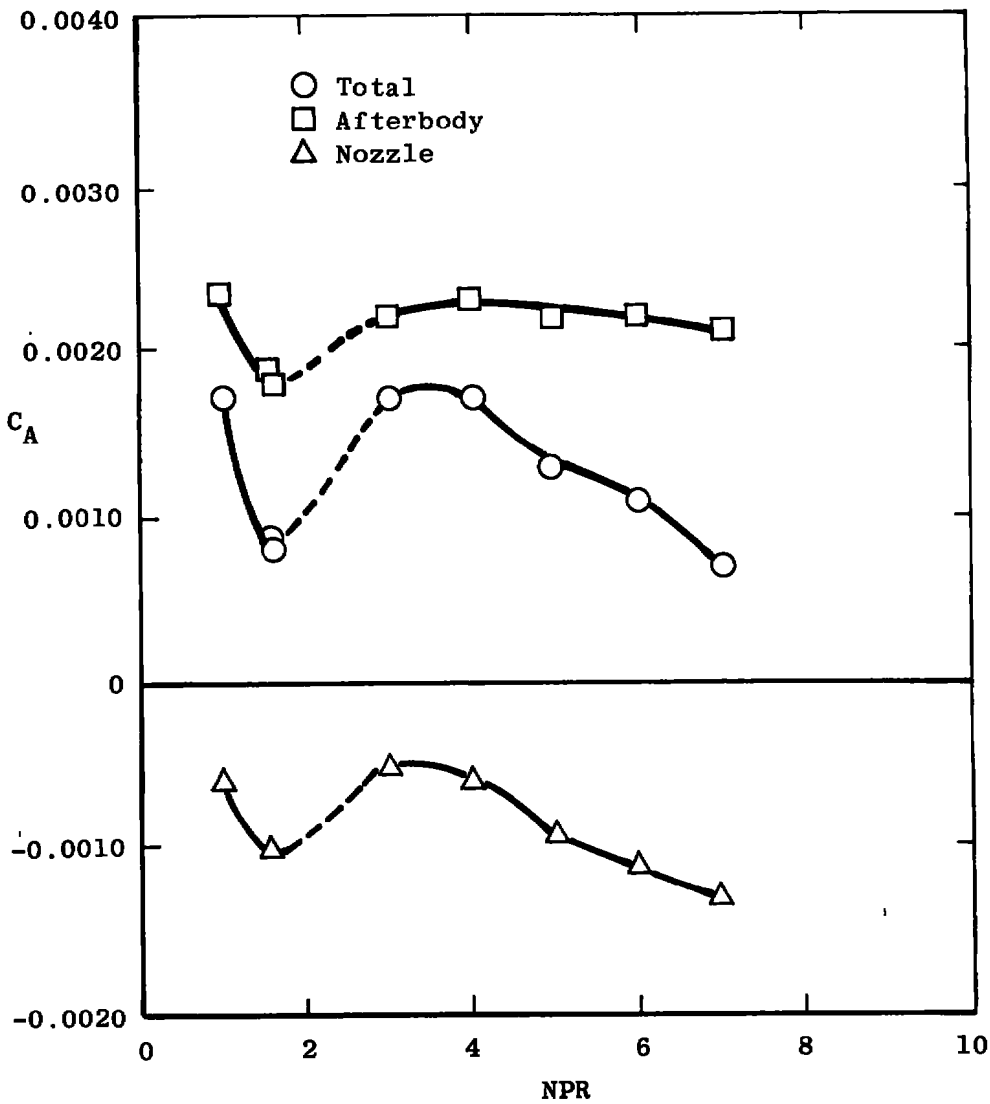

b. Reheat nozzle configuration, M_∞ = 0.9
Figure 22. Continued.

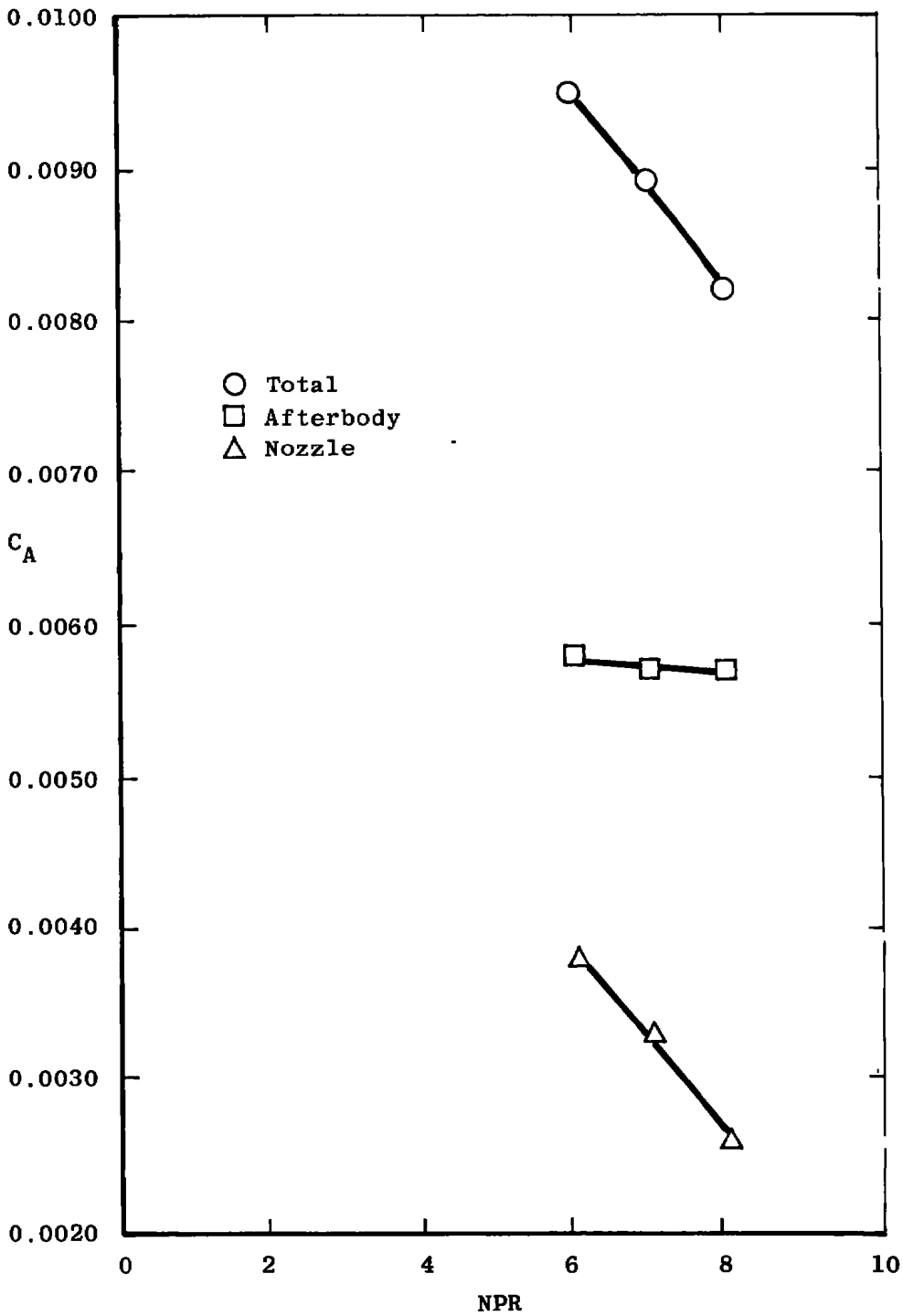

c. Reheat nozzle configuration, M_∞ = 1.2
Figure 22. Continued.

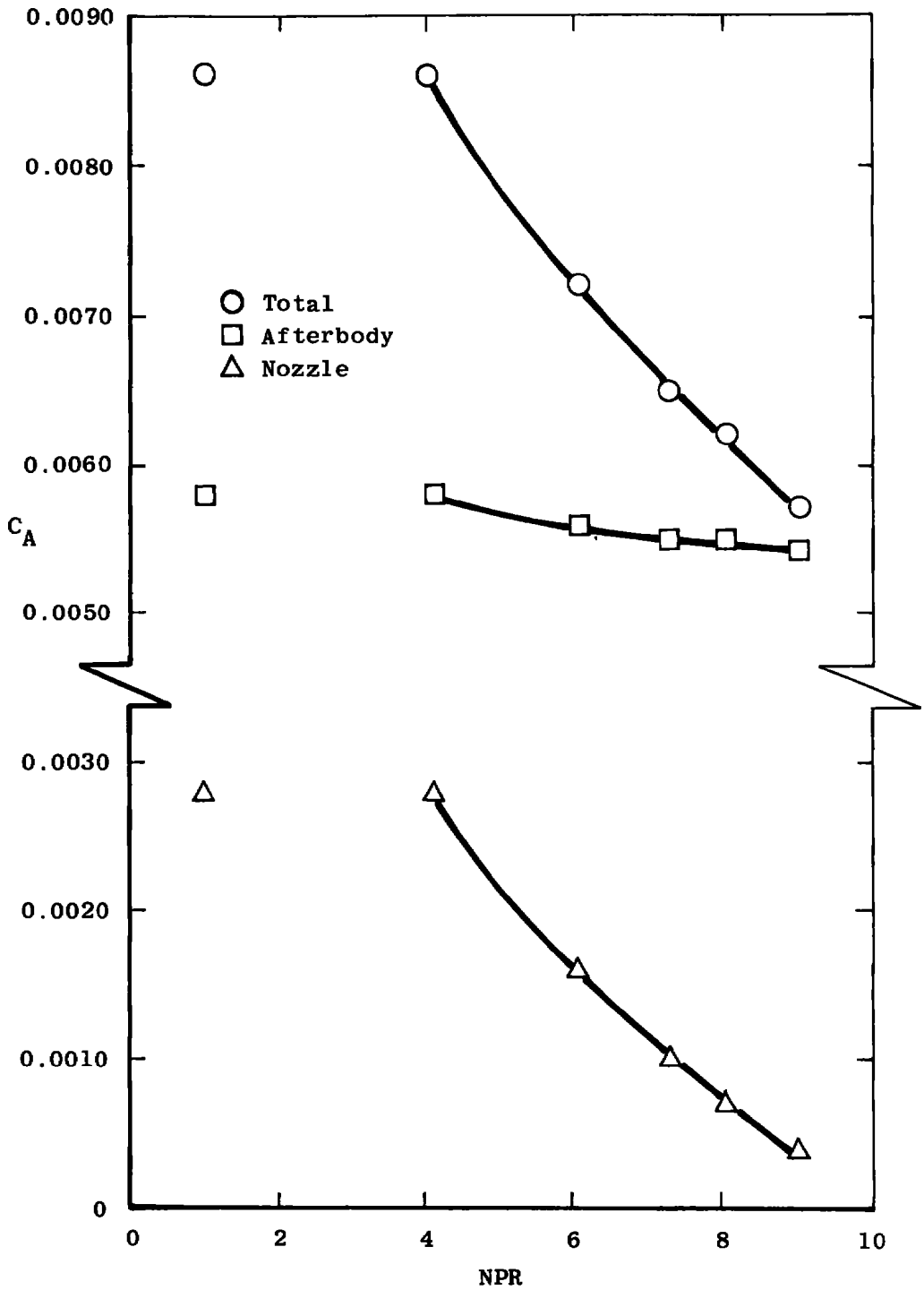

d. Maximum nozzle configuration, $M_\infty = 1.2$
Figure 22. Concluded.

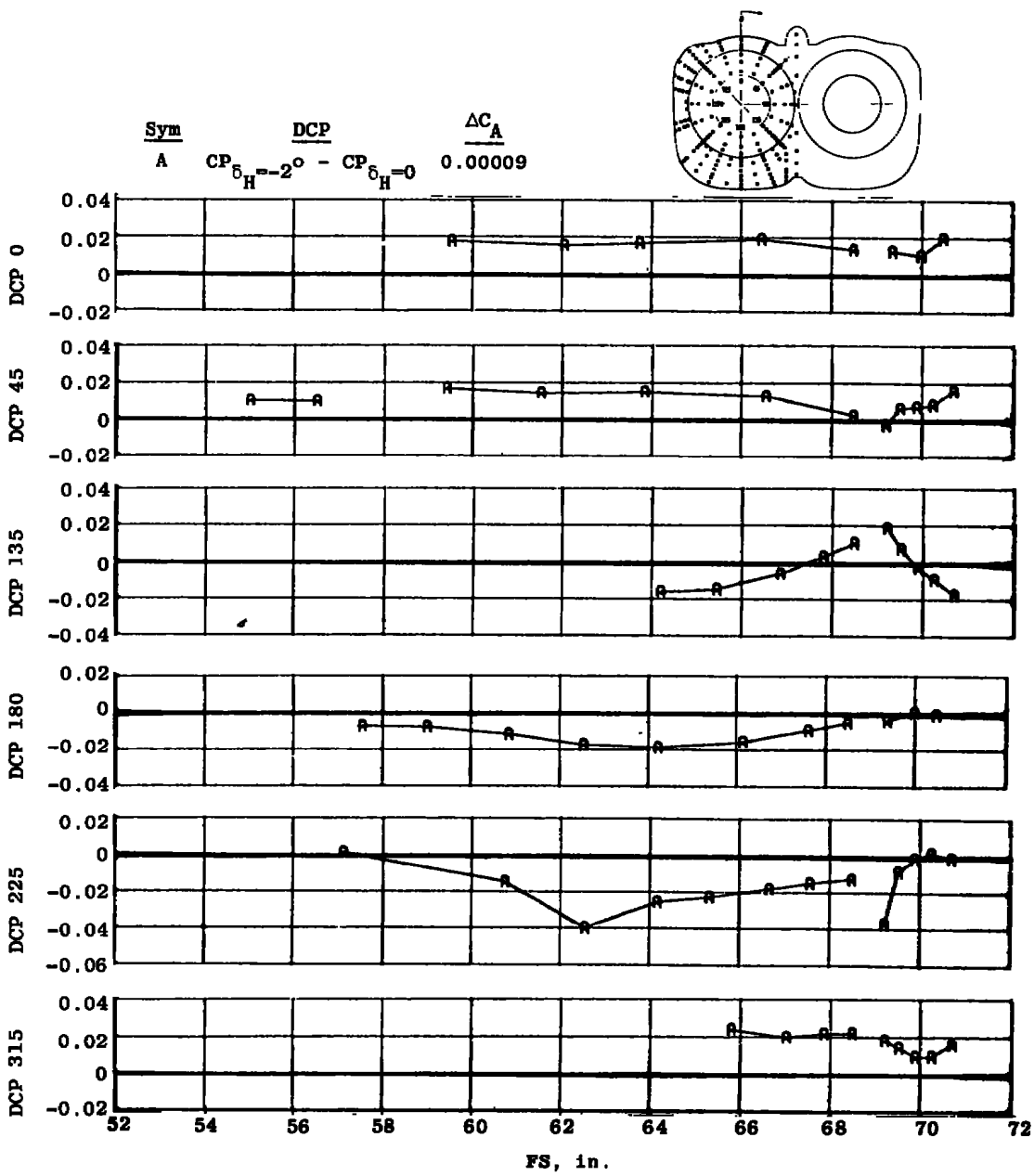

a. Cruise nozzle, M_∞ = 0.6, NPR = 3

Figure 23. Effect of incremental horizontal tail deflections on surface pressure distributions, Re = 2.8 x 10^6/ft, α = 4 deg.

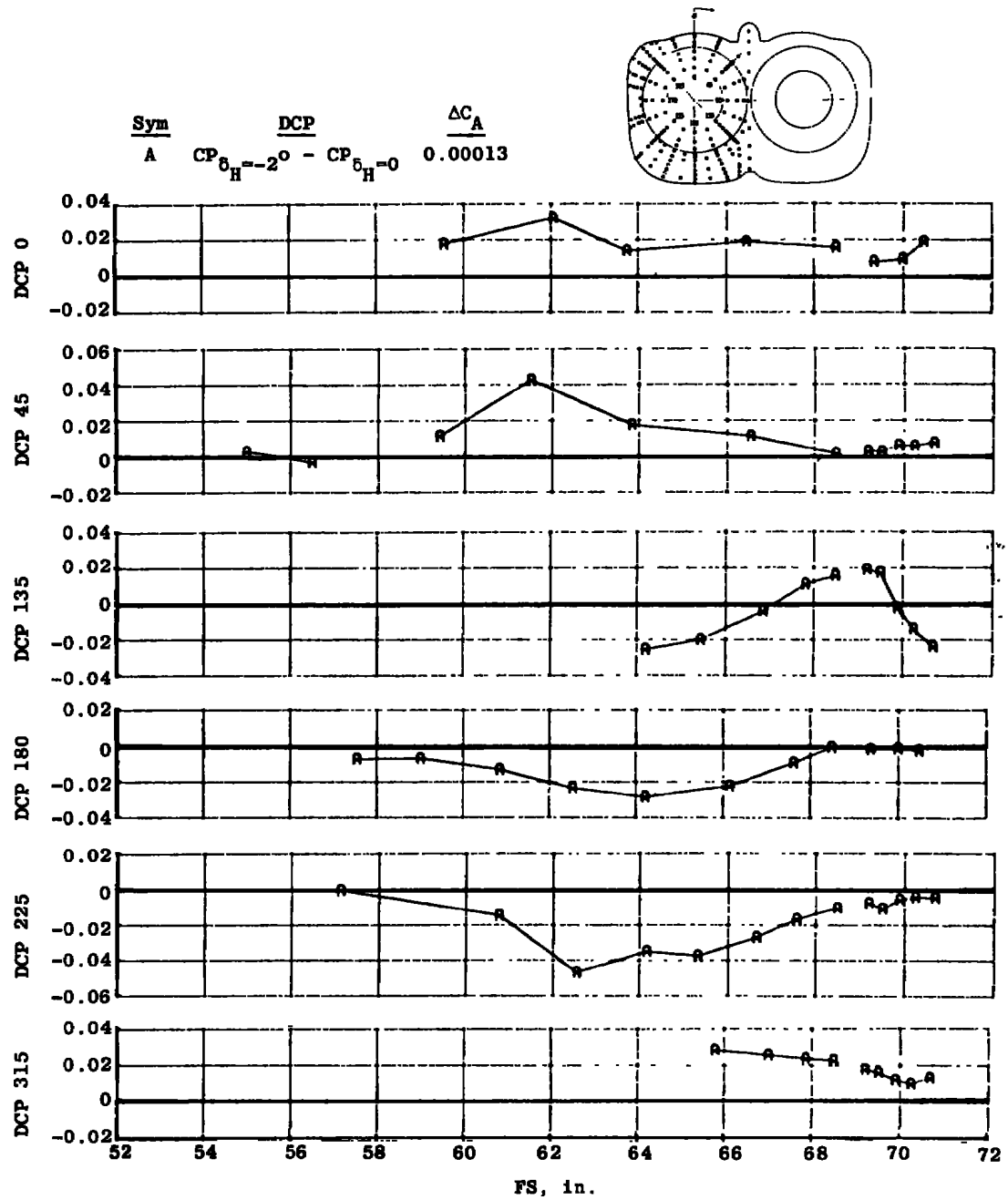

b. Reheat nozzle, M_∞ = 0.9, NPR = 5
Figure 23. Continued.

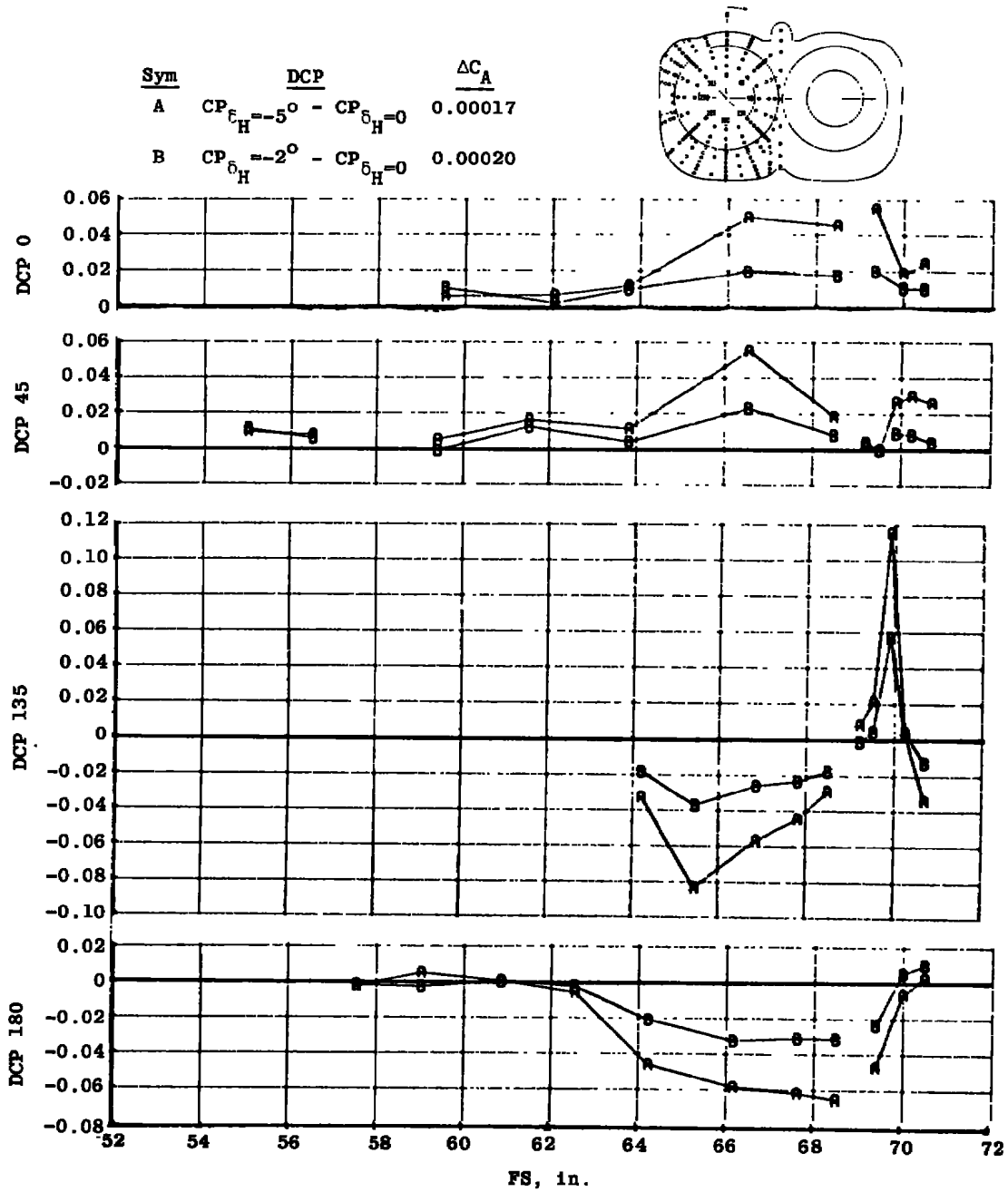

c. Reheat nozzle, M_∞ = 1.2, NPR = 6
Figure 23. Continued.

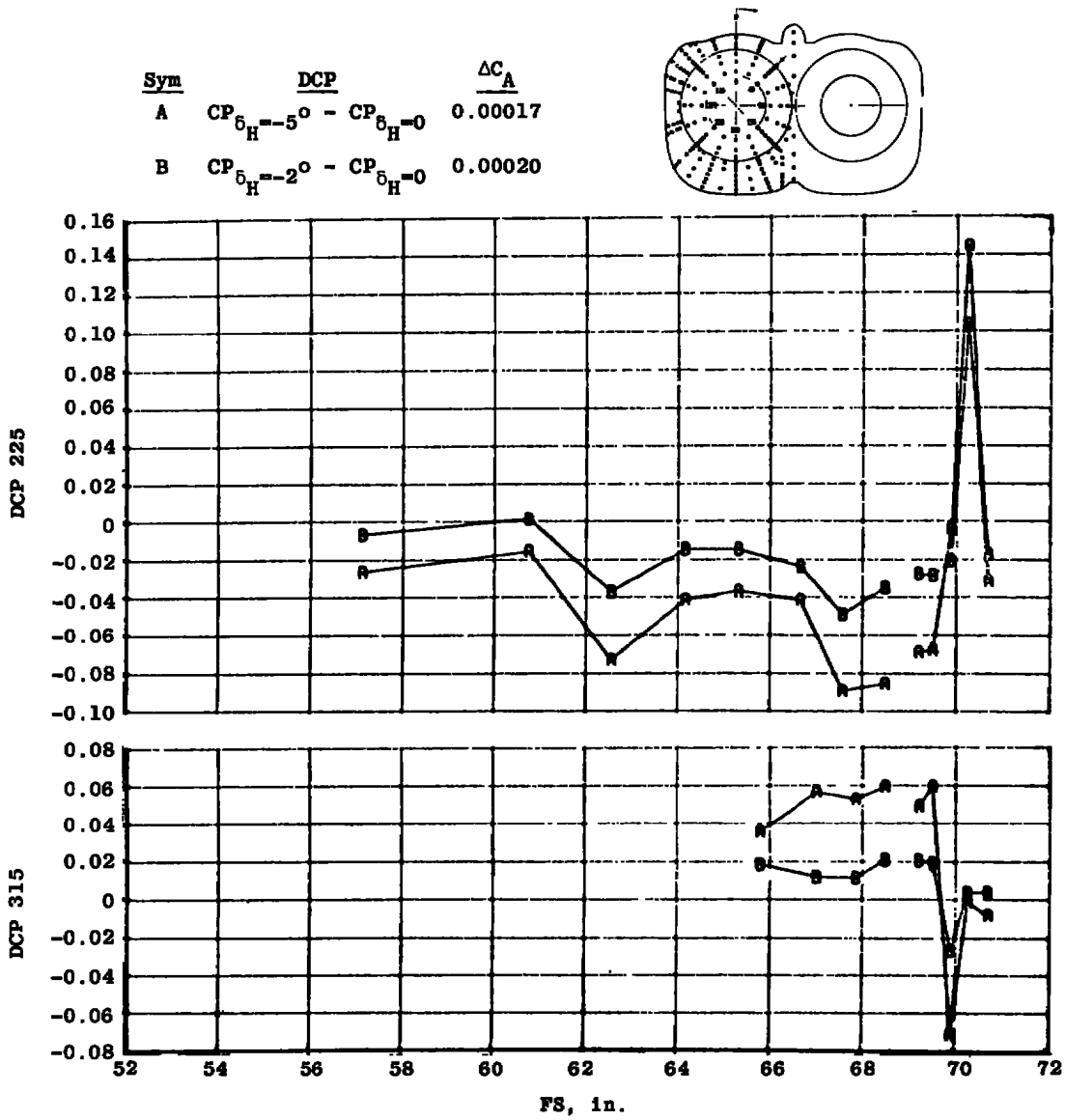

c. Concluded
Figure 23. Concluded.

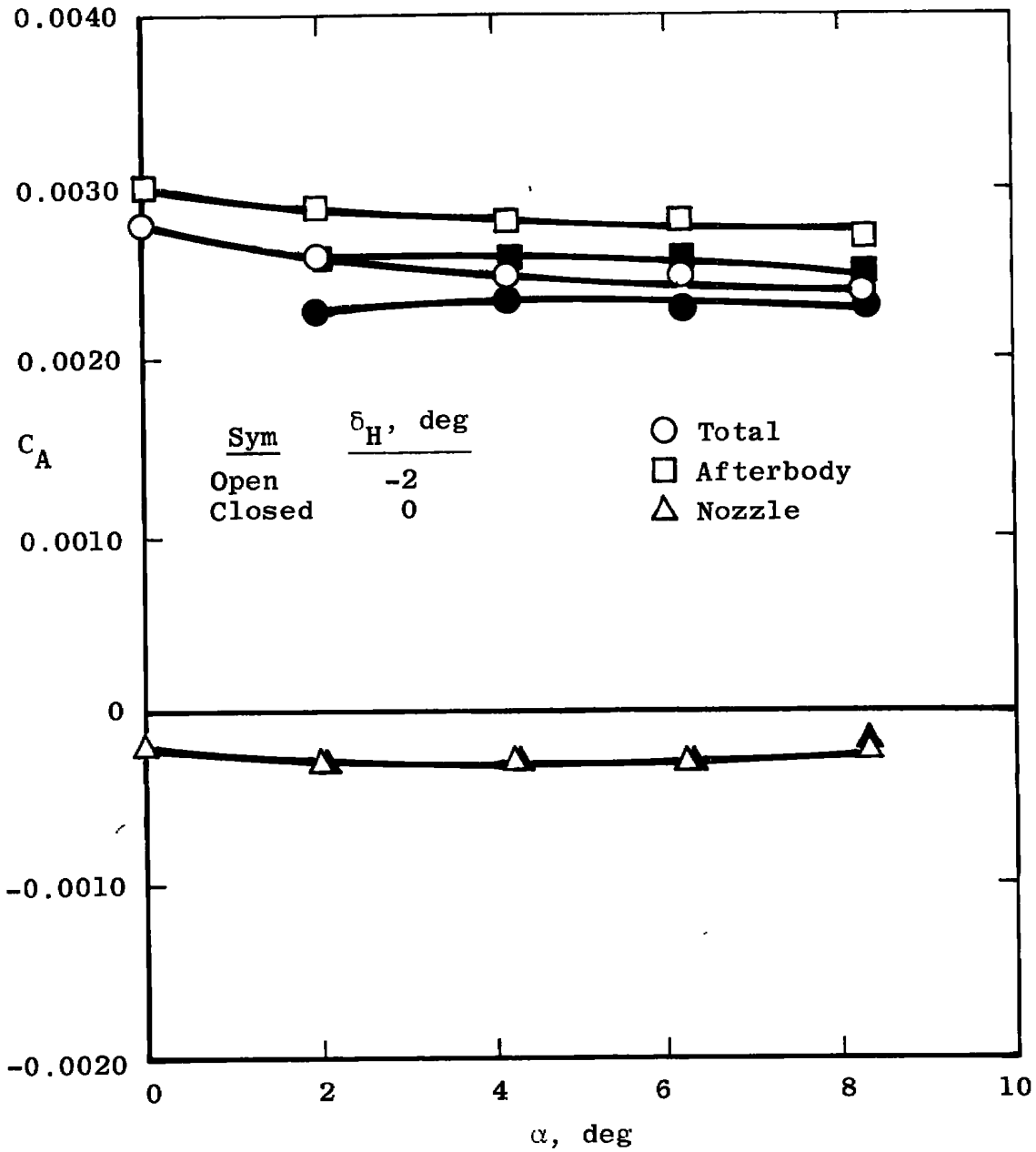

Figure 24. Effects of horizontal tail deflection on the aft end axial loads at M_∞ = 0.6 on the cruise nozzle, NPR = 3.0, and Re = 2.8 x 10^6/ft.

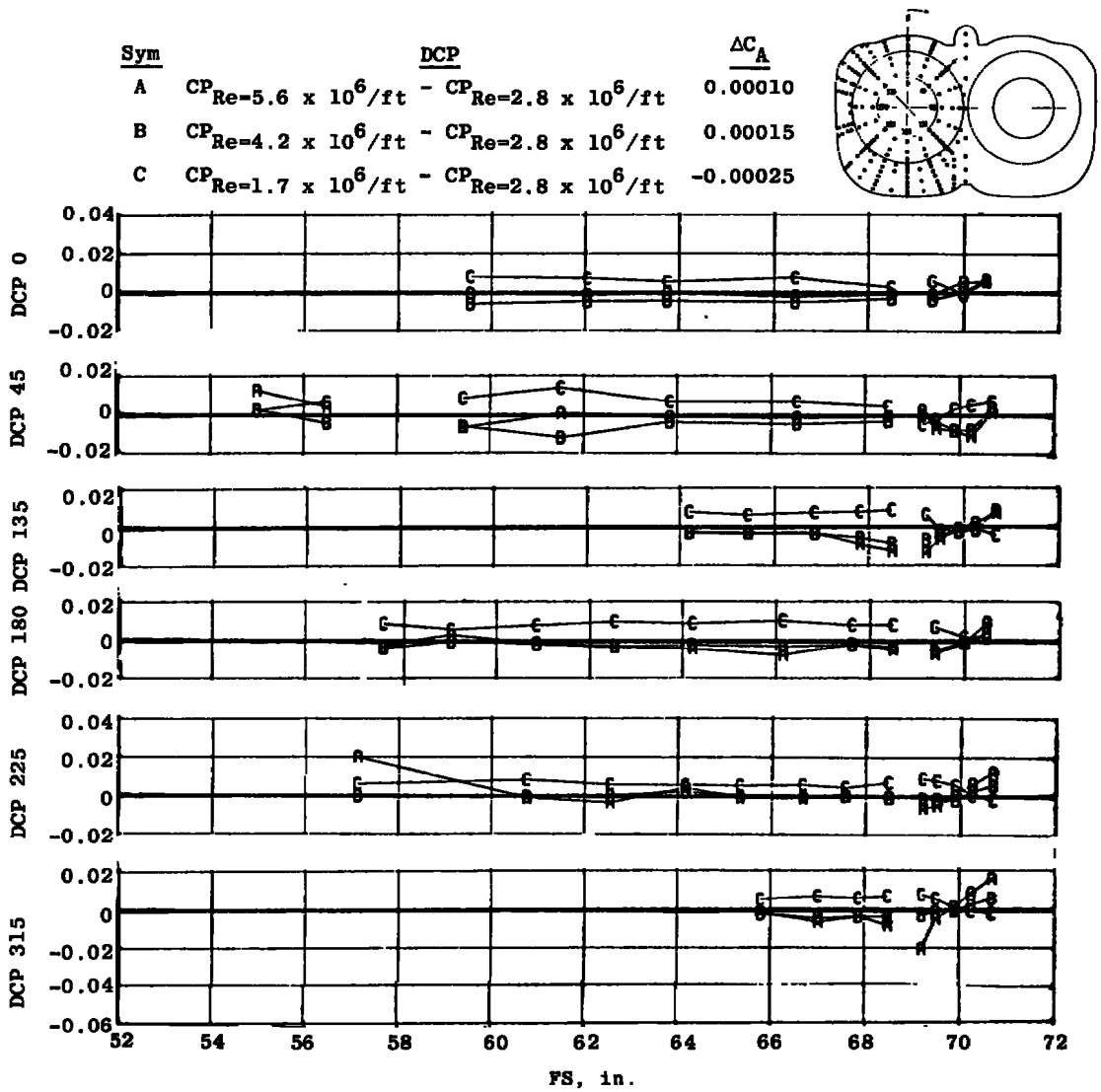

a. Changes in pressure coefficient, $M_\infty = 0.6$, $\delta_H = 0$

Figure 25. Effect of incremental Reynolds number changes on surface pressure distributions, $M_\infty = 0.6$, $\alpha = 4$ deg, $\delta_H = 0$, and NPR = 3 for the nozzle.

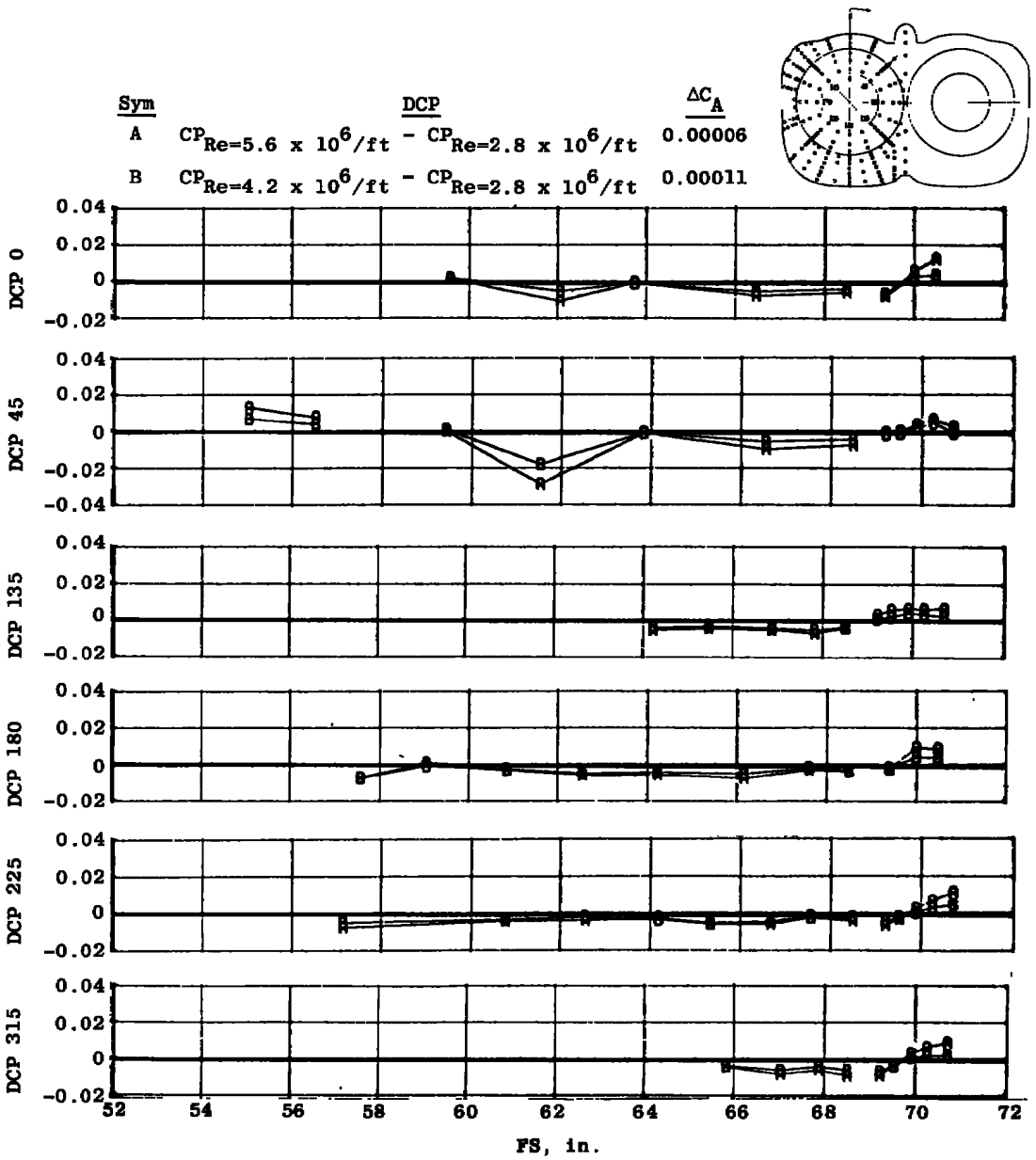

b. Changes in pressure coefficient at $M_\infty = 0.9$, $\delta_H = 0$
Figure 25. Continued.

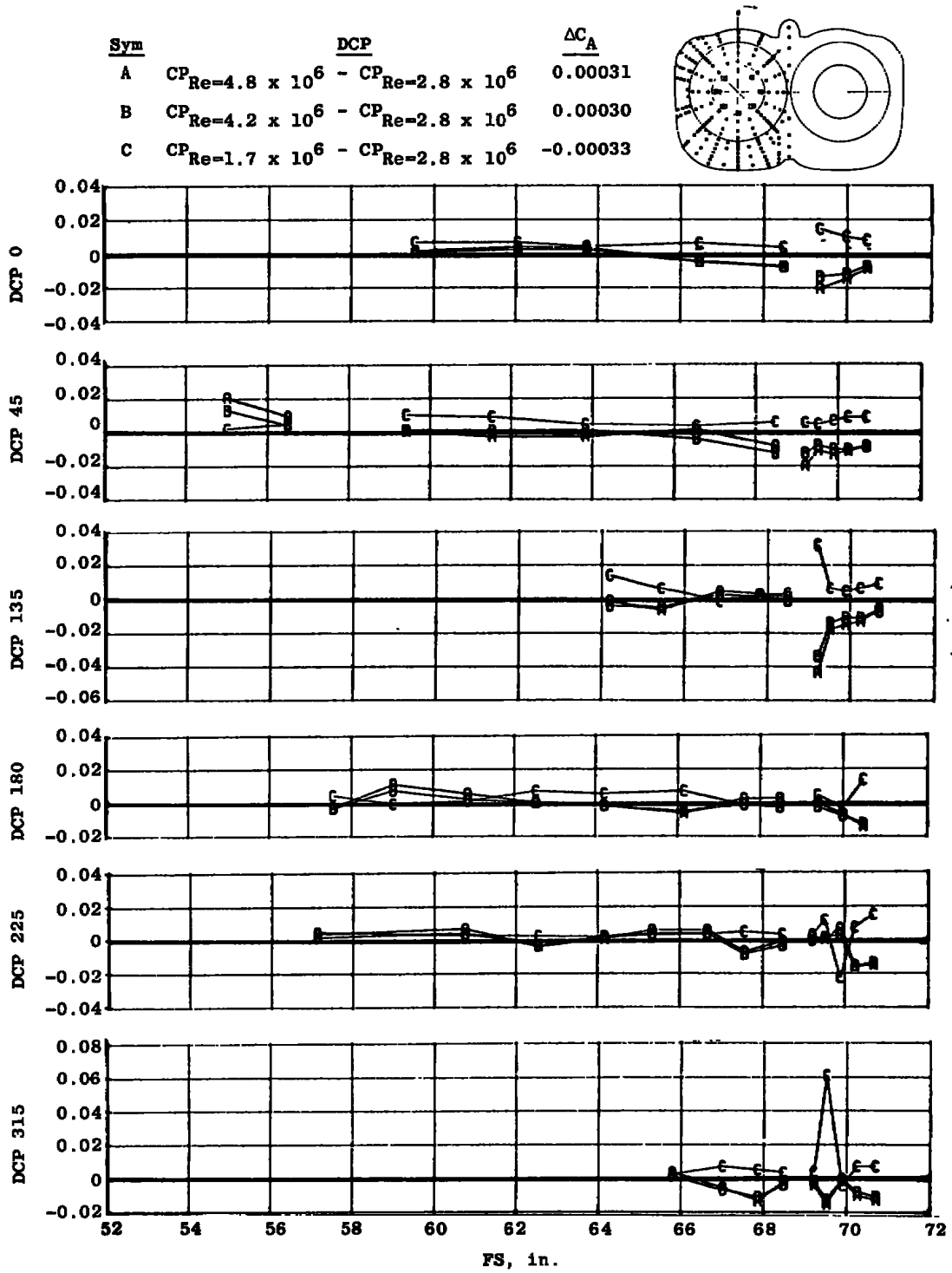

c. Changes in pressure coefficient at M_∞ = 1.2, δ_H = -2 deg
Figure 25. Continued.

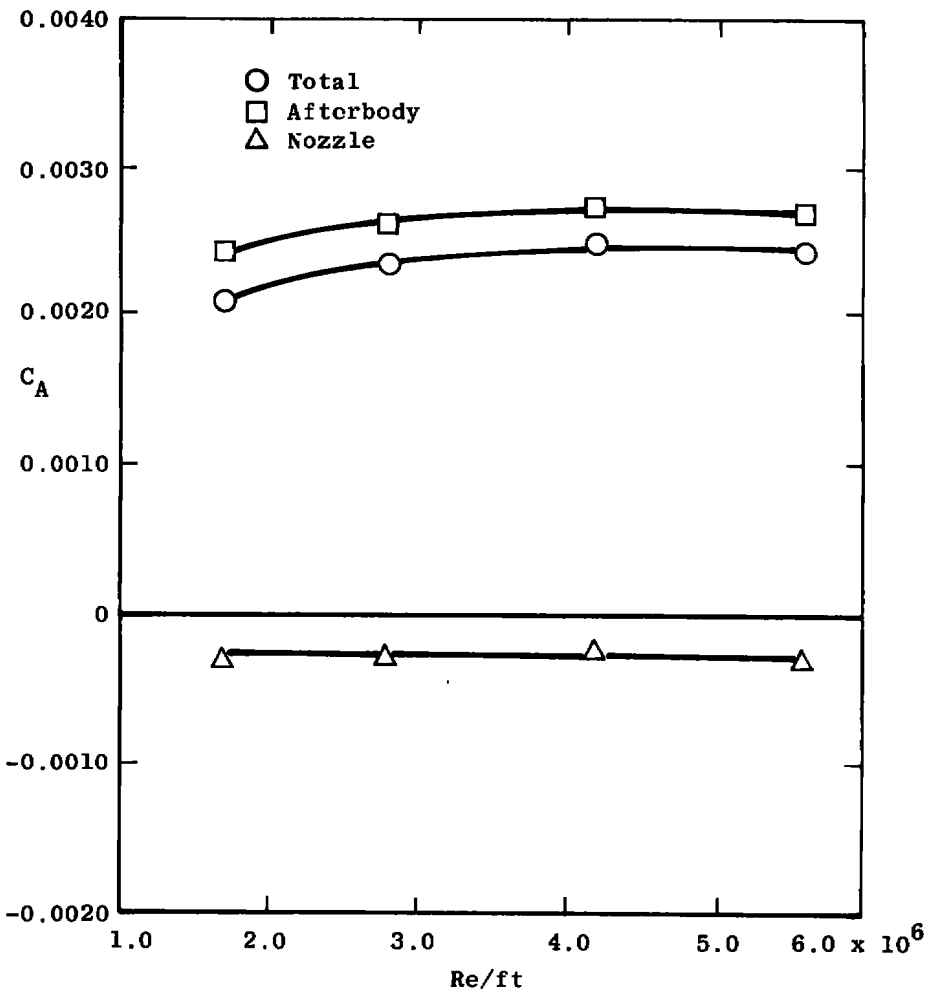

d. Aft end axial loads, M_∞ = 0.6
Figure 25. Continued.

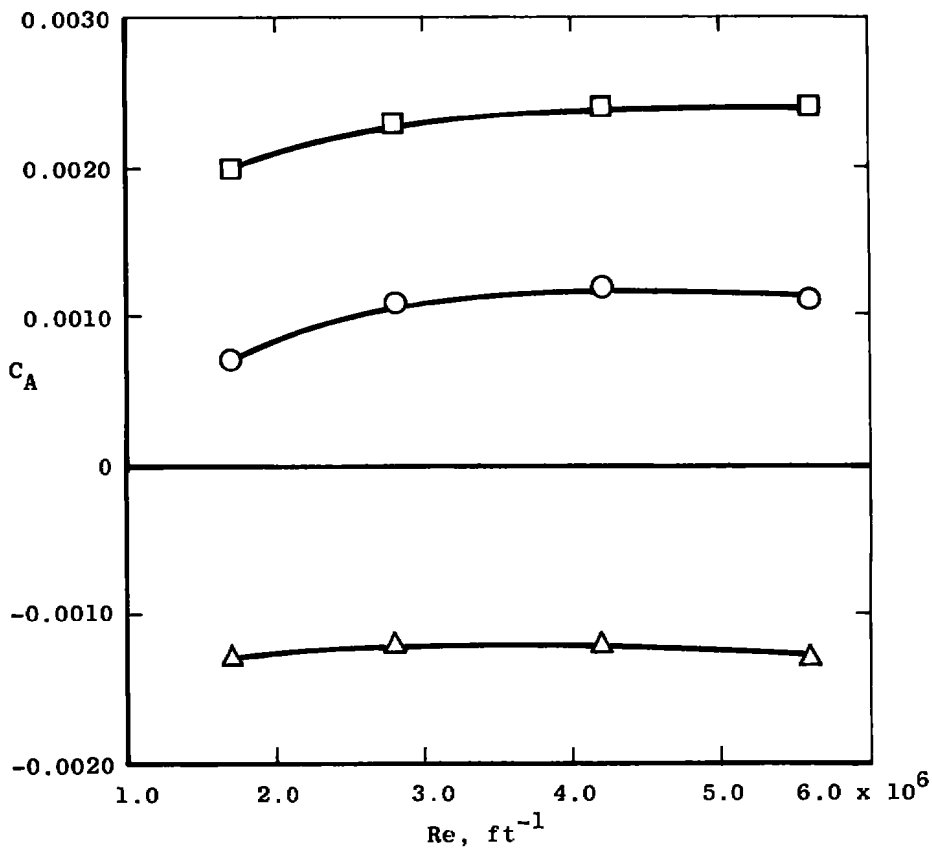

e. Aft end axial loads, M_∞ = 0.9
Figure 25. Continued.

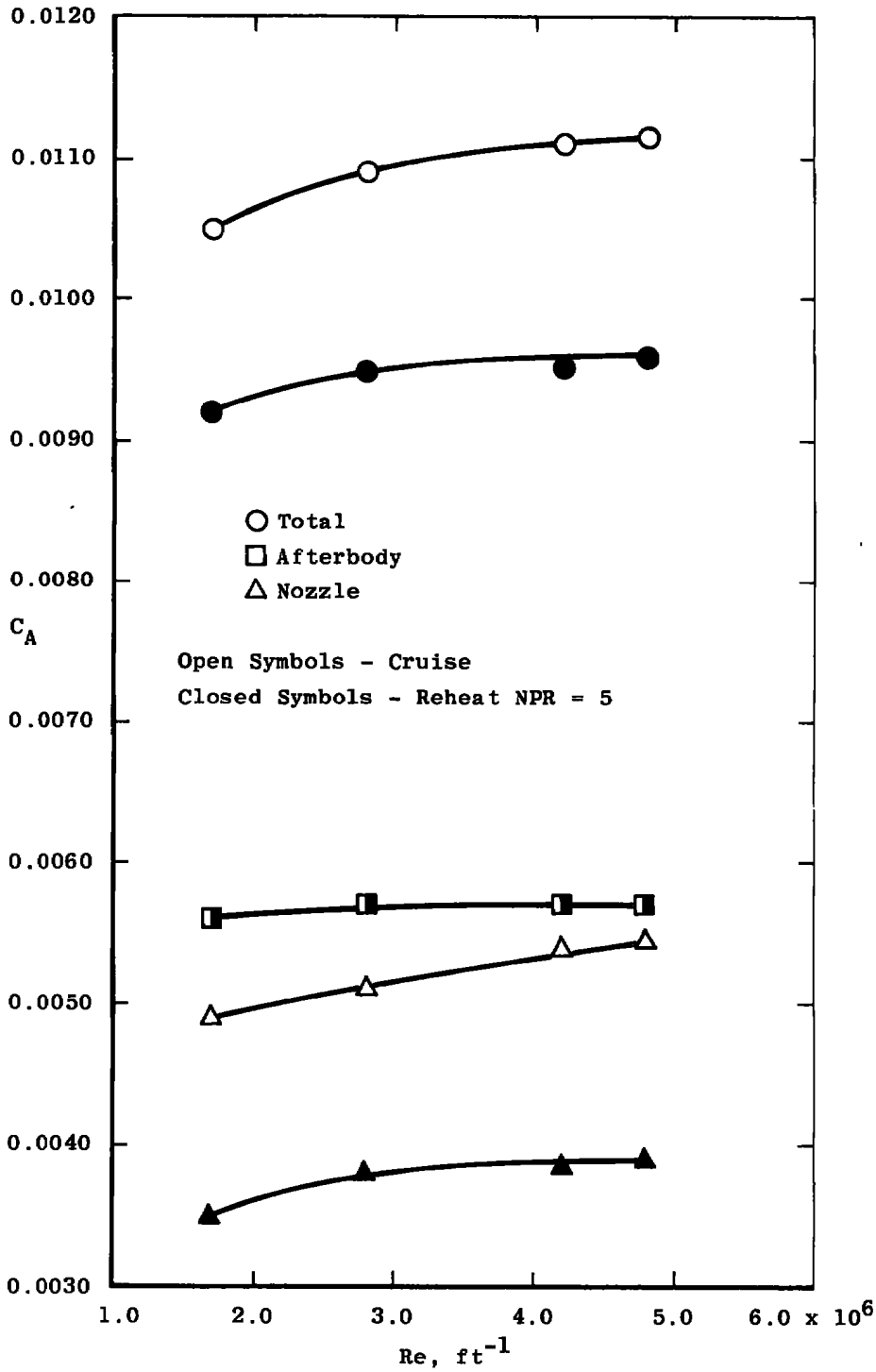

f. Supersonic aft end axial loads
Figure 25. Concluded.

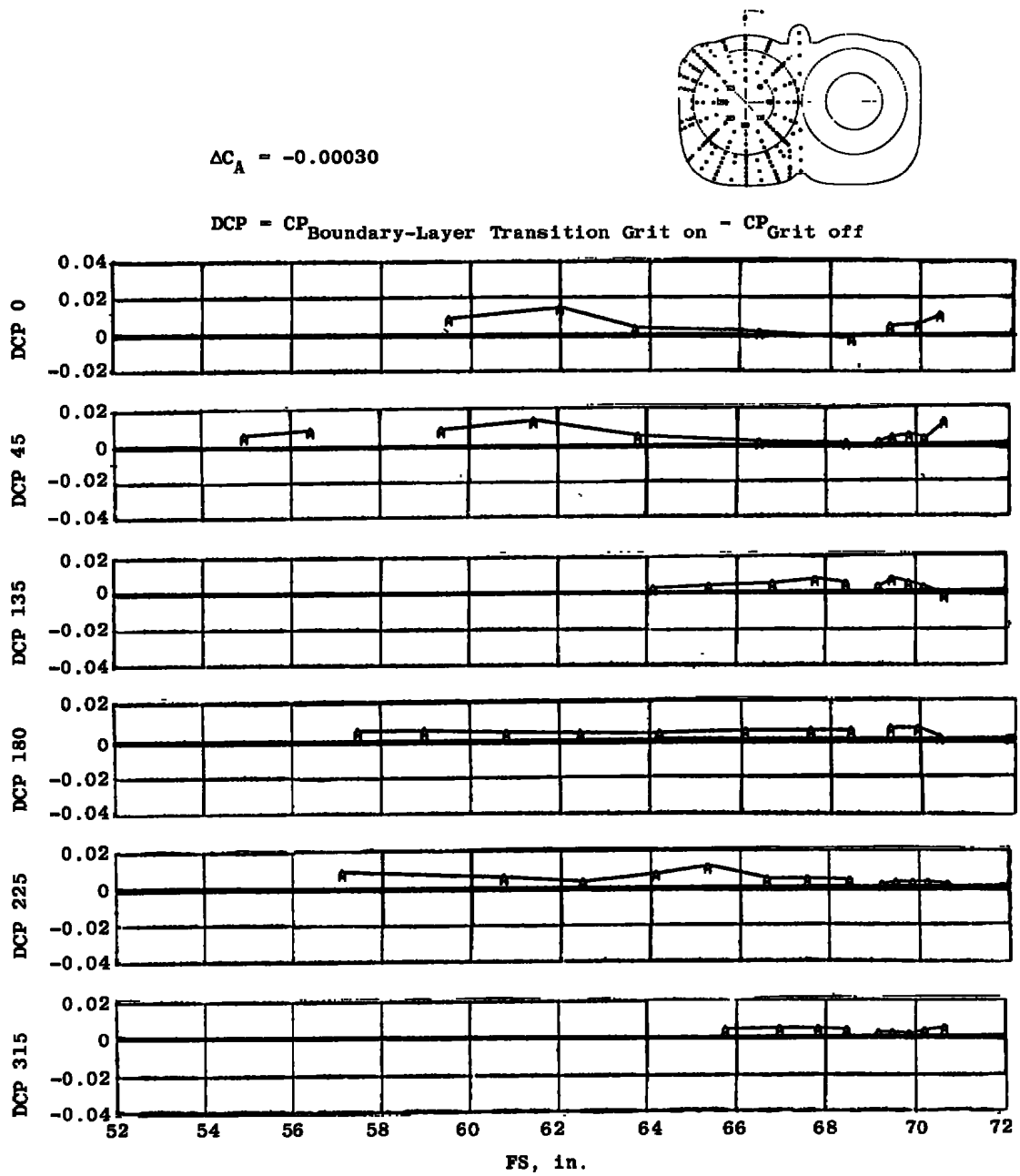

a. Changes in pressure coefficient at Re = 2.8 x 10^6/ft

Figure 26. Boundary-layer transition grit effects on the reheat nozzle, M_∞ = 0.9, α = 4 deg, δ_H = -2 deg, and NPR = 4.

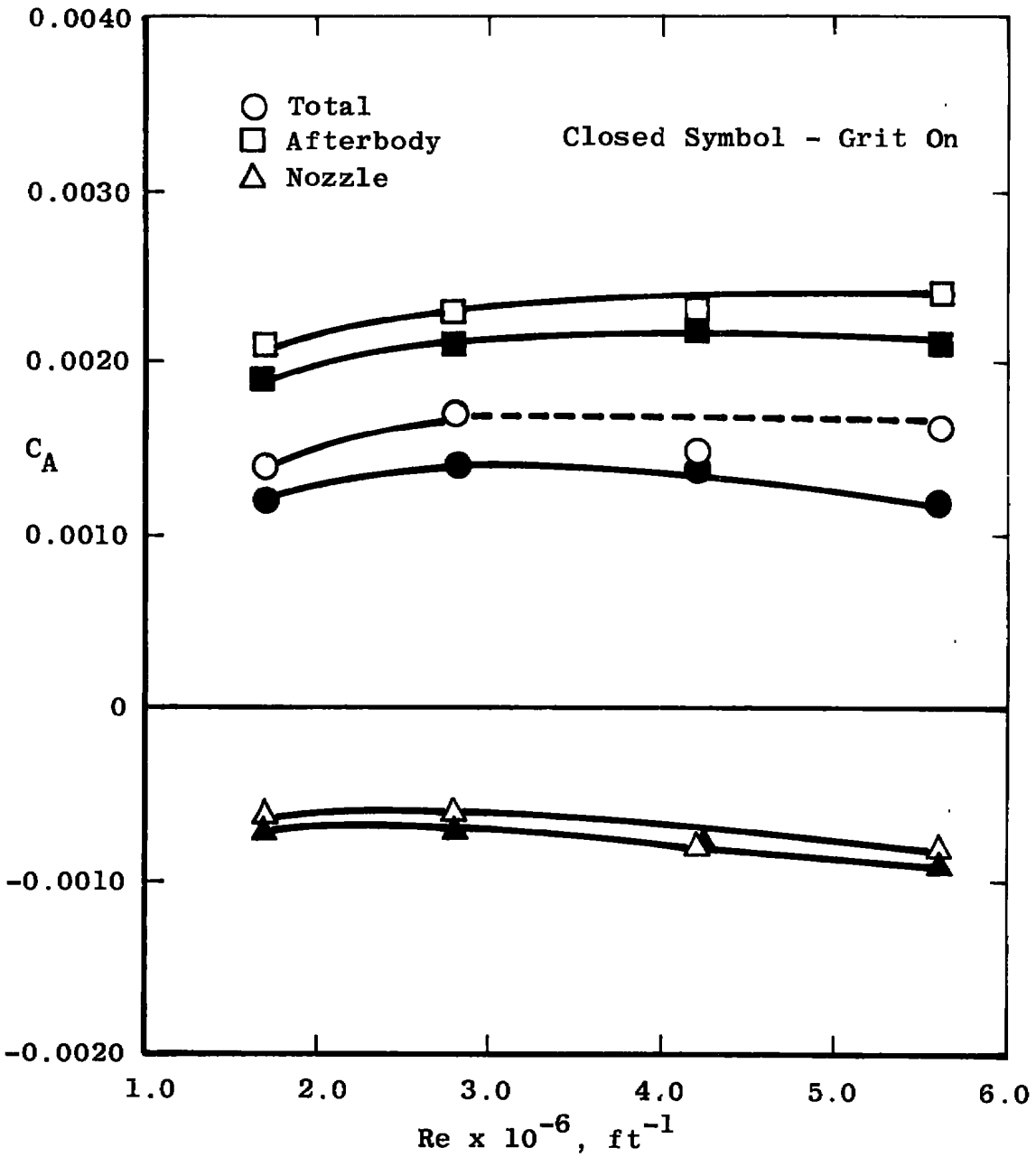

b. Aft end axial loads
Figure 26. Concluded.

Table 1. Afterbody Pressure Instrumentation Location

Pressure Orifice No.	FS, in.	Row Location (see Fig. 6) ϕ, deg	Y, in.	Z, in.	Axial Projected Area, $in.^2$
221	68.9	90.0	---	---	0.0335
222	68.5	77.0	0	---	0.0335
223	68.5	67.5	---	---	0.0804
224	66.8	---	0	0.894	0.0570
225	63.4	---	0	1.465	0.1005
226	61.2	---	0	1.867	0.0670
227	59.0	---	0	2.197	0.1307
228	59.4	---	0.36	1.810	0.0871
229	61.5	---	0.36	1.613	0.0660
230	63.8	45.0	---	---	0.1096
231	66.5	45.0	---	---	0.0815
232	68.5	45.0	---	---	0.0726
233	68.0	22.5	---	---	0.0982
234	66.1	22.5	---	---	0.0656
235	63.8	22.5	---	---	0.0655
236	62.0	22.5	---	---	0.0659
237	60.1	22.5	---	---	0.0938
238	59.5	0	---	---	0.0804
239	62.0	0	---	---	0.0622
240	63.7	0	---	---	0.0711
241	66.4	0	---	---	0.0769
242	68.5	0	---	---	0.0685
302	67.9	340.0	---	---	0.0803
303	65.9	340.0	2.4	---	0.0656
304	63.6	340.0	---	---	0.0678
305	59.6	340.0	---	---	0.0754
306	59.6	---	3.15	---	-0.0366
307	64.0	326.2	---	---	0.0804
308	66.2	326.2	---	---	0.0732
309	68.1	326.2	---	---	0.0732
310	68.5	315.0	---	---	0.0361
311	67.8	315.0	---	---	0.0405
312	67.0	315.0	---	---	0.0545
313	65.8	315.0	---	---	0.0657
314	64.4	315.0	---	---	0.0603
315	58.8	326.2	---	---	-0.0366
316	58.9	303.8	---	---	0.0335
317	64.1	303.8	---	---	0.0658
318	66.0	303.8	---	---	0.0660
319	67.2	303.8	---	---	0.0548
320	---	---	---	---	---
321	68.5	303.8	---	---	0.0363

Table 1. Continued

Pressure Orifice No.	FS. in.	Row Location (see Fig. 6) ϕ, deg	Y, in.	Z, in.	Axial Projected Area, $in.^2$
322	68.5	292.5	---	---	0.0351
323	68.1	292.5	---	---	0.0395
324	65.8	292.5	---	---	0.0531
325	63.2	292.5	---	---	0.0640
326	58.2	292.5	---	---	0.0603
327	60.5	282.0	---	---	0.1005
328	63.7	282.0	---	---	0.0670
329	66.6	282.0	---	---	0.0536
330	68.5	282.0	---	---	0.0402
331	68.5	272.0	---	---	0.0268
332	68.5	264.0	---	---	0.0302
333	68.5	252.8	---	---	0.0402
334	66.7	252.8	---	---	0.0469
335	64.6	252.8	---	---	0.0636
336	58.8	252.8	---	---	0.1072
337	57.4	247.5	---	---	0.0402
338	62.7	247.5	---	---	0.0487
339	65.9	247.5	---	---	0.0486
340	67.8	247.5	---	---	0.0486
341	66.4	236.2	---	---	0.1646
342	62.4	236.2	---	---	0.1675
402	57.1	225.0	---	---	0.0469
403	60.7	225.0	---	---	0.0737
404	62.5	225.0	---	---	0.0654
405	64.1	225.0	---	---	0.0655
406	65.3	225.0	---	---	0.0657
407	66.6	225.0	---	---	0.0545
408	67.5	225.0	---	---	0.0405
409	68.5	225.0	---	---	0.0361
410	68.5	220.0	---	---	---
411	68.5	213.8	---	---	0.0578
412	66.6	213.8	---	---	0.1068
413	63.8	213.8	---	---	0.1318
414	61.5	213.8	---	---	0.2010
415	58.9	202.5	---	---	0.1005
416	60.8	202.5	---	---	0.0666
417	62.1	202.5	---	---	0.0659
418	63.5	202.5	---	---	0.0661
419	65.0	202.5	---	---	0.0663
420	66.4	202.5	---	---	0.0662
421	68.1	202.5	---	---	0.0661
422	68.2	191.2	---	---	0.1646
423	65.8	191.2	---	---	0.1318

Table 1. Concluded

Pressure Orifice No.	FS. in.	Row Location (see Fig. 6) ϕ, deg	Y, in.	Z, in.	Axial Projected Area, $in.^2$
424	59.5	191.2	---	---	0.1608
425	57.5	180.0	---	---	0.0436
426	59.0	180.0	---	---	0.0660
427	60.8	180.0	---	---	0.0654
428	62.5	180.0	---	---	0.0655
429	64.2	180.0	---	---	0.0657
430	66.1	180.0	---	---	0.0545
431	67.6	180.0	---	---	0.0405
432	68.5	180.0	---	---	0.0361
433	66.6	168.8	---	---	0.1646
434	63.0	168.8	---	---	0.1318
435	59.4	168.8	---	---	0.1708
436	57.5	157.5	---	---	0.0636
437	59.1	157.5	---	---	0.0697
438	60.7	157.5	---	---	0.0701
439	62.4	157.5	---	---	0.0694
440	63.9	157.5	---	---	0.0696
441	65.4	157.5	---	---	0.0698
442	66.8	157.5	---	---	0.0579
521	67.9	157.5	---	---	0.0431
522	68.5	157.5	---	---	0.0384
523	68.5	145.0	---	---	0.0578
524	66.9	145.0	---	---	0.0740
525	65.6	145.0	---	---	0.0477
526	64.2	---	0.36	-1.810	0.0951
527	62.0	---	0.36	-1.986	0.0657
528	61.5	---	0.36	-2.149	0.0663
529	59.8	---	0.36	-2.300	0.0366
530	58.1	---	0.36	-2.441	0.0335
531	58.6	---	0	-2.197	0.0502
532	62.1	---	0	-1.867	0.0570
533	64.6	---	0	-1.465	0.1005
534	65.4	---	0.36	-1.613	0.0477
535	66.8	135.0	---	---	0.0789
536	67.8	135.0	---	---	0.0384
537	68.5	135.0	---	---	0.0342
538	67.6	123.8	---	---	0.0704
539	67.1	---	0	-0.894	0.0302
540	68.5	112.5	---	---	0.0704
541*	68.9	22.5	---	---	---
542*	68.9	315.0	---	---	---
543*	68.9	225.0	---	---	---
544*	68.9	145.0	---	---	---

*Diagnostic Taps

Table 2. Nozzle Pressure Instrumentation
a. Cruise Nozzle

Tap Numbers

	R, in.	1.62	1.588	1.54	1.41	1.36	1.26	1.06	1.007	Exit Static
	FS	69.2	69.3	69.5	69.8	69.9	70.2	70.6	70.7	71.0
ϕ, deg	0	—	102	—	—	103	—	104	—	—
	22.5	—	107	—	—	106	—	105	—	—
	45.0	108	—	109	110	—	111	—	112	113
	67.5	—	116	—	—	115	—	114	—	—
	90.0	—	117	—	—	118	—	119	—	—
	112.5	—	122	—	—	121	—	120	—	—
	135.0	123	—	124	125	—	126	—	127	128
	157.5	—	131	—	—	130	—	129	—	—
	180.0	—	132	—	—	133	—	134	—	—
	202.5	—	137	—	—	136	—	135	—	—
	225.0	138	—	139	140	—	141	—	142	202
	247.5	—	205	—	—	204	—	203	—	—
	270.0	—	206	—	—	207	—	208	—	—
	292.5	—	211	—	—	210	—	209	—	—
	315.0	212	—	213	214	—	215	—	216	217
	337.5	—	220	—	—	219	—	218	—	—

Table 2. Continued
b. Reheat Nozzle

Tap Numbers

	R, in.	1.647	1.617	1.59	1.495	1.462	1.38	1.288	1.22	Exit Static
	FS	69.2	69.3	69.5	69.8	69.9	70.2	70.4	70.6	70.8
ϕ, deg	0	—	102	—	—	103	—	104	—	—
	22.5	—	107	—	—	106	—	105	—	—
	45.0	108	—	109	110	—	111	—	112	113
	67.5	—	116	—	—	115	—	114	—	—
	90.0	—	117	—	—	118	—	119	—	—
	112.5	—	122	—	—	121	—	120	—	—
	135.0	123	—	124	125	—	126	—	127	128
	157.5	—	131	—	—	130	—	129	—	—
	180.0	—	132	—	—	133	—	134	—	—
	202.5	—	137	—	—	136	—	135	—	—
	225.0	138	—	139	140	—	141	—	142	202
	247.5	—	205	—	—	204	—	203	—	—
	270.0	—	206	—	—	207	—	208	—	—
	292.5	—	211	—	—	210	—	209	—	—
	315.0	212	—	213	214	—	215	—	216	217
	337.5	—	220	—	—	219	—	218	—	—

Table 2. Concluded
c. Maximum Nozzle

Tap Numbers

ϕ, deg	R, in.	1.675	1.648	1.559	1.590	1.510	1.466	Exit Static
	FS	69.2	69.5	70.0	69.8	70.2	70.4	70.5
	0	—	102	103	—	—	104	—
	22.5	—	107	106	—	—	105	—
	45.0	108	109	—	110	111	112	113
	67.5	—	116	115	—	—	114	—
	90.0	—	117	118	—	—	119	—
	112.5	—	122	121	—	—	120	—
	135.0	123	124	—	125	126	127	128
	157.5	—	131	130	—	—	129	—
	180.0	—	132	133	—	—	134	—
	202.5	—	137	136	—	—	135	—
	225.0	138	139	—	140	141	142	202
	247.5	—	205	204	—	—	203	—
	270.0	—	206	207	—	—	208	—
	292.5	—	211	210	—	—	209	—
	315.0	212	213	—	214	215	216	217
	337.5	—	220	219	—	—	218	—

Table 3. Test Summary
a. Wingtip Support

Nozzle	δ_H, deg	Remarks	Variable	M_∞														
				0.6				0.8	0.9				1.2				1.5	1.6
				Re*														
				1.7	2.8	4.2	5.6	2.8	1.7	2.8	4.2	5.6	1.7	2.8	4.2	4.8	2.8	2.8
Cruise	0	—	α	—	X	—	—	—	—	X	X	—	—	—	—	—	—	—
			NPR	X	—	X	X	X	X	—	X	X	—	X	—	—	—	X
↓	−2	—	α	—	X	—	—	—	—	X	X	—	—	—	—	—	—	—
			NPR	—	—	—	—	X	X	X	X	X	X	X	X	X	—	—
	—	Empennage Removed	α	—	X	—	—	—	—	X	—	—	—	X	—	—	—	—
			NPR	—	—	—	—	—	—	—	—	—	—	—	—	—	—	—
Reheat	0	—	α	—	X	—	—	—	—	X	—	—	—	—	X	—	—	—
			NPR	—	—	—	—	X	X	X	X	X	—	X	—	—	—	X
↓	−2	—	α	—	—	—	—	—	—	—	—	—	—	—	—	—	—	—
			NPR	—	—	—	—	—	X	X	X	X	X	X	X	X	—	—
	−5	—	α	—	—	—	—	—	—	—	—	—	—	X	—	—	—	—
			NPR	—	—	—	—	—	—	—	—	—	—	X	—	—	—	—
↓	−2	Boundary Transition Grit	α	—	—	—	—	—	—	X	—	—	—	—	—	—	—	—
			NPR	—	—	—	—	—	X	X	X	X	—	—	—	—	—	—
Maximum	0	—	α	—	—	—	—	—	—	X	—	—	—	—	—	—	—	—
			NPR	—	—	—	—	—	X	X	X	X	—	X	X	—	X	X
Maximum	−2	—	α	—	—	—	—	—	—	X	—	—	—	—	—	—	—	—
			NPR	—	—	—	—	—	X	X	X	X	—	X	X	X	X	X

*Re – Reynolds number per million per foot

Table 3. Concluded
b. Sting Support

($Re = 2.8 \times 10^6/ft$)

Nozzle	δ_H, deg	$\dot{w}_{BP}$, lb/sec	Remarks	M_∞									
				0.6		0.9		1.2		1.4		1.5	
				Wingtip Support Simulation									
				On	Off	On	Off	On	Off	On	Off	On	Off
Cruise	0	Off	α Varied	X	X	X	—	X	X	—	—	—	—
↓	0	0.02	↓	X	X	X	—	X	—	—	—	—	—
	0	0.035		X	—	X	—	X	—	—	—	—	—
	-2	Off		X	X	X	—	X	X	—	—	—	—
Reheat	0	Plugged	α Varied	X	X	X	X	X	X	X	X	—	—
Reheat	-2	Plugged	α Varied	X	X	X	X	X	X	—	X	—	—
Maximum	0	Plugged	α Varied	—	—	X	X	X	X	X	X	X	X
↓	↓	0.01	↓	—	—	—	—	—	X	—	—	—	—
		0.02		—	—	—	X	—	X	—	X	—	X
		0.035		—	—	—	—	—	X	—	X	—	X
	-2	Plugged		—	—	X	X	X	X	X	X	X	X

NOMENCLATURE

A_i	Projected area assigned to each aft end surface pressure tap for integrating the axial and normal pressure loadings, in.^{2}
A_x	Fuselage axial projected cross-sectional area at fuselage station X, in.^{2} (see Fig. 9)
C_A	Pressure-integrated axial-force coefficient $\sum_i CP_i A_i/S$
C_D	Drag coefficient from pressure-integrated loads
CP_i	Local pressure coefficient $(P_i - P_\infty)/Q_\infty$
DCP	Differential pressure coefficient from two specified configurations or test conditions (see Fig. 6b for angular orientation of pressure rows)
FS	Fuselage axial station, in.
HRL	Horizontal reference line
M_∞	Free-stream Mach number
NPR	Nozzle pressure ratio (model chamber total pressure/free-stream static pressure)
P_i	Local surface pressure, psia
P_∞	Free-stream static pressure, psia
Q_∞	Free-stream dynamic pressure, psi
R	Nozzle outer surface contour radius, in. (see Fig. 5b)
Re	Free-stream Reynolds number per foot, per million
r	Internal nozzle surface radius, in. (see Fig. 5b)
S	Wing reference area, 505 in.^{2}
t	Strake width, in. (Fig. 4)
$\dot{w}_{BP}$	Bay purge flow rate, lb/sec, model scale

X	Longitudinal distance from FS 68.9 in. (see Fig. 5b)
Y	Lateral distance from model centerline, in.
Z	Vertical distance from IIRL, in.
α	Model angle of attack, deg (nose up-positive)
Δ	Prefix indicating a difference between two configurations or test conditions
δ_H	Horizontal tail deflection angle, deg (leading edge down-negative)
ϕ	Pressure tap angular orientation, deg (see Fig. 6b)

Nozzle Closure

CR-Cruise
RH-Reheat
MX-Maximum
} (see Figs. 5a and b)

SUBSCRIPT

i	Individual surface pressure